



**HAL**  
open science

# Innovative non-destructive methodology for energy diagnosis of building envelope

Yingying Yang

► **To cite this version:**

Yingying Yang. Innovative non-destructive methodology for energy diagnosis of building envelope. Mechanics [physics]. Université de Bordeaux, 2017. English. NNT: 2017BORD0913 . tel-01719261

**HAL Id: tel-01719261**

**<https://theses.hal.science/tel-01719261>**

Submitted on 28 Feb 2018

**HAL** is a multi-disciplinary open access archive for the deposit and dissemination of scientific research documents, whether they are published or not. The documents may come from teaching and research institutions in France or abroad, or from public or private research centers.

L'archive ouverte pluridisciplinaire **HAL**, est destinée au dépôt et à la diffusion de documents scientifiques de niveau recherche, publiés ou non, émanant des établissements d'enseignement et de recherche français ou étrangers, des laboratoires publics ou privés.

THÈSE PRÉSENTÉE  
POUR OBTENIR LE GRADE DE  
**DOCTEUR DE**  
**L'UNIVERSITÉ DE BORDEAUX**

ÉCOLE DOCTORALE: SCIENCES PHYSIQUES ET DE L'INGÉNIEUR (SPI)  
SPÉCIALITÉ: MÉCANIQUE

Par Yingying YANG

**INNOVATIVE NON-DESTRUCTIVE METHODOLOGY FOR  
ENERGY DIAGNOSIS OF BUILDING ENVELOPE**

Sous la direction de : Jean-Christophe BATSALE  
(Co-encadrant: Tingting VOGT WU, Alain SEMPEY)

Soutenue le Dec.18th, 2017

Membres du jury :

M. BRUNEAU, Denis	Professeur (HDR), ENSAP Bordeaux	Président
M. DEFER, Didier	Professeur (HDR), Université d'Artois	Rapporteur
M. DUMOULIN, Jean	Ingénieur de recherche, IFSTTAR	Examineur
M. IBOS, Laurent	Maître de conférences (HDR), Université de Paris-Est	Rapporteur
M. BATSALE, Jean-Christophe	Professeur (HDR), Arts et Métiers Paris Tech	Directeur
Mme. VOGT WU, Tingting	Maître de conférences, Université de Bordeaux	Co-encadrant
M. SEMPEY, Alain	Maître de conférences, Université de Bordeaux	Co-encadrant



# METHODOLOGIES INNOVANTES NON DESTRUCTIVES APPLIQUEES AU DIAGNOSTIC ÉNERGÉTIQUE DE L'ENVELOPPE DU BÂTIMENT

## Résumé

Le secteur du bâtiment représente 35% des la consommations énergétiques dans les pays membres de l'agence international de l'énergie en 2010 et 39,8% aux Etats-Unis en 2015. Plus de 50% de cette consommation a été utilisée pour la production de chaleur et de froid. Néanmoins cette consommation peut être réduite par l'amélioration la performance énergétique du bâtiment. La performance thermique de l'enveloppe du bâtiment joue un rôle primordial. Par conséquent, le diagnostic thermique de l'enveloppe du bâtiment est nécessaire pour, par exemple, la réception de nouvelles constructions, l'amélioration de la performance énergétique des anciens bâtiments, ainsi que la vente et la location des logements. Pourtant, il existe très peu de méthodes quantitatives pour la caractérisation des parois épaisses. L'objectif de cette étude est d'explorer des méthodes quantitatives innovantes de diagnostic thermique de l'enveloppe du bâtiment. Des mesures expérimentales ont été réalisées en laboratoire (à l'IFSTTAR à Nantes) et in situ (à l'IUT de Bordeaux). Différents capteurs et méthodes d'instrumentation ont été étudiés pour mesurer la densité de flux et la température de surfaces des parois, afin de procurer des recommandations pour le choix des capteurs ainsi que des protocoles de traitement de données. A partir des données mesurées (température et densité de flux des surfaces de l'enveloppe), trois approches numériques ont été proposées pour estimer des paramètres thermiques des parois multicouches épaisses : par méthode inverse, par réponse à un échelon et par réponse impulsionnelle. En outre, une méthode innovante non-destructive utilisant la rayonnement térahertz a été étudiée. Les mesures ont été effectuées au sein du laboratoire I2M. Cette méthode permet de caractériser le coefficient d'absorption des matériaux constructifs ordinaires comme isolation, plâtre, béton, bois... Elle pourrait postérieurement être combinée avec une méthode thermique pour apporter des informations complémentaires.

**Mots clés :** CND (Contrôle non destructif), enveloppe du bâtiment, caractérisation des propriétés thermiques, diagnostic quantitatif, quadripôle thermique, méthode inverse, réponse impulsionnelle, réponse à un échelon, instrumentation



# INNOVATIVE NON-DESTRUCTIVE METHODOLOGY FOR ENERGY DIAGNOSIS OF BUILDING ENVELOPE

## Abstract

Buildings represent a large share in terms of energy consumption, such as 35% in the member countries of IEA (2010) and 39.8% in U.S. (2015). Climate controlling (space heating and space cooling) occupies more than half of the consumption. While this consumption can be reduced by improving the building energy efficiency, in which the thermal performance of building envelope plays a critical role. Therefore, the thermal diagnosis of building envelope is of great important, for example, in the case of new building accreditation, retrofitting energy efficiency of old building and the building resale and renting. However, very few diagnostic methods exist for the characterization of thick walls. The present measurement standards that based on steady state heat transfer regime need a long time (several days). The classical transient technologies, such as flash method, are difficult to implement on the walls because of the large thickness of walls and the complex conditions in situ. This thesis aims to explore innovative methodologies for thermal quantitative diagnosis of building envelope. Two experimental cases were carried out: one is in laboratory (IFSTTAR, Nantes) and the other is in situ (IUT, Bordeaux). Different sensors and instruments were studied to measure the wall heat flux and surface temperature, and provided some guidelines for the choice of sensors and data processing protocols as well. Using these measured data, three estimation approaches were proposed to estimate the thermal parameters of the multilayer thick wall: pulse response curve method, step response curve method and inverse method, which can be applied for different diagnostic situations. In addition, an innovative NDE (non-destructive evaluation) method using terahertz (THz) radiation was also investigated. Measurements were carried out in I2M laboratory to characterize the absorption coefficient of standard building materials (insulation, plaster, concrete, wood ...). This THz method can be combined with a previous thermal method to provide some complementary information.

**Keywords :** NDE (non-destructive evaluation), building envelope, thermal properties characterization, quantitative diagnosis, thermal quadrupoles solution, inverse method, pulse response, step response, instrumentation.

---

**Unité de recherche**

I2M-TREFLE, UMR CNRS 5295, Esplanade des arts et Metiers 33405 Talence



# Acknowledgement

I am deeply grateful for the generosity and kindness of the many people who have supported me in producing this research. I am very excited to think of I could have an experience studying in France.

I would like to first thank to my supervisor and co-directors. Prof. Jean-Christophe BATSALE, the director of I2M, gave me a lot of help on numerical analyses of this reserach. With his deep knowledge and his visions, he laid the foundation of this thesis. He showed much interest in my work and has been a source of motivation. This research would not have been possible without Tingting VOGT WU and Alain SEMPEY, who always spent time to give advice and feedback. They have made remarkable efforts for this project. I am deeply thankful for their kindness, their trust and concern for my work. In addition, I sincerely thank to Jean Dumoulin, who has given me support, assistance and advice when I was in Nantes for experiments. Then I would like to thank Christophe PRADERE and Alain SOMMIER, who helped me a lot on experiments. Consequencely, I would like to thank the reviewers Didier DEFER and Laurent IBOS for their valuable efforts, which help me improving this thesis. I also thank to Denis BRUNEAU for being an examiner.

More specially, I would like to thank the financial support of the European project Built2Spec which I do believe will make meaningful improvement on the energy conservation. I am deeply grateful for the China Scholarship Council (CSC) for 3 years' financial supporting.

I greatly appreciated working in I2M. Thank all the colleagues who constantly understand and support me. Thanks to Miguel, Marita, Yibao, Hugo, Dung, Romain, Radhouan, Jose, Jérémy, Maïmouna, Nicolas, Audrey, Cécile, Muriel, Sandrine, Fouzia, Ludovic, Stéphanie,... I also thank to the friends I met in Bordeaux and Nantes, and my roommates as well, who enriched my life.

I enjoyed my time in France, which has been a totally life-changing experience. I love Bordeaux. 'If you are lucky enough to have lived in Bordeaux as a young man, then wherever you go for the rest of your life, it stays with you, for Bordeaux is a movable artwork'. This experience gave me some new ideas about life and values, it is so meaningfull that will be unforgettable all my life.

Finally but not least, I thank my family and friends in China for their encouragement and patience, they made this hard work worthwhile. I sincerely thank to my parents for their endless love to me.





# Content

Résumé .....	3
Abstract .....	5
Acknowledgement.....	7
List of Figures .....	13
List of Tables.....	18
Nomenclature .....	20
Chapter 1 Introduction .....	23
1.1 Context .....	23
1.1.1 Importance and necessity.....	23
1.1.2 Conventional thermal diagnosis metrology for solids on lab-scale.....	25
1.1.3 Challenges for thermal diagnosis on building walls in situ.....	32
1.2 Review on thermal diagnostic methodologies for building walls .....	33
1.2.1 Steady state heat transfer techniques .....	33
1.2.2 Transient heat transfer techniques .....	37
1.2.3 Application of infrared thermography (IRT) technique .....	40
1.2.4 Terahertz radiation method.....	46
1.3 Objective and outline .....	48
Chapter 2 Experimental sensors and facilities .....	51
2.1 Sensors .....	52
2.1.1 Infrared camera.....	52
2.1.2 Thermocouples .....	53
2.1.3 Heat flux sensors .....	53
2.2 Sensors calibration .....	56
2.2.1 Calibration of thermocouple.....	56

2.2.2 Calibration of heat flux sensors .....	59
2.3 Experiments in the laboratory .....	65
2.3.1 Experimental scheme and configuration .....	65
2.3.2 Facilities.....	67
2.4 Experiments in situ.....	69
Chapter 3 Measurements and data processing .....	75
3.1 Emissivity.....	75
3.1.1 Emissivity measurement.....	75
3.1.2 Fundamental and data processing.....	76
3.1.3 Emissivity results.....	80
3.2 Heat flux.....	83
3.2.1 Measurements.....	83
3.2.2 Data processing of heat flux .....	84
3.2.3 Heat flux results.....	87
3.3 Temperature measurement with IR camera .....	92
3.4 Thermography processing .....	95
3.4.1 Basic principles of SVD .....	95
3.4.2 Processing multi IR images by PCT.....	98
3.4.3 Image filter .....	101
Chapter 4 Estimation approaches for thermal parameters characterizing .....	103
4.1 Steady state heat transfer method.....	103
4.2 Thermal quadrupoles solution.....	106
4.2.1 Basics of thermal quadrupoles model.....	106
4.2.2 Simulations for several heating signals .....	108
4.2.3 Application to experiments.....	112
4.2.4 Approximated expressions .....	113
4.3 Pulse response curve method .....	114

4.3.1 Simulation analysis of pulse response curve .....	115
4.3.2 Deconvolution of experimental data.....	119
4.3.3 Experimental pulse response results.....	122
4.4 Step response curve method.....	129
4.4.1 Simulation analysis of step response curve .....	129
4.4.2 Experimental results of step response .....	133
4.5 Inverse method to estimate thermal parameters.....	137
4.5.1 Inverse method basics.....	137
4.5.2 Optimal results.....	138
4.6 Comparisons of the three thermal methods.....	149
Chapter 5 Terahertz radiation diagnostic method.....	151
5.1 Introduction .....	151
5.2 Experimental setup.....	153
5.3 Results and analysis .....	156
5.4 Discussion of combination .....	160
Chapter 6 Conclusion and perspectives .....	163
Bibliography .....	167
Appendix.....	175
Appendix A: Infrared camera, FLIR A325 .....	175
Appendix B: Thermocouples fundamentals.....	176
Appendix C: Calibration results of thermocouples .....	179
Appendix D: Calibration of halogen lamps.....	180
Appendix E: ISO 18434-1:2008(E) .....	182
Appendix F: Temperature and heat flux results of the laboratory-case ( $T_1$ $T_2$ $q_1$ $q_2$ ).....	185
Appendix G: Temperature and heat flux results of in situ-case ( $T_1$ $T_2$ $q_1$ $q_2$ ) .....	187
Appendix H: Absorbance and emissivity values of references.....	189
Appendix I: Usual Laplace transform .....	190

Appendix J: Matlab algorithm ..... 191

# List of Figures

Fig. 1-1: Total energy consumption [1] .....	24
Fig. 1-2: Buildings site energy consumption by end use [7] .....	24
Fig. 1-3: Guarded hot plate techniques: (a) NETZSCH instrument, (b) details of the device	27
Fig. 1-4: HFM techniques: (a) NETZSCH instrument. (b) details of device .....	28
Fig. 1-5: Hot box techniques [13] (a) scheme of the guarded hot box (b) the calibrated hot box. ....	28
Fig. 1-6: Transient techniques for thermal diagnosis.....	29
Fig. 1-7: (a) hot disc for transient plane source measurements (b) needle probe for transient line source measurements .....	29
Fig. 1-8: Dimensionless plot of rear surface temperature response [18] .....	31
Fig. 1-9: (a) NETZSCH instrument and (b) its principle based on Flash method.....	32
Fig. 1-10: The instrumented building and the test room walls [21].....	35
Fig. 1-11: Schematic vertical cross-section of guarded hot-box apparatus (dimensions in mm) [32]. ....	36
Fig. 1-12: Exploded view of the hot box apparatus [13] .....	37
Fig. 1-13: Experimental set up [58] .....	38
Fig. 1-14: Scheme of the experiment [37] .....	39
Fig. 1-15: The general concept of EPM—applying a triangular temperature pulse to the surface and measuring heat flux responses on two sides of the wall [60]. ....	40
Fig. 1-16: Principles of heat transfer.....	42
Fig. 1-17: Arrangement for determination of reflected temperature and emissivity [71] .....	43
Fig. 1-18: Instruments for inside and outside of wall in situ [72].....	44
Fig. 1-19: Temperature differences between thermocouple and corrected infrared measurements for three zones of the western facade [73]; .....	44
Fig. 1-20: Principle of the transmission active IRT [75] .....	45
Fig. 1-21: Principle of the reflection active IRT [74] .....	46
Fig. 1-22: Frequency band of THz in electromagnetic spectrum .....	46
Fig. 1-23: Absorption coefficient of a variety of thermal insulating polymer foams in the frequency range between 1.35 THz and 5.0 THz. ....	48

Fig. 1-24: Relation between absorption coefficient at selected THz frequencies and the thermal conductivity of polymer foams.....	48
Fig. 2-1: Principle of IR camera .....	52
Fig. 2-2: FLIR A325 .....	52
Fig. 2-3: (a) The balanced self-generating panel; (b) Flat plate heat flux meter (Captec) .....	54
Fig. 2-4: Peltier module schematic [91].....	55
Fig. 2-5: Peltier sensor .....	55
Fig. 2-6: The correction temperature at 7 ambient temperatures for 17 thermocouples.....	57
Fig. 2-7: Average correction temperature VS the ambient temperature .....	57
Fig. 2-8: Setup of calibration test.....	59
Fig. 2-9: Global scheme of system for calibration test .....	60
Fig. 2-10: Output voltage of Peltier sensor with supplier current ranging from 0.02 to 0.225 A .....	61
Fig. 2-11: Calibration of Peltier 1: output voltage VS heat flux.....	62
Fig. 2-12: Calibration of fluxmeter: output voltage VS heat flux.....	63
Fig. 2-13: Main principle of experiment.....	65
Fig. 2-14: Diagram of experimental set-up.....	66
Fig. 2-15: Photos of instruments (a): Experiment setup (b): Test Area 1 .....	66
Fig. 2-16: Wall box (a) inside of wall box. (b) diagram of wall box.....	67
Fig. 2-17: Scheme of objective wall .....	67
Fig. 2-18: Six halogen lamps .....	69
Fig. 2-19: Heater installed inside the wall box .....	69
Fig. 2-20: Data logger: GRAPHTEC GL840 .....	69
Fig. 2-21: A demonstration building-Platform SYNERGI.....	70
Fig. 2-22: The exterior wall of building that to be tested: outdoor (left) and indoor (right). ..	70
Fig. 2-23: Scheme of objective wall .....	71
Fig. 2-24: Photos and infrared images of wall for defects detecting .....	72
Fig. 2-25: Fluxmeters and thermocouples installed on the test areas .....	72
Fig. 2-26: Photos of facilities.....	73
Fig. 3-1: Test area of emissivity measurement .....	76
Fig. 3-2: Radiation propagation principle .....	77
Fig. 3-3: Planck's law: Blackbody emissive power as a function of wavelength and temperature. ....	78

Fig. 3-4: Schematic of IR camera when measuring temperature [98] .....	78
Fig. 3-5: Test area of emissivity measurement: (left) photo with visible camera, (right) infrared thermography .....	80
Fig. 3-6: radiance of each target area that output from IR camera .....	81
Fig. 3-7: Emissivity results of wall .....	81
Fig. 3-8: Emissivity results .....	82
Fig. 3-9: Square wave heating signal (left) and half sine wave heating signal (right) at period of 24 hours .....	84
Fig. 3-10: Heat flux balance of a target surface .....	85
Fig. 3-11: Temperatures of wall measured by thermocouples.....	88
Fig. 3-12: Temperatures of sensors and wall .....	88
Fig. 3-13: Convection coefficients for Peltier sensor and fluxmeter .....	89
Fig. 3-14: Convection, radiation and total heat flux results of wall for transient heat transfer test.....	90
Fig. 3-15: Comparison of total heat fluxes .....	91
Fig. 3-16: Comparison of convection heat flux .....	91
Fig. 3-17: Comparison of radiation heat flux.....	91
Fig. 3-18: Input parameters of ResearchIR system.....	92
Fig. 3-19: Temperatures measured by thermocouples versus temperature measured by IR camera with setting reflected temperature of 20 °C. ....	93
Fig. 3-20: Temperatures measured by thermocouples versus corrected temperature measured by IR camera. ....	94
Fig. 3-21: (a) Thermographic data rearrangement from a 3D sequence to a 2D matrix of M in order to apply SVD; (b) Rearrangement of 2D U matrix into a 3D matrix containing the EOFs [7] .....	97
Fig. 3-22: Measured infrared image.....	98
Fig. 3-23: $p_j$ values versus the number of singular value.....	98
Fig. 3-24: The comparison of calculated temperature and the measured temperature (left) and the temperature difference (right). ....	99
Fig. 3-25: PCT results .....	100
Fig. 3-26: An original IR image.....	101
Fig. 3-27: Singular values of matrix M (left) and the percentage (Equ. 3-41). ....	101
Fig. 3-28: IR images of each j-value (j is from 1 to 12). ....	102



Fig. 4-1: Temperature results of each layer for steady state heat transfer .....	104
Fig. 4-2: Heat flux results of wall for steady state heat transfer measurement.....	104
Fig. 4-3: Thermal resistance values for steady state heat transfer measurement.....	105
Fig. 4-4: Transient heat transfer in homogenous medium: (a) geometry; (b) matrix representation.....	107
Fig. 4-5: Temperature responses to a pulse heating signal .....	109
Fig. 4-6: Temperature responses to a continuous step heating signal.....	110
Fig. 4-7: Temperature responses to a square wave heating signal.....	111
Fig. 4-8: Temperature responses to a periodic square wave heating signal.....	111
Fig. 4-9: Superposition principle: (a) random heat flux at each interval time step. (b) temperatures generated by heat flux of each time step .....	112
Fig. 4-10: Quadrupole network of considering heat loss .....	113
Fig. 4-11: Heat transfer model of a high resistance medium: (a) network expression; (b) matrix expression.....	113
Fig. 4-12: Heat transfer model of a high conductivity medium: (a) network expression; (b) matrix expression.....	114
Fig. 4-13: Four cases to be simulated .....	115
Fig. 4-14: Simulated pulse response at adiabatic boundary condition.....	116
Fig. 4-15: Simulated pulse response when considering heat loss at the rear face. ....	118
Fig. 4-16: Simulated pulse response .....	119
Fig. 4-17: $\delta$ -values versus j-values .....	121
Fig. 4-18: Front face temperature and heat flux of a test with a periodic heating signal (period of 24 hours).....	122
Fig. 4-19: Pulse response results in the lab-case (test with square wave heating signal of period of 24 hours).....	123
Fig. 4-20: Front face temperature and heat flux of a test with a periodic heating signal (period of 96 hours).....	123
Fig. 4-21: Pulse response results in the lab-case (test with square wave heating signal of period of 96 hours).....	124
Fig. 4-22: Linear fitting of experimental pulse response curve .....	125
Fig. 4-23: Results of test with a step heating signal (test 1) .....	126
Fig. 4-24: Results for test with a step signal (test 2).....	127
Fig. 4-25: Results for test with a periodic heating signal (test 3) .....	128

Fig. 4-26: Three typical wall models: C is concrete layer; I is insulating layer; P is plaster layer; $T_1$ is front face temperature; $q$ is heat flux. ....	130
Fig. 4-27: Estimation of front face step response for three wall models at semi-infinite condition (a) exact quadrupoles model (b) approximated quadrupoles model.....	131
Fig. 4-28: Sensitivity of front face temperature to thermal parameters .....	133
Fig. 4-29: Measured front face temperature and its linear fitting in the laboratory case.....	134
Fig. 4-30: Measured front face temperature and its linear fitting (Test 1) .....	136
Fig. 4-31: Inverse method flow chart.....	138
Fig. 4-32: The sensitivity of front face temperature ( $T_1$ ) to the 8 thermal parameters .....	139
Fig. 4-33: The sensitivity of rear face temperature ( $T_2$ ) to the 8 thermal parameters.....	139
Fig. 4-34: Correlation study of sensitivities between $\lambda_{\text{block}}$ and $\rho_{\text{Cblock}}$ .....	140
Fig. 4-35: The predicted temperature versus measured temperature .....	141
Fig. 4-36: Sensitivity of front face temperature ( $T_1$ ) for the 8 thermal parameters .....	145
Fig. 4-37: $T_1$ of test area without defect VS $T_1$ of test area with defect .....	147
Fig. 5-1: Beer-Lambert law for multilayer materials.....	152
Fig. 5-2: The CW THz method system.....	153
Fig. 5-3: Experimental setup.....	154
Fig. 5-4: Building materials tested by THz wave .....	155
Fig. 5-5: Dried concrete in vacuum box. ....	155
Fig. 5-6: Absorption coefficient results for XPS, plaster and fiberglass .....	157
Fig. 5-7: Absorbance of plaster at different thickness .....	159

## List of Tables

Table 1-1: Experimental results [30] .....	35
Table 2-1: Parameters of FLIR A325 .....	53
Table 2-2: Parameters of fluxmeters.....	54
Table 2-3: Calibration results of thermocouples in IUT lab .....	58
Table 2-4: Sensitivity of Peltier 1 at 10 values of heat flux.....	61
Table 2-5: Calibration results of Peltier sensors .....	62
Table 2-6: Uncertainties of calibration test.....	63
Table 2-7: Uncertainty of measurement heat flux .....	64
Table 2-8: Reference values of wall thermal properties .....	68
Table 2-9: Thermal properties of each layer of wall [92]–[94] .....	71
Table 3-1: Results of measured emissivity .....	83
Table 3-2: Physical properties of atmospheric air .....	86
Table 3-3: First 10 values of $w_i$ and $p_j$ .....	98
Table 3-4: First 10 values of $w_i$ and $p_j$ .....	101
Table 4-1: Thermal resistance results of each layer.....	105
Table 4-2: Thermal properties of insulation and concrete block .....	115
Table 4-3: j-values of 4 tests when $\delta$ is 0.1, 0.2 and 0.3 .....	122
Table 4-4: Global effusivity of mortar and cinder block .....	125
Table 4-5: Thermal properties of materials for simulation.....	129
Table 4-6: Equations of three wall models at semi-infinite condition.....	130
Table 4-7: Concrete block effusivity results through analyzing temperature response method .....	135
Table 4-8: Thermal resistance results through analyzing temperature response method .....	136
Table 4-9: Iteration information.....	141
Table 4-10: Output solutions with different initial values .....	142
Table 4-11: Output solutions in different characterization time .....	143
Table 4-12: Optimal values with front face temperature .....	143
Table 4-13: Optimal values with rear face temperature.....	144
Table 4-14: Optimal results with the front face temperature in the in situ-case.....	146
Table 4-15: Optimal thickness of insulation in defect-area .....	147

Table 5-1: Absorption coefficient results for 15 building materials.....	158
Table 5-2: Results of Plaster at different thickness .....	158
Table 5-3: Absorption coefficient for multilayer samples.....	159

## Nomenclature

$A$	Absorbance	-
$a$	Absorptivity	-
$b$	Effusivity	$J \cdot K^{-1} \cdot m^{-2} \cdot s^{-0.5}$
$B_e$	The bias error	
$c$	Specific heat capacity	$J \cdot K^{-1} \cdot kg^{-1}$
$C_t$	Heat capacity	$J \cdot K^{-1}$
$e_r$	Relative error	
$E$	Emittance radiation	$W \cdot m^{-2}$
$G$	Total ambient radiation	$W \cdot m^{-2}$
$Gr$	Grashof number	
$g$	Pulse response	
$h$	Heat transfer coefficient	$W \cdot K^{-1} \cdot m^{-2}$
$I$	Current	A
$I_t$	Intensity of output signal	V
$I_0$	Intensity of input signal	V
$j$	Truncation parameter for TSVD	
$k$	Sensitivity of heat flux sensors	$\mu V \cdot W^{-1} \cdot m^{-2}$
$L$	Thickness	m
$Nu$	Nusselt number	
$p$	Laplace transformed time	
$q$	Heat flux	$W \cdot m^{-2}$
$Q$	Pulse power	$J \cdot m^{-2}$
$r$	Residual	
$R$	Thermal resistance	$K \cdot m^2 \cdot W^{-1}$
$Ra$	Rayleigh number	
$R_l$	Electrical resistance	$\Omega$
$R^2$	Coefficient of determination	
$R'$	Correlation coefficient	
$R_e$	The random error	
$S$	Area	$m^2$
$T$	Temperature	K or $^{\circ}C$
$t$	Time	s or h

$\bar{U}$	Thermal transmittance	$W \cdot K^{-1} \cdot m^{-2}$
$U_p$	Output voltage by heat flux sensor	$\mu V$
$U_s$	Supplier voltage	V
$v$	Wind velocity	$m \cdot s^{-1}$
$W$	Radiation	$W \cdot m^{-2}$ or $W/sr \cdot cm^2$
$x$	Location inside medium	

***Subscript***

<i>air</i>	Air
<i>atm</i>	Atmosphere
<i>Alu</i>	Aluminum
<i>b</i>	Black heat flux sensor or black body
<i>obj</i>	Target object
<i>cam</i>	Camera
<i>cap</i>	Fluxmeter
<i>cal</i>	Calculated
<i>c</i>	Cooling
<i>conv</i>	Convection
<i>correction</i>	Corrected values
<i>exp</i>	Experiments
<i>h</i>	Heating
<i>in</i>	Internal
<i>i</i>	Indoor
<i>IR</i>	Parameters for infrared camera
<i>o</i>	Outdoor
<i>obj</i>	objective
<i>objective</i>	Parameters from object / objective
<i>out</i>	External
<i>Ps</i>	Shiny Peltier sensor
<i>Pb</i>	Black Peltier sensor
<i>r</i>	Radiant
<i>rad</i>	Radiation
<i>refl</i>	Reflected
<i>refe</i>	Reference
<i>reference</i>	Parameters from reference

<i>s</i>	Shiny heat flux sensor	
<i>surf</i>	Surface	
<i>t</i>	Output	
<i>thermocouple</i>	Measured by thermocouple	
<i>tot</i>	Total	
<i>wall</i>	Parameters for wall	
<i>0</i>	Input	
<i>1</i>	Front face of wall	
<i>2</i>	Rear face of wall	
<b><i>Greek alphabet</i></b>		
$\alpha$	Thermal diffusivity	$\text{m}^2 \cdot \text{s}^{-1}$
$\kappa$	Absorption coefficient	
$\lambda$	Thermal conductivity	$\text{W} \cdot \text{m}^{-1} \cdot \text{K}^{-1}$
$\lambda'$	Wavelength	$\mu\text{m}$
$\varepsilon$	Emissivity	
$\theta$	Temperature (Laplace domain)	
$\Phi$	Heat flux (Laplace domain)	
$\rho$	Density	$\text{Kg} \cdot \text{m}^{-3}$
$\sigma$	Stefan-Boltzmann constant	$\text{W} \cdot \text{K}^{-4} \cdot \text{m}^{-2}$
$\delta$	Standard deviation	
$\tau$	Transmissivity	
$\gamma$	Reflectivity	
$\Delta$	Uncertainty/difference	

# Chapter 1

## Introduction

---

---

### 1.1 Context

#### 1.1.1 Importance and necessity

Environmental degradation and energy crisis problems are becoming more and more obvious since last century. The total energy consumption is rising in the last several decades [1] (Fig. 1-1 and will keep increasing in the future decades if we do nothing. The global CO<sub>2</sub> emissions have increased by 51% since 1990. Awareness of energy conservation and environment protection is growing and the analytical works are into concrete actions. Many countries all over the world are making efforts on the energy and environment. More than 170 countries have signed a legally binding and universal agreement on climate (Paris agreement) negotiated in 2015 COP21 (Conference of Parties) to reduce greenhouse gas emissions. Fortunately, the primary energy intensity is decreasing in 80% of World Energy Council's member countries and most regions. There is also a decreasing trend in energy consumption per household.

In the energy structure, buildings consume the largest share comparing with industry, transport and others, and also consumes half of global electricity. Meanwhile, buildings are also



responsible for about 17% of total direct energy-related CO<sub>2</sub> emissions from final energy consumers [2]–[5]. According to the IEA(International Energy Agency) statistics [6], buildings represent 35% (2010 edition) of total final energy consumption. In terms of primary energy consumption, buildings represent around 40% in most IEA countries. U.S. buildings represent 39.8% of total energy use in 2015 (residential and commercial sectors are combined). Moreover, with the increasing population, economic development and improving living levels, the building consumption will rise sharply in the future and form additional pressure on the energy system. Energy demand in buildings will rise in the future decades.

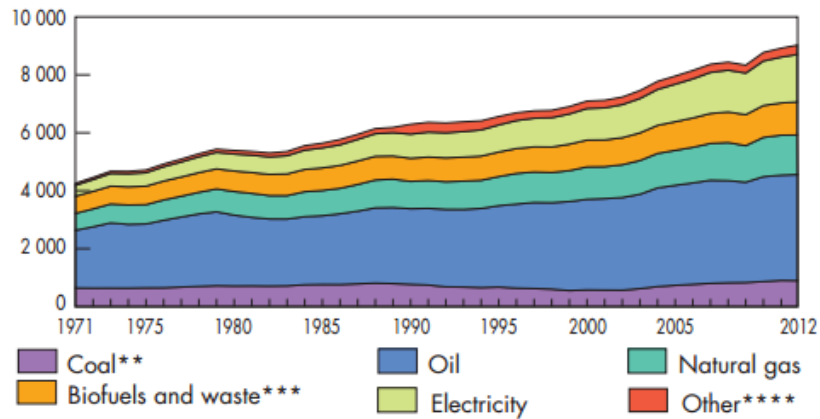


Fig. 1-1 Total energy consumption [1]

Building energy consumption mainly includes climate controlling (space heating and cooling), water heating, applications, lighting and other installed equipment. As shown in Fig.1-2 [7], the top four end uses space heating, space cooling, water heating, and lighting—accounted for close to 70% of site energy consumption. Climate controlling occupies more than half of the consumption, which can be improved by rising the building energy efficiency.

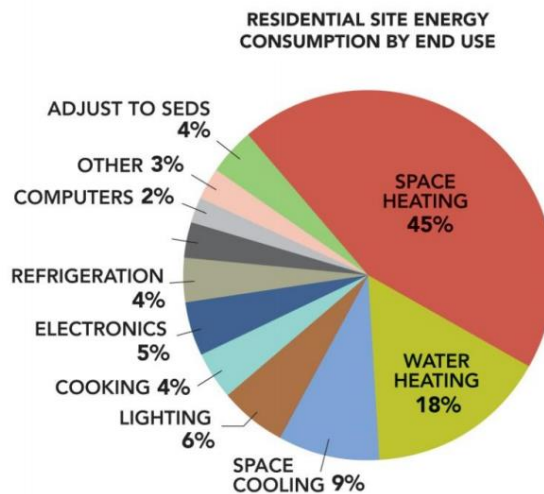


Fig. 1-2 Buildings site energy consumption by end use [7]

Meanwhile, direct CO<sub>2</sub> emissions in the residential and commercial building sectors are largely from space heating, space cooling, water heating, and cooking equipment. The CO<sub>2</sub> emissions associated with the use of electricity in these sectors exceed the direct emissions from these sectors.

A building with high energy efficiency can reduce the energy consumption and CO<sub>2</sub> emissions by climate controlling. Improving the building energy efficiency is of great importance. Methods and policies are encouraged to renovate and improve the energy efficiency of both existing buildings and future buildings. The building envelope plays a critical role in determining levels of comfort and building efficiency. A building envelop with good thermal performance can prevent heat loss from indoor to outdoor in winter and protect from heated by outdoor ambient in summer.

Research and development on the thermal diagnostic methodology in building envelop become a hot topic and inevitable trend, for example, it is necessary in the following cases:

- (1) New building accreditation: for new buildings, though the wall performances have been designed, once built, the wall characteristics may be not the designed values because of the faults of construction management, humidity, the compaction or expansion of the thermal insulation, materials defects and so on. This performance Gap (the difference between the energy use that buildings are designed to achieve and what they actually achieve when built and in use) is a real problem. Therefore, the wall properties of a new building is recommended to be verified when it was built.
- (2) Renovating energy efficiency of existing building: the thermal properties of old buildings evolve from that when it was built. The properties data of the old building may be lost or incomplete. The in situ inspection on old building wall is required to improve the energy efficiency.
- (3) Building resale and renting: Energy Performance Certifications (EPCs) are important obligations, the building envelope plays evidence role.
- (4) New energy-efficient building materials characterization: the new energy-efficient building materials should be characterized before the application to minimize energy required and decrease heat loses.

### **1.1.2 Conventional thermal diagnosis metrology for solids on lab-scale**

There are three heat transfer forms: radiation, convection and conduction. All the three forms are considered in the thermal properties measurement.

For the thermal radiation heat transfer, the equation of radiation energy ( $E$ ) is based on the Stefan Boltzmann law, the radiation heat flux ( $q$ ) from body  $a$  to body  $b$  is given by:

$$q = F_{a-b}\sigma(T_a^4 - T_b^4) \quad 1-1$$

Where  $F_{a-b}$  is the view factor, for the situation of a small grey object (body  $a$ ) in a large environment (body  $b$ ), the solutions of view factor are:  $F_{a-b} \cong \varepsilon_a$   $F_{b-a} \cong 1$ .

For the convection heat transfer, the heat flux calculation is based on Newton's law:

$$q = h(T_{surf} - T_{air}) \quad 1-2$$

The equation for heat conduction is:

$$\frac{\partial^2 T}{\partial x^2} + \frac{\partial^2 T}{\partial y^2} + \frac{\partial^2 T}{\partial z^2} + \frac{q}{\lambda} = \frac{1}{\alpha} \frac{\partial T}{\partial t} \quad 1-3$$

Generally, the following parameters are used for representing the heat transfer ability of materials: thermal conductivity ( $\lambda$ ), thermal effusivity ( $b$ ), thermal diffusivity ( $\alpha$ ), thermal transmittance ( $\bar{U}$ ) and thermal resistance ( $R$ ), where

$$b = \sqrt{\lambda\rho c} \quad 1-4$$

$$\alpha = \lambda/\rho c \quad 1-5$$

$$R = L/\lambda \quad 1-6$$

$$\bar{U} = 1/R \quad 1-7$$

Many methodologies have been developed to estimate these thermal parameters of solids. According to the heat transfer regimes, these methods are divided into steady-state techniques and transient (dynamic) techniques [8]. These methods are usually used on small-scaled solids and mainly implement in the laboratory. The followings will introduce some well-developed diagnosis technologies on lab-scale.

### 1.1.2.1 Steady state techniques

The steady-state techniques are the earliest group of measurement techniques. These measurements are based on a steady state heat transporting: establishing a temperature gradient on a sample with known thickness, controlling the heat flow from one side to the other and ensuring a one-dimensional flow approach. The thermal conductivity and thermal resistance can be calculated by Equ. 1-7 and Equ. 1-8, which are simply obtained by measuring the temperature gradient and the heat flow through the sample. These methods are primarily suitable for analyzing materials with low or average thermal conductivities at moderate

temperatures [8]. The difficulties of this method are to build the steady state heat transfer regime and to obtain the heat flux ( $q$ ).

$$R = q/\Delta T \quad 1-8$$

Three measurement techniques are commonly used: the guarded hot plate technique, the heat-flow meter technique and the hot-box technique.

The guarded hot plate method has become a standard: ISO 8302 [9]. Heat was supplied electrically at a known rate to the hot plate, the cold plates were maintained at constant temperature by circulation of either water or brine through the plates, so that a constant temperature difference was maintained between the hot and cold plates. The thermal conductivity of the sample can be obtained with the constant temperature difference and the given heat flow based on Equ. 1-8. Industrial instruments have been manufactured based on this techniques. For instance, Fig. 1-3 is the device of NETZSCH GHP 456 for measuring thermal conductivity.

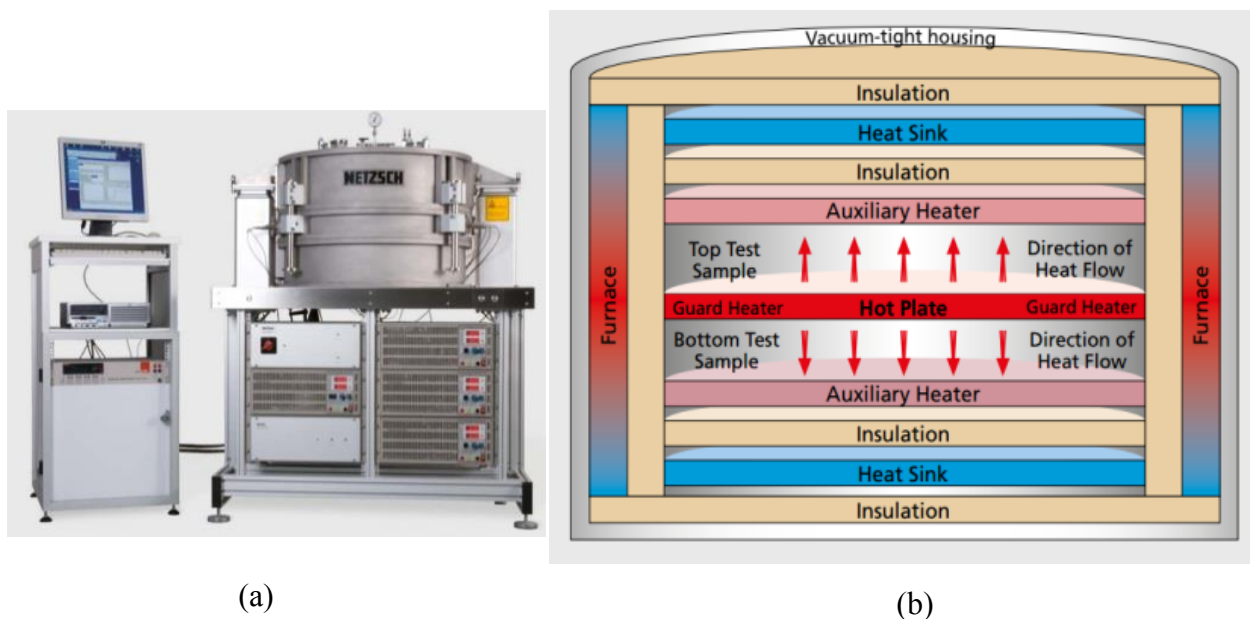


Fig. 1-3 Guarded hot plate techniques: (a) NETZSCH instrument, (b) details of the device

The heat-flow meter technique is to use a heat flow sensor to measure the heat flux. Similarly, the thermal conductivity of tested sample can be calculated with this measured heat flux and temperature difference based on Equ. 1-8. This method has also become the standards: ASTM C518 [10] and ISO 8301 [11]. Fig. 1-4 is the manufactured instrument: NETZSCH HFM 436 Lambda.

## 1.1 Context

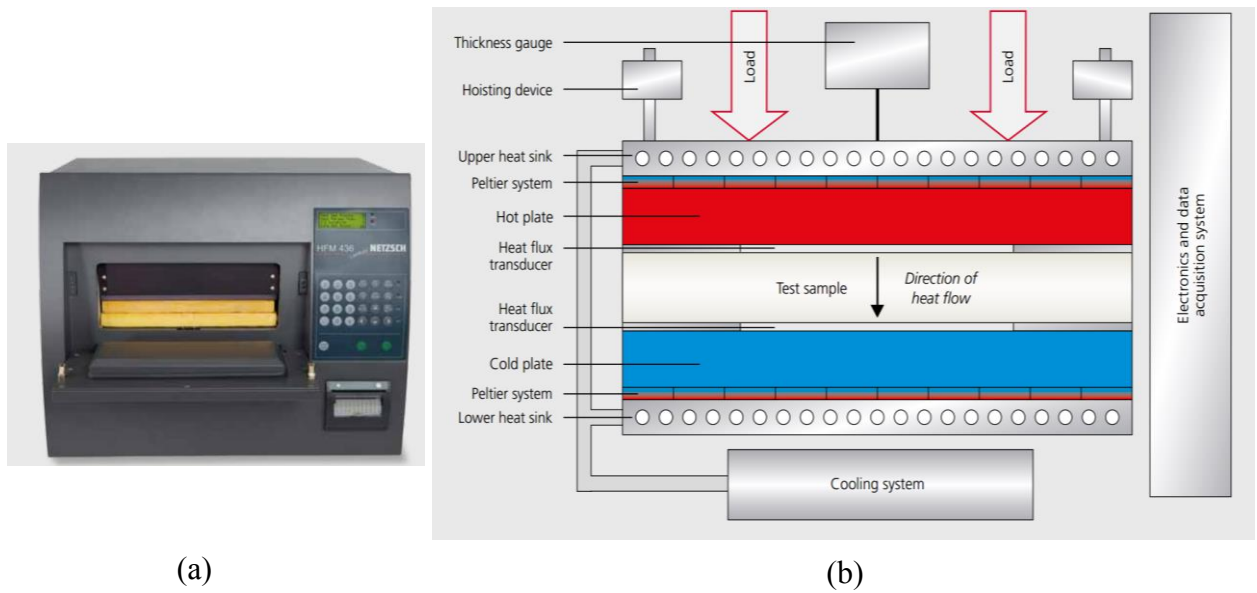


Fig. 1-4 HFM techniques: (a) NETZSCH instrument. (b) details of device

The hot box technique (ISO 8990) [12] is usually used for estimating the overall thermal resistance or thermal transmittance (heat transfer from air to air). It includes the Guarded Hot Box and the Calibrated Hot Box. In the Guarded Hot Box method, as shown in Fig. 1-5 (a) [13], a large specimen is placed between a hot and a cold chamber operating at fixed temperatures and humidity. With the guarded chamber, the heat losses of the metering chamber is zero, the heat flow of specimen is determined by the input heat. Without the guarded chamber (Fig. 1-5 (b)), the entire apparatus is located in a surrounding ambient whose temperature is known, the specimen heat flow can be obtained based on the heat flow balance.

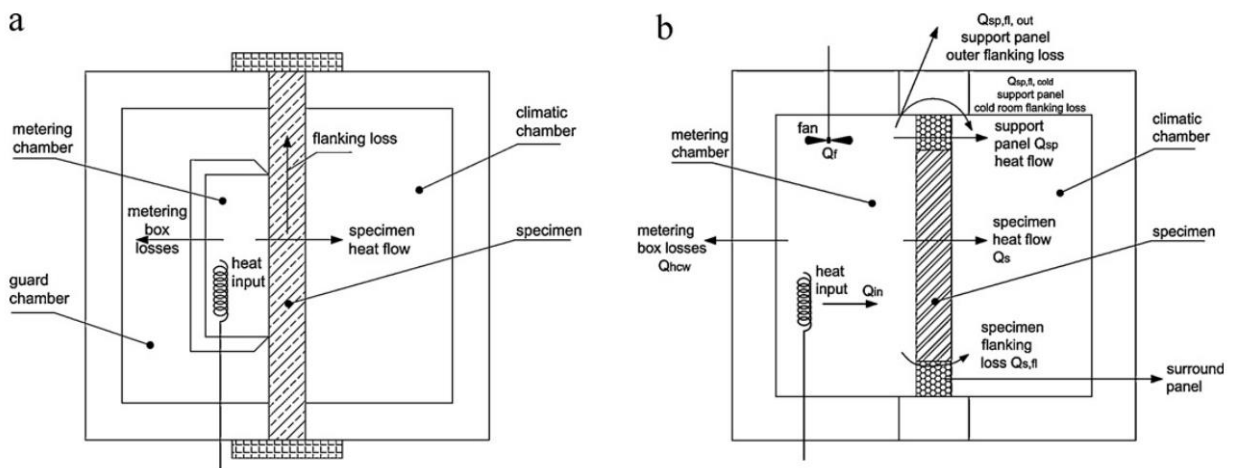


Fig. 1-5 Hot box techniques [13] (a) scheme of the guarded hot box (b) the calibrated hot box.

### 1.1.2.2 The transient techniques

The transient techniques are based on the generation of a dynamic temperature field inside the sample. Temperature response is measured when a heat signal is sent to the sample. This signal can be in the form of a heat pulse or a step-wise heat flux. Generally, according to the apparatus, these techniques are divided into contact transient method and optical transient method (Fig. 1-6).

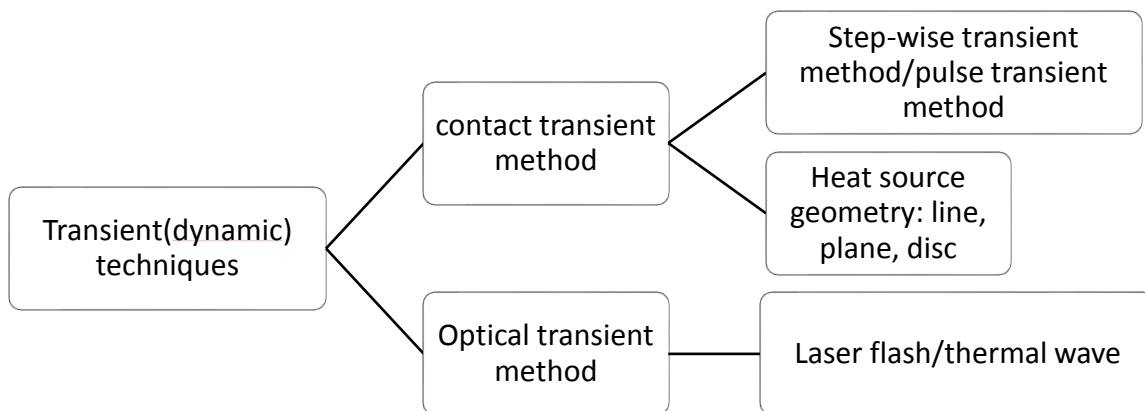


Fig. 1-6 Transient techniques for thermal diagnosis

In the contact transient method, the heat signal is in contact with the sample. The heat source and thermometer are placed inside of the specimen. The dynamic temperature field is generated by an electrical resistance. The heat signal is a pulse or a periodic heat flux. The geometries of the heating resistance can be line, plane or disc. This method is widely used because it is simple and easy to be implemented. Fig. 1-7 (a) shows the sensors for transient plane source method and Fig. 1-7 (b) shows the sensors for transient line source method.



Fig. 1-7 (a) hot disc for transient plane source measurements (b) needle probe for transient line source measurements

Kubicar and Bohac [14] made a review on the transient methods to measure thermal parameters, and summarized several contact transient techniques, including Pulse Transient Method, Hot Wire Method, Step-wise Transient Method, Hot Plate Transient Method and Hot Disc Transient. More details are analyzed in this reference: the mathematical models, experiment arrangements, and sensitivity.

The step-wise transient method was studied in research [15] with a planar heat source. M. J. Assael [16] applied the transient hot-wire technique to measure the thermal conductivity based on the finite-element method. Silas E. Gustafsson [17] studied the pulse transient method to measure the thermal conductivity and thermal diffusivity using hot square and hot disk elements.

The optical transient technologies are more advanced, more expensive and have higher requirements on the equipment. This method can directly measure the thermal diffusivity of specimen. The heat source signal is an energy pulse (Laser flash) or thermal waves. The most widely used technique is the flash method.

The flash method was first approved and described by W. J. PARKER et al. [18] in 1960 for measuring the thermal diffusivity, heat capacity, and thermal conductivity. It has become the main technique to measure the thermal diffusivity of solids.

A laser or a flash lamp is applied on one surface of the specimen, the temperature sensors (thermocouples or IR camera) is installed at the rear face. The thermal diffusivity can be calculated with the temperature-time response curve and the thickness of the specimen.

The temperature-time response for a flash signal is:

$$T(x, t) = \frac{Q}{\rho c L} \left[ 1 + 2 \sum_{n=1}^{\infty} \cos \frac{n\pi x}{L} \cdot \frac{\sin(n\pi l/L)}{n\pi l/L} \exp\left(-\frac{n^2 \pi^2}{L^2} \alpha t\right) \right] \quad 1-9$$

Define  $l$ :  $T(x,0) = Q/\rho c l$  ( $0 < x < l$ );  $T(x,0) = 0$  ( $l < x < L$ ). For opaque materials,  $l$  is very small, that is  $l \ll L$ , the temperature-time response at the rear surface of the specimen is:

$$T(L, t) = \frac{Q}{\rho c L} \left[ 1 + 2 \sum_{n=1}^{\infty} (-1)^n \exp\left(-\frac{n^2 \pi^2}{L^2} \alpha t\right) \right] \quad (x = L) \quad 1-10$$

The maximum temperature at the rear surface is:

$$T_m = \frac{Q}{\rho c L} \quad 1-11$$

Define V as:

$$V(L, t) = \frac{T(L, t)}{T_m} \quad 1-12$$

$$V = 1 + 2 \sum_{n=1}^{\infty} (-1)^n \exp(-n^2 \omega) \quad \omega = \pi^2 \alpha t / L^2$$

Equ. 1-12 is plotted in Fig. 1-8:

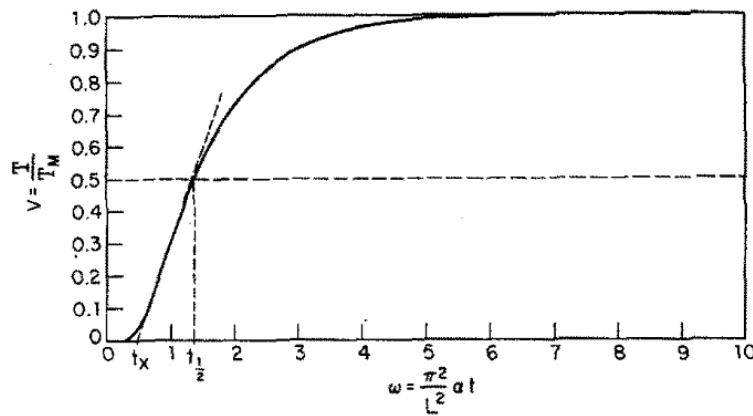


Fig. 1-8 Dimensionless plot of rear surface temperature response [18]

$t_{1/2}$  is the time that the rear surface temperature reaches to half of the maximum temperature, that is  $w = 1.38$ . The thermal diffusivity is then calculated by:

$$\alpha = \frac{1.38L^2}{\pi^2} t_{1/2} \quad 1-13$$

The following assumptions are generally used in the flash method:

- The radiative flux absorbed across the sample surface is consistent.
- Uniform temperature equals to the room temperature at  $t = 0$ .
- Convective heat transfer coefficient is identical on all sides.

Four major error sources are responsible for the uncertainties of this method:



- The radiative and convective heat loss from the sample.
- The inhomogeneity of the incident heat flux.
- The length and shape of the pulse.
- The effects of non-linearity.

Fig. 1-9 is the instrument NETZSCH LFA 427/457 used for laser flash measurement.

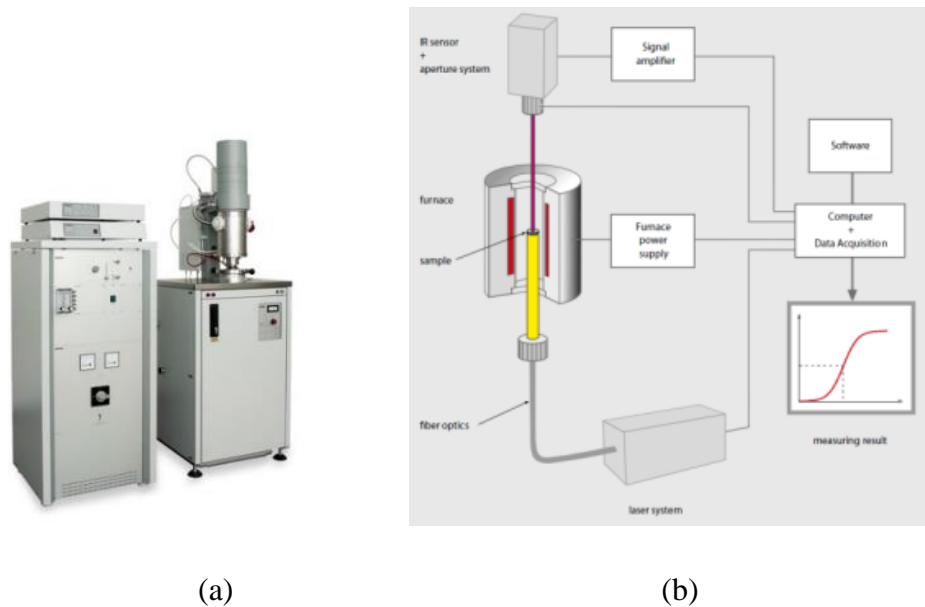


Fig. 1-9 (a) NETZSCH instrument and (b) its principle based on Flash method

This technique has undergone many changes with the technological development on instrumentation (lasers, calculation tools, measuring devices, and so on), as well as the development of models (one or two dimensional models or models that better reflect the reality heat transfer within the materials [19], [20]).

### 1.1.3 Challenges for thermal diagnosis on building walls in situ

The methods described in subsection 1.1.2 are well developed and widely used as standards to measure the thermal parameters of solids in laboratory conditions. However, referring to the building walls, these methods are difficult to implement. The main difficulties are:

- (1) Some well-developed conventional methods and Standards for the building walls, such as the Heat Fluxmeter Method [21] (ISO 9869:2014 [22]) and Hot Box Method [13] (ASTM C236 [23]), are based on steady state heat transfer techniques. These methods need to spend several days on the measurement and the steady state heat transfer is difficult to achieve.

- (2) The classical transient technology, such as flash method, is also difficult to implement on the wall in situ. Normally, it takes a very long time for the rear face of wall to be in response to the heating signal because of the large scale with insulating materials built-in.
- (3) The measurement should be non-destructive because the buildings are still in service. It is better not to take out a specimen from the building. The facilities and sensors are difficult to install on the thick walls in situ. Non-contact measurement is advised [24].
- (4) The in situ scale makes the experimental conditions uncontrolled. The measurement is easily affected by the thermal bridges, weather conditions and solar radiation. The wall heat flow is difficult to obtain accurately because that the heat flow balance becomes very complex in the in situ condition. It is also difficult to build a 1D heat transfer regime inside the wall.

Generally, the building walls are multi-layers. Sometimes the wall structures (thickness and nature of materials) are unknown or uncertain. The inhomogeneous case should be considered. A proper numerical heat transfer modeling in multi-layer walls needs to be built.

## 1.2 Review on thermal diagnostic methodologies for building walls

This part will make a review on in situ thermal diagnostic methodologies for building walls in situ. Generally, there are thermal qualitative and quantitative diagnoses for building walls. This review will focus on the quantitative diagnostic methods. Normally, the diagnosis methods for building walls are based on the fundamental of the techniques described in subsection 1.1.2 and divided into steady state heat transfer techniques and transient heat transfer techniques.

### 1.2.1 Steady state heat transfer techniques

For the steady state heat transfer, the numerical modeling is simple and easy to calculate. Normally, the average method is used and allows the application of steady-state heat transfer equation ( $R = \Delta T/q$ ). The capabilities and limitations of the linear regression method based in averages were studied. However, these methods are valid provided that some hypotheses are accomplished. Particularly the thermal properties of the material and the heat transfer coefficients are constant during the test and the change of heat amount stored in the element is negligible when compared to the heat amount going through the element.

In the reference [25], the authors make the identification of the optimum integration period and the identification of the maximum accuracy obtained using average methods amongst the considered options. Reference [26] reports the application of multiple regression using daily averages to the energy performance analysis of 10 single family houses located different European countries. Reference [27] proposed a pseudo dynamic analysis tool based on multiple regression using daily averages to estimate the energy performance parameters of dwellings. The measurements based on the HFM and hot box method will be introduced hereby.

The conventional HFM (described in subsection 1.1.2) has been applied to the diagnosis of walls in situ. The standard ISO 9869:2014 [22] describes the apparatus that to be used, the calibration procedure for the sensors, the installation, the measurement procedures and the analysis of the measured data, including the correction of systematic errors and the reporting format. The thermal properties of plane building envelop can be obtained by this measurement, such as (total) thermal resistance, thermal conductivity and thermal transmittance. The HFM method has been widely studied and applied [21] [28] [29] [27] [28].

Ahmad and Maslehuiddin (2014) [21] applied this HFM to measure the thermal transmittance and thermal resistance of hollow reinforced precast concrete walls. The thermal performance of two exterior walls of a building was determined in situ. The instrumented building and the test room walls are shown in Fig. 1-10. The main instruments include the heat flux sensors, air temperature sensors and thermocouples. An air conditioner is installed to control the air temperature inside. The trial lasts for about two months in the summer. The results show that a measurement period of six days is needed to obtain in situ thermal performance properties of reinforced precast concrete walls.

Peng and Wu [28] studied this method for measuring thermal resistance of buildings by recording the heat flux and surface temperatures of walls. A chamber was tested in situ. The thermocouples and heat flux meters were arranged in the room. The air-conditioning unit is equipped for cooling to keep temperature and humidity constant. A pyrliometer and a small meteorological station are used for recording the climate outside. To calculate the total thermal resistance in situ, the authors proposed three analysis methods: the synthetic temperature method, the surface temperature method and the frequency response method (thermal quadrupoles solution with Fourier transform). The results show that the frequency response method is better than the other two methods to evaluate the thermal resistance of building walls in situ.



Fig. 1-10 The instrumented building and the test room walls [21]

Desogus and Mura [29] implemented a similar measurement on two chambers. The results show that the thermal resistance value is reliable when the temperature difference between cold chamber and warm chamber is equal to or higher than 10 °C.

In the research [30], four cubicles (2.4×2.4×2.4 m) were measured for 2 weeks. Two cubicles with different insulation materials and a reference cubicle with no insulation are compared. In the polyurethane cubicle (PUR), the insulation material used is 5 cm of spray foam polyurethane. In the Mineral wool cubicle (MW), the insulation material used is 5 cm of mineral wool. Table 1-1 shows the experimental results. Table 1-1 shows the experimental results.

Table 1-1 Experimental results [30]

Comparison between experimental and theoretical wall thermal transmittances for the selected periods of two weeks pervasive fog in winter 08-09.

		Average temperature difference (°C)	Average heat flux (W/m <sup>2</sup> )	Thermal transmittance (W/m <sup>2</sup> K)	Standard deviation	theoretical value of Thermal transmittance	errors
Last week of Dec. 8	Reference	13.87	-20.69	1.49	0.060	2.02	26%
	PUR	18.53	-6.62	0.36	0.039	0.33	-7%
	MW	16.00	-7.47	0.47	0.047	0.52	10%
Week in the middle of Jan. 09	Reference	16.30	-23.03	1.42	0.092	2.02	30%
	PUR	20.88	-7.05	0.34	0.042	0.33	-1%
	MW	20.26	-9.89	0.49	0.066	0.52	6%

In this research, the uncertainty of the experimental thermal transmittance decreases when the temperature difference between external and internal walls is large. Applying the standard method for determining uncertainty propagation, for temperature differences in the range 16–208 °C, the uncertainty is in the range 15-20 %. This uncertainty is acceptable but the measurement take a long time (one weeks).

Generally, the HFM is widely studied and can be referred in the standards. The disadvantages of this measurement are that the characterization time lasts too long (several weeks) and it

needs a steady and regular ambient during the measurement since it is based on the steady state heat transfer regime.

The hot box technique is usually used for measuring the overall thermal resistance or thermal transmittance, and it is widely applied to the wall diagnosis in the researches [10],[23],[24],[25]. This measurement method is described in the Standards ASTM C236 [23] and ASTM C1363 [35].

T. Nussbaumer and K. Ghazi Wakili [32] detected the thermal performance of vacuum-insulation panels in the wall, and made comparisons with the conventional insulation and vented vacuum panels. Steady-state condition and stepwise condition are applied. As shown in Fig. 1-11. The measurements were carried out using a guarded hot-box apparatus complying with the standard ISO 8990, the metering zone was surrounded by a guard zone held at a stable temperature. The wall system was incorporated in a surround panel made of an insulation material of known thermal properties, and it was fully encompassed by the metering area on the warm side. The total surface resistance was determined based on these values and the heat flux through the specimen.

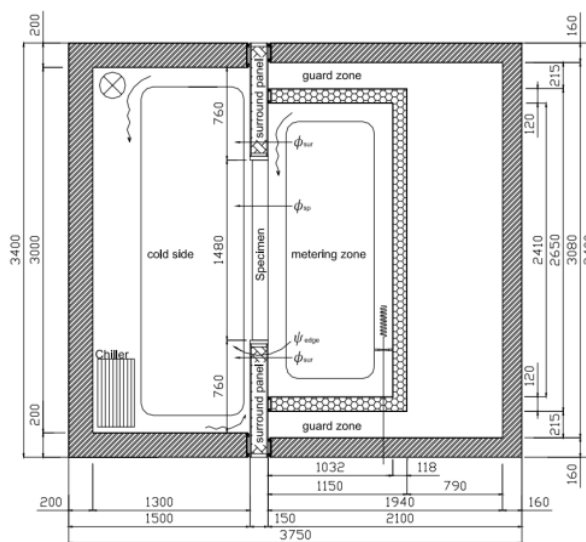


Fig. 1-11 Schematic vertical cross-section of guarded hot-box apparatus (dimensions in mm) [32].

In the research [13], the evaluation experiments of thermal transmittance for inhomogeneous components has been carried out through the hot box method following three different standards: EN ISO 8990, ASTM C1363-05, and GOST 26602.1-99. The three standards have been compared and analyzed by the experiments of thermal transmittance evaluation. Fig. 1-12 shows the apparatus used in the measurement. The authors proposed that an ideal procedure should include the GOST 26602.1-99 method to define the thermal behavior of each part of the

component under analysis, with a contemporary validation of the global results to be performed with one of the other two approaches (EN ISO 8990 or ASTM C1363-05).

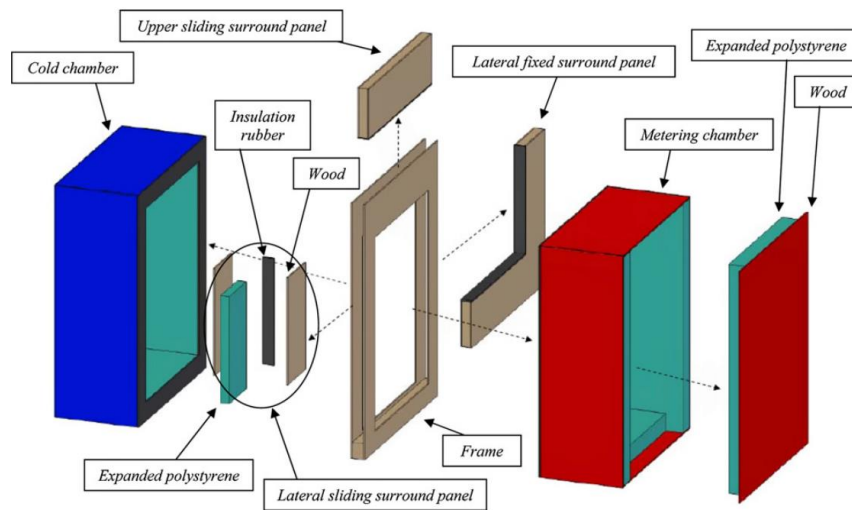


Fig. 1-12 Exploded view of the hot box apparatus [13]

### 1.2.2 Transient heat transfer techniques

The transient methodology is to establish a dynamic temperature field inside the wall. The transient technique involves one face of the wall to be heated by a heat source (contact or non-contact) with temperatures and heat flux meters installed at the two surfaces of the wall. The thermal properties are evaluated by recording the temperature time response. Normally, a numerical model of heat transfer and inverse method are used in this methodology.

The proper numerical heat transfer modeling is important to characterize the thermal parameters. The finite difference (or finite element) model and thermal quadrupoles model are widely studied in recent years.

Finite difference model is one of the most widely used tool to analyze the dynamic heat transfer. The finite differences and finite element numerical models have been studied widely [36]–[41].

The thermal quadrupoles method [42] is developed as a tool for developing new technologies of thermal property measurement. An experiment involving heat transfer is carried on a sample, whose thermal properties are to be detected (thermal conductivity, heat capacity, etc.). The thermal excitation and measured data (heat flux and temperature) are recorded. The thermal parameters of the sample can be estimated by fitting these measured data with the output of a thermal model (for example, through least squares minimization). This thermal quadrupoles method is studied as a solution of heat equation [43]–[47]. For example, D. Defer [48] studied

the wall thermal impedance through this thermal quadrupoles model to provide the quantitative evaluation using natural thermal signals.

This thermal quadrupoles model has been described in subsection 4.2 to process the surface temperature and heat flux of wall.

In recent years, the theory and application of inverse heat transfer problem [49], [50] have been developed in many fields of science and engineering: mechanical, building energy, chemical and nuclear engineers, et al. In the field of building energy, the inverse method is widely used for predicting the energy performance of the whole building [51]–[54] and is also used to estimate the thermophysical properties of a building envelope [37], [39], [55]–[57]. The measurements of heat flux and temperatures on the surface of a wall is difficult to characterize the thermal property by using the conventional direct method, but it can be estimated by an inverse analysis using a transient heat transfer modeling.

Many researches have been focus on the transient heat transfer regime of the walls.

Derbal et al. [58] applied a sandwiched structure to simultaneously determine the thermal conductivity and heat capacity of a construction material without any control of boundary conditions (Fig. 1-13). The material to be characterized is placed between two layers of materials with known thermal properties. Thermocouple probes are placed at the interfaces and the temperatures were recorded when the whole object is stimulated by the heat resistance. Four multilayer objects have been tested: 3 successive PVC layers, PVC/EPS/PVC layers, PVC/Plaster/PVC layers, PVC/Concrete/PVC. The finite difference numerical approach is applied. Conductivities and volumetric heat capacities are estimated with better than 7% accuracy. This method is particularly appropriate for materials presenting good homogeneity because it is based on punctual measurements of temperature. It will be inconvenient to implement this method in situ because of its complex setups.

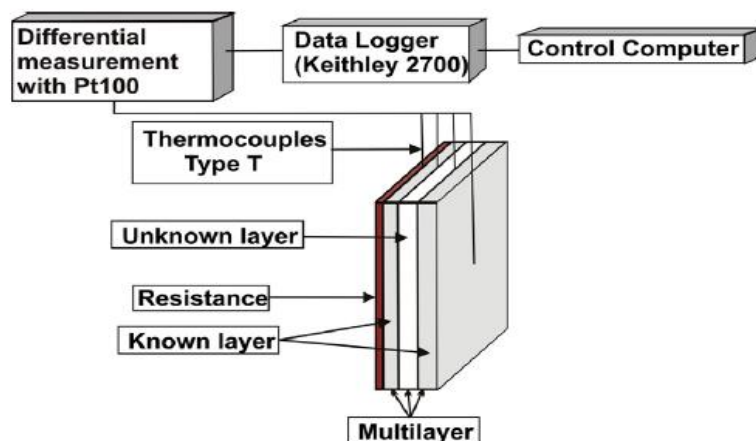


Fig. 1-13 Experimental set up [58]

Chaffar et al. [37] applied a heat flow on a wall and studied the temperature response on the opposite face. The thermal conductivity and heat capacity can be estimated with the heat signals and rear face temperatures by finite differences numerical model and inverse method. The experimental design is illustrated in Fig. 1-14, a reinforced concrete shell of 15cm was studied in summer, a flat heating resistance and the insulating plate installed on the outside surface of the wall 10 h before the test in order to obtain a uniform temperature distribution. The fluxmeter is installed outside. The rear face temperature was recorded by the IR camera, the heating time is 120 min, and the data acquisition lasts 22 h. The results in situ appear to be identified closing to the reference values, this method is of validity. However, this method is only adapted for homogeneous walls, it is unavailable for the multi-layer walls.

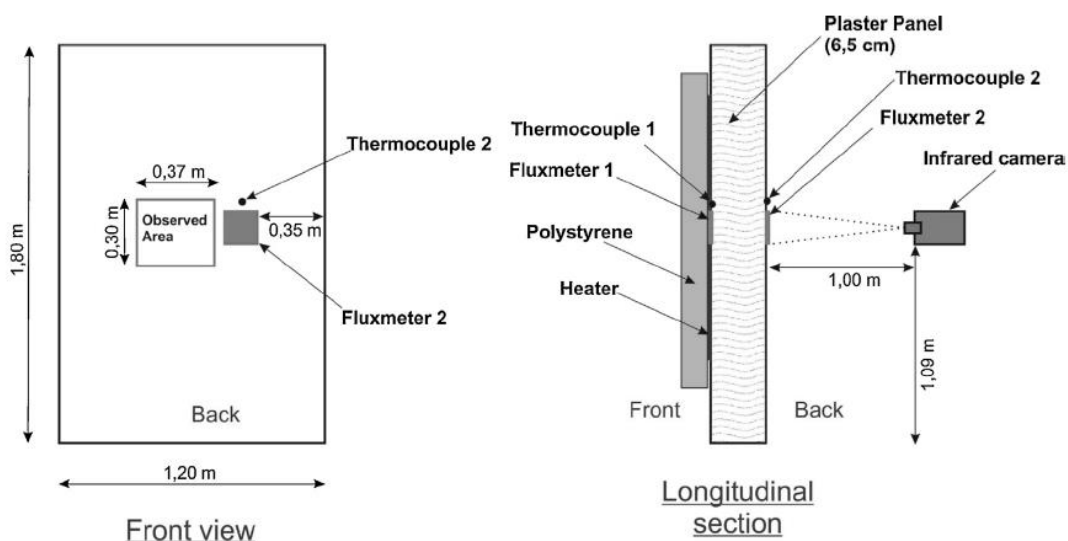


Fig. 1-14 Scheme of the experiment [37]

Authors of [59] proposed a new straight-forward and low cost transient method to determine the wall thermal properties. The measured surface temperature of wall is imposed as boundary equations to Fourier's equation, in such a way the transient surface heat flux can be predicted. With this, the thermal diffusivity is estimated by using the effective thermal diffusivity of the wall material as a tuning parameter to regression fit the predicted and measured heat flux curves.

In reference [60], authors derived a new transient in situ measurement method (Excitation Pulse Method, EPM) to measure the thermal resistance of wall. The idea of EPM is based on the theory of RFs (Room thermal response factors) [11]. The benefit of the RFs method is that it is independent from the wall's internal temperature. The RFs are calculated from the wall thermal properties. As shown in Fig. 1-15, the heat fluxes at two surfaces of the wall can be calculated as a function of surface temperatures.  $X$  is the inner heat flux time-series RFs to a triangular surface temperature pulse of 1 K, and  $Y$  is the outer heat flux time-series RFs to the same pulse. In EPM, the problem is reversed: if it is possible to control the wall's surface



temperature to form a triangular profile, then it is possible to determine the RFs  $X$  and  $Y$  by measuring the heat fluxes  $q_1$  and  $q_2$ . Therefore, in EPM, the wall's interior surface is linearly heated and cooled to generate a triangular surface temperature profile. Meanwhile, the heat fluxes on two sides of the wall are measured leading to the RFs to this excitation pulse. Not only can these RFs be used directly in dynamic simulations, but also they can lead to the determination of the R-value and other thermal properties. Three walls were measured by this method and the experimental results were compared with the values that measured by ISO 9869 method, which shows a good agreement. The authors concluded that it is possible to measure the thermal resistance value within less than 2 hours by the EPM method.

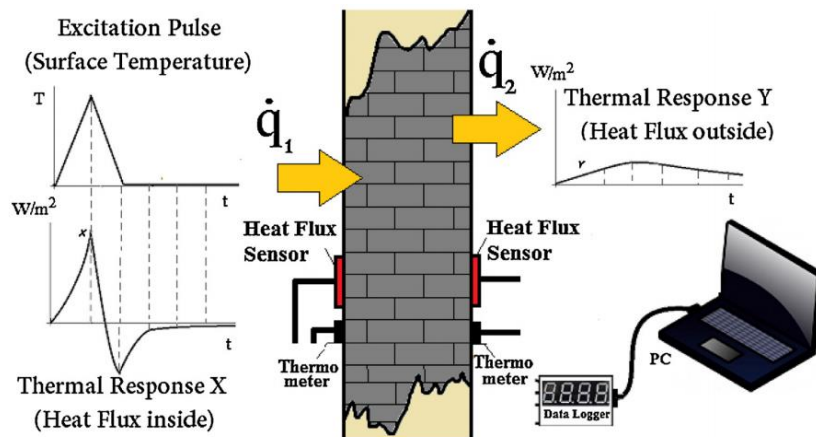


Fig. 1-15 The general concept of EPM—applying a triangular temperature pulse to the surface and measuring heat flux responses on two sides of the wall [60].

### 1.2.3 Application of infrared thermography (IRT) technique

Infrared thermography (IRT) is a very popular method for building qualitative diagnostics [61]–[63]. IRT can be a powerful tool for fast and accurate building qualitative diagnostics, such as the detection of thermal bridging or excessive heat loss areas, air leakages, missing or damaged thermal insulation in the building's elements, sources of moisture, the location of building components, as well as the monitoring for the preservation of historical buildings and monuments. These defects can produce different superficial temperatures, which have characteristic shapes in a thermal image [64].

Moreover, IRT techniques also have a large potentiality for the evaluation of the thermal characteristics of the building. This quantitative evaluation has been introduced by X. Maldague [65]–[67]. The reference [68] made a review of state-of-the-art literature and research on the IRT for building diagnostic. Fundamentals of IRT and the thermographic process for building diagnostics is also presented. As the IRT is a useful tool, it needs a great

prospect for the development of more advanced and accurate approaches. For the IRT inspecting, the influence of solar radiation and wind should be considered.

The advantages of applying IRT on building diagnostic are [65]–[68]:

- (1) The IRT is remote sensing. It is non-direct contact between the sensor and the object, which makes the measurements non-intrusive and convenient.
- (2) The IRT has the ability of performing real-time surface measurements. The process is fast and safety.
- (3) The IRT can provide a large monitoring capacity. The IR cameras are able to record the temperatures at many different points within the scene simultaneously.
- (4) A global thermography can be easily interpreted. The anomalous thermal behaviors (local thermal bridges, areas with high moisture and so on) can be avoided during the measurements.

However, there are also several problems:

- (1) The IRT is limited to a certain depth of the target when it is used for subsurface defect detection.
- (2) The target's emissivity and the reflective apparent temperature have to be known for temperature measurement.
- (3) Current industry standard cameras have  $\pm 2\%$  accuracy or worse in temperature measurement, or advanced models can reach up to  $\pm 1\%$  accuracy, while either of them is not as accurate as contact sensors.
- (4) The IRT is sensible to the heating sources and the natural radiation.
- (5) The interpretation of the IR images requires considerable experience and judgment.

According to the numerical heat transfer regime, IRT techniques are divided into steady state IRT and transient IRT. According to the approaches of thermographic inspections, IRT techniques are divided into 'Passive IRT' and 'Active IRT'. For the passive IRT technology, there is no artificial heating or cooling applying in the measurement, it highlights temperature differences between the environment and the studied object. For the Active IRT, an artificial thermal signal is required to observe the response on envelopes. The active one includes active pulsed thermography, active step-heating thermography, active lock-in thermography and active vibro thermography [69]. Several IRT techniques will be introduced in the followings.

Albatici and Tonelli [70] applied a fast and less invasive measurement with an IR camera to measure the thermal transmittance ( $\bar{U}$ -value) of walls. It is a kind of steady state method. Convection (due to air temperature and speed) and irradiation (due to the temperature of the

surfaces positioned near and around the element) are considered in this method. Fig. 1-16 shows the principles of heat transfer.

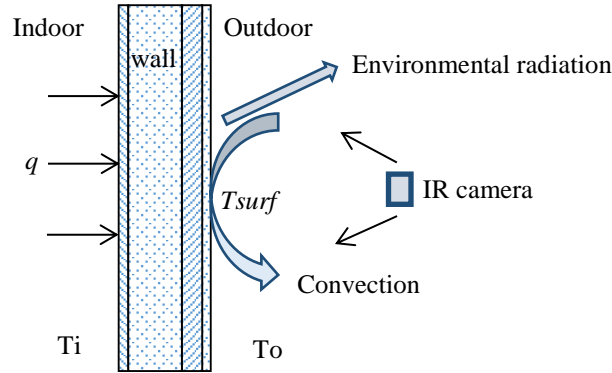


Fig. 1-16 Principles of heat transfer

The total heat flux of outdoor can be:

$$q = q_{conv} + q_{rad} \quad 1-14$$

According to the convection heat flux Equ. 1-1 and Stefan–Boltzman Law Equ. 1-2, the transmittance  $\bar{U}$  is calculated as:

$$\bar{U} = \frac{5.67\varepsilon \left[ \left( \frac{T_{surf}}{100} \right)^4 - \left( \frac{T_o}{100} \right)^4 \right] + 3,8054v(T_{surf} - T_o)}{T_i - T_o} \quad 1-15$$

Where  $v$  is the wind velocity,  $T_{surf}$  is the outdoor surface temperature,  $T_o$  and  $T_i$  are the air temperature of outdoor and indoor.  $\varepsilon$  is the emissivity on the entire spectrum. A soldering iron is used for measuring the  $\varepsilon$ .

Usually, the following equipment is needed in the measurement: an IR camera to take infrared thermal images of building at both outdoor and indoor, a hot-wire anemometer to measure wind speed, a soldering iron to measure  $\varepsilon$ . 3 cases are studied by both IRT method and HFM method, in one case, the results of HFM method is 59% higher compared to the theoretic one. And with the IRT method, it is 31% higher compared to the theoretic one.

This steady state-IRT method was developed by Fokaides and Kalogirou [71] later. The reflective ambient temperature is evaluated by a crumpled sheet-smoothed aluminum. The emissivity of the wall is evaluated by correction using a piece of black tape known emissivity,

shown in Fig. 1-17. The percentage absolute deviation between the reference values and the measured U-values is in the range of 10–20%. A sensitivity analysis is made in this research, the thermal emissivity and the reflective ambient temperature have a significant impact on the measured temperature. The test is implemented indoor. Indoor measurement is better than test outdoor because the reflected temperature is more stable than external exposed outdoor.

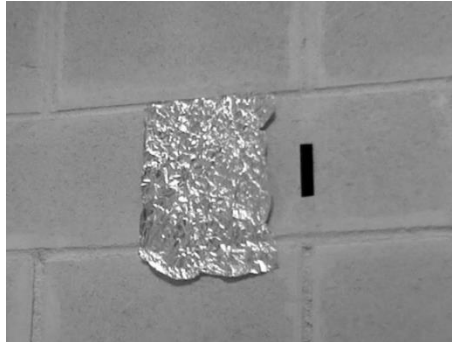


Fig. 1-17 Arrangement for determination of reflected temperature and emissivity [71]

The procedure of this method is sufficiently fast. As concluded in this reference [70], a medium size building can be analyzed in situ in about 2–3 h (plus 15 h of data handling in office). However, there are still some limits for this method:

- The measurement can be done only during the evening in order to avoid direct solar radiation.
- Wind speed must be lower than 1m/s (best condition is lower than 0.2 m/s) in order to avoid convective phenomena out of control.
- The building elements must have stored a sufficient amount of heat during previous days in order to have a dispersed thermal power significantly measurable. The meteorological situation must have been fair (clear sky, possibly sunny and non-rainy or windy).
- The difference between inner and outer temperature during the measurement must be of at least 10–15 °C in order to allow a measurable heat exchange through the element.

Youcef et al. [72] applied the passive IRT the in situ quantitative diagnosis of insulated building walls. An experimental test bench was used in real conditions to examine a multi-layered wall, as shown in Fig. 1-18. The atmospheric parameters (temperature, pressure, relative humidity, solar heat flux) are acquired from a weather station. The indoor and outdoor wall temperatures are measured by IR cameras and thermocouples. The test lasts about 8 days.

The measured parameters are associated with heat transfer numerical modeling (finite elements or finite differences) in order to estimate the insulation properties of the wall. The inverse problem is used in this model. The results firstly showed that it was possible to estimate either the thickness or the thermal conductivity of the insulating layer by analyzing the measurement

data. The main limit of this measurement is that the measurement time is long and the structure of wall and the thickness of each layer should be known, which is difficult for some old buildings.

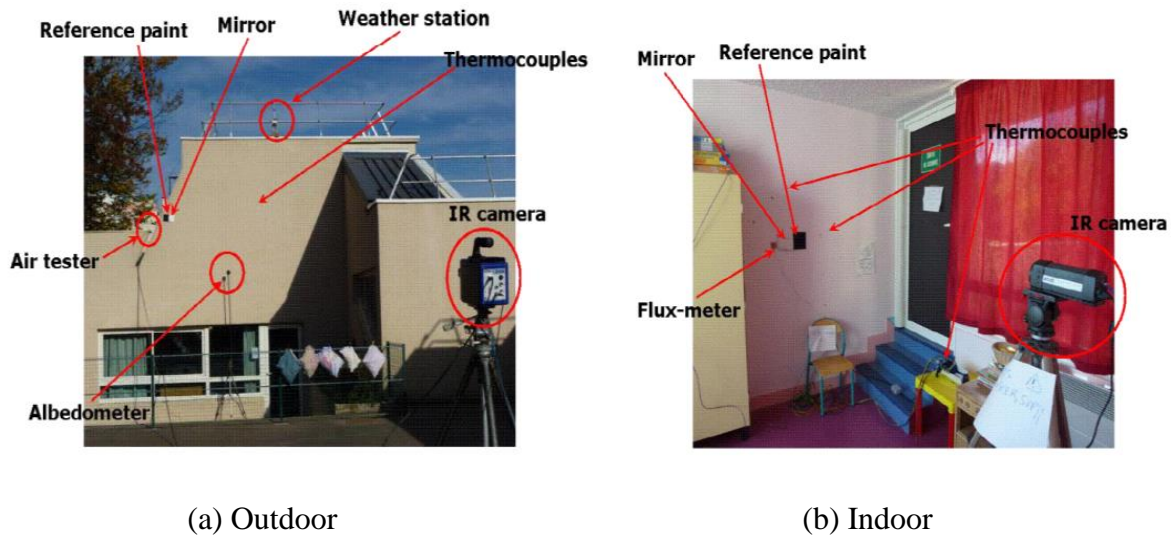


Fig. 1-18 Instruments for inside and outside of wall in situ [72]

Monchau et al [73] use the passive IRT to detect a multi-layered wall. In this research, the temperatures measured by thermocouples and that measured by IR camera are compared. Fig. 1-19 shows the temperature differences for three test areas. There is a satisfactory agreement between thermocouple and IR camera measurements excepted for some cloudy and sunny alternating short periods.

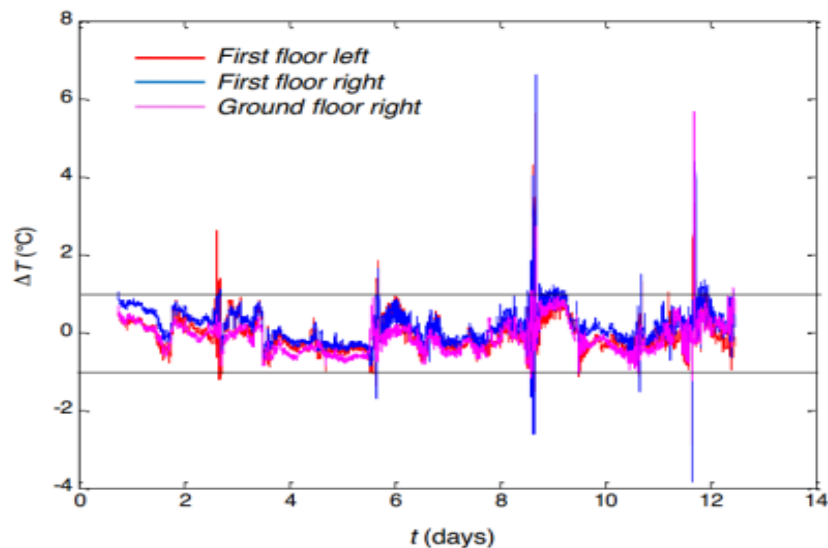


Fig. 1-19 Temperature differences between thermocouple and corrected infrared measurements for three zones of the western facade [73];

The active IRT technology needs a stimulation effecting on the object through heating or cooling, including Pulsed thermography and Lock-in thermography.

Generally, there are two kinds of active IRT technologies: transmission (Fig. 1-20) and reflection (Fig. 1-21). When heating the objective on one surface, for the transmission active IRT, the IRT recording is on the other face of the objective, while, for the reflection active IRT, the IRT recording is at the same face of the objective.

Ch. Maierhofer and A. Brink [36] quantitatively detected the void defects inside the wall based on this active IRT method with an impulse. Locating defects in concrete with concrete covers up to 10 cm has been performed successfully. If the material parameters are well known, it will be possible to determine the depth of real voids by comparing simulated and measured values.

Wiecek and Poksiska [74] carried out investigations of works of art and architectural monuments with a heating lamp to provide a step wise signal and IR camera measures the temperature at the same side, see in Fig. 1-21. Examined structure can be penetrated with a thermal wave on small depth. Shapes of bricks under the plaster can be visualized without special problems. Materials from different periods can be differentiated. However, this new method has not been fully developed, especially for the quantitative evaluation.

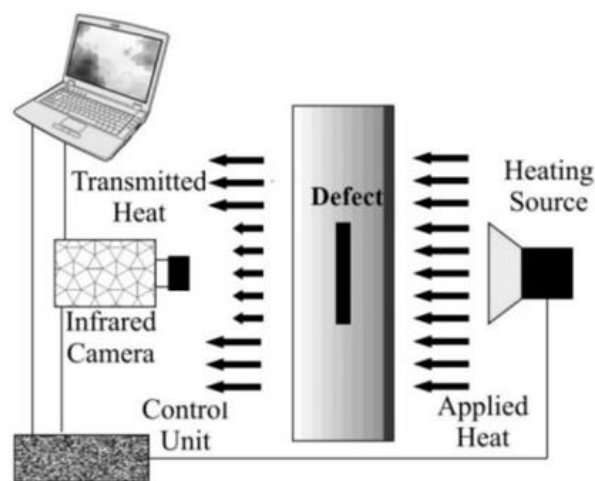


Fig. 1-20 Principle of the transmission active IRT [75]

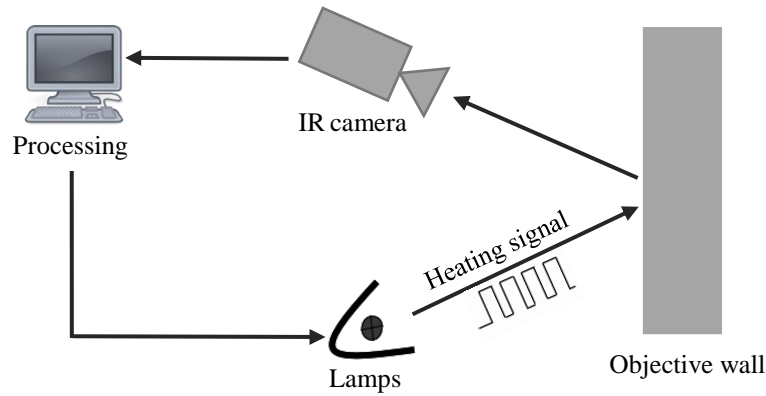


Fig. 1-21 Principle of the reflection active IRT [74]

### 1.2.4 Terahertz radiation method

More and more attentions are paid to the study of THz technology in the last two decades due to its remarkable properties, and it has been widely applied to many potentialities in the fields of safety inspection, NDT, atmospheric physics, biology, military applications, ecology and medicine [76]. One of the key points of development now is NDT.

The frequency band of THz designates electromagnetic waves ranging from 0.1 to 10 THz (wavelength from 3mm to 3 $\mu$ m) [77], which is between the microwaves and infrared (Fig. 1-22).

THz is particularly suitable for NDT, it allows the development of non-destructive, non-contact, non-ionizing methods that could advantageously replace other NDT methods based on X-rays, ultrasound and thermography. THz radiation can penetrate through composite materials to detect the defects, such as voids, delamination, mechanical damage, and heat damage [78]–[80]. In addition, it can be used for analyzing the structure of materials, such as insulating polymer foams, and for characterizing properties of materials [81]–[84].

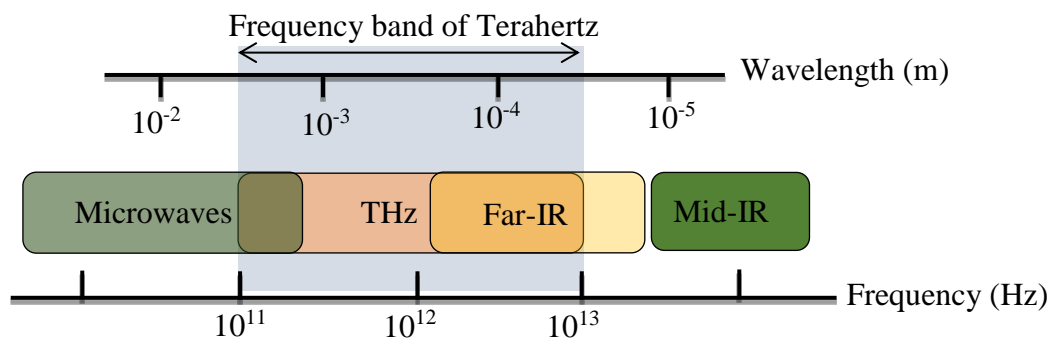


Fig. 1-22 Frequency band of THz in electromagnetic spectrum

The advantages of NDT THz method in the field of building thermal diagnostics are:

1. THz radiation can penetrate non-conductive materials with a very low phase shift.
2. THz radiation does not cause any danger problems to the operators and walls.
3. The absorption coefficient varies greatly with the proportion of water in the medium. The amount of water, as well as the degradation due to the penetration of water in the wood or the concrete, can be detected from the attenuation of radiation. Some defects caused by water can be detected easily. While this performance can also influence the measurements of thermal parameters characterization.

THz radiation method has been studied by some researchers in the field of building materials diagnostic [83]–[86]. In addition, THz NDE technology can also be combined with other NDE methods to improve the accuracy and efficiency [85]. The most accuracy and reliability analysis is obtained by combining different methods.

In the reference [83], the author proposed that THz spectroscopy and imaging can be used to analyze different types of thermal building insulation materials. The absorption coefficients of polymer foams are calculated, which presents an inverse relationship with the thermal conductivity. In addition, manufacturing imperfections and internal structures within the foams are clearly visualized with the THz amplitude imaging. THz has a big potential to detect the thermal performance of wall as a non-destructive method.

Fig. 1-23 shows the absorption coefficients of the most used thermal insulating polymer foams in the frequency range between 1.35 THz and 5.0 THz. The THz absorption coefficient varies the most for Bakelite foam whose thermal conductivity is the largest. Whereas, for EPS foam, the value of absorption coefficient is almost unchanged for all three selected THz frequencies. Fig. 1-24 presents the relationship between the thermal conductivity and THz absorption coefficient of polymer foams. One can notice that the thermal conductivity is inversely proportional to the absorption coefficient given at all three selected THz frequencies.

Generally, the THz spectroscopy is studied in both pulsed modes and continuous wave (CW), and mainly fall into two categories: pulsed Terahertz domain spectroscopy (THz-TDS) and CW THz imaging system [71]. The CW THz method affords a more compact, simple, faster and relatively low-cost system since it does not require a pump probe system and it does not require a time delay scan. The CW THz method is applied in our work.



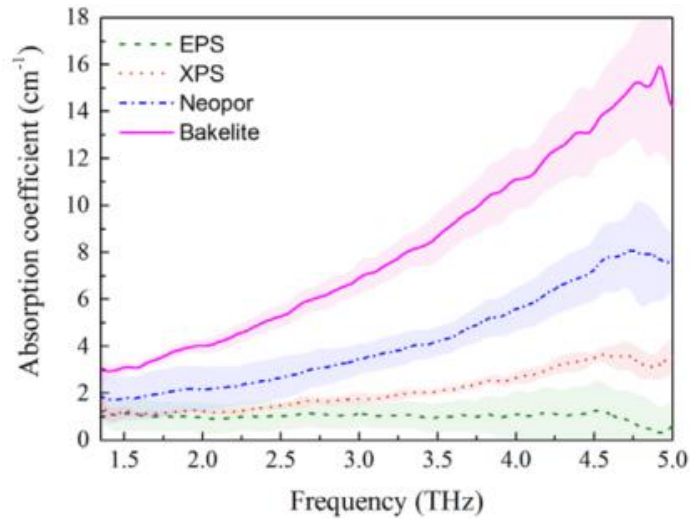


Fig. 1-23 Absorption coefficient of a variety of thermal insulating polymer foams in the frequency range between 1.35 THz and 5.0 THz.

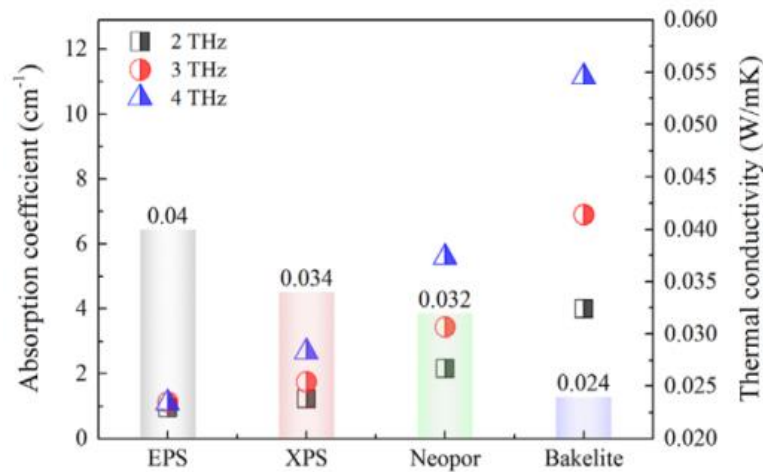


Fig. 1-24 Relation between absorption coefficient at selected THz frequencies and the thermal conductivity of polymer foams.

## 1.3 Objective and outline

The objective of this study is to make the quantitative diagnosis of building envelope in order to obtain the thermal properties (thermal conductivity and heat capacity), analyze and explore the diagnostic methodologies aiming to propose a precise, fast, convenient, less-cost, and fewer instruments method which could be widely used in the future.

On one hand, this work focus on the sensors utilization, studying the measurement of emissivity, heat flow and temperature to provide some guidelines for the choice of sensors, and provide the data processing protocol as well.

On the other hand, this work concentrates on the numerical approach analysis to obtain the thermal properties with the surface temperature and heat flux of the wall.

This chapter has introduced the context of our study and provide a bibliography on the thermal diagnosis methodologies of building walls. Chapter 2 will describe the sensors and facilities used in the experiments we carried out in the laboratory and in situ. Chapter 3 will show the principles of data processing and results. Surface temperature and wall heat flux can be obtained. Chapter 4 will propose and analyze the estimation approaches to compute the thermal properties of wall with the results of temperature and heat flux. Chapter 5 will introduce a new method using terahertz radiation. This method will be analyzed and discussed by combining with the classical thermal probe method. Finally, Chapter 6 will give the conclusions and perspectives of this work.



# Chapter 2

## Experimental Sensors And Facilities

---

---

As describe in Chapter 1, the goal of this reserach is to investigate thermal quantitative diagnostic of building walls. Experiments both in laboratory and in situ were carried out to investigate the methodologies. In the laboratory-case, a multi-layer practical scale wall fixed on a caisson placed in a climatic chamber was studied. In the in situ-case, an exterior wall of a building in Bordeaux was measured.

Generally, the measurement of wall surface temperature and heat flow are necessary to measure to characterize the wall thermal properties. So the experiments aim at investigating measurements of wall surface temperature, emissivity and heat flux with kinds of sensors (contact sensors and non-contact sensors), including Peltier module sensors, flat plate heat flux sensors (fluxmeter), infrared camera and thermocouples. Then the measured data will be processed and compared in Chapter 3. This chapter will mainly describe the implement approach of the two experiments, including sensors utilization, calibration of sensors, system scheme and experimental apparatus.

## 2.1 Sensors

### 2.1.1 Infrared camera

The IR (infrared) wavelength ranges from 0.7  $\mu\text{m}$  to 1 mm [87], including NIR (Near-infrared, 0.75-1.4  $\mu\text{m}$ ), SWIR (Short-wavelength infrared, 1.4-3  $\mu\text{m}$ ), MWIR (Mid-wavelength infrared, 3-8  $\mu\text{m}$ ), LWIR (Long-wavelength infrared, 8-15  $\mu\text{m}$ ) and FIR (Far-infrared, 15  $\mu\text{m}$  -1 mm). IR radiation can not be detectable by the human eye. An IR camera can convert IR radiation to a visual image which expresses thermal variations of an objective surface. This thermography allows us to make non-contact measurements of surface temperatures. In this research, the IR camera spectrum which ranges from 7.5-13  $\mu\text{m}$  was chosen.

Fig. 2-1 shows the principles of an IR camera [88]. First, the IR camera collects a certain energy signal that emitted by the target object through its lens. This certain signal can be focus on long wavelength infrared or mid wavelength infrared. The collection involves a photon detector or a thermal detector, such as a micro bolometer. Then, the collected energy will cause the detector to produce a voltage that results in a digital count through the system's A/D converter. After the camera is calibrated with a blackbody, radiance values can be estimated by measuring this digital counts. Finally, the camera convert radiance values to temperature with knowing the emissivity of the target surface and the ambient parameters.

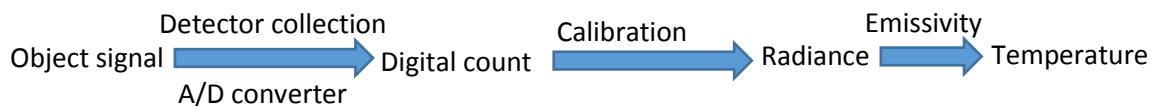


Fig. 2-1 Principle of IR camera

FLIR A325 (Fig. 2-2) was used in our experiments. Part of parameters of FLIR A325 is shown in Table 2-1. The spectral range that the camera can detect is 7.5-13  $\mu\text{m}$  (long wave IR). The camera resolution is 320×240 pixels. This IR camera is connected to a laptop and controlled by the software ReacherIR. Appendix A shows all the information of FLIR A325.



Fig. 2-2 FLIR A325

Table 2-1 Parameters of FLIR A325

Parameters	Values
Spectral range	7.5-13 $\mu$ m
IR resolution	320 $\times$ 240 pixels
Accuracy	$\pm 2^{\circ}\text{C}$ ( $\pm 2$ - $6^{\circ}\text{F}$ ) or $\pm 2\%$ of reading
Object temperature range	-20 to +120 $^{\circ}\text{C}$ /0 to +350 $^{\circ}\text{C}$
Image frequency	60 Hz
Field of view (FOV)	25 $^{\circ}$ $\times$ 18.8 $^{\circ}$ / 0.4 m (1.31 ft.)
Focal length	18 mm (0.7 in.)
Thermal sensitivity/NETD	< 0.05 $^{\circ}\text{C}$ @ +30 $^{\circ}\text{C}$ (+86 $^{\circ}\text{F}$ ) / 50 mK
Spatial resolution (IFOV)	1.36 mrad

### 2.1.2 Thermocouples

Thermocouple is a widely used type of temperature sensors in science and industry. It is an electrical device consisting of two dissimilar conductors to form electrical junctions at differing temperatures. The fundamental is described in [89] and Appendix B. A thermocouple produces a temperature-dependent voltage as a result of the thermoelectric effect, and this voltage is characterized by the temperature that to be measured.

Type T (copper–constantan) thermocouples were used in our experiments to measure the wall temperature, ambient temperature and temperature of heat flux sensors. Part of thermocouples are installed in the internal wall between each layer when the wall was built. Some thermocouples were installed on the wall surface and have been protected from the radiation by a shiny aluminum coat. All the thermocouples have been calibrated in laboratory before the test.

### 2.1.3 Heat flux sensors

Two kinds of heat flux sensors were used in this work: Peltier module and flat-plate heat flux sensor made by Captec manufacture [90] (marked as fluxmeter). The usage of Peltier sensors is economic, for example, 20 euros for one Peltier sensor, while 200 euros for one fluxmeter.

Such fluxmeters are based on the Seebeck effect by sensing tangential gradients of electric potential produced by heat flux across the balanced self-generating panel or planar thermopile (Fig. 2-3 (a)). Numerous plated junctions are connected in series on the balanced self-generating panel. The terminal ends have soldered lead wires for the electrical connection. Each junction ends is covered by a thermal insulating layer in order to produce unbalanced heat flux incident on the coated ends. This unbalanced heat flux on the junction ends results into

gradients of electric potential, collected along the meander to finally build a millivolt output voltage. This device is then cover by two plates of copper on each side (Fig. 2-3 (b)), enabling to prevent any influence by the thermal properties of the material in which they are embedded. Such fluxmeters can simultaneously measure the heat flux and temperature with a thermocouple type T built-in.

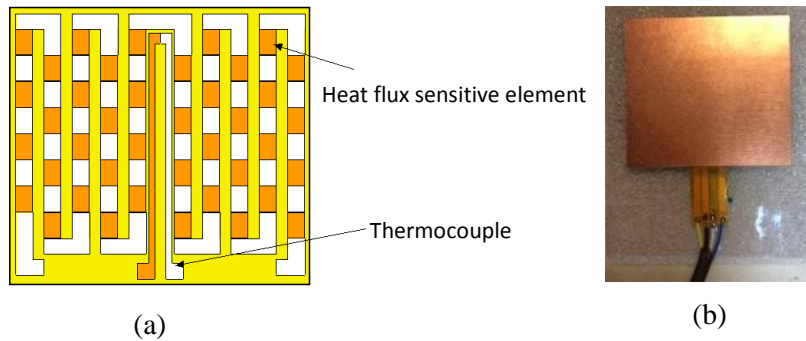


Fig. 2-3 (a) The balanced self-generating panel; (b) Flat plate heat flux meter (Captec)

The parameters of fluxmeter used in our test are listed in Table 2-2:

Table 2-2 Parameters of fluxmeters

Parameters	Values
Size	50×50 mm
Sensitivity	17.8-18.5 $\mu\text{V}/(\text{W}/\text{m}^2)$
Thermal resistance	0,00015 $\text{K} \cdot \text{m}^2/\text{W}$
Temperature range	-200 $^{\circ}\text{C}$ -200 $^{\circ}\text{C}$
Response Time:	150 ms
Thickness	0.4 mm

The sensitivity of each fluxmeter is given by the manufacturer. Moreover, it has also been calibrated in the laboratory LGCgE in Bethune and laboratory I2M to validate the sensitivity values.

Peltier module sensors (marked as Peltier sensors) were used as heat flux sensors in this work. Peltier module, which is also called thermoelectric cooler [91], normally operates as a cooler by the Peltier effect to create a heat flux between the junction of two different types of materials. As shown in Fig. 2-4, the device has two sides, when a DC current flows through the device, it brings heat from one side to the other, so that one side gets cooler while the other gets hotter.

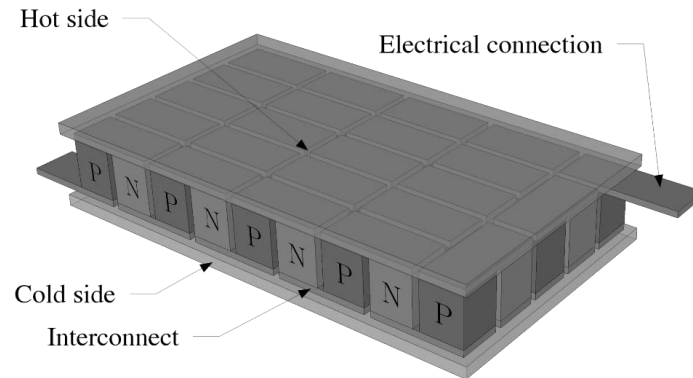
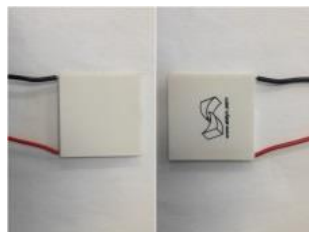
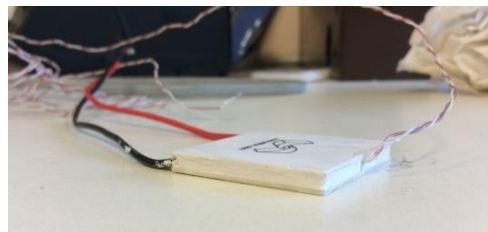


Fig. 2-4 Peltier module schematic [91]

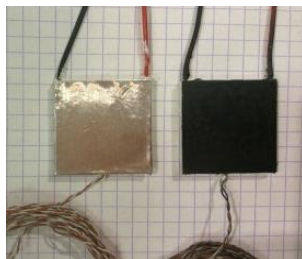
The Peltier module can also be used as a thermoelectric generator. One side of the device is heated to a temperature higher than the other side, as a result, a difference in voltage is build up between the two sides (the Seebeck effect). For the measurement of heat flux, when the Peltier module is heated at a certain heat flux, it can convert this heat directly into electricity at the junction of different types of wire. This electrical signal will be detected as an output voltage. Therefore, the heat density can be estimated by knowing the relationship between the output voltage and input heat (usually named the sensitivity of sensor). The sensitivity of Peltier sensor should be calibrated before applying on the measurement. Fig. 2-5 shows the Peltier sensors used in our work.



(a) Initial Peltier sensors



(b) Peltier enclosed by silicone mastic neutral



(c) shiny Peltier sensor and black Peltier sensor



(d) black paint with unknown emissivity

Fig. 2-5 Peltier sensor



The size of Peltier sensor is 30×30×3.5 mm (width×length×thickness) Fig. 2-5(a). Some improvements were made on the Peltier sensors. Firstly, a T-type thermocouple is embed to the internal center of each sensor. Then, in order to avoid the environment influence, silicone mastic neutral is daubed around the four sides of sensor, as shown in Fig. 2-5(b). Finally some sensors are coated with shiny aluminum foil and the other ones are painted black by the paint with unknown emissivity (Fig. 2-5(d)). The ones that coated with aluminum foil and that painted black (Fig. 2-5(c)) are marked as shiny Peltier sensor and black Peltier sensor respectively. Both kinds of sensors are installed on the test area of wall simultaneously for the calculation of wall heat flux.

## 2.2 Sensors calibration

### 2.2.1 Calibration of thermocouple

All the thermocouples were calibrated through a reference calibration thermometer, WIKA CHT 6500 model with Pt100. The accuracy of CHT 6500 Pt100 is 0.03°C, ranging from -50 °C to +199.99 °C. The thermocouples and Pt100 were concentrated placed in a BINDER chamber, in which the temperature can be stably controlled. 17 thermocouples were calibrated at 7 ambient temperatures of 15 °C, 25 °C, 30 °C, 40 °C, 50 °C, 60 °C, 70 °C.

The temperature difference between the reference and thermocouple is the correction temperature, marked as  $\Delta T_{correction}$ .

$$\Delta T_{correction} = T_{reference} - T_{thermocouple} \quad 2-1$$

Where  $T_{reference}$  is the temperature that measured by Pt100 and  $T_{thermocouple}$  is the temperature that measured by each thermocouple.

Fig. 2-6 shows the correction temperature obtained from the calibration test. The correction temperature is stable enough at a certain ambient temperature but varies a lot at different ambient temperatures. The average value of correction temperature is calculated at each ambient temperature. A linear relationship (Equ. 2-2) is fitted between the average correction temperature and the ambient temperature, see in Fig. 2-7. The linear fitting results are listed in Table 2-3. In this table,  $m$  is the slope of the fitting curve,  $n$  is the intercept and  $R'$  is the correlation coefficient. The temperature unit is in centigrade degree (°C).

$$\Delta T_{correction} = m \cdot T_{reference} + n$$

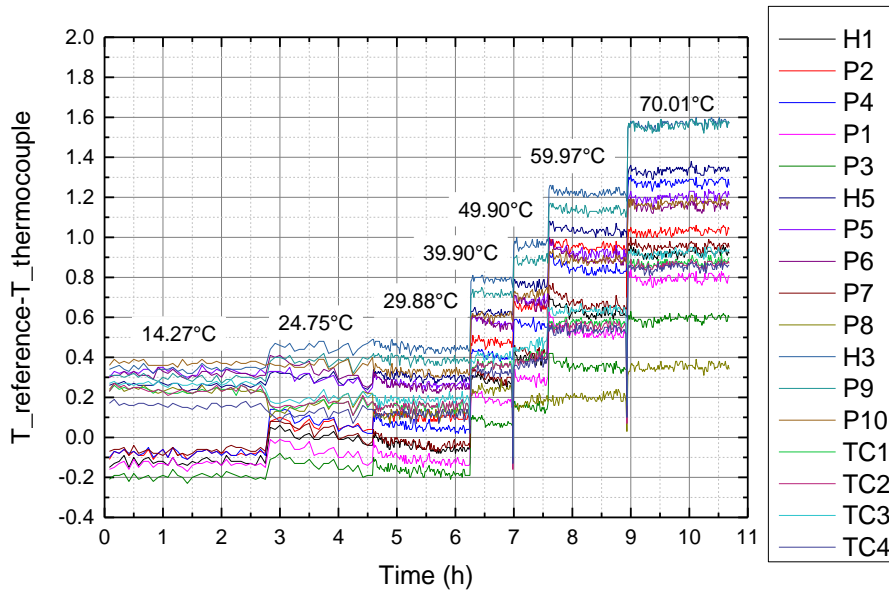


Fig. 2-6 The correction temperature at 7 ambient temperatures for 17 thermocouples

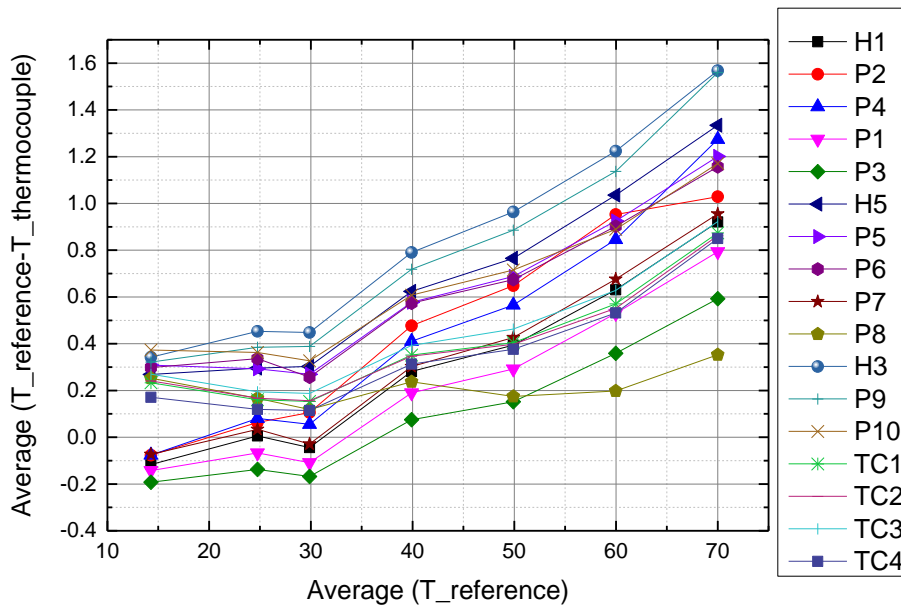


Fig. 2-7 Average correction temperature VS the ambient temperature

Table 2-3 Calibration results of thermocouples in IUT lab

Thermocouples	$m$	$n$	$R'$	Uncertainty $\Delta T$ (°C)
H1	0.0188	-0.481	0.979	0.036
P2	0.0219	-0.447	0.988	0.036
P4	0.0239	-0.535	0.979	0.037
P1	0.0173	-0.501	0.973	0.038
P3	0.0144	-0.497	0.970	0.036
H5	0.0201	-0.170	0.973	0.034
P5	0.0171	-0.098	0.958	0.036
P6	0.0163	-0.071	0.958	0.040
P7	0.0190	-0.454	0.976	0.038
P8	0.0017	0.143	0.458	0.037
H3	0.0224	-0.099	0.983	0.034
P9	0.0224	-0.154	0.972	0.035
P10	0.0151	0.013	0.954	0.034
TC1	0.0118	-0.095	0.911	0.044
TC2	0.0114	-0.080	0.903	0.046
TC3	0.0122	-0.068	0.918	0.045
TC4	0.0123	-0.154	0.922	0.044

According to Equ. 2-1 and Equ. 2-2, the reference temperature that we want to obtain is expressed in Equ. 2-3.

$$T_{objective} = T_{reference} = \frac{T_{thermocouple} + n}{1 - m} \quad 2-3$$

The overall uncertainty, for which the bias error and random error were considered, was calculated by propagation equation of errors, as expressed by Equ. 2-4.

$$\Delta T = \sqrt{B_e^2 + R_e^2} \quad 2-4$$

Where  $\Delta T$  is the overall uncertainty of thermocouple,  $B_e$  is the bias error and  $R_e$  is the random error. The bias error is the difference between the true temperature of object and the obtained temperature of object ( $T_{objective}$ ). As the thermocouples have been calibrated by Pt100 thermometer, the bias error of thermocouple is equal to the accuracy of CHT 6500 with Pt100, which is 0.03K. The standard deviation ( $\delta$ ) of measured data at a certain temperature is set as the random error ( $R_e = \delta$ ). The overall uncertainty ( $\Delta T$ ) of each thermocouple is listed in Table 2-3.

Finally, the corrected temperature is:

$$T_{objective} = \frac{T_{thermocouple} + n}{1 - m} + \Delta T \quad 2-5$$

Similarly, the calibration results in IFSTTAR lab (in Nantes) is shown in Appendix C.

### 2.2.2 Calibration of heat flux sensors

All the heat flux sensors should be precisely calibrated before applied to heat flux measurement. As described in Section 2.1.2, the sensitivity of the heat flux sensors  $k$  (Equ. 2-6) should be measured. The calibration test is carried out in I2M to determine this sensitivity  $k$ , expressed in  $\mu\text{V}/(\text{W}/\text{m}^2)$ .

$$k = \frac{U_p}{q} \quad (\mu\text{V}/(\text{W}/\text{m}^2)) \quad 2-6$$

Where  $U_p$  is the output voltage by Peltier sensor and  $q$  is the heat flux that acts on the Peltier sensor. This  $k$  value is assumed evenly distributed for the Peltier sensor and fluxmeter.

The experimental setup is shown in Fig. 2-8: a heating resistance (size of  $1 \times 1$  cm) was placed on one surface of Peltier sensor to produce a heat signal. The other surface of Peltier sensor is in well contact with an iron block, whose heat capacity is large enough for the heat dissipation to keep the temperature constant. The upper surface of the heating resistance was covered by insulation materials as well as surfaces around the iron block to prevent heat loss and ensure the heat flow going down to the Peltier sensor. The surface temperatures of the iron block were measured by two thermocouples respectively beside the Peltier sensor and on the foot.

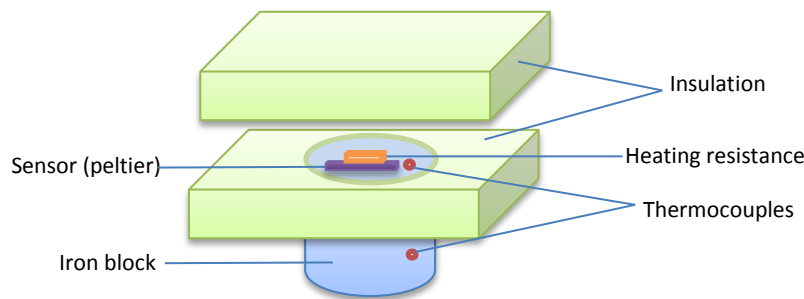


Fig. 2-8 Setup of calibration test

ISO-TECH-IPS 303DD works as a power supplier for the heating resistance. The supplier current can be regulated from 0 to 3 A. Uncertainty of this current is  $\Delta I = 0.002$  A. Peltier sensors were calibrated at two ambient temperatures: 23 °C and 35 °C. An oven is used to regulate the ambient temperature. The general scheme is shown in Fig. 2-9.

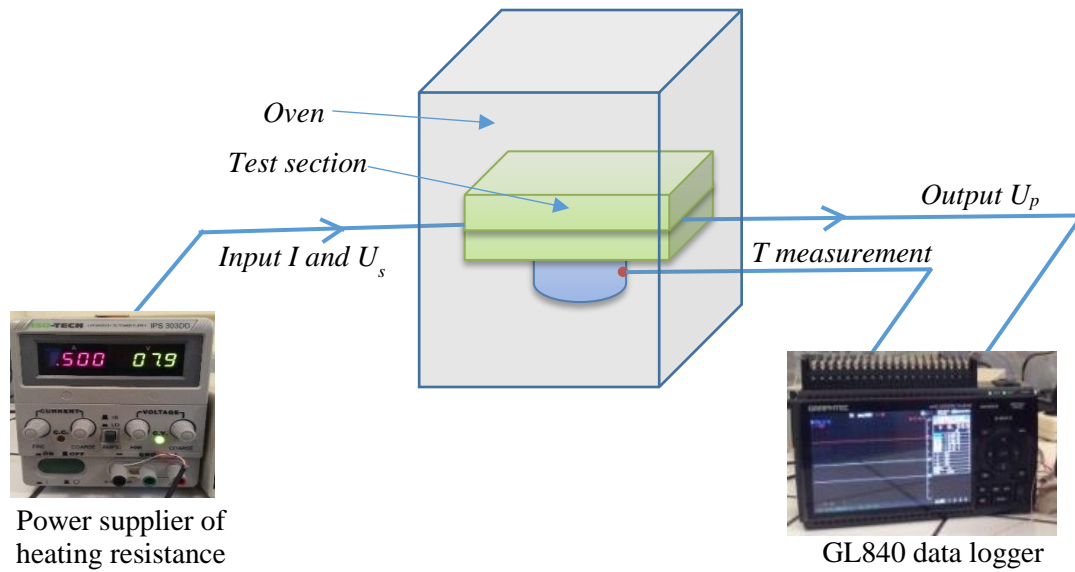


Fig. 2-9 Global scheme of system for calibration test

The output voltage of Peltier sensor was recorded by a data logger GL840 with an uncertainty of 0.1% of F.S. (FS: Full scale). The heat flux that effects on the Peltier sensor is computed by the thermal resistance (or supplier-voltage) and current:

$$q = \frac{I^2 R_I}{S} = \frac{U_s I}{S} \quad 2-7$$

Where  $I$  and  $U_s$  are respectively supplier current and voltage by ISO-TECH,  $R_I$  is resistance of heating ( $R_I = 20 \Omega$ ) and  $S$  is area. Through an analysis of a pre-test,  $I^2 R_I$  is more accuracy and stable to calculate the heat flow rate than  $U_s I$ .  $I^2 R_I$  was used in this research, so that the sensitivity  $k$  was calculated as:

$$k = \frac{U_p \cdot I^2 \cdot R_I}{S} \quad 2-8$$

In order to cover a representative range of values that typically encountered in civil engineering applications, the range of the heat flux was chosen from 10 to 1000  $\text{W/m}^2$  by regulating the supplier current.

The experimental output voltages of one Peltier sensor (Peltier 1) were shown in Fig. 2-10 when adjusting the supplier current from 0.02 to 0.225 A (10 values totally) at an ambient temperature of 23°C. For each supplier current, the output voltage is recorded for about 20 mins. The supplier heat flux  $q$  and the mean value of output voltage  $U_p$  at each current are listed in Table 2-4. When the current ranges from 0.02 to 0.225 A, the heat flux that effects on the sensor ranges from 8 to 1125  $\text{W/m}^2$ .

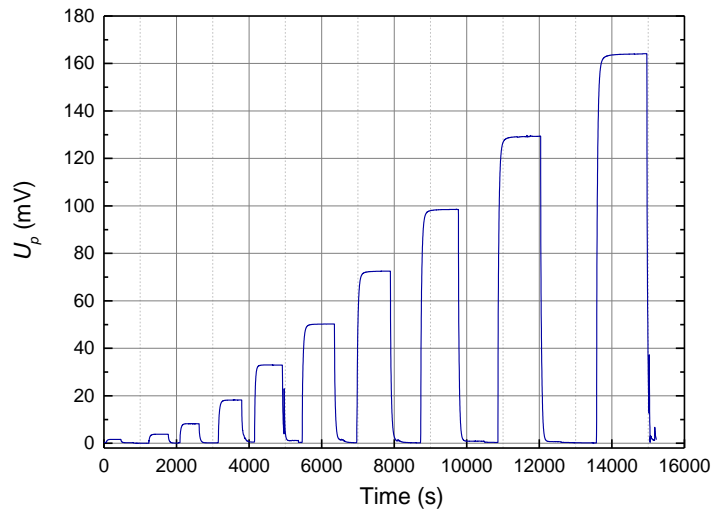


Fig. 2-10 Output voltage of Peltier sensor with supplier current ranging from 0.02 to 0.225 A

Table 2-4 Sensitivity of Peltier 1 at 10 values of heat flux

$I$ (A)	$q$ (W/m <sup>2</sup> )	$U_p$ (mV)
0.02	8.89	1.62
0.04	27.22	3.81
0.05	55.56	8.25
0.08	125.00	18.22
0.10	222.22	32.97
0.13	347.22	50.24
0.15	500.00	72.51
0.18	680.56	98.51
0.20	888.89	129.32
0.23	1125.00	164.00

The output voltage of Peltier and supplier heat flux is plotted and fitted in Fig. 2-11, which means the sensitivity of Peltier 1 is 145.48  $\mu\text{V}/(\text{W}/\text{m}^2)$  at an ambient temperature of 23 °C.

With the same principles, the calibration results of other Peltier sensors were obtained at ambient temperature of 23 °C and 35°C, as listed in Table 2-5.

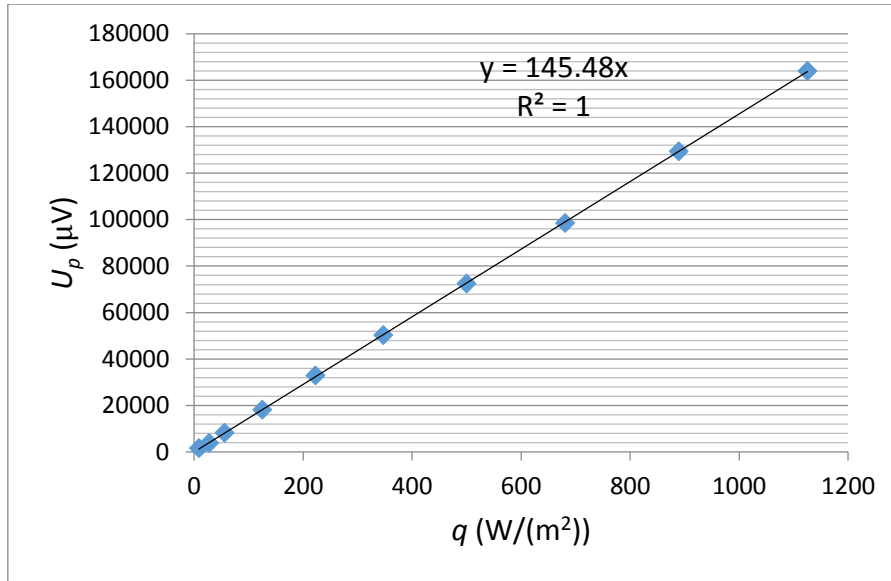


Fig. 2-11 Calibration of Peltier 1: output voltage VS heat flux

Table 2-5 Calibration results of Peltier sensors

Sensors	$k$ (23°C)	$R^2$	$k$ (35°C)	$R^2$
Peltier 1	145.48	1	150.54	1
Peltier 2	146.57	0.9998	152.56	1
Peltier 3	149.74	1	155.03	1
Peltier 4	149.44	0.9998	152.07	0.9998

According to the manufacturer, the relationship between sensitivity and operation temperature (ambient temperature) is nearly linear in the range from 0 °C to 50 °C. Linear fitting is made for the two temperatures. Finally, the sensitivity of each Peltier sensor is:

Peltier 1:  $k_{P1}=0.42T+135.78$

Peltier 2:  $k_{P2}=0.50T+135.09$

Peltier 3:  $k_{P3}=0.42T+139.60$

Peltier 4:  $k_{P4}=0.22T+144.40$

Where  $T$  is the ambient temperature in °C.

With the same setup, a fluxmeter is also calibrated, see the result in Fig. 2-12. The calibrated sensitivity is 18.459, which has a good agreement with that refers to the manufacture of 18.5 µV/(W/m<sup>2</sup>).

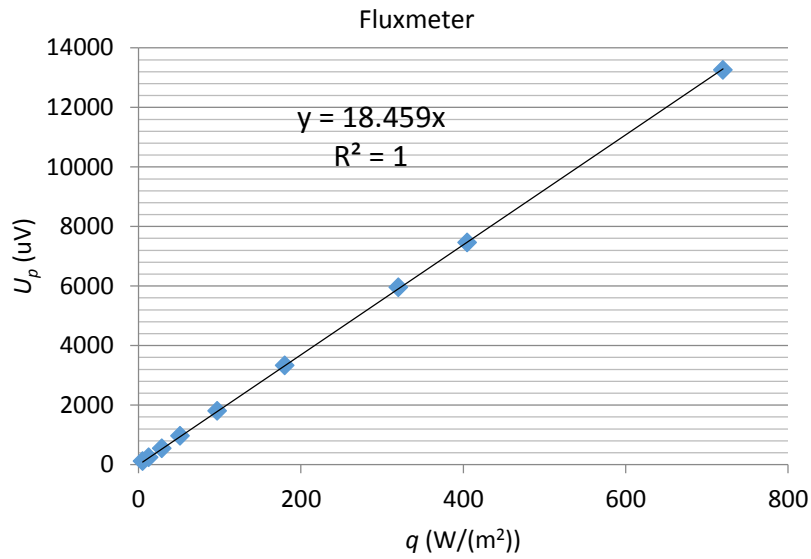


Fig. 2-12 Calibration of fluxmeter: output voltage VS heat flux

According to the Equ. 2-8, the sensitivity is described by  $k=f(U_p, S, I, R)$ , the uncertainty of sensitivity is given by Equ. 2-9 based on the uncertainty propagation equation.

$$\Delta k = \sqrt{\left(\frac{\partial k}{\partial U_p} \Delta U_p\right)^2 + \left(\frac{\partial k}{\partial S} \Delta S\right)^2 + \left(\frac{\partial k}{\partial I} \Delta I\right)^2 + \left(\frac{\partial k}{\partial R} \Delta R\right)^2} \quad 2-9$$

Where  $S=L^2$ ;  $\Delta S = \sqrt{\left(\frac{\partial S}{\partial L} \Delta L\right)^2}$

The uncertainties of different parameters and the mean sensitivity of all the heat flux range for each sensor are calculated and listed in Table 2-6.

Table 2-6 Uncertainties of calibration test

Uncertainties of parameters	Values
$\Delta U_p$	0.1% of FS (10 µV/200 µV)
$\Delta I$	0.0003 (A)
$\Delta R_I$	0.05 (Ω)
$\Delta L$	$2 \times 10^{-5}$ (m)
$\Delta S_{\text{Captec}}$	$2 \times 10^{-6}$ (m <sup>2</sup> )
$\Delta S_{\text{Peltier}}$	$1.2 \times 10^{-6}$ (m <sup>2</sup> )
$\Delta k_{\text{Captec}}$	0.13
$\Delta k_{\text{Peltier}}$	1.14



## 2.2 Sensors calibration

With the uncertainty analysis, the finally calibration results of sensor are:

Peltier sensor 1:  $k_{P1}=(0.42T+135.78) \pm 1.14$

Peltier sensor 2:  $k_{P2}=(0.50T+135.09) \pm 1.14$

Peltier sensor 3:  $k_{P3}=(0.42T+139.60) \pm 1.14$

Peltier sensor 4:  $k_{P4}=(0.22T+144.40) \pm 1.14$

Fluxmeter:  $k_{Cap1} = 18.46 \pm 0.13$

Where  $T$  is the ambient temperature in °C.

The uncertainty of heat flux ( $q$ ) that measured by the calibrated sensors should be estimated.

$$q = U_p/k \quad 2-10$$

The uncertainty of measurement heat flux is then

$$\Delta q = \sqrt{\left(\frac{\partial q}{\partial U_p} \Delta U_p\right)^2 + \left(\frac{\partial q}{\partial k} \Delta k\right)^2} \quad 2-11$$

That is:

$$\Delta q = (k^2 \cdot \Delta U_p^2 + U_p^2 \cdot \Delta k^2)^{0.5} / k^2 \quad 2-12$$

The measurement uncertainty of heat flux is also determined by the output voltage of sensor, which is not a constant value. Normally, two heat flux ranges are considered in this research: 0-20 W/m<sup>2</sup> and 0-500 W/m<sup>2</sup>. Table 2-7 lists the uncertainty values that measured by fluxmeter and Peltier sensor.

Table 2-7 Uncertainty of measurement heat flux

	Maximum heat flux (W/m <sup>2</sup> )	$U_p$ (μV)	$\Delta U_p$ (μV)	$k$	$\Delta k$	$\Delta q$ (W/m <sup>2</sup> )	$\Delta q/q$
fluxmeter	20	370	10	18.46	0.13	0.56	2.80%
	500	9230	10	18.46	0.13	3.56	0.70%
Peltier	20	2910	10	145.48	1.14	0.17	0.86%
	500	72740	200	145.48	1.14	4.15	0.83%

These calibrated sensors were used in two experiments: experiment in the laboratory and experiment in situ.

## 2.3 Experiments in the laboratory

### 2.3.1 Experimental scheme and configuration

The main principle of this experiment is that several different heating signals are provided on one surface of a multilayer wall. Both the temperature of front surface (the heated surface) and temperature of rear surface will perform as different temperature curves corresponding to each heating signal (see some examples in Fig. 2-13). The heat flux of the two surfaces of wall can be obtained by heat flux sensors. The wall thermal properties will be characterized by using different numerical approaches which involves the surface heat flux and temperatures.

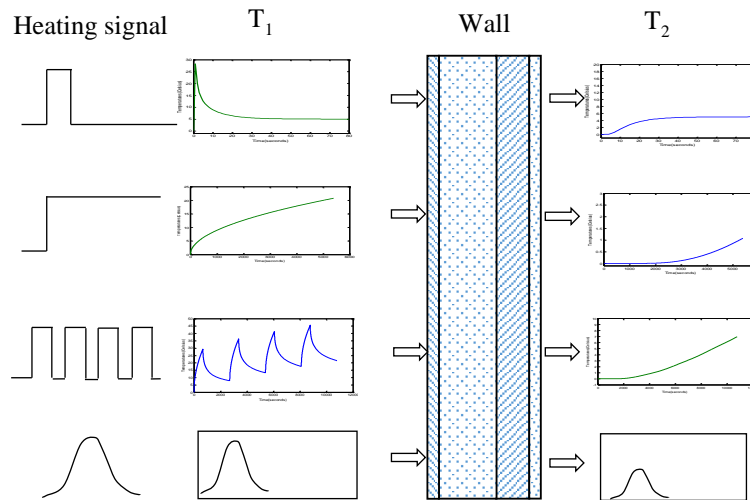


Fig. 2-13 Main principle of experiment

The experiments were implemented in laboratory. Fig. 2-14 shows the diagram of experimental set-up. The tested wall is installed on a wall box, the wall box is fixed in an enclosed climatic chamber, in which temperature and humidity can be controlled by an air conditioner unit. The heating lamps and IR camera are placed in front of the wall (distance of 1 m between wall surface and lamps; 1.7 m between wall surface and IR camera). Test area 1 is the center of wall. The IR camera and center of lamps are fixed at the same height of test area 1. The temperatures of two faces of test area 1, respectively  $T_1$  and  $T_2$ , are measured. Test area 2 is on the side of wall box and test area 3 is on the top of wall. Test area 2 and test area 3 will be measured for providing complementary information during the test. A heater is installed inside the wall box to control temperature. A hole is on the back of the wall box in order to fix an IR camera to take internal thermography.

## 2.3 Experiments in the laboratory

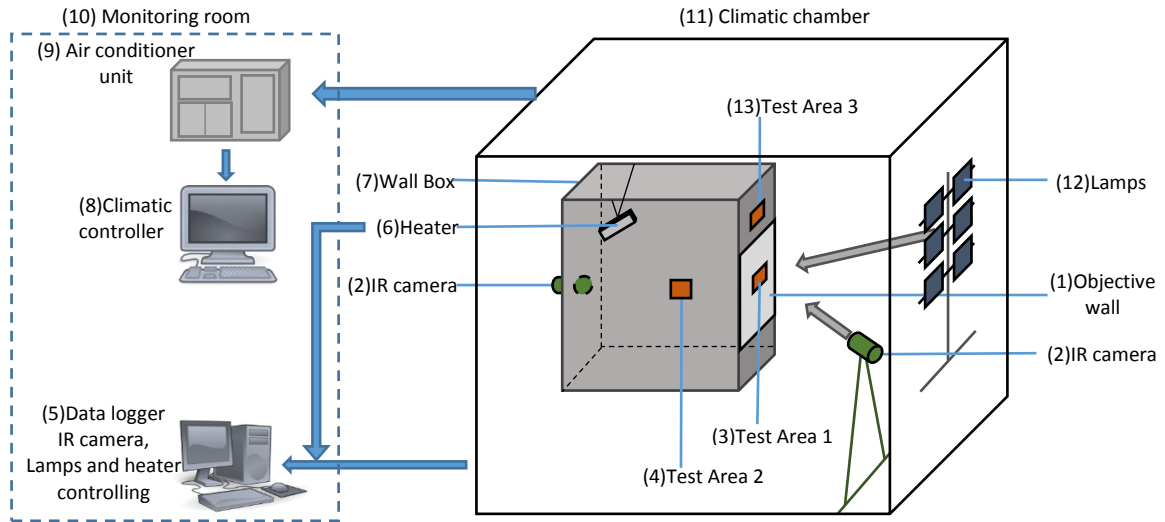


Fig. 2-14 Diagram of experimental set-up

The photos of instruments are shown in Fig. 2-15 (a). The collector of IR camera, controller of lamps, the data logger and also the air conditioner unit are placed in the monitoring room, which is just next to the climatic chamber. When the test is carrying on, the lamps will be launched with a given signal, and the IR camera and data logger will start recording at the same time. Fig. 2-15 (b) shows the test area 1 with the sensors installed on.

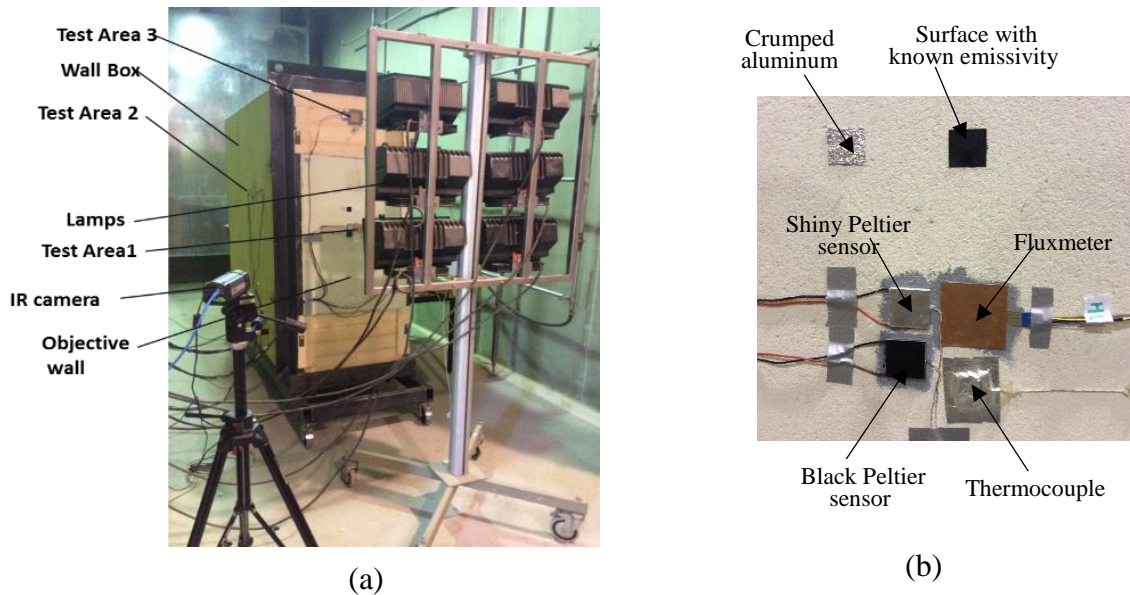


Fig. 2-15 Photos of instruments (a): Experiment setup (b): Test Area 1

### 2.3.2 Facilities

The size of wall box is  $200 \times 195.8 \times 85.2$  cm. The objective wall is installed on the frame fixed between the insulation materials at the top and down of the wall, which can reduce the heat loss of wall in the vertical direction.

Fig. 2-16(a) shows the inside of wall box, the internal surface is covered by reflecting coats to ensure that the internal radiation can be reflected to the wall to reduce the heat loss. The envelope of wall box contains reflecting coats, insulation materials and wood. The diagram of wall box is shown in Fig. 2-16(b).

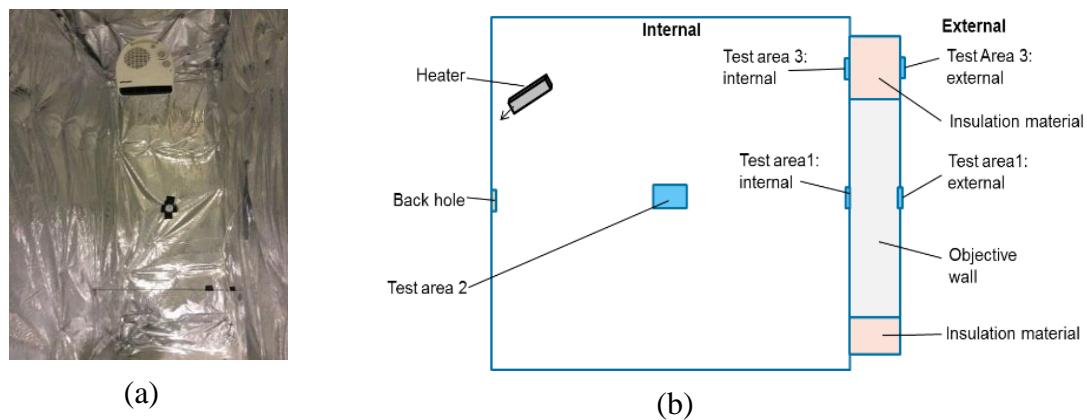


Fig. 2-16 Wall box (a) inside of wall box. (b) diagram of wall box.

The size of the objective wall (Fig. 2-17) is  $100 \times 70 \times 26.25$  cm, which consists of 4 layers: cement mortar of 10 mm, concrete block of 200 mm, insulation of 40 mm and plaster of 12.5 mm. Thermocouples are installed between the layers when it is built. The red spots in Fig. 2-5 are the positions where the thermocouples are fixed. The reference values of wall thermal properties (from handbooks [92]–[94]) are listed in Table 2-8.

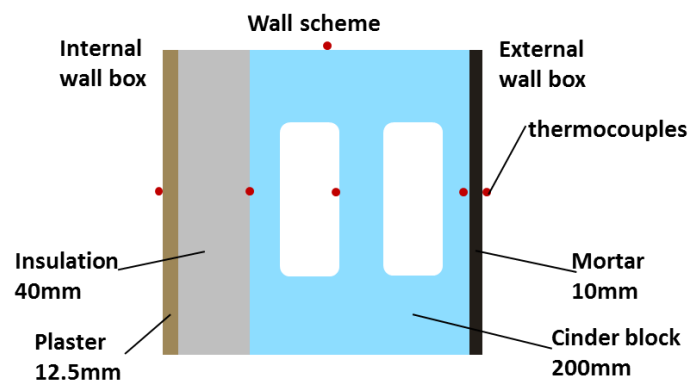


Fig. 2-17 Scheme of objective wall

Table 2-8 Reference values of wall thermal properties

Layers	$L$ (m)	$\lambda$ (W/(m · K))	$\rho c$ (J/(K · m <sup>3</sup> ))
Mortar cement	0.01	1.15	1.7x10 <sup>6</sup>
Concrete block	0.2	0.87	0.9x10 <sup>6</sup>
Insulation layer	0.04	0.038	0.03x10 <sup>6</sup>
Plaster	0.0125	0.25	0.9x10 <sup>6</sup>

The solar irradiation that effects on the wall is imitated by six halogen lamps, as shown in the Fig. 2-18 Six halogen lamps. The halogen lamps produce a continuous spectrum of light, from near ultraviolet to deep into the infrared [95]. The majority of the emitted energy (up to 85%) lies in the infrared and near-infrared regions of the spectrum, with 15% - 20% falling into the visible (400 to 700 nm), and less than 1% in the ultraviolet wavelengths (below 400 nm). The most important advantage is that the light output can be regulated by input different voltages. The light output is reported as proportional to  $V^3$  ( $V$  is input voltage), and the luminous efficacy proportional to  $V^{1.3}$  [96].

The distance between the lamps and the objective wall is 1 m. The power of lamps is supplied by an input voltage of 10V. This input voltage can be converted to 230V through three transformers. A program is built to regulate the input voltage. With this program, the input voltage ranges from 0 V to 10 V and performs as different signal shapes, for example, half sine wave and square wave. The heat flux intensity at the wall surface ranges from 0 to 1380 W/m<sup>2</sup>. Calibration was carried out on the lamps in order to obtain the relationship between the input voltage and the irradiation intensity. The calibration test is described in Appendix D

A heater (Fig. 2-19) was installed inside the wall box in order to regulate the temperature of internal wall box. The heater is controlled by a PC program: if the temperature is lower than the set temperature, a voltage will output to the heater and then the heater works. On the contrary, if the temperature rises to the set temperature, the output voltage stops.

In this work, GRAPHTEC GL840 is used for data acquiring and collecting. GL840 has 40 channels and can record both temperatures and voltages, it is managed by a software GL840-APS on the laptop. GL840 can work offline with a 4G built-in SD card. Fig. 2-20(a) shows the data logger connecting with sensors. Fig. 2-20(b) shows the working screen of software GL840-APS.

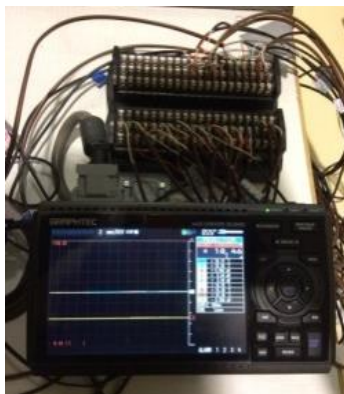
## 2.4 Experiments in situ



Fig. 2-18 Six halogen lamps



Fig. 2-19 Heater installed inside the wall box



(a)



(b)

Fig. 2-20 Data logger: GRAPHTEC GL840

## 2.4 Experiments in situ

In the in situ-case, an exterior wall of a demonstration building in Bordeaux is diagnosed. Fig. 2-21 is the overall photo of this building. This building is the platform SYNERGI of the department of civil engineering and sustainable building of the University Institute of Technology of Bordeaux. The wall that the red arrow points is the target wall.



Fig. 2-21 A demonstration building-Platform SYNERGI

Fig. 2-22 shows the indoor and outdoor pictures of the target wall. The red square is the test area. Fig. 2-23 shows the structure of the target wall: a plaster layer of 10 mm, an insulation layer of 100 mm (CALIBEL APV), a concrete block layer of 250 mm and a mortar layer of 10 mm.

Table 2-9 is the thermal properties of each layer from handbooks [92]–[94].



Fig. 2-22 The exterior wall of building that to be tested: outdoor (left) and indoor (right).

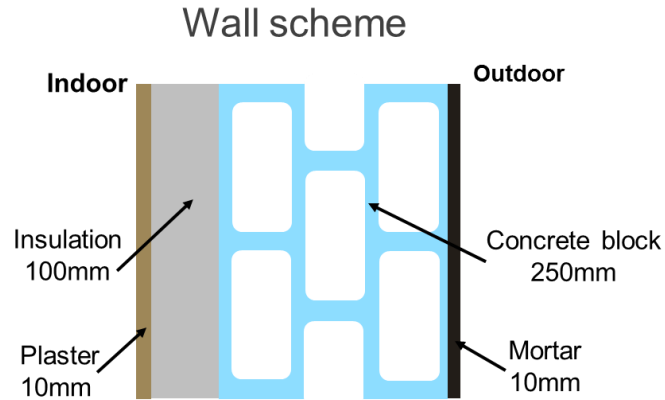


Fig. 2-23 Scheme of objective wall

Table 2-9 Thermal properties of each layer of wall [92]–[94]

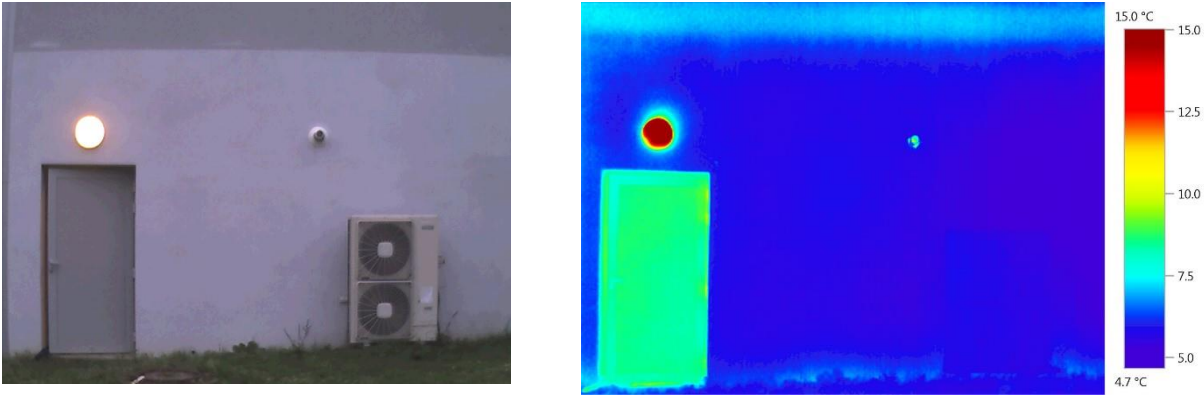
Layers	$L$ (m)	$\lambda$ (W/(m · K))	$\rho c$ (J/(K · m <sup>3</sup> ))
Mortar cement	0.01	1.15	$1.7 \times 10^6$
Concrete block	0.25	0.893	$0.9 \times 10^6$
Insulator layer	0.1	0.034	$0.03 \times 10^6$
Plaster	0.01	0.25	$0.9 \times 10^6$

Before quantitative characterizing tests, passive thermography was used to detect the defects and chose adapted test areas.

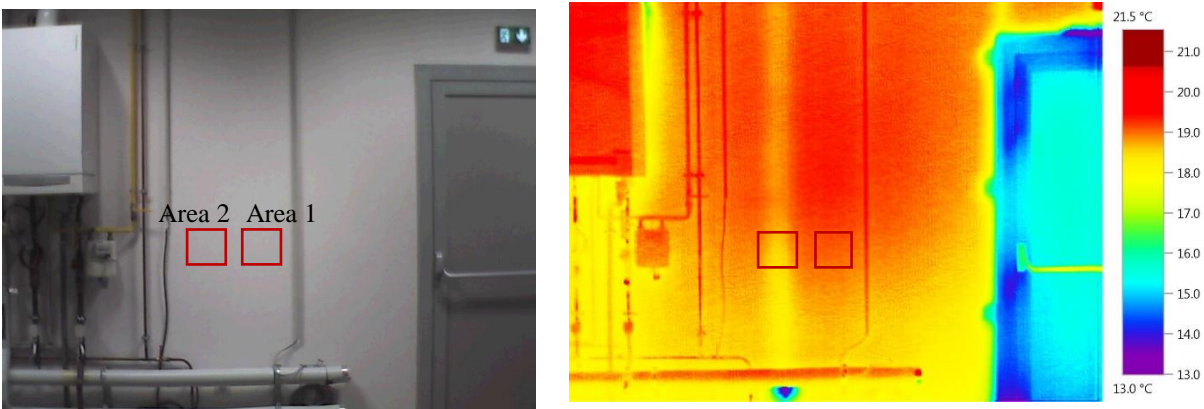
Infrared images were taken for the tested wall under the following conditions: indoor temperature was 19.5 °C, outdoor temperature was 8 °C measured by thermocouple, the sky was without clouds and the ground temperature was about 4 °C measured by the IR camera. Fig. 2-24 shows the photos and infrared images of internal and external surfaces of the wall. According to these figures, the external composition of wall is homogeneous, while there is a vertical defect near the internal surface of wall. Therefore, two test areas are chosen: one area (Area 1) without defect and the other one (Area 2) with this defect.



2.4 Experiments in situ



(a) External surface of objective wall



(b) Internal surface of objective wall

Fig. 2-24 Photos and infrared images of wall for defects detecting

Fluxmeters that coated with aluminum (shiny fluxmeter) and that painted black (black fluxmeter) are pasted on the two test areas, as shown in Fig. 2-25.

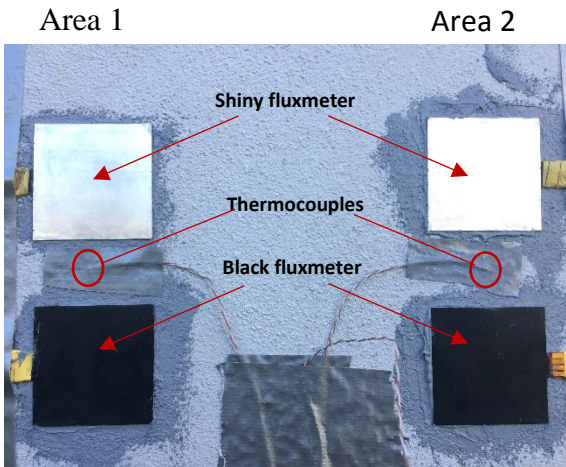


Fig. 2-25 Fluxmeters and thermocouples installed on the test areas

## 2.4 Experiments in situ

---

As shown in Fig. 2-26 (a), 16 artificial solar lamps were used to heat the wall. The incident heat flux of test area can be almost uniform. IR cameras are fixed beside the lamps. Fig. 2-26 (b) shows the overall photo of this experiment. The infrared lamps are focused on the center of the test areas indoor and will heat the wall with predefined signals. A radiative heat flux sensor was also fixed on the wall to roughly obtain the radiation of lamps affected on the wall.



(a) artificial solar lamps and IR cameras



(b) overall photo of experiment

Fig. 2-26 Photos of facilities



# Chapter 3

## Measurements And Data Processing

---

---

As described in Chapter 2, experiments were carried out in laboratory and in situ. In this Chapter, the measurement methods and data processing will be introduced for the emissivity, temperatures and wall heat flux. The thermography processing will be described as well.

### 3.1 Emissivity

Research on emissivity measurement for buildings is necessary and popular. In this work, emissivity is an important parameter to calculate wall heat flux. The emissivities of wall, painted black surface, shiny aluminum surface and fluxmeter surface (totally 4 target surfaces) should be measured to make further analysis of wall heat flux.

#### 3.1.1 Emissivity measurement

The emissivity measurement is based on the standard ISO 18434-1:2008(E) (Appendix E). A fully crumple aluminum is fixed on the test area to measure the reflected apparent temperature. A black paint (NEXTEL Velvet Coating 811-21) with known emissivity of 0.97 is painted on

the target surface considering as the reference surface. The emissivity measurements were carried out in laboratory, whose steps were as followings (Fig. 3-1):

- (1) Paste a square piece of very crumple aluminum on the center of wall in order to measure the reflected apparent temperature;
- (2) Paint an area of 30×30 mm on the wall directly with the paint NEXTEL, this area is near the crumpled aluminum. By this way, the wall emissivity can be computed out.
- (3) The shiny surface and fluxmeter surface are half-area painted by the NEXTEL. A new Peltier sensor is painted with the NEXTEL and pasted near the black Peltier sensor.
- (4) Focus the heating lamps and IR camera on the test area of wall, the distance from the wall to camera and lamps is 1.7 m.
- (5) Close the climatic chamber door, launch the lamps for 3 hours and then stop, start the IR camera and GL840 to record data. The cooling period lasts for about 10 hours.
- (6) Data processing: with the IR images and temperatures by the thermocouples, the emissivity of 4 target surfaces can be obtained (shown in subsection 3.1.1).

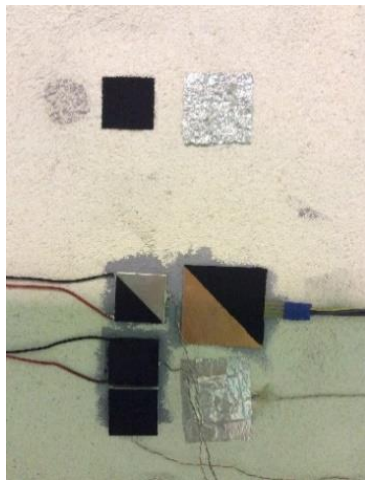


Fig. 3-1 Test area of emissivity measurement

#### 3.1.2 Fundamental and data processing

All the objects that temperature is over than 0 K can emit thermal radiation. The intensity of this emitted energy is determined by the temperature and radiation wavelength. If the object temperature is less than 500 °C, the emitted radiation lies completely within IR wavelengths [88]. The higher the temperature, the greater the intensity of the infrared energy emitted.

In addition to emitting radiation, an object also reacts to incident radiation from its surroundings through absorbing and reflecting a portion of it, or allowing some of it to pass, as shown in Fig. 3-2.

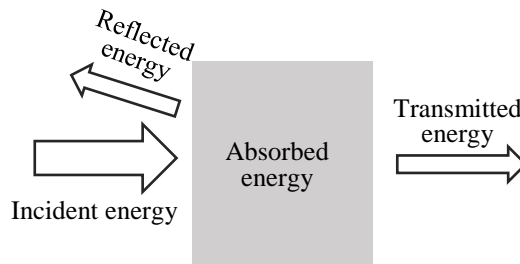


Fig. 3-2 Radiation propagation principle

This physical principle can be expressed by Equ. 3-1.

$$W = a_{\lambda'}W + \gamma_{\lambda'}W + \tau_{\lambda'}W \quad 3-1$$

Where  $W$  is the total incident radiation,  $a_{\lambda'}, \gamma_{\lambda'}, \tau_{\lambda'}$  are the coefficients of absorptivity, reflectivity and transmissivity respectively. For an opaque material, the transmissivity is 0 ( $\tau_{\lambda'} = 0$ ). According to Planck's law [97], the spectral radiance emitted from a blackbody ( $a_{\lambda'}=1$ ) per wavelength can be calculated as:

$$W_{\lambda'b} = \frac{C_1 \lambda'^{-5}}{e^{\frac{C_2}{\lambda'T}} - 1} \quad 3-2$$

Where  $C_1, C_2$  are constants,  $\lambda'$  is the wavelength ( $\mu\text{m}$ ) and  $T$  is the temperature (K).

The emissive power curves depending on wavelength and temperature are shown in Fig. 3-3. The curves show that objects with high temperatures (800-1000 K) emit most of the radiation in the SWIR (1.4-3  $\mu\text{m}$ ) and MWIR (3-8  $\mu\text{m}$ ). Objects with low temperatures (250-400 K) emit most of the radiation in the LWIR (8-15  $\mu\text{m}$ ). In the field of civil engineering, generally, the temperature is below 373 K.

According to the Stefan–Boltzmann formula, the total hemispherical radiation intensity of a blackbody over all wavelength can be obtained:

$$W_b = \sigma \cdot T^4, \sigma = 5.67 \times 10^{-8} \text{ W} \cdot \text{K}^{-4} \cdot \text{m}^{-2} \quad 3-3$$

Where  $\sigma$  is the Boltzmann constant.

For a gray body radiators:

$$W = \varepsilon \cdot \sigma \cdot T^4, \text{ where } \varepsilon = \frac{W}{W_b} \quad 3-4$$

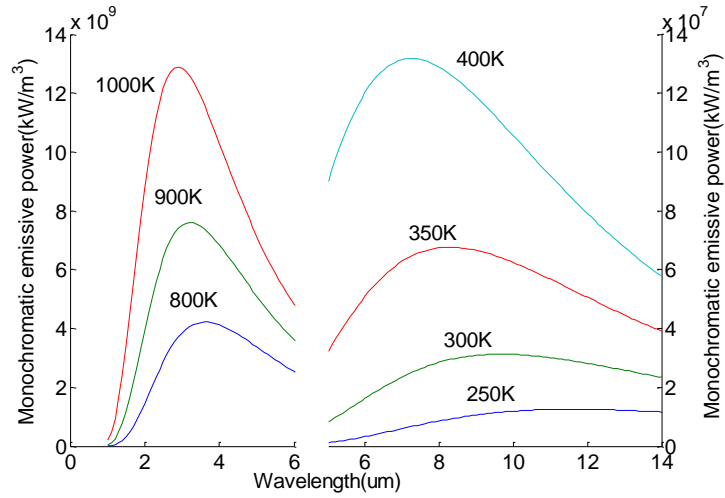


Fig. 3-3 Planck’s law: Blackbody emissive power as a function of wavelength and temperature.

As described in Fig. 3-4 [98], the total radiation received by the camera ( $W_{tot}$ ) comes from three sources: the emission of the target object ( $W_{obj}$ ), the emission of the surroundings and reflected by the object ( $W_{refl}$ ) and the emission of the atmosphere ( $W_{atm}$ ). Both of these radiation components become attenuated when they pass through the atmosphere. Since the atmosphere absorbs part of the radiation, it will also radiate some itself (Kirchhoff’s law). It can be expressed as following equation:

$$W_{tot} = W_{obj} + W_{refl} + W_{atm} \quad 3-5$$

Where

$$W_{obj} = \varepsilon_{obj} \cdot \tau_{atm} \cdot \sigma \cdot T_{obj}^4 \quad 3-6$$

$$W_{refl} = (1 - \varepsilon_{obj}) \cdot \tau_{atm} \cdot \sigma \cdot T_{refl}^4 \quad 3-7$$

$$W_{atm} = (1 - \tau_{atm}) \cdot \sigma \cdot T_{atm}^4 \quad 3-8$$

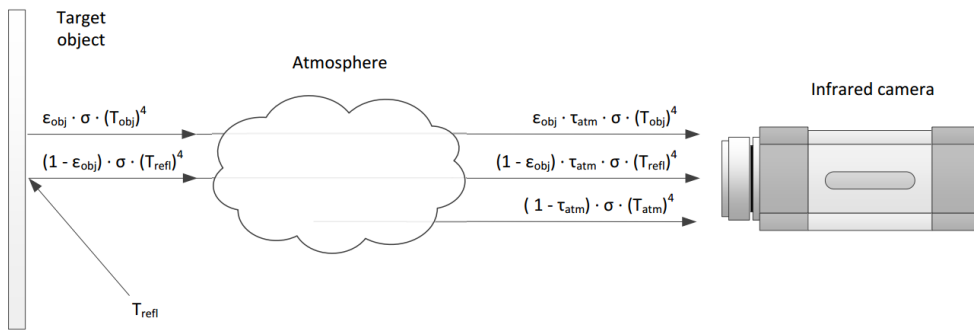


Fig. 3-4 Schematic of IR camera when measuring temperature [98]

So that the total radiation received by the camera  $W_{tot}$  (W/m<sup>2</sup>) is:

$$W_{tot} = \varepsilon_{obj} \cdot \tau_{atm} \cdot \sigma \cdot T_{obj}^4 + (1 - \varepsilon_{obj}) \cdot \tau_{atm} \cdot \sigma \cdot T_{refl}^4 + (1 - \tau_{atm}) \cdot \sigma \cdot T_{atm}^4 \quad 3-9$$

The temperature of object can be calculated:

$$T_{obj} = \left( \frac{W_{tot} - (1 - \varepsilon_{obj}) \cdot \tau_{atm} \cdot \sigma \cdot T_{refl}^4 - (1 - \tau_{atm}) \cdot \sigma \cdot T_{atm}^4}{\varepsilon_{obj} \cdot \tau_{atm} \cdot \sigma} \right)^{1/4} \quad 3-10$$

As described in 3.1.1, a fully crumple aluminum was fixed to measure the reflected apparent temperature. The radiation received by IR camera from this crumple aluminum  $W_{tot}^{Alu}$  is:

$$W_{tot}^{Alu} = \varepsilon_{Alu} \cdot \tau_{atm} \cdot \sigma \cdot T_{Alu}^4 + (1 - \varepsilon_{Alu}) \cdot \tau_{atm} \cdot \sigma \cdot T_{refl}^4 + (1 - \tau_{atm}) \cdot \sigma \cdot T_{atm}^4 \quad 3-11$$

This crumple aluminum is assumed as a reflector, whose emissivity is 0, that is  $\varepsilon_{Alu} = 0$ , Equ. 3-11 can be reduced as:

$$W_{tot}^{refl} = W_{tot}^{Alu} = \tau_{atm} \cdot \sigma \cdot T_{refl}^4 + (1 - \tau_{atm}) \cdot \sigma \cdot T_{atm}^4 \quad 3-12$$

For the target surface of reference material with known emissivity, the radiation received by IR camera  $W_{tot}^{refe}$  can be written as:

$$W_{tot}^{refe} = \varepsilon_{refe} \cdot \tau_{atm} \cdot \sigma \cdot T_{refe}^4 + (1 - \varepsilon_{refe}) \cdot \tau_{atm} \cdot \sigma \cdot T_{refl}^4 + (1 - \tau_{atm}) \cdot \sigma \cdot T_{atm}^4 \quad 3-13$$

For the target surface of the objective that to be measured, the radiation received by IR camera  $W_{tot}^{obj}$  is:

$$W_{tot}^{obj} = \varepsilon_{obj} \cdot \tau_{atm} \cdot \sigma \cdot T_{obj}^4 + (1 - \varepsilon_{obj}) \cdot \tau_{atm} \cdot \sigma \cdot T_{refl}^4 + (1 - \tau_{atm}) \cdot \sigma \cdot T_{atm}^4 \quad 3-14$$

From the Equ. 3-12, Equ. 3-13 and Equ. 3-14, the emissivity of objective  $\varepsilon_{obj}$  can be obtained:

$$\varepsilon_{obj} = \varepsilon_{refe} \cdot \frac{W_{tot}^{obj} - W_{tot}^{refl}}{W_{tot}^{refe} - W_{tot}^{refl}} \cdot \frac{T_{refe}^4 - T_{refl}^4}{T_{obj}^4 - T_{refl}^4} \quad 3-15$$

If assumed that  $T_{obj} = T_{refe}$ , the emissivity of objective becomes:

$$\varepsilon_{obj} = \varepsilon_{refe} \cdot \frac{W_{tot}^{obj} - W_{tot}^{refl}}{W_{tot}^{refe} - W_{tot}^{refl}} \quad 3-16$$

The output from IR camera ( $W_{tot-IR}$ ) is the radiance in W/(sr·cm<sup>2</sup>), so a transform is needed:

$$W_{tot} = k' \cdot W_{tot-IR} \quad 3-17$$



Where  $k'$  is the coefficient between  $W/(sr \cdot cm^2)$  and  $W/m^2$ . During the test, the camera is fixed and the angle between the camera lens and test area is constant, so that  $k'$  is a constant in our research. Therefore, Equ. 3-16 becomes:

$$\varepsilon_{obj} = \varepsilon_{refe} \cdot \frac{W_{tot-IR}^{obj} - W_{tot-IR}^{refl}}{W_{tot-IR}^{refe} - W_{tot-IR}^{refl}} \quad 3-18$$

In summary, the emissivity of target object can be obtained by Equ. 3-18 with the hypothesis that  $\varepsilon_{crum\_Alu} = 0$  and  $T_{refe} = T_{obj}$ .

### 3.1.3 Emissivity results

The test area was continuously heated by the lamps for 3 hours and then was cooling down for 15 hours. Fig. 3-5 shows an infrared image of test area.

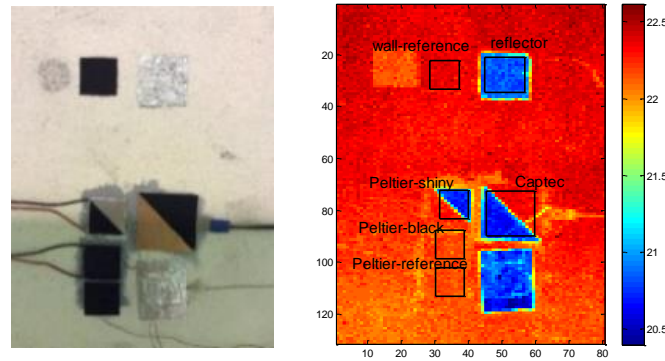


Fig. 3-5 Test area of emissivity measurement: (left) photo with visible camera, (right) infrared thermography

Fig. 3-6 shows the radiance values output from IR camera. The time step is 5 minutes, for each time step, 25 frames are taken in 1 second. The radiance value ( $W_{tot-IR}$ ) of a target surface for each time step is the mean value of all pixels of 25 frames. The radiance uncertainty ( $\Delta W_{tot-IR}$ ) is the standard deviation of all the pixels. For example, the target surface of reflector is  $10 \times 10$  pixels, so that there are 100 pixels for each frame, that is 2500 values of radiance are obtained by camera for each time step.  $\Delta W_{tot-IR}$  for each target surface in the measurement is less than 0.5%.

### 3.1 Emissivity

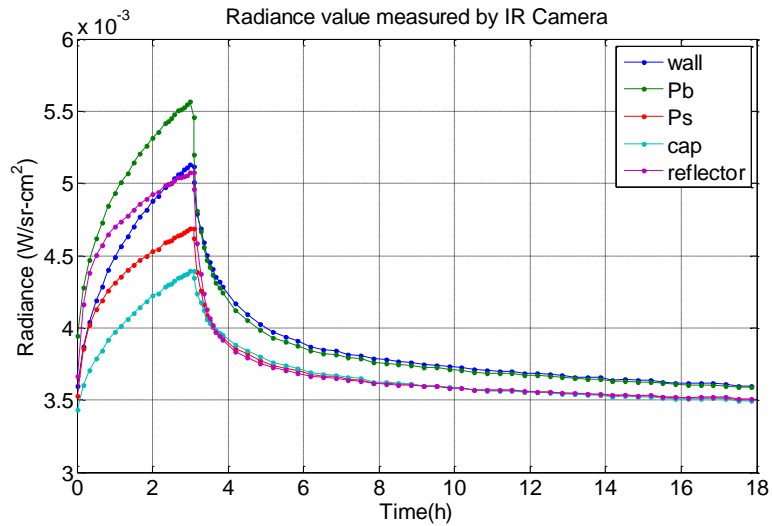


Fig. 3-6 radiance of each target area that output from IR camera

40 groups of data in the cooling period (4-18 hours) are chosen to calculate the emissivity of wall based on the Equ. 3-18. Fig. 3-7 shows the calculated emissivity results of wall.

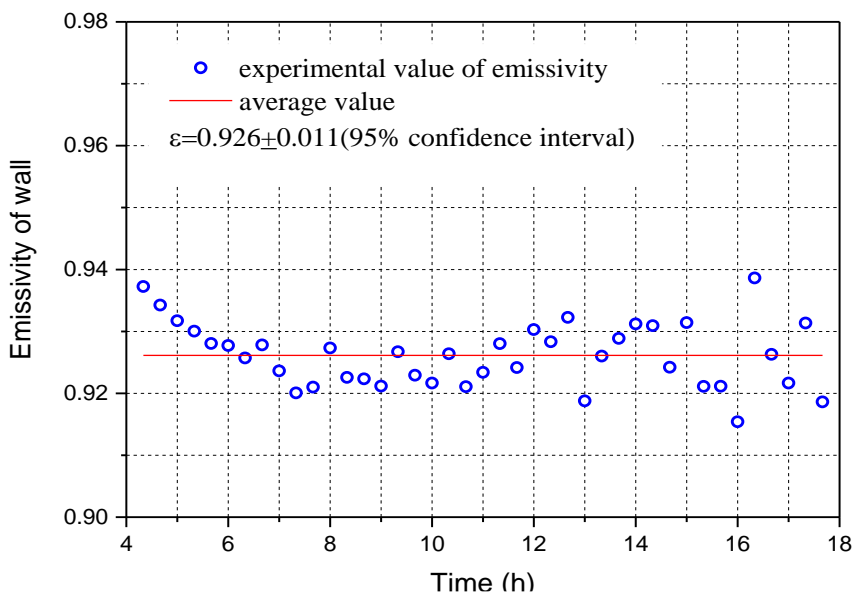
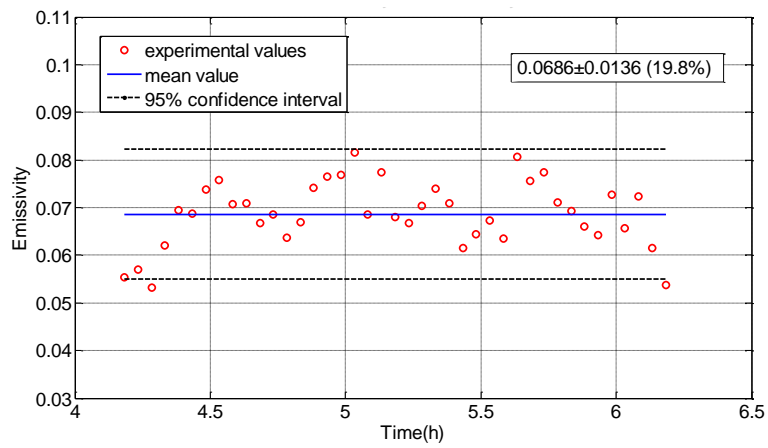


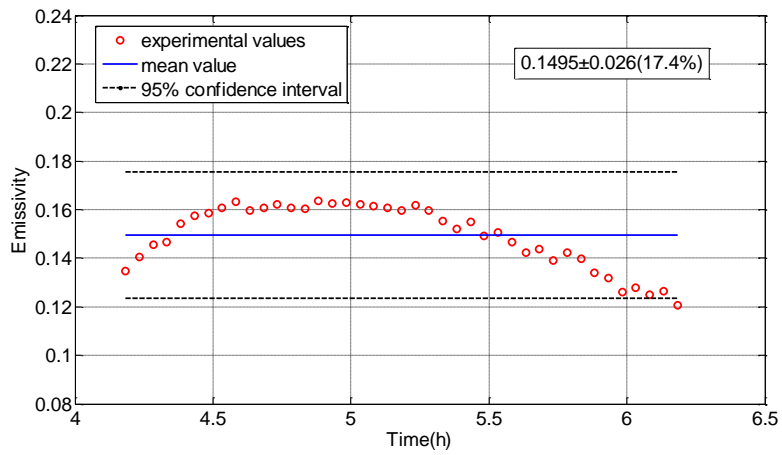
Fig. 3-7 Emissivity results of wall

For shiny surface and fluxmeter surface whose emissivity are low, 40 groups of data in the cooling period (4-6 hours) are chosen. Because for the low emissivity objects, the reflected apparent temperature effect a lot during the measurement. The emissivity can possible be obtained only when the temperature difference between the target surface and the ambient is high. Fig. 3-8 and Table 3-1 show the emissivity results. Actually, the data in this 2 hours were enough to estimate the emissivities.

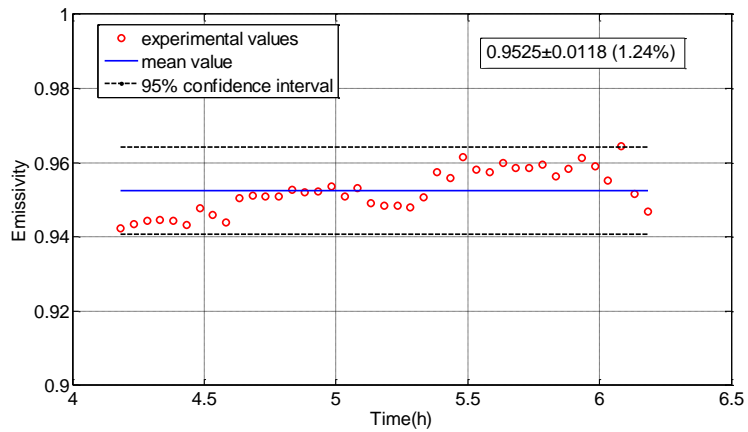
### 3.1 Emissivity



(a) Emissivity of shiny surface



(b) Emissivity of fluxmeter surface



(c) Emissivity of black surface

Fig. 3-8 Emissivity results

## 3.2 Heat flux

Table 3-1 Results of measured emissivity

	wall	Black surface	Shiny surface	Fluxmeter surface
Emissivity	0.926 ± 0.011	0.953 ± 0.012	0.069 ± 0.014	0.150 ± 0.026

The experimental results match well with the reference values (listed in Appendix H), which means that this method is applicable to the emissivity measurement of building envelopes. The emissivity should be measured in the cooling period in order to avoid the influence of other radiance. This estimation method is more accuracy and stable for high emissivity object, it is a good method to measure the emissivity of building materials (emissivity generally between 0.85-0.95).

## 3.2 Heat flux

### 3.2.1 Measurements

Because of the differences of emissivity and absorptivity between the sensors and wall, the heat flux measured by heat flux sensors is not the value of wall heat flux. Therefore, the wall heat flux is calculated indirectly based on heat flux balance equation by using two heat flux sensors: one is covered by an aluminum film (shiny heat flux sensor) and the other is painted black (black heat flux sensor).

In the laboratory-case, one black Peltier sensor and one shiny Peltier sensor were installed on the test area of wall to split convection and radiation effect on the wall. A fluxmeter was also installed to compare with the measurement of Peltier sensors. For the test in situ, a shiny fluxmeter and a black fluxmeter were used.

In this laboratory-case, the objective wall was tested in both steady state and transient heat transfer regimes. In order to build a steady state heat transfer on the wall, the temperature inside the wall box is set at 27°C (regulated by the heater). This wall box was placed in a chamber whose temperature is about 18°C. This temperature difference lasts for 91 hours which is long enough to ensure a stable heat transfer and avoid the influence of heat capacity of wall. Several signals were provided to heat the wall for the transient measurements: the square-wave heating signals with the periods of 2 hours, 24 hours, 48 hours and 96 hours, the half sine wave heating

signal with a period of 24 hours. Fig. 3-9 shows the square wave and half sine wave heating signals measured by the sensor SP Lite. Thermography was taken by IR camera, data of heat flux sensors and thermocouples was recorded by the GL840. For the test in situ, square wave signals of period of 1 hours, 2 hours, 6 hours and step signals were applied.

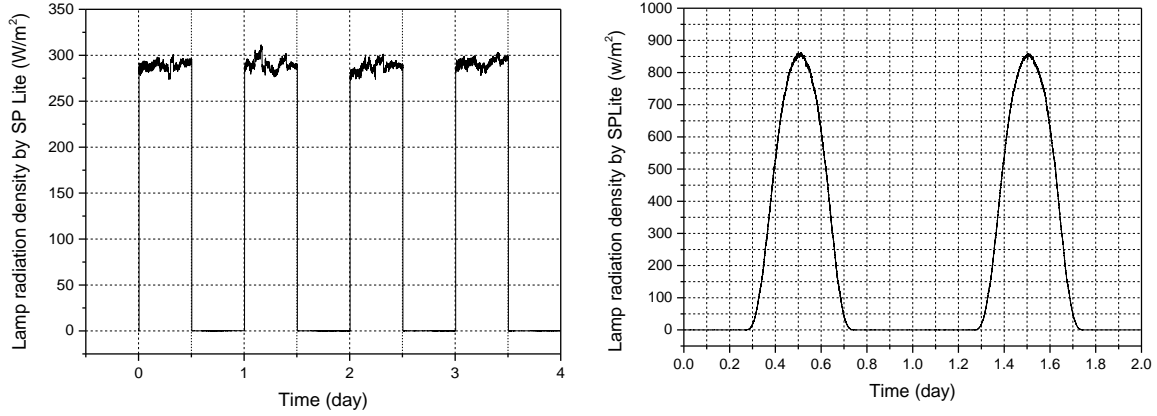


Fig. 3-9 Square wave heating signal (left) and half sine wave heating signal (right) at period of 24 hours

### 3.2.2 Data processing of heat flux

According to the heat flux balance law (see in Fig. 3-10), the total heat flux that permeates into a surface ( $q_{tot}$ ) is the sum of total radiation ( $q_{rad}$ ) and convection ( $q_{conv}$ ) (Equ. 3-19). The total radiation involves the ambient radiation ( $G$ ), emitted radiation ( $E$ ) and reflective radiation ( $G_{refl}$ ) by the surface, expressed by Equ. 3-20.

$$q_{tot} = q_{conv} + q_{rad} \quad 3-19$$

$$q_{rad} = G - E - G_{refl} \quad 3-20$$

With the Fourier's Law (Equ. 3-21) and Stefan–Boltzmann law (Equ. 3-22), the total heat flux of a target surface becomes Equ. 3-24.

$$q_{conv} = h(T_{air} - T_{surf}) \quad 3-21$$

$$E = \varepsilon \cdot \sigma \cdot T_{surf}^4 \quad 3-22$$

$$G_{refl} = (1 - a)G \quad 3-23$$

$$q_{tot} = a G + h(T_{air} - T_{surf}) - \varepsilon \cdot \sigma \cdot T_{surf}^4 \quad 3-24$$

Where  $h$  is the convection coefficient between air and target;  $T_{air}$  is the air temperature and  $T_{surf}$  is the surface temperature of the target;  $\varepsilon$  is the surface emissivity of target and  $a$  is the surface solar absorbance of target.

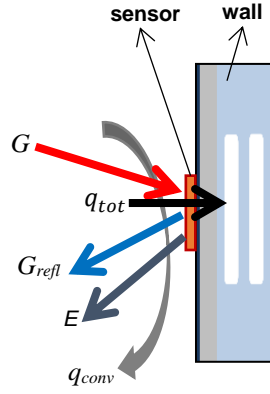


Fig. 3-10 Heat flux balance of a target surface

In order to calculate  $q_{tot}$  of wall (Equ. 3-25),  $G$  was obtained by using two heat flux sensors whose emissivities are different. The total heat fluxes of the two sensors are expressed in Equ. 3-26 and Equ. 3-27.

$$q_{tot-wall} = a_{wall} G + h_{wall}(T_{air} - T_{surf-wall}) - \varepsilon_{wall} \cdot \sigma \cdot T_{surf-wall}^4; \quad 3-25$$

$$q_{tot-b} = a_b G + h_b(T_{air} - T_{surf-b}) - \varepsilon_b \cdot \sigma \cdot T_{surf-b}^4; \quad 3-26$$

$$q_{tot-s} = a_s G + h_s(T_{air} - T_{surf-s}) - \varepsilon_s \cdot \sigma \cdot T_{surf-s}^4; \quad 3-27$$

Where the subscript  $b$  is for black heat flux sensor and  $s$  is for shiny heat flux sensor. With the assumption of  $h_b = h_s$ , the ambient radiation ( $G$ ) is obtained from Equ. 3-26 and Equ. 3-27.

$$G = \frac{(T_{air} - T_{surf-b})(q_{tot-s} + \varepsilon_s \sigma T_{surf-s}^4) - (T_{air} - T_{surf-s})(q_{tot-b} + \varepsilon_b \sigma T_{surf-b}^4)}{a_s(T_{air} - T_{surf-b}) - a_b(T_{air} - T_{surf-s})} \quad 3-28$$

The convection coefficient of sensor is:

$$h_b = h_s = \frac{a_s(q_{tot-b} + \varepsilon_b \sigma T_{surf-b}^4) - a_b(q_{tot-s} + \varepsilon_s \sigma T_{surf-s}^4)}{a_s(T_{air} - T_{surf-b}) - a_b(T_{air} - T_{surf-s})} \quad 3-29$$

The definition of Kirchhoff's law states: for an arbitrary body emitting and absorbing thermal radiation in thermodynamic equilibrium, the emissivity is equal to the absorptivity. However, the equality of emissivity and absorptivity often does not hold when the material of the body is not in thermodynamic equilibrium, such as in our cases. The solar absorbance values are given by the reference [97], [99]:  $a_s = 0.15$ ;  $a_b = 0.97$ ;  $a_{wall} = 0.65$ . The emissivities were measured previously:  $\varepsilon_s = 0.07$ ;  $\varepsilon_b = 0.95$ ;  $\varepsilon_{wall} = 0.93$ . With the measured heat flux and temperatures by sensors,  $G$  and  $h_b$  are obtained.

When the fluxmeters were used in the measurement, the convection coefficient of wall can be assumed the same with the fluxmeters ( $h_{wall} = h_b$ ) because of its thin thickness. Therefore the

total heat flux of wall was computed out. The radiation and convection can be split by Equ. 3-19- Equ. 3-21.

However, when the Peltier sensors were used for the measurement, the convection coefficient of wall is different with the Peltier sensors ( $h_{wall} \neq h_b$ ) because of its large thickness (3.5mm), which will enhance the convection heat transfer. This drawback was solved by installing a fluxmeter nearby the Peltier sensors or by prediction of numerical correlations.

Heat flux balance for this fluxmeter is expressed by Equ. 3-30.

$$q_{tot-cap} = a_{cap} G + h_{cap}(T_{air} - T_{surf-cap}) - \varepsilon_{cap} \cdot \sigma \cdot T_{surf-cap}^4; \quad 3-30$$

The solar absorbance of copper [97], [99]:  $a_{cap} = 0.18$ ; the emissivity was measured previously:  $\varepsilon_{cap} = 0.12$ . With the values of  $G$  and the measured  $q_{tot-cap}$ ,  $h_{cap}$  can be calculated. Therefore the convection coefficient of wall can be obtained if assumed that  $h_{cap} = h_{wall}$ .

The convection coefficients of wall can be predicted by Churchill numerical correlation [100]. For the free convection on a vertical plate, the Grashof number and Rayleigh number are:

$$Gr = \frac{g\beta(T_{wall} - T_{air})H^3}{\nu^2}; \beta = \frac{1}{T_f}, T_f = (T_{wall} + T_{air})/2 \quad 3-31$$

$$Ra = Gr \cdot Pr \quad 3-32$$

Where  $T_{wall}$  is the surface temperature of wall.  $H$  is the height of the vertical plate.  $g$  is standard gravity  $g = 9.8 \text{ m/s}^2$ . In this research, the vertical plate is  $H= 1.958 \text{ m}$  high. The physical properties of atmospheric air at 300 K and 283 K are listed in Table 3-2.

Table 3-2 Physical properties of atmospheric air

Properties	300 K	283 K
Density $\rho$ (kg/m <sup>3</sup> )	1.1774	1.2473
$c$ (kJ/kg·K)	1.0057	1.004
$\nu$ (m <sup>2</sup> /s×10 <sup>-6</sup> )	15.68	14.18
$\lambda$ (W/m.K)	0.02624	0.02486
$Pr$	0.708	0.714

Equ. 3-33 is used for the calculation of  $Nu$ . The convection coefficient of wall can be estimated by Equ. 3-34.

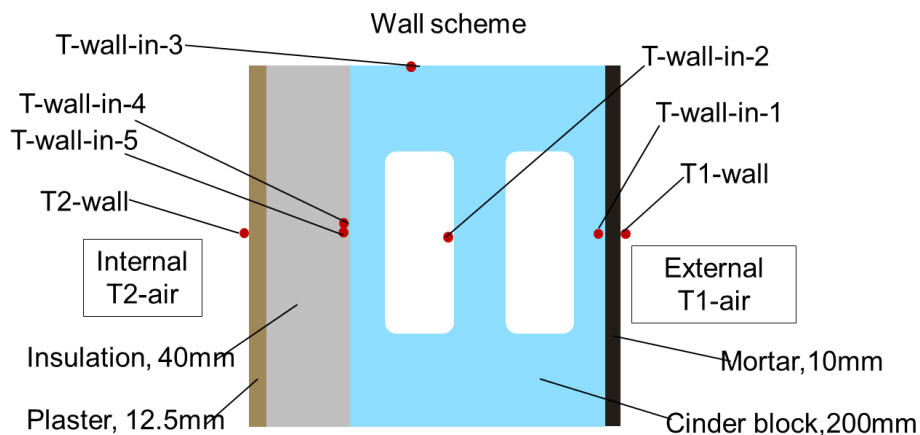
$$Nu^{1/2} = 0.825 + \frac{0.387Ra^{1/6}}{\left[1 + (0.492/Pr)^{9/16}\right]^{1/4}} \quad \text{for } 10^{-1} < Ra < 10^{12} \quad 3-33$$

$$h_{wall} = \frac{\lambda \cdot Nu}{H} \quad 3-34$$

### 3.2.3 Heat flux results

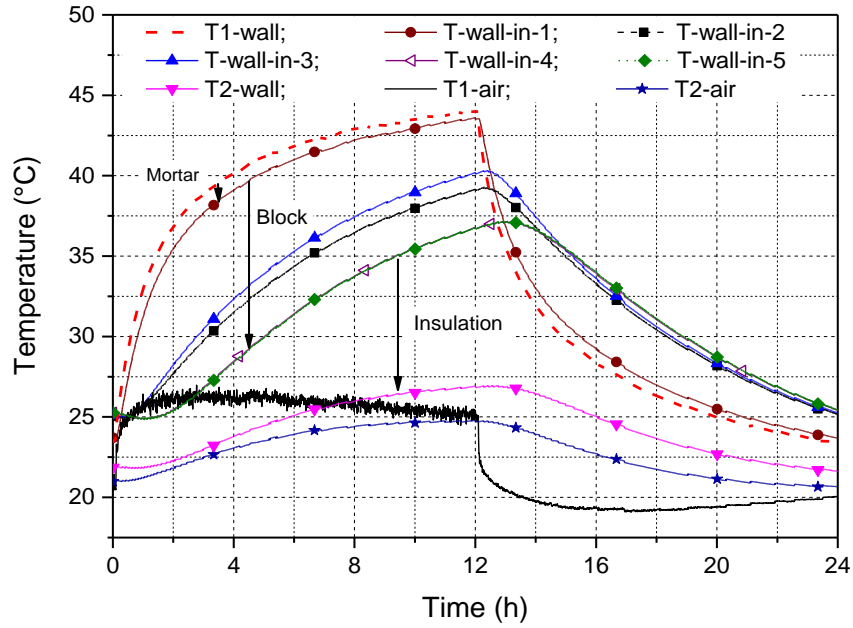
A test with a square-wave heating signal of period of 24 hours in the laboratory case is analyzed as an example in this part. Fig. 3-11 shows the temperatures of each layer measured by thermocouples. The temperature differences that caused by each layer are marked in this figure. Fig. 3-12 shows the measured front face temperatures for fluxmeter ( $T_{I-cap}$ ), black Peltier sensor ( $T_{I-Pb}$ ), shiny Peltier sensor ( $T_{I-Ps}$ ) and wall ( $T_{I-wall}$ ). In the heating period, the temperature of black Peltier sensor is the largest because of its high absorptivity. The temperature of shiny Peltier sensor and fluxmeter is about 2 °C lower. The temperature of wall is the lowest because it has not been effected by radiation with a shiny aluminum coat.

Convection coefficients of Peltier sensor and fluxmeter were calculated, convection coefficient of wall was predicted by the Churchill correlations, as shown in Fig. 3-13. It is obvious that the convection coefficients of Peltier sensor is higher than that of fluxmeter. The predicted convection coefficient of wall is closed to the fluxmeter. Therefore the correlation prediction method is available to obtain the convection coefficient of wall instead of using one more fluxmeter in the measurement.



(a) Positions of thermocouples





(b) Temperature results

Fig. 3-11 Temperatures measured by thermocouples

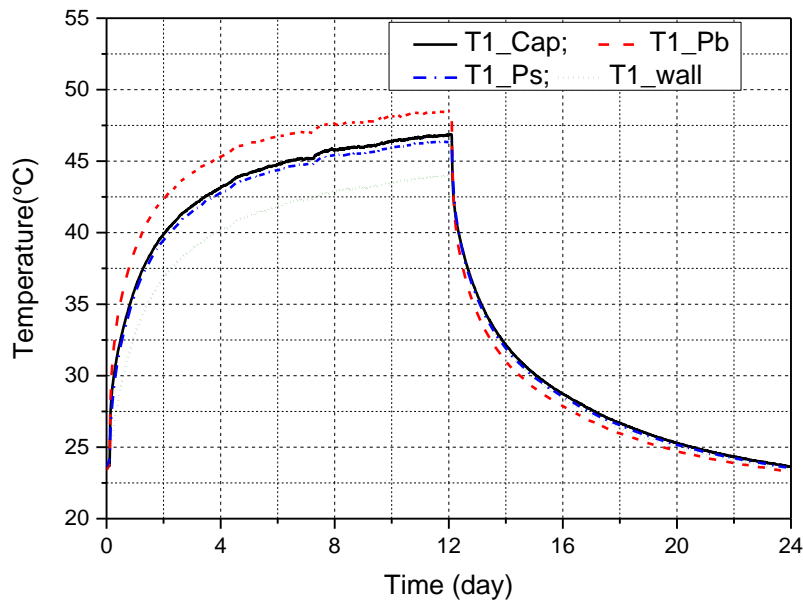


Fig. 3-12 Temperatures of sensors and wall

Fig. 3-14(a) shows the front face heat flux results of wall.  $q_{1-wall-tot}$ ,  $q_{1-wall-rad}$ ,  $q_{1-wall-conv}$  are respectively the total heat flux, radiation and convection effect on the front face of wall.  $\Delta T_{1-wall}$  is the temperature difference between the wall surface and air.  $h_{1-wall}$  is the convection coefficient of wall. The similar nomenclature for the Fig. 3-14 (b) which shows the results for

### 3.2 Heat flux

rear face of wall.  $q_{2-wall-tot}$  begin to increase after 2 hours, which indicates the wall has been penetrated through.

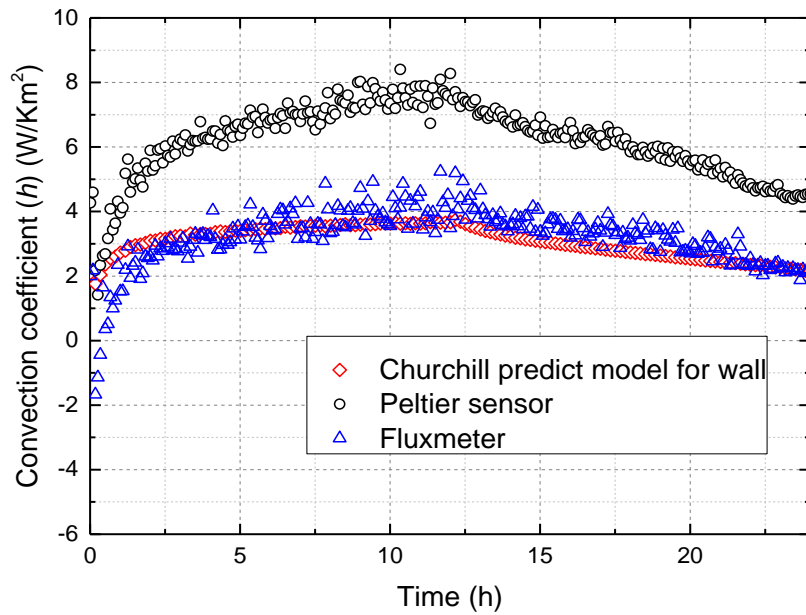
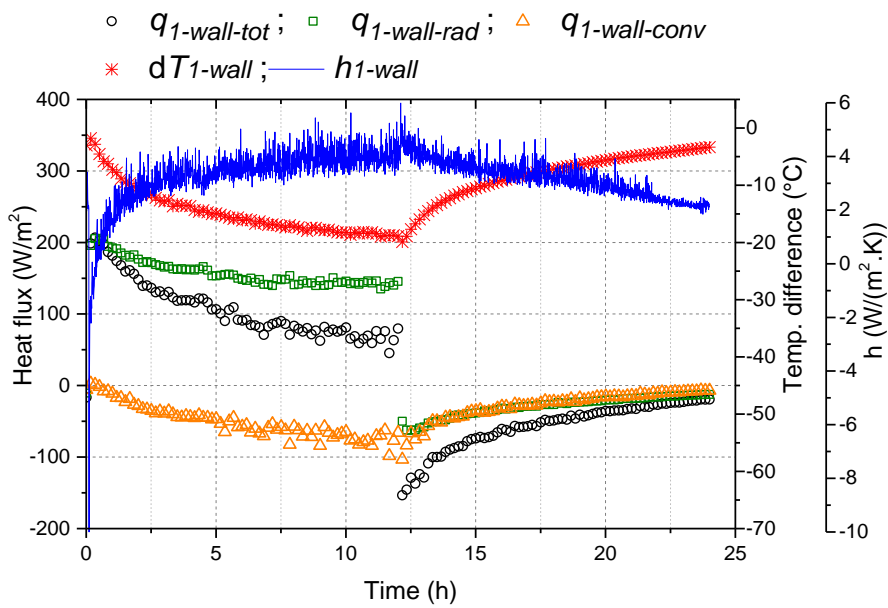
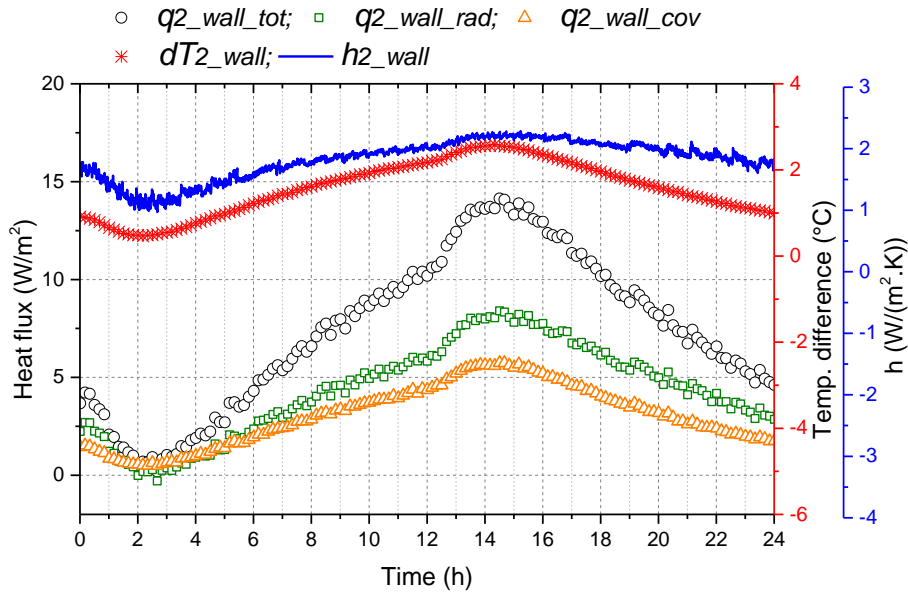


Fig. 3-13 Convection coefficients for Peltier sensor and fluxmeter



(a) Front surface

### 3.2 Heat flux



(b) Rear surface

Fig. 3-14 Convection, radiation and total heat flux results of wall for transient heat transfer test

Fig. 3-15 to Fig. 3-16 show the comparison of the 4 target surfaces: black Peltier sensor, shiny Peltier sensor, fluxmeter and the wall.

As shown in Fig. 3-15, the total heat fluxes of all the 4 target surface are decreasing during the heating period. This is caused by the increase of temperature difference between each target surface and air, which will enhance the convection heat transfer (Fig. 3-16). So that the total heat flux will decrease. The convection of Peltier sensor is higher than that of the fluxmeter and wall, which has been described previously (Fig. 3-12). While the fluxmeters will not cause this problem.

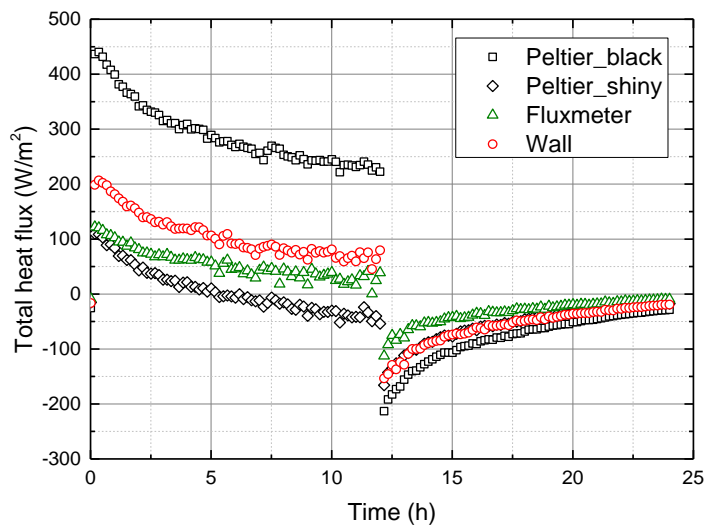


Fig. 3-15 Comparison of total heat fluxes

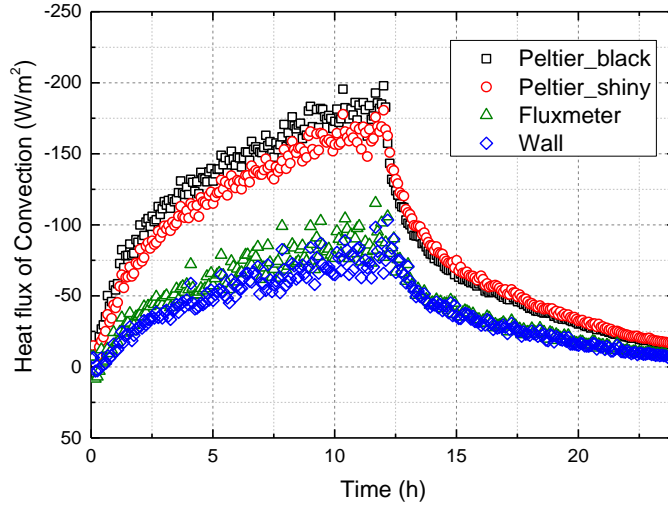


Fig. 3-16 Comparison of convection heat flux

In Fig. 3-17, the radiation heat flux of lower emissivity surfaces (the fluxmeter and shiny Peltier sensor) are nearly constant during heating period and close to 0 in cooling period (performing a square wave shape). While for the high emissivity surfaces (wall and black Peltier sensor), the radiation heat flux decreases in heating period and increases from negative to 0 in cooling period. This is because the total radiation heat flux is the sum of absorbed radiation from environment and emitted radiation by the target. For high emissivity targets, the emitted radiation is influenced a lot by the surface temperature (Equ. 3-22), resulting in an obviously change of total radiation. While, for the low emissivity surfaces, the emitted radiation is hardly effected by the surface temperature and has very little change during the test.

In addition, the radiation of shiny Peltier sensor is nearly 0 when there is no heating signal, the measured total heat flux is very close to the convection heat flux. A heat flux sensor with very shiny surface has a large potentiality to be used for the convection measurement of buildings envelope.

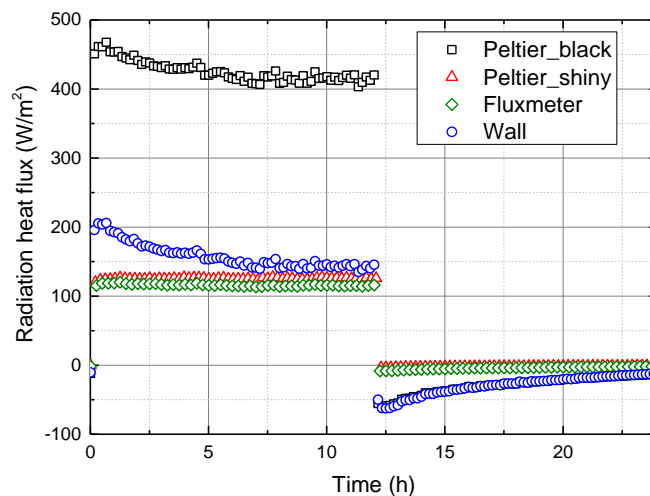


Fig. 3-17 Comparison of radiation heat flux

The idea that two heat flux sensors whose surfaces are different can measure the wall heat flux and split the radiation and convection has been validated. This measurement method can also be applied for other thermal performance analysis in the field of building energy.

The Peltier sensor is economical and more sensitive because of its high sensibility but the response time is longer. When measuring the heat flux with Peltier sensors, the convection coefficient of Peltier sensors is not the same with the wall due to the thickness of this sensor, which enhances the convection coefficient. The convection coefficient of wall can be obtained by the numerical correlation prediction or by using the thin fluxmeter.

Appendix F and Appendix G show all the results ( $T_1$ ,  $T_2$ ,  $q_1$ ,  $q_2$ ) measured in the laboratory-case and the in situ-case.

### 3.3 Temperature measurement with IR camera

As described in subsection 2.1.1, IR camera can convert the detected radiance values to temperature values using the target emissivity by Equ. 3-10. Parameters should input to the ResearchIR system (management software of IR camera), as shown in Fig. 3-18.

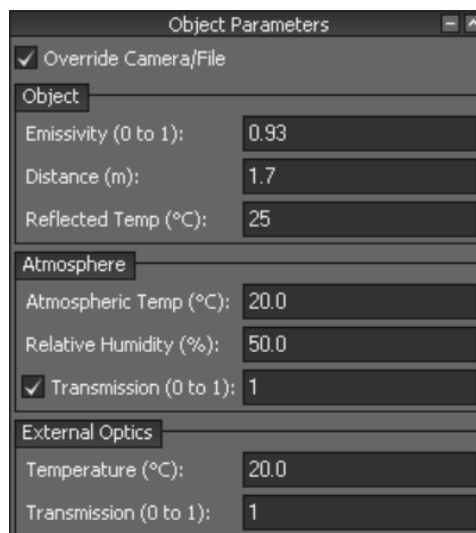
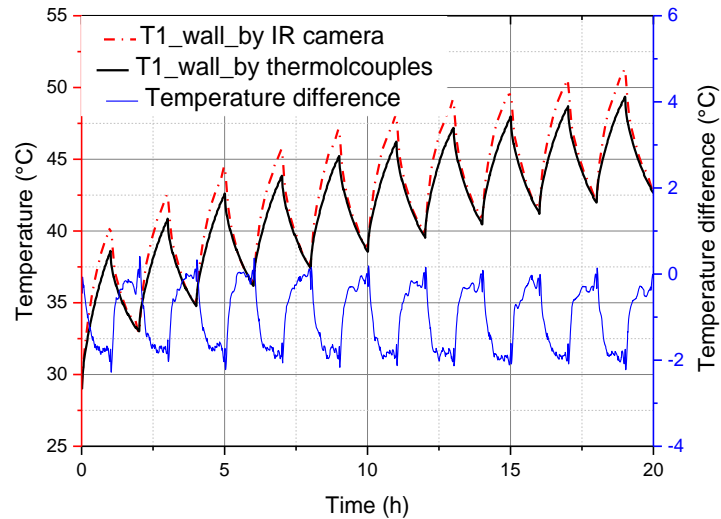
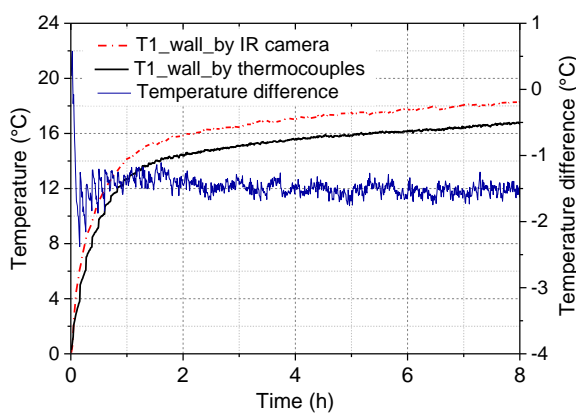


Fig. 3-18 Input parameters of ResearchIR system

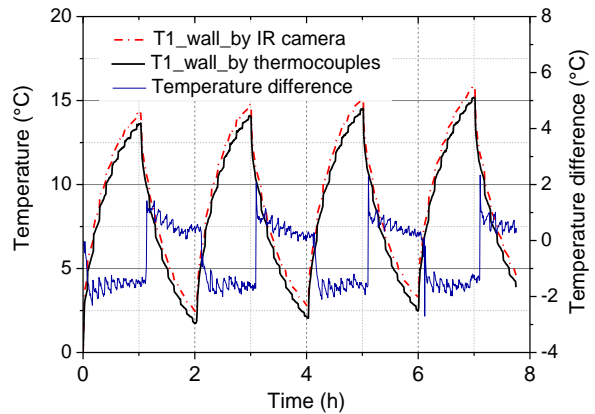
For example, in the laboratory-case, when set the reflected temperature at 20 °C, the wall surface temperature is exported from ResearchIR system. Fig. 3-19 shows the comparison of temperature that measured by IR camera and thermocouples.



(a) A square wave heating signal of period of 2 hours in the laboratory-case



(b) A continuous heating signal in the in situ-case



(c) A square wave heating signal of period 2 hours in the in situ-case

Fig. 3-19 Temperatures measured by thermocouples versus temperature measured by IR camera with setting reflected temperature of 20 °C.

Fig. 3-19 shows the temperature measured by IR camera is 1-2 °C higher than the temperature that measured by thermocouples in the heating period, especially for high temperatures. While, during the cooling period, this difference becomes weak. We suppose this phenomenon is caused by the constant setting of reflected temperature. While, during the test, the reflected temperature increases obviously.

Therefore, a new calculation approach is proposed to solve this problem. The reflected temperature  $T_{refl}$  can be measured by a crumpled aluminum. The target surface temperature is then re-calculated by correcting the reflected temperature.

### 3.3 Temperature measurement with IR camera

If we reset the parameters in the ResearchIR system as  $\varepsilon = 1$ ; distance = 0 and then export the data in unit of Kelvin, according to the Equ. 3-9, the export temperature  $T_{wall\_cam}$  is:

$$\sigma \cdot T_{wall\_cam}^4 = \varepsilon_{wall} \cdot \tau_{atm} \cdot \sigma \cdot T_{wall}^4 + (1 - \varepsilon_{wall}) \cdot \tau_{atm} \cdot \sigma \cdot T_{refl}^4 + (1 - \tau_{atm}) \cdot \sigma \cdot T_{atm}^4 \quad 3-35$$

It can be assumed that  $\tau_{atm} = 1$  when the distance between IR camera and object is 0, so that Equ. 3-35 becomes:

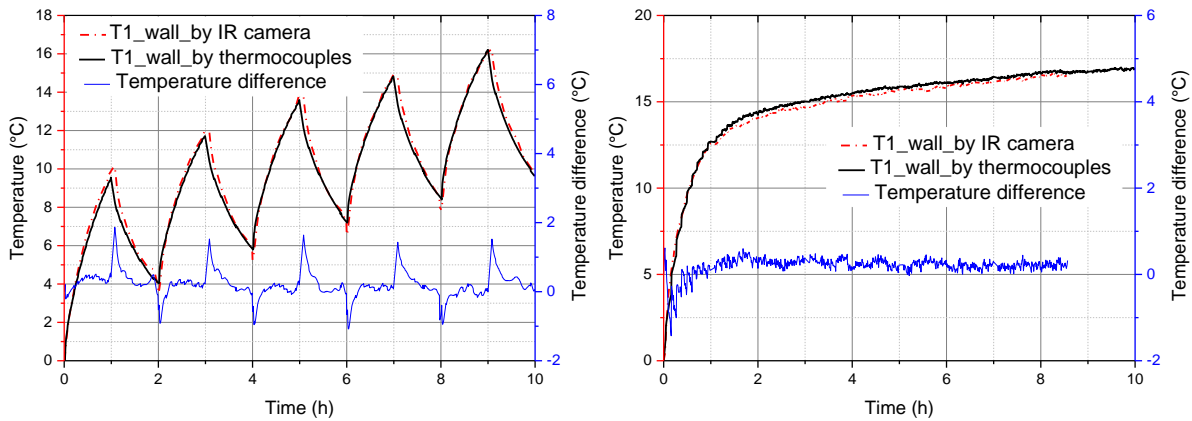
$$\sigma \cdot T_{wall\_cam}^4 = \varepsilon_{wall} \cdot \sigma \cdot T_{wall}^4 + (1 - \varepsilon_{wall}) \cdot \sigma \cdot T_{refl}^4 \quad 3-36$$

The corrected temperature of wall is:

$$T_{wall} = \left( \frac{(T_{wall\_cam}^4 - (1 - \varepsilon_{wall})T_{refl}^4)}{\varepsilon_{wall}} \right)^{\frac{1}{4}} \text{ [K]} \quad 3-37$$

In Equ. 3-37,  $\varepsilon_{wall}$  is the emissivity of wall (0.93 in our case).  $T_{wall\_cam}$  and  $T_{refl}$  are that exported from the ResearchIR system by setting ' $\varepsilon_{wall} = 1$ , distance = 0'.

After the correction for the heating period, the updated temperature measured by IR camera is compared with temperatures measured by thermocouples, shown in Fig. 3-20. Temperature difference is calculated as well. The corrected temperature has a good match with the temperature measured by thermocouples except the beginning of heating or cooling period.



(a) A square wave heating signal of period 2 hours in the in situ-case (b) A continuous heating signal in the in situ-case

Fig. 3-20 Temperatures measured by thermocouples versus corrected temperature measured by IR camera.

In conclusion, the temperature that measured by IR camera directly is 1-2 °C higher than it is in the heating period, especially for high temperature measurement. This is caused by the increase of reflected ambient temperature. So a very crumpled aluminum is proposed to correct the reflected temperature. The temperature that calculated by new approach matches well with the temperature that measured by thermocouples. In the cooling period (natural (passive) heat transfer regime), the temperature that measured by IR camera has a good agreement with the temperature by thermocouples. The different between these two temperatures is less than 0.5 °C.

## 3.4 Thermography processing

The singular value decomposition (SVD) is widely used for data processing in infrared thermography measurements.

On one hand, generally, numerous IR images will be recorded in the thermal diagnostic of building. However, it is difficult to analyze the characteristic properties by observing these IR images directly. The solution idea is to process these IR images into a matrix  $M$ . The SVD algorithm is able to reduce the matrix  $M$  to a compact statistical expression in order to describe the spatial variations and temporal variations. On the other hand, the SVD algorithm can also be used as a filter to reduce the noise of an image.

### 3.4.1 Basic principles of SVD

The singular value decomposition (SVD) of any  $m \times n$  real or complex matrix (named  $M$ ) can be written as the following form:

$$M = U \cdot W \cdot V^t \quad 3-38$$

$$(m \times n) = (m \times m) \cdot (m \times n) \cdot (n \times n)$$

Where superscript  $t$  stands for the conjugate transpose of the corresponding matrix.  $U$  is a  $m \times m$  real or complex unitary matrix. The columns of  $U$  are called left-singular vectors of  $M$ , which are a set of orthonormal eigenvectors of  $MM^t$ ;  $W$  is an  $m \times n$  rectangular diagonal matrix with non-negative real numbers on the diagonal, the non-zero singular values of  $M$  (found on the diagonal entries of  $W$ ) are the square roots of the non-zero eigenvalues of both  $M^tM$  and  $MM^t$ .  $V$  is a  $n \times n$  real or complex unitary matrix. The columns of  $V$  are called right-singular vectors of  $M$ , which are a set of orthonormal eigenvectors of  $M^tM$ ;



It is often sufficient (as well as faster, and more economical for storage) to compute a reduced version of the SVD (a compact SVD). For an  $m \times n$  matrix  $M$  ( $m \geq n$ ), only the  $n$  column vectors of  $U$  corresponding to the row vectors of  $V^t$  are calculated. The remaining column vectors of  $U$  are not calculated. That is:

$$\begin{pmatrix} M \\ m \times n \end{pmatrix} = \begin{pmatrix} U \\ m \times n \end{pmatrix} \begin{pmatrix} w_1 & \cdots & 0 \\ \vdots & \ddots & \vdots \\ 0 & \cdots & w_n \end{pmatrix} \begin{pmatrix} V^t \\ n \times n \end{pmatrix} \quad 3-39$$

$U$  is a unitary matrix (orthogonal if  $M$  is real) of dimensions ( $m \times n$ ).  $W$  is a square diagonal matrix of dimensions ( $n \times n$ ), which contains the singular values of matrix  $M$ , ordered according to decreasing values:  $w_1 \geq w_2 \geq \cdots \geq w_n$ . If matrix  $M$  is square (adapted to this research), its eigenvalues and singular values are the same.  $V$  is a square unitary matrix (orthogonal if  $M$  is real) of dimensions ( $n \times n$ ).

However, for a compact SVD, some singular values approximate to 0, a TSVD (truncated SVD) method has been proposed [101] [102]. In the TSVD regularization, items containing these small singular values can be discarded, expressed by Equ. 3-40.

$$M = U \cdot W \cdot V^t = \begin{bmatrix} U_{m \cdot j} \\ 0_{m \cdot (m-j)} \end{bmatrix} \cdot \begin{bmatrix} W_{j \cdot j} & 0 \\ 0 & 0_{(m-j)(n-j)} \end{bmatrix} \begin{bmatrix} V_{n \cdot j} \\ 0_{n \cdot (n-j)} \end{bmatrix}^t \quad 3-40$$

$$M_j = U_{m \cdot j} \cdot W_{j \cdot j} \cdot V_{n \cdot j}^t$$

$j$  is the truncation parameter. A proper  $j$  value should be chosen so that the new matrix  $M_j$  can express the main statistical information of matrix  $M$ , that is  $p_j \rightarrow 1$  (Equ. 3-41). This new matrix  $M_j$  is defined as the matrices with well-determined numerical rank.

$$p_j = \frac{\|M_j\|_2}{\|M\|_2} \times 100, j = 1, \dots, \min(m, n) \quad 3-41$$

With a proper  $j$  value, a truncated temperature of order  $j$  can be re-calculated by Equ. 3-42.

$$T_{cal}(j) = \sum_{i=1}^j U_i \cdot w_i \cdot V_i^t \quad 3-42$$

Principal component thermography (PCT) technology has been studied and applied to the field of non-destructive inspection [102] [103] [105]. It is an efficient tool to process a plenty of IR images.

### 3.4 Thermography processing

According to Equ. 3-39, the columns of  $U$  represent a set of orthogonal statistical modes known as empirical orthogonal functions (EOF) describing spatial variations of data. On the other hand, the principal components (PCs), representing the time variations, are arranged row-wise in matrix  $V^t$ . These characteristics of the SVD approach are very useful for pulsed thermography applications.

PCT uses SVD to extract the spatial (EOFs) and temporal (PCs) information from a thermogram matrix. The thermographic 3D matrix needs to be rearranged as a 2D matrix with time along the columns and space, as illustrated in Fig. 3-21. After applying the SVD to the 2D matrix, the resulting  $U$  matrix, which provides the spatial information, can be rearranged as a 3D sequence as illustrated in Fig. 3-21.

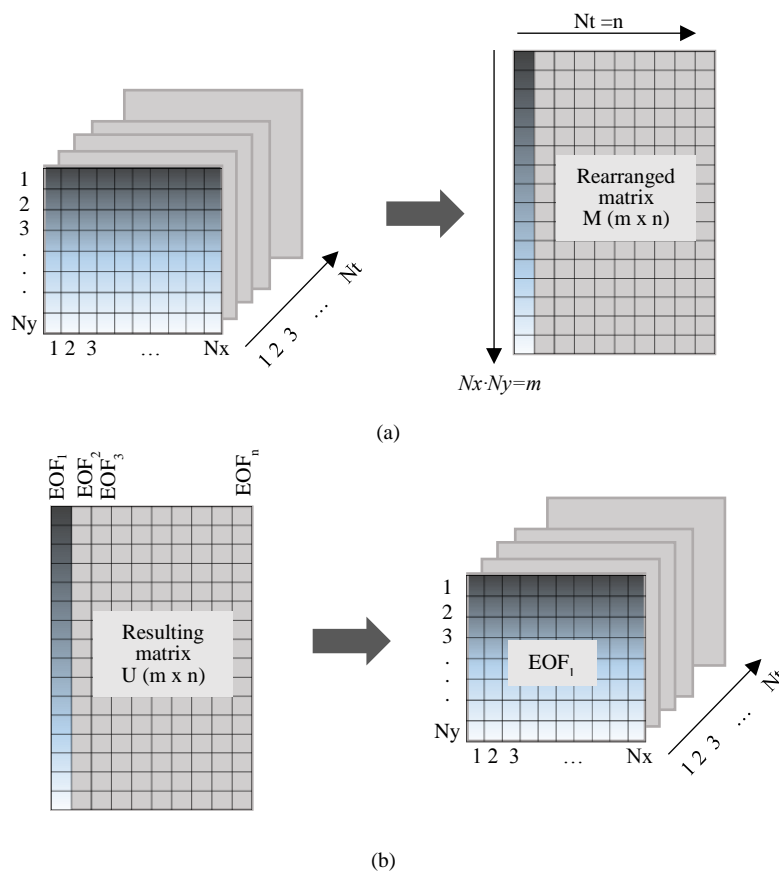


Fig. 3-21 (a) Thermographic data rearrangement from a 3D sequence to a 2D matrix of  $M$  in order to apply SVD; (b) Rearrangement of 2D  $U$  matrix into a 3D matrix containing the EOFs [7]

### 3.4.2 Processing multi IR images by PCT

The test in laboratory is analyzed here as an example of PCT application on the building diagnosis. The test of square wave heating with period of 2 hours was computed. The IR camera record 25 frames for every 5 minutes and the test lasts for more than 20 hours, totally 250 time-steps. Fig. 3-22 shows an example of infrared images. The test area is 130×60 pixels, so a total of 7800 pixels for each step. The size of  $M$  is 7800×250.

SVD of matrix  $M$  is made. Fig. 3-23 and Table 3-3 show the results of  $w_i$  and  $p_j$ . The first two modes take more than 99% of initial matrix  $M$ .  $j=2$  can be chosen in this case.

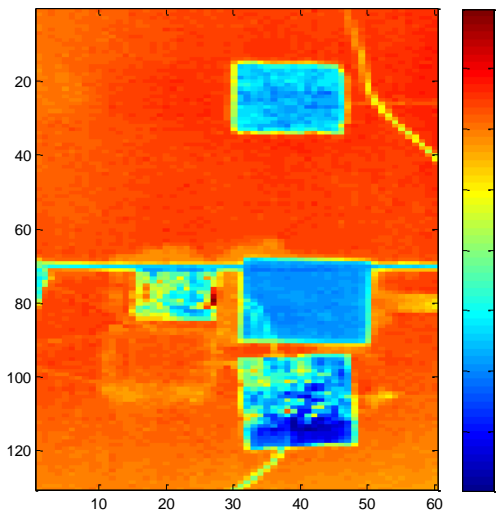


Fig. 3-22 Measured infrared image

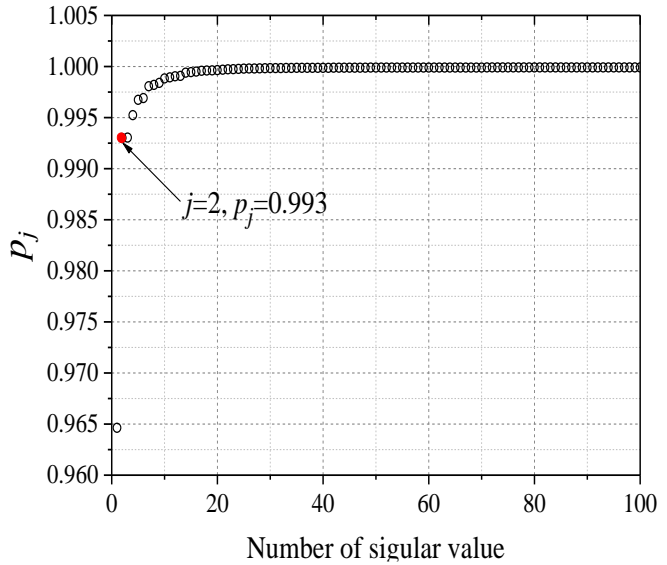


Fig. 3-23  $p_j$  values versus the number of singular value

Table 3-3 First 10 values of  $w_i$  and  $p_j$

Number of singular value	Singular value $w_i$ ( $1 \times 10^4$ )	$p_j$
1	6.1639	0.9646
2	0.2180	0.9930
3	0.0432	0.9930
4	0.0429	0.9952
5	0.0294	0.9967
6	0.0201	0.9969
7	0.0191	0.9981
8	0.0119	0.9982
9	0.0111	0.9984
10	0.0099	0.9988

These SVD analyses allow us to know that only a very few number of modes are necessary in determining the characteristic behavior. The truncated temperature was obtained when  $j=2$ . Fig. 3-24 shows the comparison of this calculated temperature and the measured temperature. The difference between this two temperatures is less than  $0.02\text{ }^{\circ}\text{C}$ .

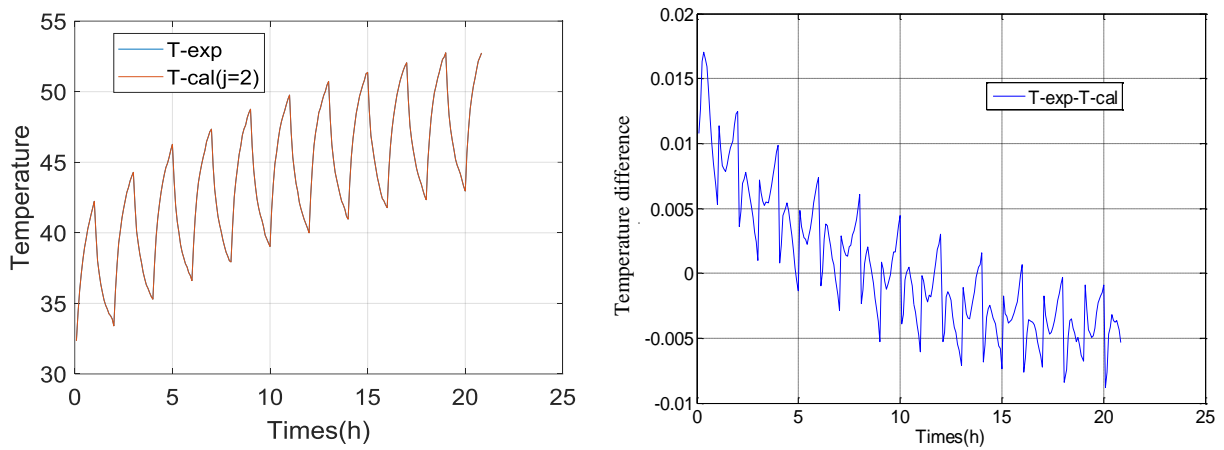
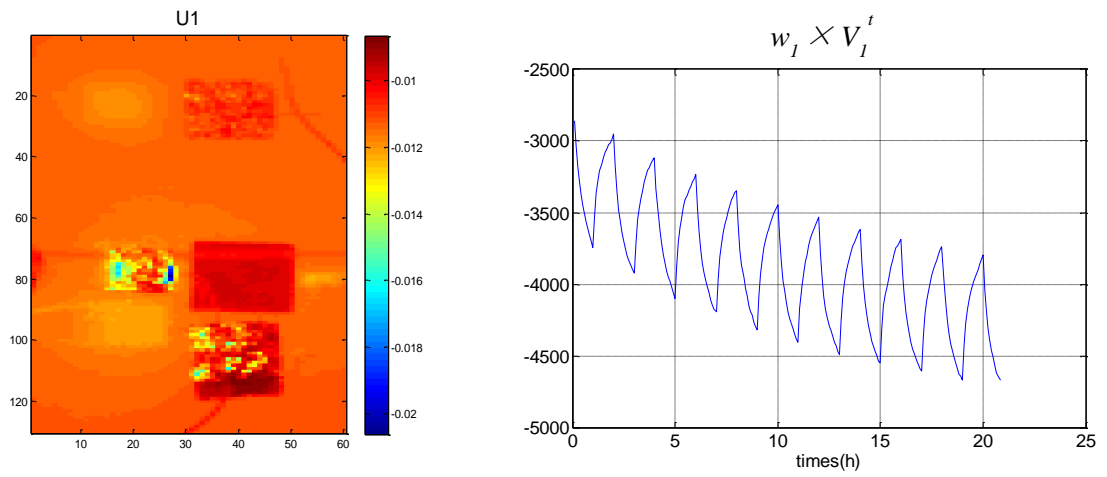


Fig. 3-24 The comparison of calculated temperature and the measured temperature (left) and the temperature difference (right).

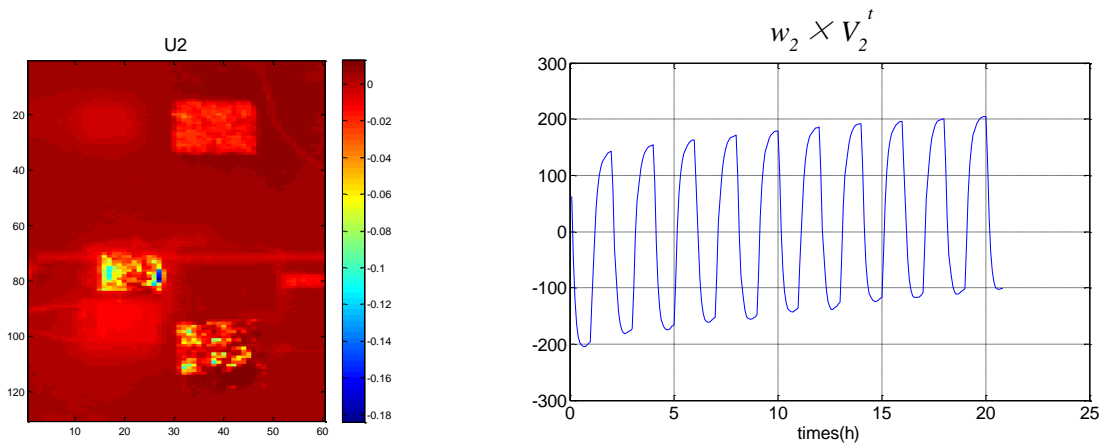
Fig. 3-25 shows the PCT results, the first mode ( $U_1$  and  $w_1 \times V_1^t$ ) represents the global dynamic behavior of the data set: the spatial variation described by  $U_1$  and the temporal variation described by  $w_1 \times V_1^t$ .  $U_1$  allows us to distinguish regions with different behavior.  $w_1 \times V_1^t$  shows the temperature response, which is corresponding to the periodic heating (period of 2 hours).

For the second and third mode,  $w_2 \times V_2^t$  and  $w_3 \times V_3^t$  are much lower than  $w_1 \times V_1^t$ , which means the second and third mode are the corrections of the global behavior.

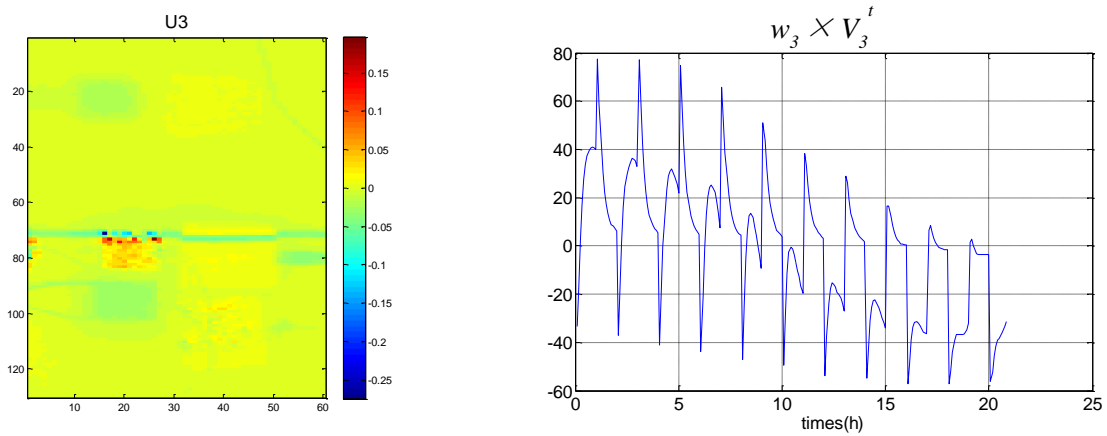
### 3.4 Thermography processing



(a)  $U_1$  and  $w_1 \times V_1^t$



(b)  $U_2$  and  $w_2 \times V_2^t$



(c)  $U_3$  and  $w_3 \times V_3^t$

Fig. 3-25 PCT results

### 3.4.3 Image filter

For an IR image, TSVD is applied to reduce the measurement noise. For example, Fig. 3-26 shows an original IR image that to be processed (referred to the visible photo in Fig. 3-1). This image can be expressed by a 2D matrix  $M$ . According to Equ. 3-40, TSVD is applied on this matrix  $M$ . Fig. 3-27 and Table 3-4 show the singular values of matrix  $M$ . When  $j=5$ , the  $p$ -value (percentage of initial  $M$  by Equ. 3-41 is more than 99.8%, so that we can use the first 5 modes to re-build the IR image.

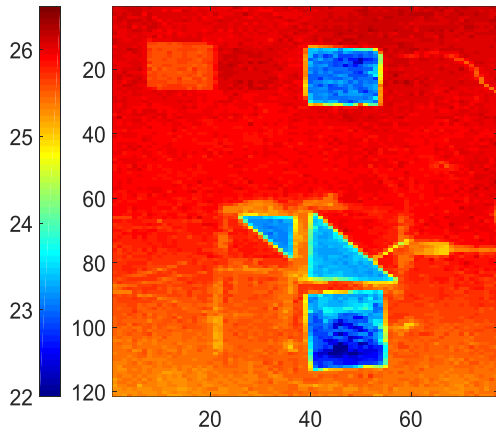


Fig. 3-26 An original IR image

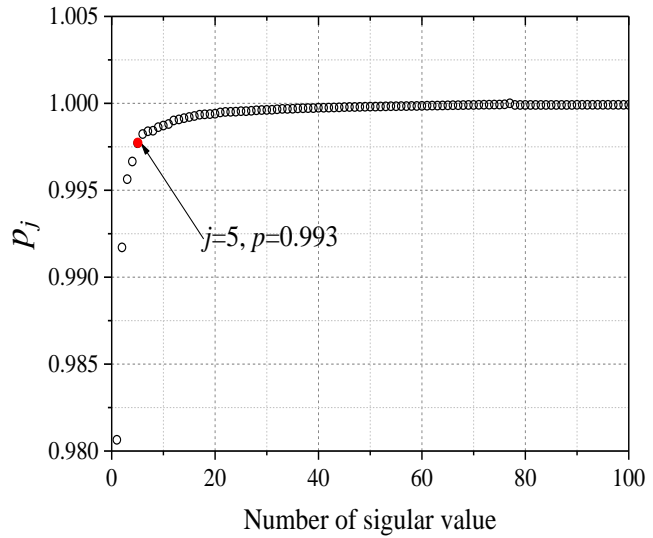


Fig. 3-27 Singular values of matrix  $M$  (left) and the percentage (Equ. 3-41).

Table 3-4 First 10 values of  $w_i$  and  $p_j$

Number of singular value	Singular value $w_i (1 \times 10^4)$	$p_j$
1	2463.626	0.980645
2	47.68288	0.991711
3	20.42172	0.995635
4	10.75348	0.996654
5	8.242318	0.997705
6	5.653693	0.998232
7	4.354671	0.99839
8	3.967589	0.998423
9	3.885519	0.998626
10	3.384177	0.998722

### 3.4 Thermography processing

Fig. 3-28 shows the IR images of each  $j$ -value ( $j$  is from 1 to 12). When  $j=1$ , the image is much different with the initial image (Fig. 3-26). When  $j=5$ , the edge of each sensor becomes clear. Generally, this processing approach is efficient to the qualitative diagnosis on a complex surface to highlight the obvious abnormal behavior.

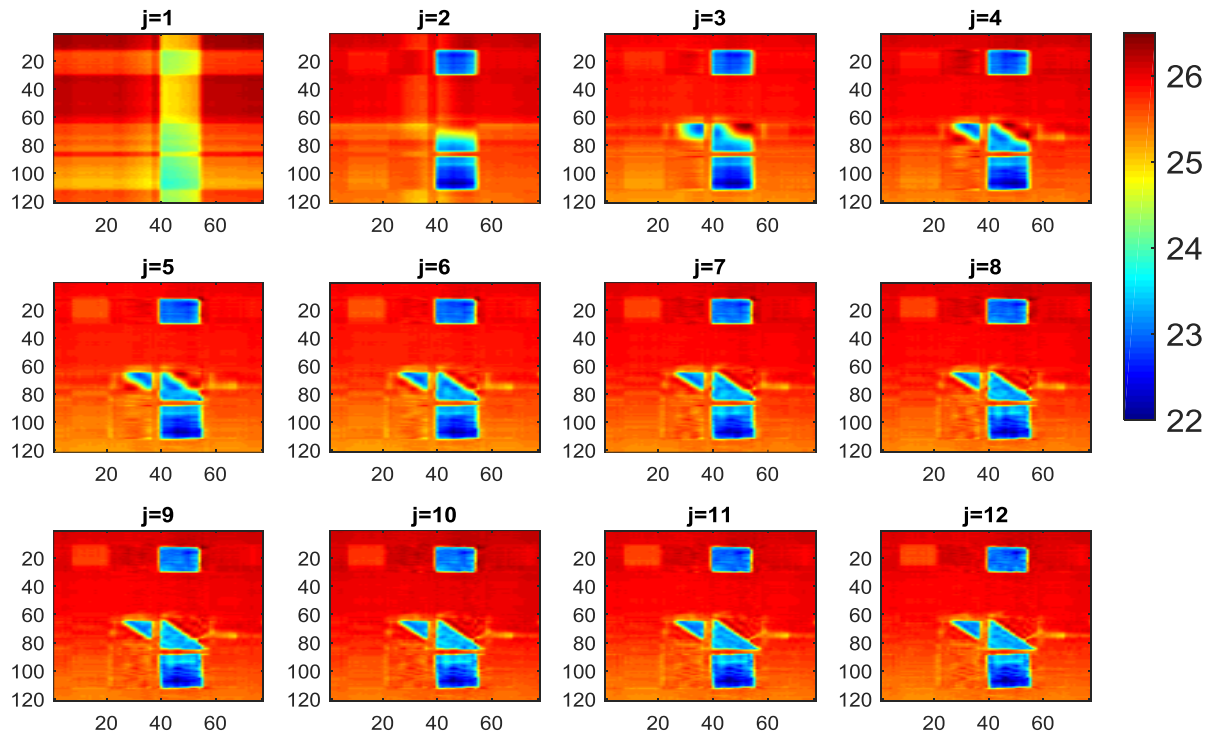


Fig. 3-28 IR images of each  $j$ -value ( $j$  is from 1 to 12).

# Chapter 4

## Estimation Approaches For Thermal Parameters Characterizing

---

---

This chapter will firstly show the results of steady state heat transfer measurements. Then three estimation approaches will be introduced and applied on the transient heat transfer measurements to characterize the thermal parameters of wall: pulse response curve method, step response curve method and inverse method.

### 4.1 Steady state heat transfer method

As described previously, the tested wall was installed on a wall box. This wall box was placed in a chamber whose temperature kept at 18 °C. The internal temperature of the wall box was regulated at 27 °C by a heater. A stable temperature difference of 9 °C was obtained for 5 hours between the two surfaces of wall. Fig. 4-1 shows the measured temperatures of surfaces and



#### 4.1 Steady state heat transfer method

each interface. The insulation layer has caused the largest temperature difference. The positions of thermocouple can refer to Fig. 3-11(a).

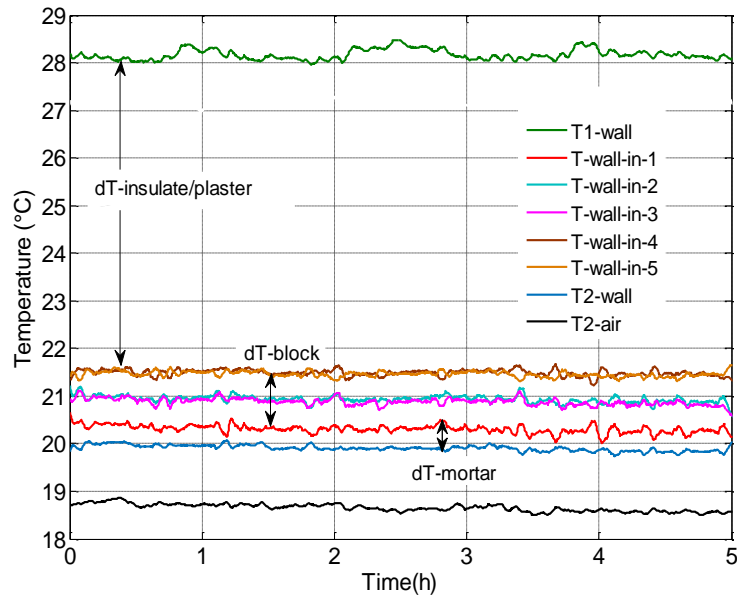


Fig. 4-1 Temperature results of each layer for steady state heat transfer

Fig. 4-2 shows the heat flux results of wall. The fluctuation of front face heat flux ( $q_{1-wall}$ ) was caused by the heater which works intermittently. The average value of  $q_{1-wall}$  and  $q_{2-wall}$  were obtained:  $q_{1-wall} = 5.72 \pm 7.56 \text{ W/m}^2$ ,  $q_{2-wall} = 6.9 \pm 0.58 \text{ W/m}^2$ . The rear face heat flux ( $q_{2-wall}$ ) was relatively stable who was to be used for the thermal resistance estimation.

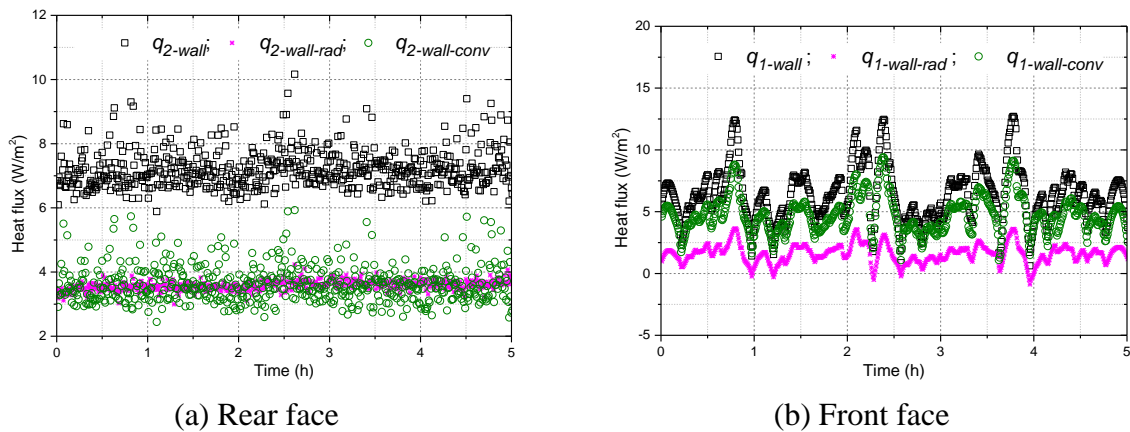


Fig. 4-2 Heat flux results of wall for steady state heat transfer measurement

Using the wall heat flux and temperature differences of each surface, the thermal resistances can be obtained by Equ. 4-1.

$$R = \Delta T/q$$

Fig. 4-3 and Table 4-1 show the thermal resistance ( $R$ ) results of each layer. The thermal resistance values for concrete block and insulate-plaster layer match well with the reference values. While the thermal resistance of mortar layer is too low to be measured precisely because of the limit of accuracy of this instrumentation. The overall thermal resistance of this wall was obtained using the temperature difference of two external surfaces of wall.  $R_{overall}=1.35\pm 0.223 \text{ K} \cdot \text{m}^2/\text{W}$ .

These results can be considered as a validation of wall heat flux calculation (subsection 3.2.2).

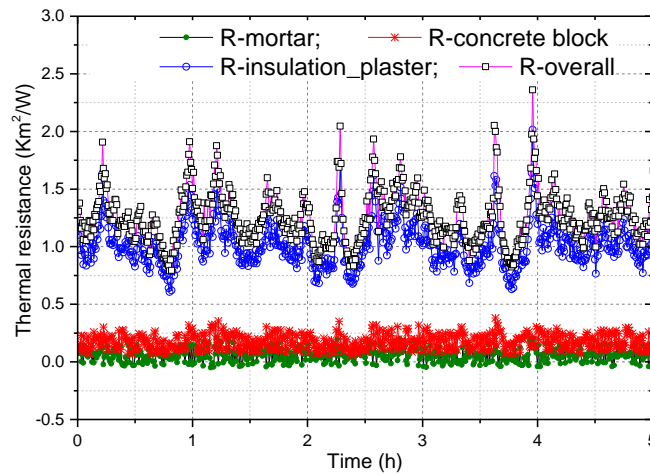


Fig. 4-3 Thermal resistance values for steady state heat transfer measurement

Table 4-1 Thermal resistance results of each layer

Layers	$R_{refe}$ ( $\text{K} \cdot \text{m}^2/\text{W}$ )	$R_{exp}$ ( $\text{K} \cdot \text{m}^2/\text{W}$ )
Mortar	0.0087	$0.0650 \pm 0.0607$
Concrete block	0.23	$0.19 \pm 0.069$
Insulate-plaster	1.103	$1.090 \pm 0.202$
Overall (4 layers)	1.34	$1.35 \pm 0.223$

## 4.2 Thermal quadrupoles solution

### 4.2.1 Basics of thermal quadrupoles model

The quadrupoles method is a kind of analytical method for solving linear partial differential equations in simple geometries. It relies on classical analytical tools such as Laplace integral transforms (in time) or space integral transforms (Fourier) related to the method of separation of variables [42]. When this quadrupoles method is applied to the heat transfer regime system, the thermal solution can be expressed in terms of linear matrix relationships between transformed temperature and transformed heat flux vectors at the boundaries of the system. So that this analytical solution is independent on these boundary conditions. Other numerical tools, such as finite differences, are usually used in the cases that the geometry is complex or the problem is nonlinear, but not adapted for the situation that a large thickness in situ and the situation with a semi-infinite boundary assumption. Stehfest's algorithm is used for Laplace transform enabling the time domain transferred to Laplace domain. An input/output linear system will be obtained by this deconvolution.

For a homogeneous and isotropic solid medium without internal heat source (Fig. 4-4(a)), the one dimensional heat transfer equation is expressed as Equ. 4-2. The heat flux ( $q$ ) at any location ( $x$ ) for inside the medium is defined as Equ. 4-3. A unit area ( $S=1\text{m}^2$ ) was considered in our work.

$$\frac{\partial^2 T}{\partial x^2} = \frac{1}{\alpha} \frac{\partial T}{\partial t} \quad (T = T_0 \text{ for } t = 0) \quad 4-2$$

$$q = -\lambda \frac{\partial T}{\partial x} \quad 4-3$$

Where  $T$  is temperature,  $t$  is time,  $\lambda$  is thermal conductivity,  $T_0$  is the initial temperature of the medium when time is 0. Then the temperature and heat flux in Laplace domain are:  $\theta(x,p)=L(T(x,t))$ ,  $\Phi(x,p)=L(q(x,t))$ . Where  $p$  is the Laplace transform of time;  $\theta_1$  and  $\theta_2$  are respectively the transformed temperatures at front face ( $x=0$ ) and rear face ( $x=L$ ,  $L$  is the thickness of medium),  $\Phi_1$  and  $\Phi_2$  are the corresponding transformed heat flux, as shown in Fig. 4-4(b). The heat transfer equation becomes Equ. 4-4. Appendix I lists the usual Laplace transforms.

$$\begin{bmatrix} \theta_1 \\ \Phi_1 \end{bmatrix} = \begin{bmatrix} A & B \\ C & D \end{bmatrix} \begin{bmatrix} \theta_2 \\ \Phi_2 \end{bmatrix} = M \begin{bmatrix} \theta_2 \\ \Phi_2 \end{bmatrix} \quad 4-4$$

$$A = D = \cosh(L\sqrt{p/\alpha}); B = \frac{1}{\lambda\sqrt{p/\alpha}} \sinh(L\sqrt{p/\alpha}); C = \lambda\sqrt{p/\alpha} \sinh(L\sqrt{p/\alpha})$$

Where  $\alpha$  is thermal diffusivity ( $\lambda/\rho c$ ). The matrix  $M$  with four coefficients  $A, B, C, D$  completely characterizes the surface temperature responses of heat flux.

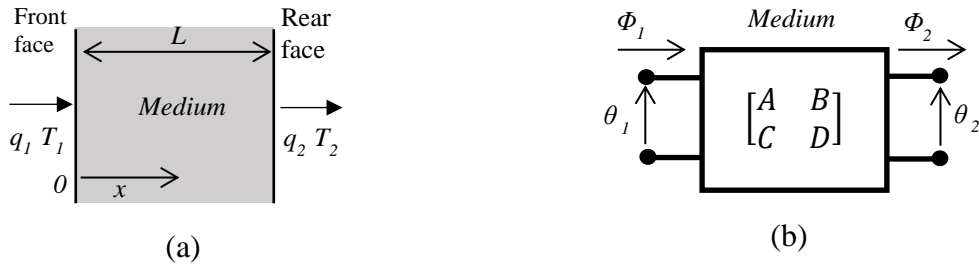


Fig. 4-4: Transient heat transfer in homogenous medium: (a) geometry; (b) matrix representation

For multilayer walls, the global equivalent transfer matrix  $M_{eq}$  can be obtained by multiplying the matrices from each layer medium  $M_1, M_2 \dots M_n$ , as shown in Equ. 4-5. The contact resistance between each layer has been ignored hereby because we suppose it is much smaller than the resistance of insulation material.

$$\begin{bmatrix} \theta_1 \\ \Phi_1 \end{bmatrix} = \begin{bmatrix} A_1 & B_1 \\ C_1 & D_1 \end{bmatrix} \begin{bmatrix} A_2 & B_2 \\ C_2 & D_2 \end{bmatrix} \dots \begin{bmatrix} A_n & B_n \\ C_n & D_n \end{bmatrix} = \begin{bmatrix} A_{eq} & B_{eq} \\ C_{eq} & D_{eq} \end{bmatrix} \begin{bmatrix} \theta_2 \\ \Phi_2 \end{bmatrix} = M_{eq} \begin{bmatrix} \theta_2 \\ \Phi_2 \end{bmatrix} \quad 4-5$$

Two boundary conditions at the rear face of wall have been considered in our research: semi-infinite and adiabatic conditions. The semi-infinite boundary can be assumed in a short characteristic time in which the wall has not been penetrated through. The adiabatic boundary is that the rear face of the wall is adiabatic to the ambient without any heat loss.

For a semi-infinite boundary condition, the thickness of medium is assumed as infinite ( $L = \infty$ ), the rear face temperature is zero, that is  $T_2 = 0$ , so  $\theta_2 = 0$ , Equ. 4-4 becomes:

$$\begin{bmatrix} \theta_1 \\ \Phi_1 \end{bmatrix} = \begin{bmatrix} 1 & z \\ 0 & 1 \end{bmatrix} \begin{bmatrix} 0 \\ \Phi_2 \end{bmatrix}, \quad z = \frac{1}{b\sqrt{p}} \quad 4-6$$

The solution of front face temperature in Lapalce domain is then:

$$\theta_1 = z \cdot \Phi_1 \quad 4-7$$

For an adiabatic boundary condition, the heat flow rate of the rear face is assumed as 0, Equ. 4-4 becomes:

$$\begin{bmatrix} \theta_1 \\ \Phi_1 \end{bmatrix} = \begin{bmatrix} A & B \\ C & D \end{bmatrix} \begin{bmatrix} \theta_2 \\ 0 \end{bmatrix} \quad 4-8$$

The front face and rear face temperatures can be estimated using the heat flux and thermal properties of the medium (Equ. 4-9).

$$\theta_1 = \frac{A}{C} \Phi_1; \quad \theta_2 = \frac{1}{C} \Phi_1 \quad 4-9$$

Actually, the temperature responses in semi-infinite condition and in adiabatic condition perform the same behaviors in a short time (a few hours) for common building walls when the wall has not been penetrated through.

### 4.2.2 Simulations for several heating signals

Simulations were made by this thermal quadrupoles solution to analyze the estimation possibilities for thick walls. For a given medium (close to concrete block material:  $\alpha = 10^{-6} \text{ m}^2/\text{s}$ ,  $\lambda = 1 \text{ W}/(\text{mK})$ ,  $L = 0.2 \text{ m}$ ), several temperature responses ( $T_1$ ,  $T_2$ ) will be simulated using different heating signals, such as a pulse signal, a continuous step signal, a square wave signal and a periodic square wave signal. The adiabatic boundary condition is assumed.

For a pulse heating signal (heat power  $Q=10^5 \text{ J}/\text{m}^2$ ), the front face and rear face temperature responses are simulated basing on Equ. 4-9. For a constant  $Q$  which is independent with time ( $t$ ), the Laplace transform is:  $\Phi_1 = L(Q) = Q$ , so

$$\theta_1 = Q \frac{A}{C} = \frac{Q}{\lambda \sqrt{p/\alpha} \tanh(L\sqrt{p/\alpha})}; \quad 4-10$$

$$\theta_2 = Q \frac{1}{C} = \frac{Q}{\lambda \sqrt{p/\alpha} \sinh(L\sqrt{p/\alpha})} \quad 4-11$$

After an inverse Laplace calculation, the front face and rear face temperatures are the function of heat power and time, marked as  $f_{pulse}$ :

$$T_{1pulse} = f_{1pulse}(Q_p, t) = Q \cdot L^{-1} \left( \frac{1}{\lambda \sqrt{p/\alpha} \tanh(L \sqrt{p/\alpha})} \right) \quad 4-12$$

$$T_{2pulse} = f_{2pulse}(Q_p, t) = Q \cdot L^{-1} \left( \frac{1}{\lambda \sqrt{p/\alpha} \sinh(L \sqrt{p/\alpha})} \right)$$

Fig. 4-5(a) shows the temperature response results of this medium. The black curve is the front face temperature, the red curve is the rear face temperature. The front face response decreases quickly in a very short time at beginning. While it is difficult to obtain any response of the rear face even in a long time. In order to make an obvious pulse response, a larger pulse power is needed, which will cause a very high temperature at the front face of wall. For an actual wall, the component of insulation material will enhance this difficulty. So that this pulse heating method is not available for the building envelope. A thin medium ( $L=0.01\text{m}$ ) was also simulated hereby (Fig. 4-5 (b)). For a thin medium, the rear face response can be obtained in a short time. Both the front face and the rear face responses are sensitive. This is why the pulse method is adapted for thin materials characterization but unavailable for thick materials.

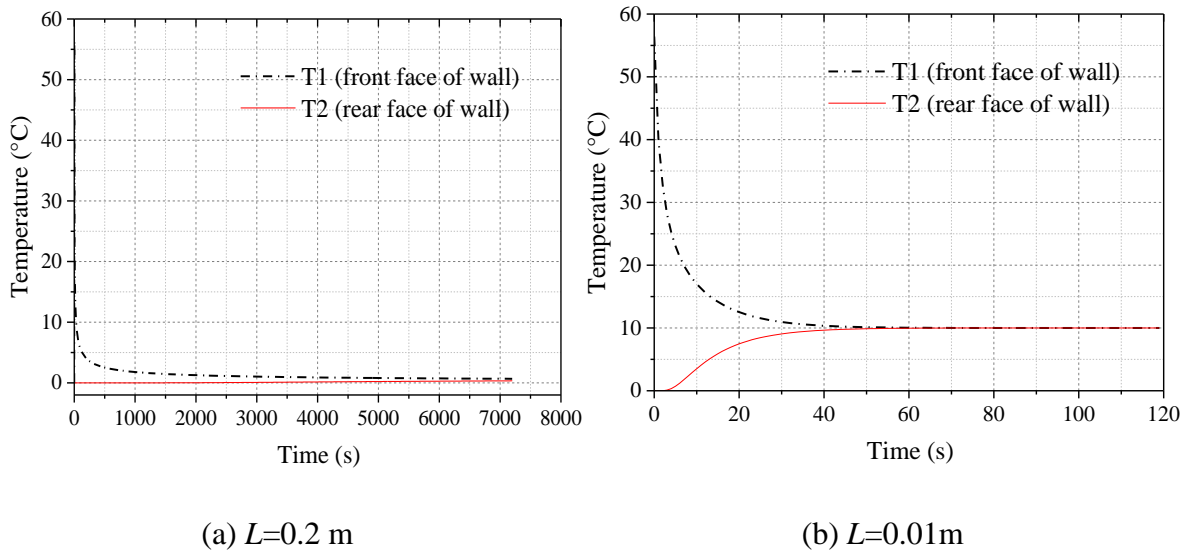


Fig. 4-5 Temperature responses to a pulse heating signal

For a continuous step heating signal (heat flux  $q_1=500 \text{ W/m}^2$ ), according to Equ. 4-9, the temperatures are calculated by Equ. 4-13.

$$\Phi_1(p) = q_1/p$$

$$\theta_1 = \frac{q_1}{p} \cdot \frac{A}{C}; \quad \theta_2 = \frac{q_1}{p} \cdot \frac{1}{C}; \quad 4-13$$

After an inverse Laplace calculation, temperature responses are the function of heat flux and time, marked as  $f_{step}$ .

$$\begin{aligned} T_{1_{step}} &= f_{1_{step}}(q_1, t) = q_1 \cdot L^{-1} \left( \frac{1}{p\lambda\sqrt{p/\alpha} \tanh(L\sqrt{p/\alpha})} \right) \\ T_{2_{step}} &= f_{2_{step}}(q_1, t) = q_1 \cdot L^{-1} \left( \frac{1}{p\lambda\sqrt{p/\alpha} \sinh(L\sqrt{p/\alpha})} \right) \end{aligned} \quad 4-14$$

Fig. 4-6 shows the temperatures results to this step heating signal. The blue curve is the heat flux values. The rear face temperature begins increasing at about 2500s.

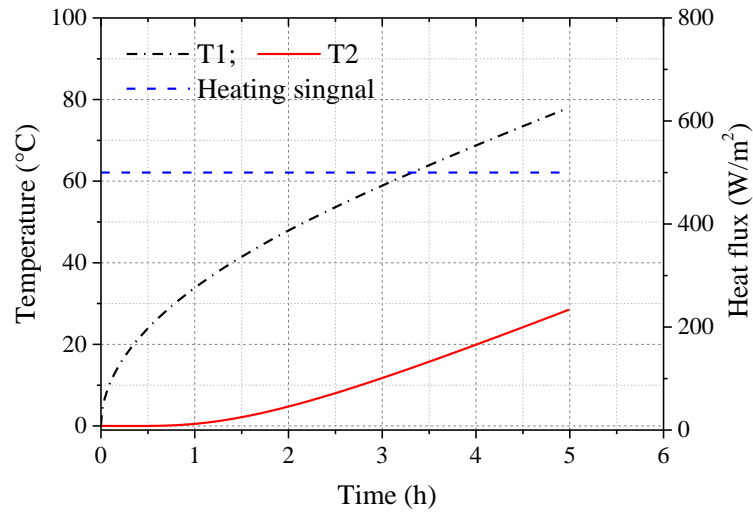


Fig. 4-6 Temperature responses to a continuous step heating signal

For a square wave signal, the temperature responses involve the response function of a step heating signal, it equals the step response in a whole time (from 0 to  $t$ ) minus the step response in the non-heating part (from  $t - t_{heat}$  to  $t$ ), expressed as the following:

$$T_{1_{square}}(t) = f_{1_{step}}(q_1, t) - f_{1_{step}}(q_1, t - t_{heat}) \quad 4-15$$

$$T_{2_{square}}(t) = f_{2_{step}}(q_1, t) - f_{2_{step}}(q_1, t - t_{heat}) \quad 4-16$$

Where  $t_{heat}$  is the heating time, as shown in Fig. 4-7,  $t_{heat}$  equals 4 hours, that is to say a signal of  $500 \text{ W/m}^2$  heats the medium for 4 hours.

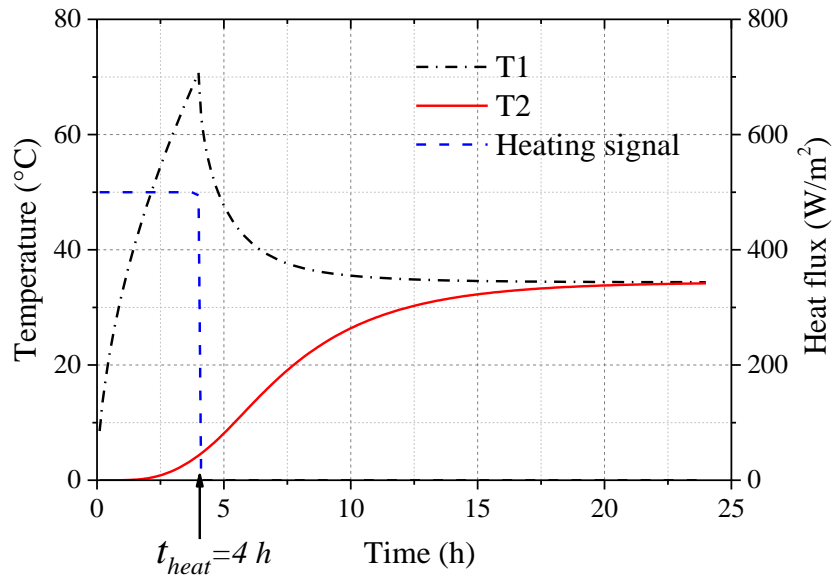


Fig. 4-7 Temperature responses to a square wave heating signal

Similarly, for a periodic square wave heating signal, the temperature responses is the sum of each square wave signal. Fig. 4-8 shows the simulation results, the blue curve is the heating signal. The front face temperature varies periodically while the rear face temperature keeps increasing.

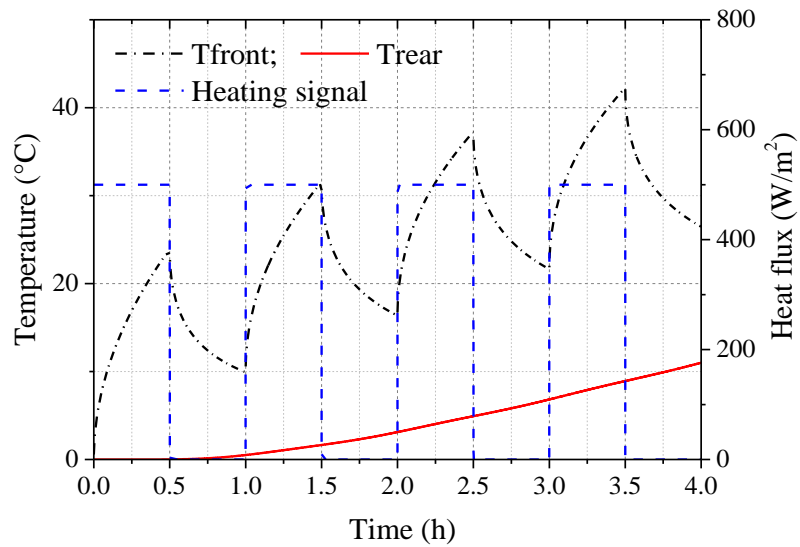


Fig. 4-8 Temperature responses to a periodic square wave heating signal



### 4.2.3 Application to experiments

In this work, as described in subsection 3.2, the input heat flux of wall is not a constant value.  $q_1$  is a set of variable values with interval time step ( $\Delta t$ ) of 30 s. Fig. 4-9 (a) shows the actual situation of input wall heat flux. For each interval time step ( $\Delta t$ ), the heat flux is:

$$q_1(1), q_1(2), q_1(3) \dots q_1(n).$$

According to Equ. 4-15, each corresponding front face temperature can be computed:

$$T_{1-1}(t), T_{1-2}(t), T_{1-3}(t) \dots T_{1-n}(t),$$

As shown in Fig. 4-9 (b). Therefore, the temperature at time  $t$  is the sum of temperatures generated by heat flux of each time step (Equ. 4-17 and Equ. 4-18).

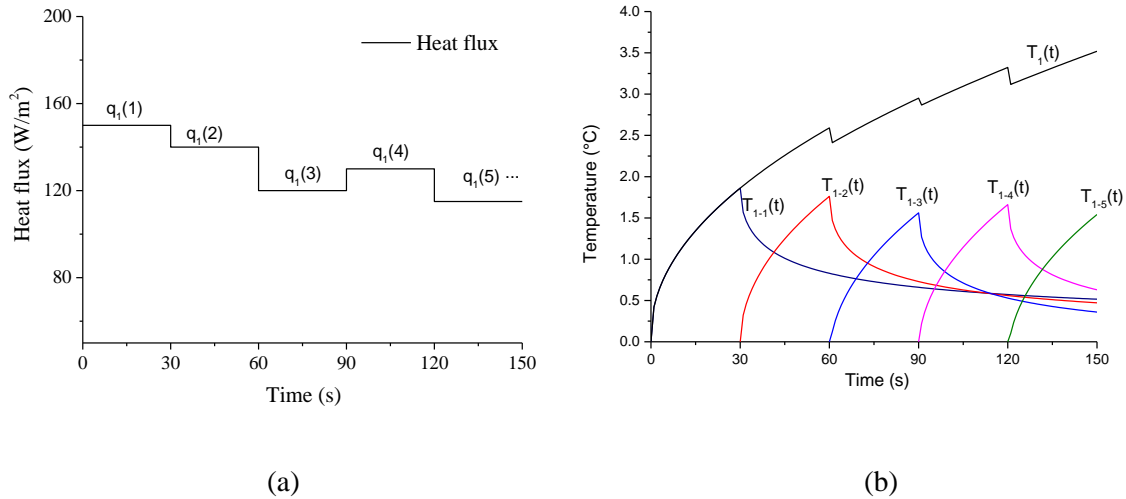


Fig. 4-9 Superposition principle: (a) random heat flux at each interval time step. (b) temperatures generated by heat flux of each time step

$$T_1(t) = f_{1\_square}(q_1(1), t) + f_{1\_square}(q_1(2), t - \Delta t) + f_{1\_square}(q_1(3), t - 2\Delta t) \dots f_{1\_square}(q_1(n), t - (n - 1)\Delta t) \quad 4-17$$

$$T_2(t) = f_{2\_square}(q_1(1), t) + f_{2\_square}(q_1(2), t - \Delta t) + f_{2\_square}(q_1(3), t - 2\Delta t) \dots f_{2\_square}(q_1(n), t - (n - 1)\Delta t) \quad 4-18$$

It is assumed  $q_2$  is zero at adiabatic boundary condition. However, in real measurements, heat flux of rear face is not always 0 even it is much lower than the heat flux of front face (see the heat flux results in test 3.2). Heat loss from the rear face to environment is considered by involving the convection heat transfer coefficient  $h$ , as shown in Fig. 4-10.

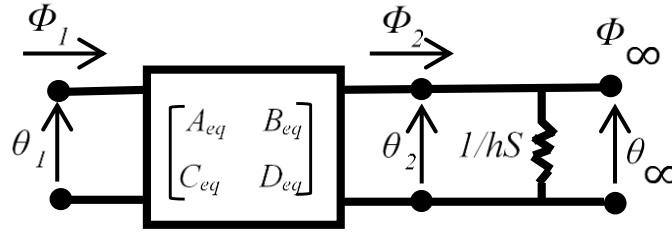


Fig. 4-10 Quadrupole network of considering heat loss

According to Equ. 4-5, the quadrupoles model becomes:

$$\begin{bmatrix} \theta_1 \\ \Phi_1 \end{bmatrix} = \begin{bmatrix} A_{eq} & B_{eq} \\ C_{eq} & D_{eq} \end{bmatrix} \begin{bmatrix} 1 & 0 \\ hS & 1 \end{bmatrix} \begin{bmatrix} \theta_2 \\ 0 \end{bmatrix} \quad 4-19$$

The linear relationship between the transformed temperature and heat flux is expressed as Equ. 4-20.

$$\theta_1 = \frac{A_{eq} + B_{eq} \cdot hS}{C_{eq} + D_{eq} \cdot hS} \cdot \Phi_1 = \frac{A_{EQ}}{C_{EQ}} \cdot \Phi_1, \quad \theta_2 = \frac{1}{C_{eq} + D_{eq} \cdot hS} \cdot \Phi_1 = \frac{1}{C_{EQ}} \cdot \Phi_1 \quad 4-20$$

### 4.2.4 Approximated expressions

In order to physically analyze the temperature responses, the previous quadrupoles equations can be simplified by assuming that the insulation materials are totally resistant and the dense building materials (plaster, mortar and concrete block) are totally capacitive.

If a medium is characterized by high resistance and very little capacity, a quadrupole equation is expressed by Equ. 4-21. Fig. 4-11 shows the heat transfer model of this high resistance medium.

$$\begin{bmatrix} \theta_1 \\ \Phi_1 \end{bmatrix} = \begin{bmatrix} 1 & R \\ 0 & 1 \end{bmatrix} \begin{bmatrix} \theta_2 \\ \Phi_2 \end{bmatrix} \quad 4-21$$



Fig. 4-11 Heat transfer model of a high resistance medium: (a) network expression; (b) matrix expression.

If a medium is characterized by high conductivity whose internal resistance can be neglected, the quadrupoles equation is expressed by Equ. 4-22. Fig. 4-12 shows the heat transfer model of this high conductivity medium.

$$\begin{bmatrix} \theta_1 \\ \Phi_1 \end{bmatrix} = \begin{bmatrix} 1 & 0 \\ pC_t & 1 \end{bmatrix} \begin{bmatrix} \theta_2 \\ \Phi_2 \end{bmatrix} \quad 4-22$$

Where  $C_t = \rho cV$  (J/K) is the heat capacity of this medium.



Fig. 4-12 Heat transfer model of a high conductivity medium: (a) network expression; (b) matrix expression.

In our work, the approximated expressions of the two walls are obtained: the wall in the laboratory-case (Equ. 4-23) and the wall in the in situ-case (Equ. 4-24).

$$\begin{bmatrix} \theta_1 \\ \Phi_1 \end{bmatrix} = \begin{bmatrix} 1 & 0 \\ pC_{t_{mortar}} & 1 \end{bmatrix} \begin{bmatrix} 1 & 0 \\ pC_{t_{block}} & 1 \end{bmatrix} \begin{bmatrix} 1 & R_{insulation} \\ 0 & 1 \end{bmatrix} \begin{bmatrix} 1 & 0 \\ pC_{t_{plaster}} & 1 \end{bmatrix} \begin{bmatrix} 1 & 0 \\ hS & 1 \end{bmatrix} \begin{bmatrix} \theta_2 \\ 0 \end{bmatrix} \quad 4-23$$

$$\begin{bmatrix} \theta_1 \\ \Phi_1 \end{bmatrix} = \begin{bmatrix} 1 & 0 \\ pC_{t_{mortar}} & 1 \end{bmatrix} \begin{bmatrix} 1 & R_{insulation} \\ 0 & 1 \end{bmatrix} \begin{bmatrix} 1 & 0 \\ pC_{t_{block}} & 1 \end{bmatrix} \begin{bmatrix} 1 & 0 \\ pC_{t_{plaster}} & 1 \end{bmatrix} \begin{bmatrix} 1 & 0 \\ hS & 1 \end{bmatrix} \begin{bmatrix} \theta_2 \\ 0 \end{bmatrix} \quad 4-24$$

## 4.3 Pulse response curve method

The flash pulse method is popularly used in the NDE, it is available for the thin materials in a very short time. Many researchers focused on the pulse response curve to estimate the thermal properties. As described previously, there are some difficulties to apply flash pulse method on thick walls. However, we can apply the periodic heating signals instead of a strong pulse in order to avoid a high temperature at beginning. The main originality of this part is to try to compute the front face pulse response with the measured front face temperature and heat flux. Such front face pulse response is obtained by a deconvolution method and a TSVD inverse method using the measurement data. It can also be simulated by thermal quadrupoles model. So these curves are directly characterized by the thermal properties of the medium and contain a lot of information. This section will introduce both the simulation and experimental approaches.

### 4.3.1 Simulation analysis of pulse response curve

According to the Equ. 4-9,  $\frac{A}{C}$  is the relationship between the transformed heat flux and transformed temperature, it is defined as the pulse response in Laplace domain, the pulse response in time domain is the inverse Laplace of  $\frac{A}{C}$ :

$$g_{simu} = L^{-1}\left(\frac{A}{C}\right) \quad 4-25$$

Basing on the Equ. 4-25, pulse response of four cases are simulated (Fig. 4-13). Case 1 is a 10 cm insulation layer. Case 2 is a 20 cm concrete block layer. Case 3 and Case 4 are the combination of the two layers. In Case 3, the insulation layer is placed near the heating source (placed near the front face of wall). In case 4, the insulation layer is placed behind the concrete block layer. Table 4-2 shows the thermal properties of these standard building materials.

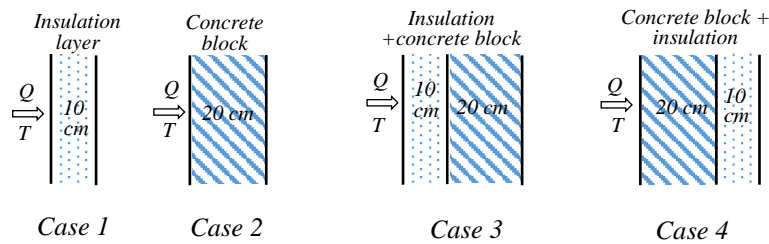


Fig. 4-13 Four cases to be simulated

Table 4-2 Thermal properties of insulation and concrete block

Layers	$L$ (m)	$\lambda$ W/(m.K)	$\rho c$ J/(K· m <sup>3</sup> )
Concrete block	0.2	0.87	$0.9 \times 10^6$
Insulation layer	0.1	0.038	$0.03 \times 10^6$

Fig. 4-14 shows the simulated pulse responses of the four cases at adiabatic boundary conditions. Both the pulse response and the time are plotted in the logarithmic axis. The black and red solid curves are the pulse responses for case 1 and case 2 respectively. The blue dash curve is the pulse response of case 3 and green dash curve is for the case 4.

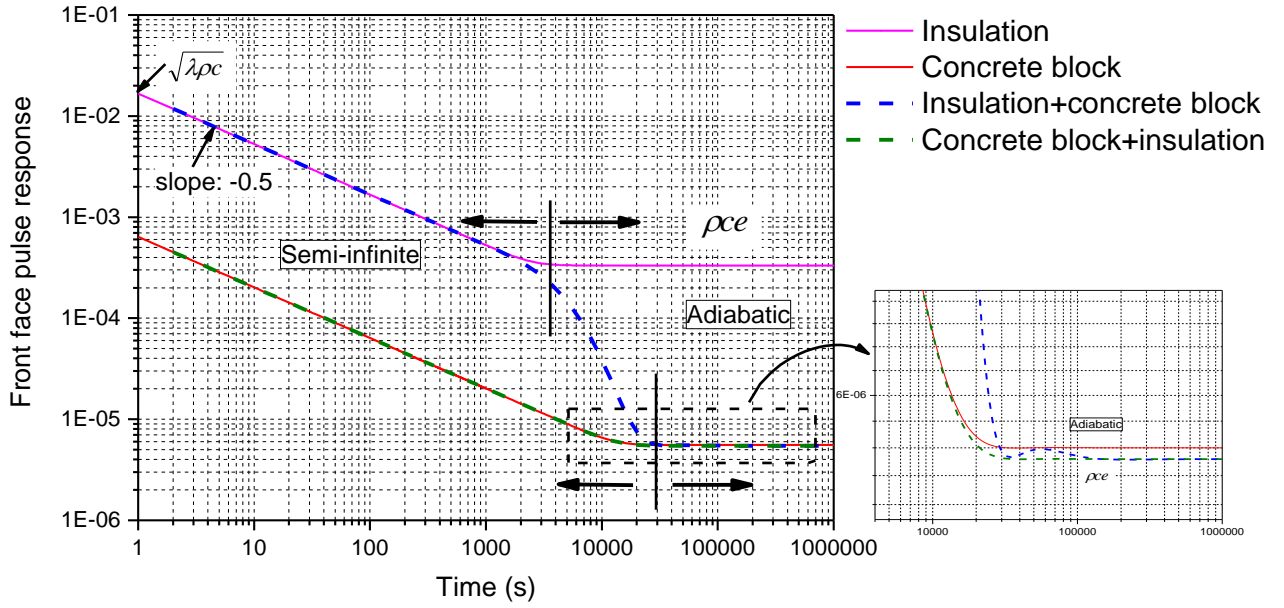


Fig. 4-14 Simulated pulse response at adiabatic boundary condition

According to Equ. 4-10, in a short time, when  $t \rightarrow 0$ , that is  $p \rightarrow \infty$ , the front face temperature becomes:

$$\theta_1 = \frac{Q}{\sqrt{\lambda \rho c} \sqrt{p}} ; p \rightarrow \infty \quad 4-26$$

Referring to Appendix I, the time domain of Equ. 4-26 is:

$$T_1 = \frac{Q}{\sqrt{\lambda \rho c} \sqrt{\pi t}} ; t \rightarrow 0 \quad 4-27$$

The pulse response in a short time is:

$$g = \frac{1}{\sqrt{\lambda \rho c} \sqrt{\pi t}} ; t \rightarrow 0 \quad 4-28$$

The pulse response in the logarithmic axis is:

$$\log(g) = -\frac{1}{2} \log(\pi) - \log(\sqrt{\lambda \rho c}) - \frac{1}{2} \log(t) \quad 4-29$$

According to Equ. 4-10, in a long time,  $t \rightarrow \infty$ , that is  $p \rightarrow 0$ , then

$$\theta_1 \cong \theta_2 \cong \frac{Q}{\rho c L p} ; p \rightarrow 0 \quad 4-30$$

$$T_1 \cong T_2 \cong \frac{Q}{\rho c L} ; t \rightarrow \infty \quad 4-31$$

The pulse response in a long time is:

$$g = \frac{1}{\rho c L} ; t \rightarrow \infty \quad 4-32$$

The pulse response in the logarithmic axis is:

$$\log(g) = \log\left(\frac{1}{\rho c L}\right) = -\log(\rho c L) \quad 4-33$$

In a short time, the pulse response curve is linear (case 1 and case 2 in Fig. 4-14), marked as linear period. The slope of this linear period equals -0.5 and the intercept is determined by the thermal effusivity  $\sqrt{\lambda \rho c}$  (Equ. 4-29). In this period, the medium has not been penetrated through totally, so it is also marked as semi-infinite period. In a long time, the pulse response curve becomes constant and is determined by the heat capacity ( $\rho c L$ ) (Equ. 4-33). This constant period is based on the adiabatic condition. Therefore, for a homogenous medium, the pulse response curve is quantitatively characterized by the thermal parameters of this medium.

This analysis method is also efficient for the two layers mediums (case 3 and case 4 in Fig. 4-14). In a short time (about 2000 s), the curve of case 3 has the same trend with the curve of case 1, which indicates that the insulation layer has not been penetrated yet. This linear period is characterized by the thermal effusivity of insulation layer. 2000 s later, the curve of case 3 goes close to the curve of case 2 and becomes constant at the end. This constant period is characterized by the heat capacity of concrete block layer. The green dash curve is the pulse response of case 4. It has the same value with the case 2 in the linear period, and a little lower in the constant period, which indicate that the heat capacity of case 4 is a bit lower than that of case 2.

Taking the practical situations into account, the heat loss should be considered in the adiabatic condition. Therefore, the pulse responses of the four cases are also calculated based on Equ. 4-20. Fig. 4-15 shows the simulation results. The convection coefficient of the rear face is  $5 \text{ W}/(\text{K} \cdot \text{m}^2)$ . As shown in this figure, in a short time (linear period), all the four pulse

response curves have the same behaviors with that in Fig. 4-14. However, after the medium has been penetrated (about 20000 s), the curves go down sharply instead of becoming constant, and finally decrease to very low values.

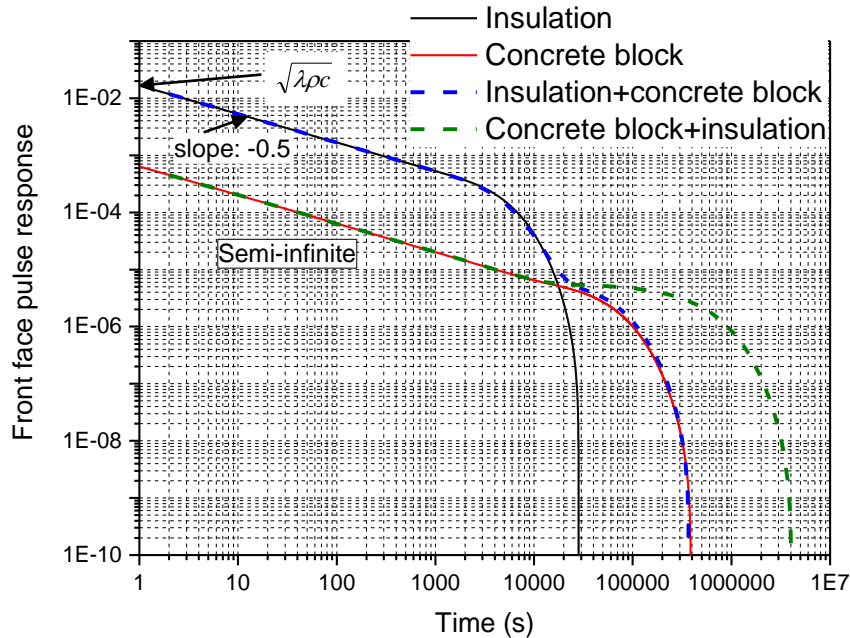
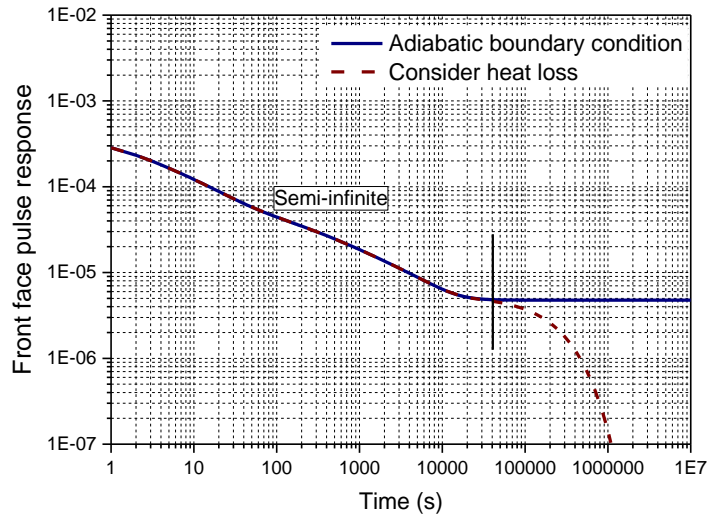
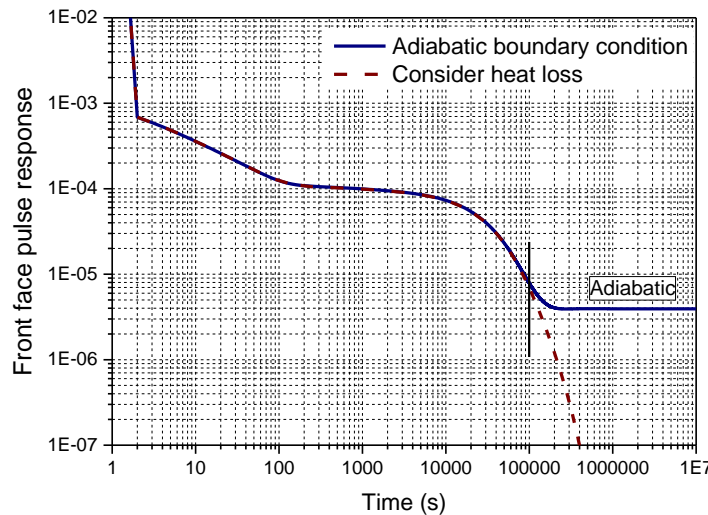


Fig. 4-15 Simulated pulse response when considering heat loss at the rear face.

Basing on the previously analysis, the pulse responses of the tested walls were simulated. Fig. 4-16 (a) shows the simulation results of wall in the lab-case. The results of wall in the in situ-case are plotted in Fig. 4-16 (b). As described in Chapter 2, in the lab-case, the block layer is near the front face, the insulation layer is behind the block layer. In the in situ-case, the insulation layer is near the front face, the block layer places behind. The two structures are conventional and have been widely used as the building envelope. In Fig. 4-16, the blue curve is the simulation result that in the adiabatic condition without considering the heat loss, while the red dash curve is the result that has considered the heat loss. These simulation results will be compared with the experimental pulse responses that calculated using the measured heat fluxes and temperatures in the subsection 4.3.3.



(a) Wall in the laboratory-case



(b) Wall in the in situ-case

Fig. 4-16 Simulated pulse response

### 4.3.2 Deconvolution of experimental data

A deconvolution calculation is introduced to obtain the experimental pulse responses using the measured front face temperature and heat flux.

As we known, the multiplication of two factors in Laplace domain is the convolution of the two factors in time domain. So Equ. 4-9 can be transformed to time domain, the front face temperature ( $T_1$ ) equals the convolution of front face pulse response ( $g(t)$ ) and heat flux ( $q_1(t)$ ), expressed by Equ. 4-34.



$$T_1(t) = g(t) * q_1(t) = \int_0^t g(t-\tau) q_1(\tau) d\tau = \int_0^t q_1(t-\tau) g(\tau) d\tau \quad 4-34$$

This integral is discretized by time ( $t=1,2,3,\dots,n$ ).  $T_1(t)$  is discretized as a vector of  $(T_1^1, T_1^2, T_1^3, \dots, T_1^n)$ ,  $q_1(t)$  is discretized as  $(q_1^1, q_1^2, q_1^3, \dots, q_1^n)$  and  $g(t)$  is discretized as  $(g_1, g_2, g_3, \dots, g_n)$ . Approximated expression of Equ. 4-34 can be described as:

$$\underbrace{\begin{bmatrix} T_1^1 \\ T_1^2 \\ T_1^3 \\ \vdots \\ T_1^n \end{bmatrix}}_{\mathbf{T}} = \underbrace{\begin{bmatrix} q_1^1 & \dots & 0 & 0 & 0 \\ q_1^2 & q_1^1 & 0 & 0 & 0 \\ q_1^3 & q_1^2 & q_1^1 & 0 & 0 \\ \vdots & \ddots & \ddots & \ddots & \vdots \\ q_1^n & \dots & q_1^3 & q_1^2 & q_1^1 \end{bmatrix}}_{\mathbf{Q}} \underbrace{\begin{bmatrix} g_1 \\ g_2 \\ g_3 \\ \vdots \\ g_n \end{bmatrix}}_{\mathbf{g}} \quad 4-35$$

The three matrices are represented by  $\mathbf{T}$ ,  $\mathbf{Q}$ ,  $\mathbf{g}$  respectively, then Equ. 4-35 is expressed by as:

$$\mathbf{T} = \mathbf{Q} \cdot \mathbf{g} \quad 4-36$$

If the model  $\mathbf{T} = \mathbf{Q} \cdot \mathbf{g}$  is linear, its Ordinary Least Square (OLS) [106] estimator can be written as:

$$\hat{\mathbf{g}}_{OLS} = (\mathbf{Q}^t \mathbf{Q})^{-1} \mathbf{Q}^t \cdot \mathbf{T} \quad 4-37$$

However, in the case  $\mathbf{Q}^t \mathbf{Q}$  is an ill-posed problem, TSVD should be applied on the matrix  $\mathbf{Q}$ . Because in ill-posed problem, some singular values of the coefficient matrix ( $\mathbf{Q}$ ) approximate to 0, the least square estimation will enormously amplify the observation noises and degrade the precision. In TSVD regularization, items containing these small singular values are discarded to maintain the stability of the solution. With a given  $j$  values, items containing singular values smaller than  $w_j$  are discarded. Thus, the amplification to the observation noises is restrained.

$$\mathbf{Q} = \mathbf{U} \cdot \mathbf{W} \cdot \mathbf{V}^t = \begin{bmatrix} U_{n-j} \\ U_{n-(n-j)} \end{bmatrix} \begin{bmatrix} W_{j,j} & 0 \\ 0 & W_{(n-j)(n-j)} \end{bmatrix} \begin{bmatrix} V_{n-j} \\ V_{n-(n-j)} \end{bmatrix}^t \quad 4-38$$

$$\mathbf{Q}_j = U_{n \cdot j} \cdot W_{j \cdot j} \cdot V_{n \cdot j}^t \quad 4-39$$

$j$  is the truncated parameter. With the new regularized  $\mathbf{Q}_j$ , the estimated pulse response becomes  $\hat{\mathbf{g}}_j^{TSVD}$ :

$$\hat{\mathbf{g}}_k^{TSVD} = V_{n \cdot j} \cdot W_{j \cdot j}^{-1} \cdot U_{n \cdot j}^t \cdot T \quad 4-40$$

In order to find a proper  $j$ -value, the discrepancy principle [107] was used. We considered the standard deviation ( $\delta$ ) of residuals between the exact temperature ( $T$ ) and the estimated temperature ( $\mathbf{Q} \cdot \hat{\mathbf{g}}_j^{TSVD}$ ), expressed by Equ. 4-41.

$$\delta = \sqrt{\frac{\|\mathbf{T} - \mathbf{Q} \cdot \hat{\mathbf{g}}_j^{TSVD}\|^2}{n}} \quad 4-41$$

$\delta$  can be calculated at each  $j$ -value ranging from 1 to  $n$ . Fig. 4-17 shows the  $\delta$ -values depending on the  $j$ -value for 4 tests (the tests of periodic heating in laboratory case).

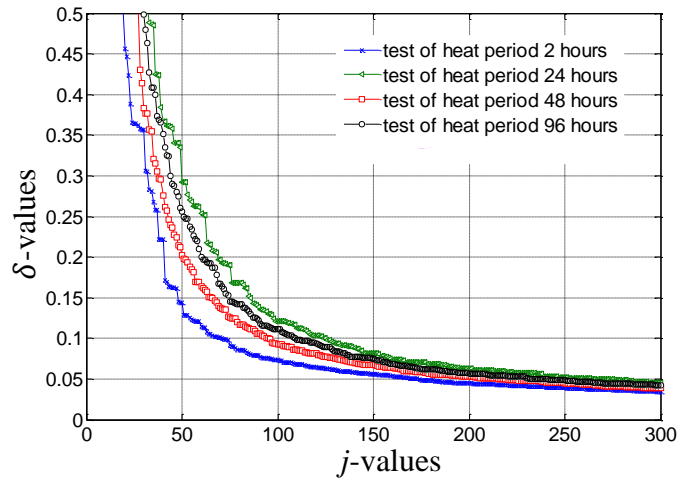


Fig. 4-17  $\delta$ -values versus  $j$ -values

For a given  $\delta$ -value, for example,  $\delta = 0.1^\circ\text{C}$  can be chosen for an independent and identically distributed normal noise of standard deviation, the  $j$ -value we choose should satisfy Equ. 4-42. The  $j$ -values of each test are listed in Table 4-3 for different  $\delta$  values (0.1, 0.2 and 0.3). When  $\delta = 0.1$ ,  $j = 110$  was chosen for test 1.

$$\|T - Q \cdot \hat{g}_j^{TSVD}\|^2 < n \cdot \delta^2$$

$$\|T - Q \cdot \hat{g}_{j-1}^{TSVD}\|^2 \geq n \cdot \delta^2$$

4-42

Table 4-3  $j$ -values of 4 tests when  $\delta$  is 0.1, 0.2 and 0.3

		$\delta = 0.1$	$\delta = 0.2$	$\delta = 0.3$
Test 1	Period of 96h	110	61	44
Test 2	Period of 48h	96	51	38
Test 3	Period of 24h	126	69	50
Test 4	Period of 2h	72	41	33

In our cases,  $\delta = 0.1$  °C was chosen,  $j$  is about 100 for the 4 tests. With the optimal  $j$ -value, the pulse response vector  $g$  can be obtained by inputting the experimental heat flux  $q_1$  and temperature  $T_1$  (Appendix F and Appendix G).

### 4.3.3 Experimental pulse response results

With the calculation approach described previously, the experimental pulse responses were obtained for the tests in the lab-case and in the in situ-case. These experimental results will be shown and analyzed in this part.

#### 4.3.3.1 Results for laboratory case

Experimental temperature and heat flux of the front face of wall for one test are shown in Fig. 4-18. In the test, the period of this heating signal is 24 hours.

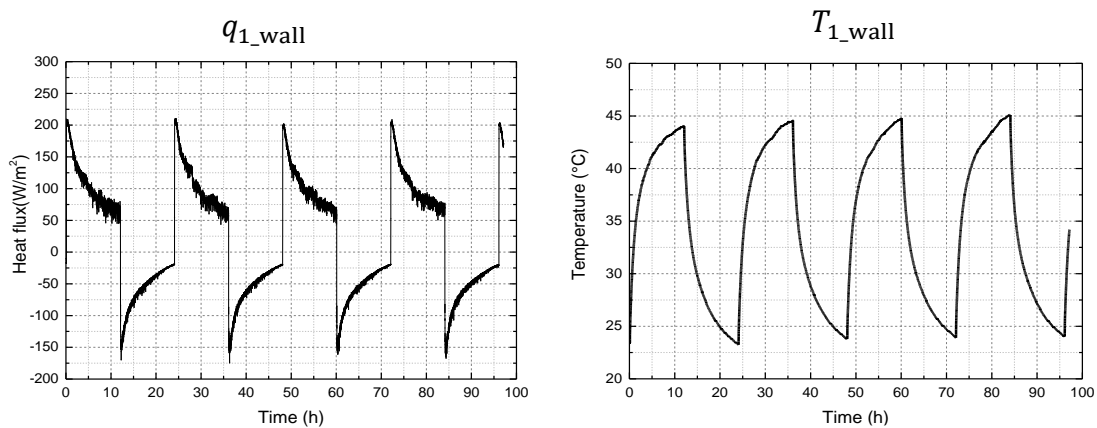


Fig. 4-18 Front face temperature and heat flux of a test with a periodic heating signal (period of 24 hours)

### 4.3 Pulse response curve method

Fig. 4-19 shows the pulse response results. The blue curve is the experimental pulse response and the red one is the simulated pulse response (subsection 4.3.1).

Comparing the experimental and simulated curves in Fig. 4-19, the experimental results have a good agreement with the simulated results in the linear period except a few data at beginning (in 1000 s). These undesirable data may be caused by the inaccuracy of heat flux at beginning or the wall inertia. However, there is an obvious difference after the linear period. This difference could be caused by the reference values of the thermal properties which are a bit difference with the actual ones. Even though, the trends of the two curves are similar.

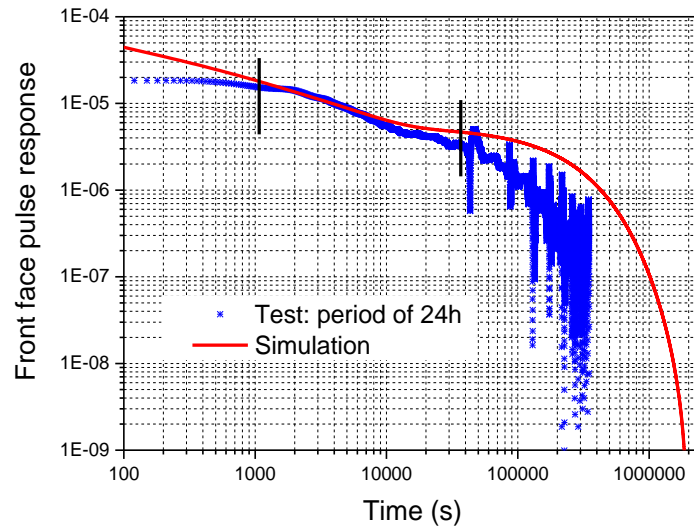


Fig. 4-19 Pulse response results in the lab-case (test with square wave heating signal of period of 24 hours).

Fig. 4-20 shows the experimental temperature and heat flux of another test. A heating signal of period 96 hours was used.

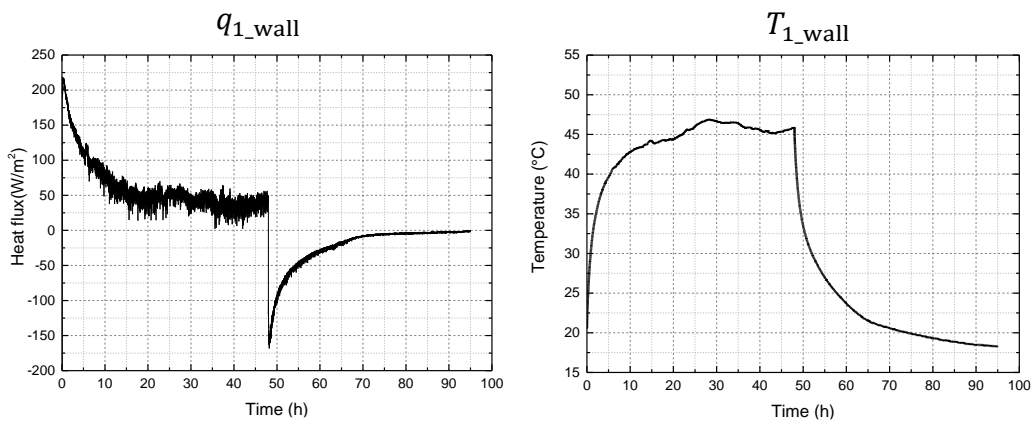


Fig. 4-20 Front face temperature and heat flux of a test with a periodic heating signal (period of 96 hours)

Similarly, Fig. 4-21 shows the pulse results of this test, the blue points are the experimental results and the red curve is the simulated results. It also has a good agreement at the linear period. The two experimental results in Fig. 4-19 and Fig. 4-21 are similar, indicating that the difference of heating signals has no effects on the pulse response results. At the end of the experimental curve, it has less fluctuations than that in Fig. 4-19. These fluctuations are caused by the suddenly change of heat flux. When the heating signal is launched on or off, the heat flux in a short time was unstable and inaccuracy, resulting in the noise of pulse response curve.

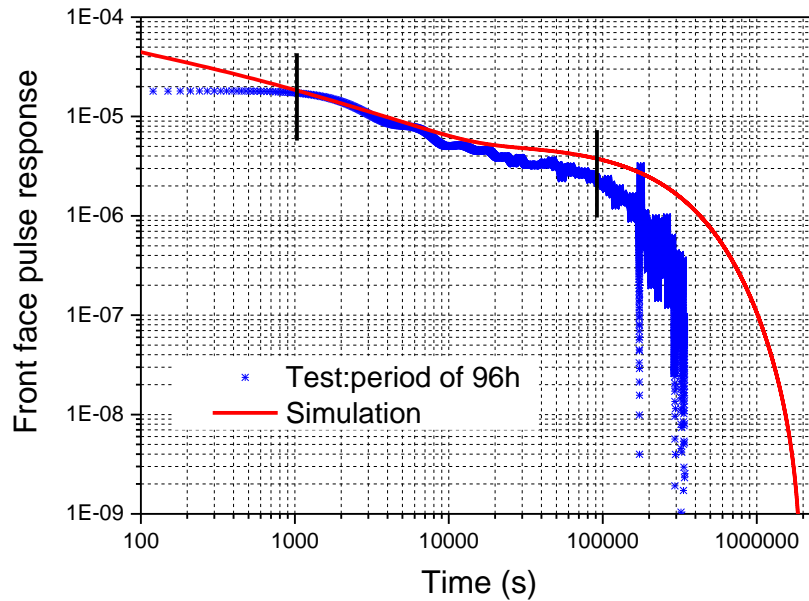
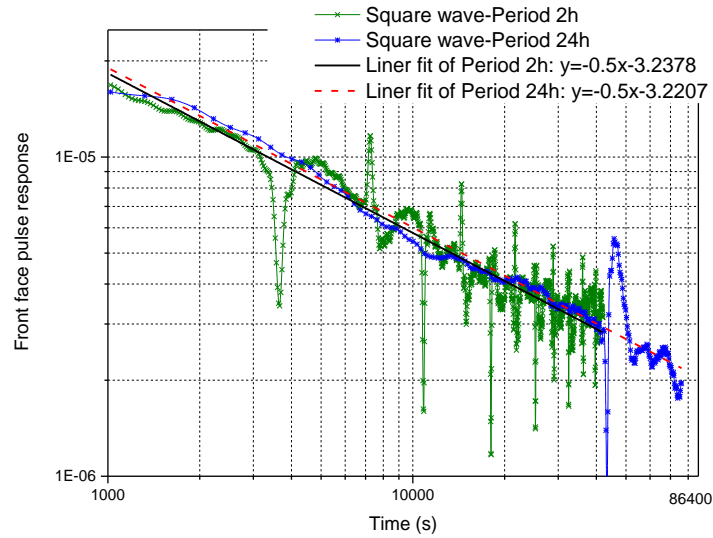


Fig. 4-21 Pulse response results in the lab-case (test with square wave heating signal of period of 96 hours).

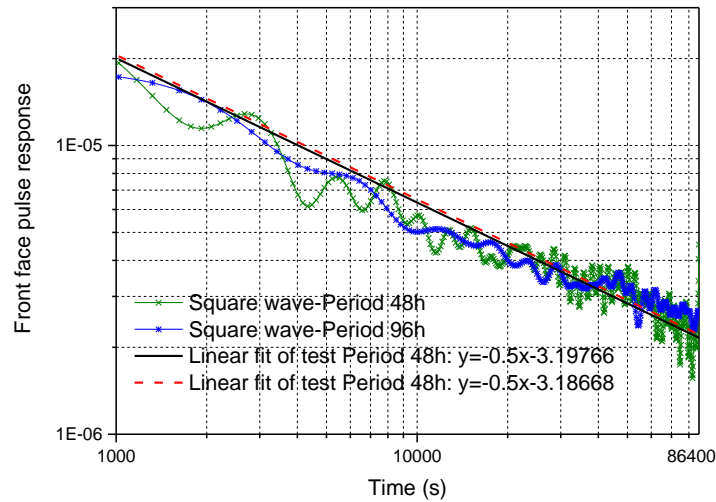
According to the analysis in subsection 4.4.1, in the linear period, the slope of the response curve is -0.5 and the intercept is determined by the thermal effusivity  $\sqrt{\lambda\rho c}$  (Equ. 4-29). Therefore, the experimental curve in the linear period can be fitted to estimate a thermal effusivity, which can be considered as the global effusivity value of mortar layer and cinder block layer. One reason is that the two layers are near the heating source. The other reason is that the two layers are highly effusive materials which crucially determine the global effusivity of wall, while the insulation layer can be ignored because of its low effusivity.

The experimental data between 1000 s to 20 hours were chosen. Fig. 4-22 shows the linear fitting results of the experimental data in the test of Period 2 h, 24 h, 48 h and 96 h. With the fitting intercept, the thermal effusivity was obtained by Equ. 4-29 and the results are shown in Table 4-4. The relative errors between the experimental effusivity and the reference value is less than 7%.

### 4.3 Pulse response curve method



(a) Tests with period of 2 h and 24 h



(b) Tests with period of 48 h and 96 h

Fig. 4-22 Linear fitting of experimental pulse response curve

Table 4-4 Global effusivity of mortar and cinder block

Test	slope	intercept	R <sup>2</sup>	Global effusivity of mortar and cinder block (J · K <sup>-1</sup> · m <sup>-2</sup> · s <sup>-0.5</sup> )	Relative errors with reference value
2 h (Appendix F (b))	-0.5	-3.2378	0.78	975	6.97%
24 h (Appendix F (a))	-0.5	-3.22079	0.84	937	2.87%
48 h (Appendix F (c))	-0.5	-3.19766	0.85	889	2.47%
96 h (Appendix F (d))	-0.5	-3.18668	0.89	866	4.91%
Reference value				911	

**4.3.3.2 Results for in situ-case**

Three test results will be analyzed in this part: two with step heating signals and one with a periodic heating signal.

Fig. 4-23 (a) and (b) show the wall heat flux at front face and wall surface temperature at the same face, the calculated pulse response result is plotted in Fig. 4-23 (c). The experimental pulse response match well with the simulated curve except a few data at the beginning (the same problem with the test in the lab-case).

For a similar test, as shown in Fig. 4-24, the same results was obtained. In Fig. 4-24 (c), there is a fluctuation at the end of the curve, which is caused by the sharply change of the heat flux when the heating signal stops. This influence is more obvious in the test with a periodic heating signal, as shown in Fig. 4-25. In Fig. 4-25 (c), there are more fluctuation noises. Therefore, a continue step heating signal is suggested in the future test to avoid the data noise.

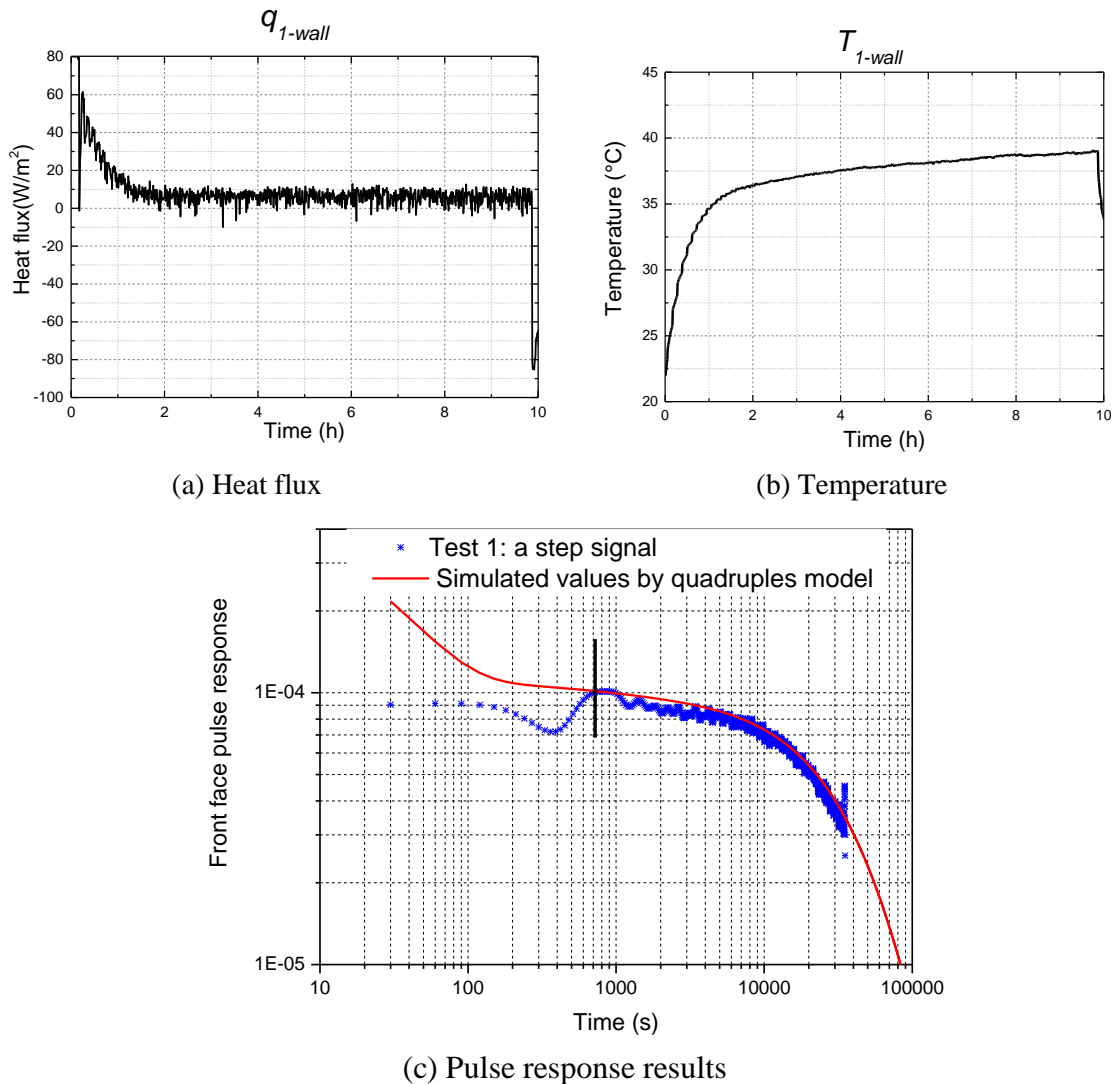
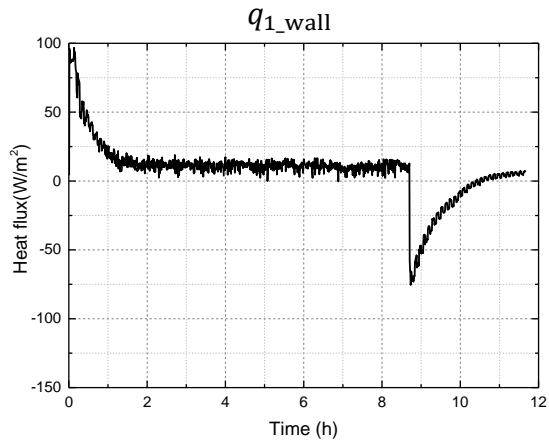
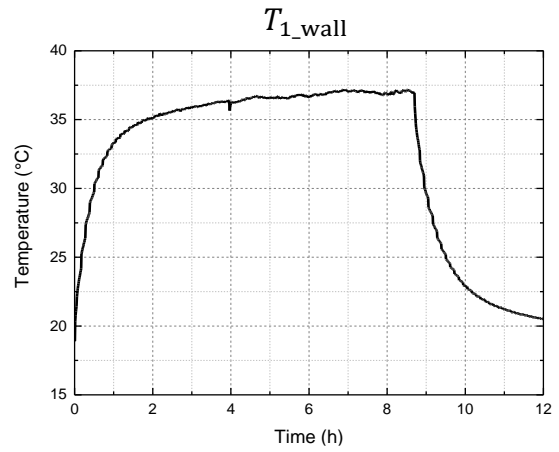


Fig. 4-23 Results of test with a step heating signal (test 1)

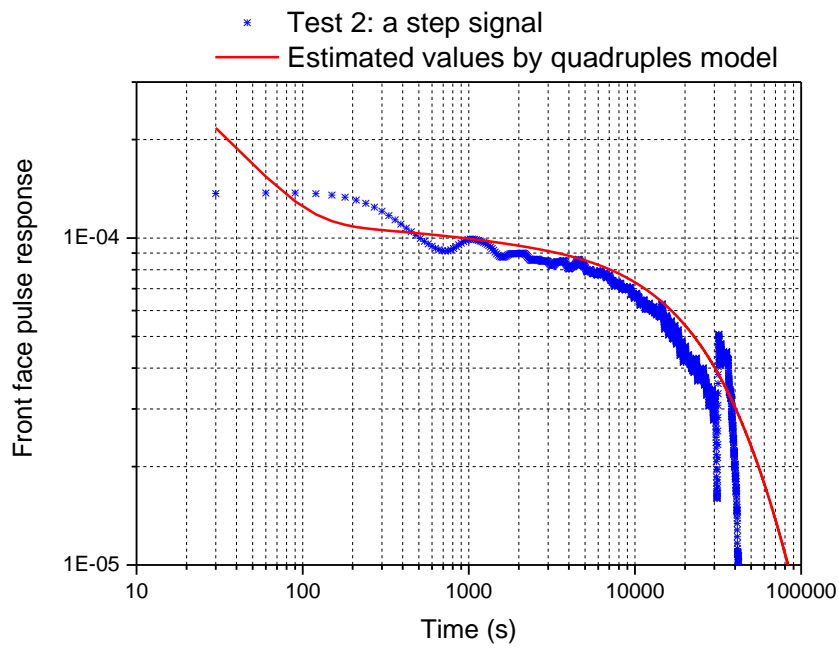
### 4.3 Pulse response curve method



(a) Heat flux



(b) Temperature



(c) Pulse response results

Fig. 4-24 Results for test with a step signal (test 2)



### 4.3 Pulse response curve method

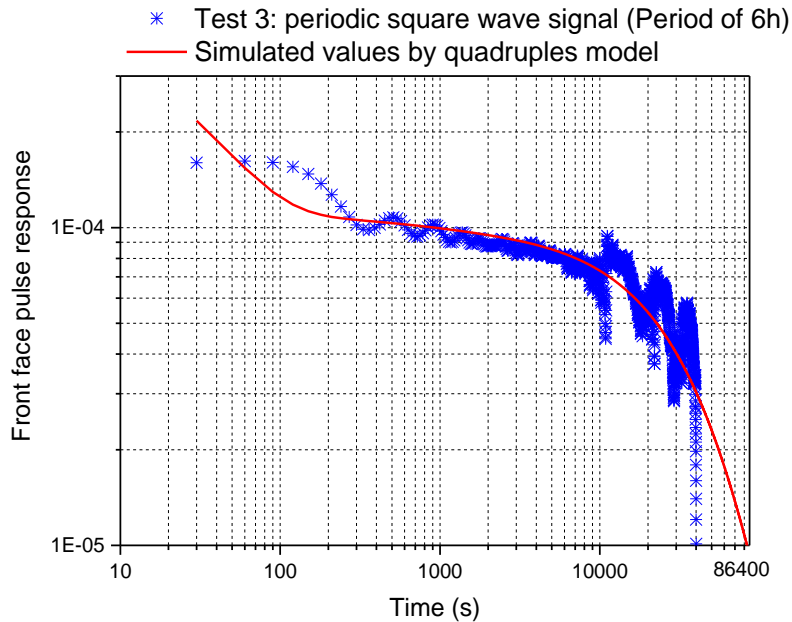
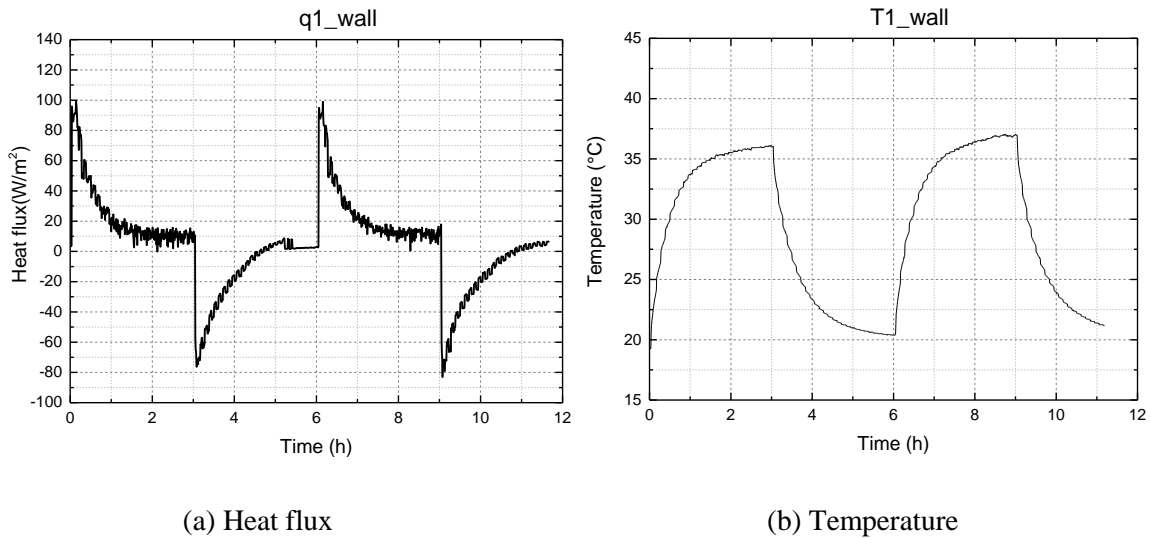


Fig. 4-25 Results for test with a periodic heating signal (test 3)

In summary, these experimental pulse response results are encouraging and the analyses are preliminary. Pulse response curve was obtained through an innovative deconvolution method in the test with step or periodic heating signals instead of pulse signal. The pulse response curve plotted in logarithmic axis is a better method to characterize the thermal parameters than using the temperature curve. This pulse response curve is characterized directly by the thermal parameters, and the curve trend is obviously sensitive to the properties. Plotting in the logarithmic axis amplifies the characterization and make it easy to analyze the thermal

parameters. The estimation results for the laboratory case is promising. A global thermal effusivity was obtained with a high accuracy. This method is for 1D heat transfer in the thick homogenous medium. In the future, more analyses on this pulse response curve will be done to estimate thermal properties quantitatively.

## 4.4 Step response curve method

When the wall heat flux is close to be constant, it can be assumed as a step heating signal, the step response curve (curve of measured temperature) can be used to estimate the thermal parameters of wall. The assumption of semi-infinite boundary condition is used in this method.

### 4.4.1 Simulation analysis of step response curve

Three typical multilayer concrete-supporting walls of building (see Fig. 4-26) are estimated by this thermal quadrupoles method. In model 1, the first layer of wall is concrete (dense layer), which can be supposed as a semi-infinite layer, so that the other layers behind concrete will not be considered. In model 2, an insulation layer (resistance-dominated layer) is added to the front of concrete layer. In model 3, a plaster layer (capacity-dominated layer) is added as the first layer based on model 2. The thermal properties of concrete, insulation and plaster are shown in Table 4-5. The front face of the walls are heated by a  $10 \text{ W/m}^2$  constant heat flux. With this known heat flux, the front surface temperature ( $T_1$ ) can be predicted through the thermal quadrupoles model (Equ. 4-5). The concrete layer can be supposed semi-infinite in a short characterization time because of the high heat capacity and large thickness. Simulations are made for the three wall models at semi-infinite boundary condition.

Table 4-5 Thermal properties of materials for simulation

Materials	$\lambda$ ( $\text{W}\cdot\text{m}^{-1}\cdot\text{K}^{-1}$ )	$\alpha$ $10^{-6}(\text{m}^2\cdot\text{s}^{-1})$	$L$ (m)
Concrete	1.65	0.75	Infinite/0.1
Insulation	0.039	1.08	0.1
Plaster	0.25	0.28	0.0125

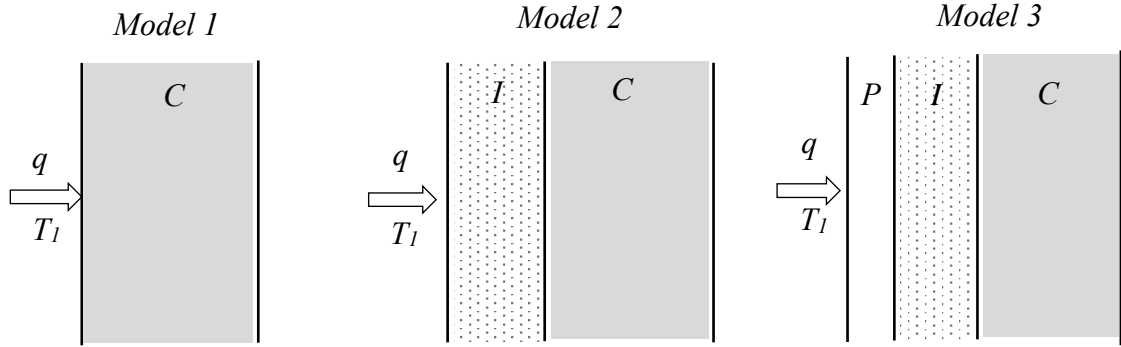


Fig. 4-26 Three typical wall models:  $C$  is concrete layer;  $I$  is insulating layer;  $P$  is plaster layer;  $T_1$  is front face temperature;  $q$  is heat flux.

Based on Equ. 4-6, quadrupoles equations for each model are listed in group 1, Table 4-6. Step response of each model were estimated by these exact quadrupole equations. Fig. 4-27(a) shows the estimated front face step responses under the semi-infinite condition.

Table 4-6 Equations of three wall models at semi-infinite condition

		Model 1	Model 2	Model 3
Group 1	Exact quadrupoles expression	$\begin{bmatrix} \theta_1 \\ \Phi_1 \end{bmatrix} = \begin{bmatrix} 1 & z \\ 0 & 1 \end{bmatrix} \begin{bmatrix} \theta_2 \\ \Phi_2 \end{bmatrix}$	$\begin{bmatrix} \theta_1 \\ \Phi_1 \end{bmatrix} = \begin{bmatrix} A_I & B_I \\ C_I & D_I \end{bmatrix} \begin{bmatrix} z \cdot \Phi_2 \\ \Phi_2 \end{bmatrix}$	$\begin{bmatrix} \theta_1 \\ \Phi_1 \end{bmatrix} = \begin{bmatrix} A_P & B_P \\ C_P & D_P \end{bmatrix} \begin{bmatrix} A_I & B_I \\ C_I & D_I \end{bmatrix} \begin{bmatrix} z \cdot \Phi_2 \\ \Phi_2 \end{bmatrix}$
Group 2	Approximated quadrupoles expression	$\begin{bmatrix} \theta_1 \\ \Phi_1 \end{bmatrix} = \begin{bmatrix} 1 & z \\ 0 & 1 \end{bmatrix} \begin{bmatrix} \theta_2 \\ \Phi_2 \end{bmatrix}$	$\begin{bmatrix} \theta_1 \\ \Phi_1 \end{bmatrix} = \begin{bmatrix} 1 & R \\ 0 & 1 \end{bmatrix} \begin{bmatrix} z \cdot \Phi_2 \\ \Phi_2 \end{bmatrix}$	$\begin{bmatrix} \theta_1 \\ \Phi_1 \end{bmatrix} = \begin{bmatrix} 1 & 0 \\ C_2 \cdot p & 1 \end{bmatrix} \begin{bmatrix} 1 & R \\ 0 & 1 \end{bmatrix} \begin{bmatrix} z \cdot \Phi_2 \\ \Phi_2 \end{bmatrix}$
Group 3	Approximated Laplace front temperature	$\theta_1 = z \cdot \Phi_1$	$\theta_1 = (z + R) \cdot \Phi_1$	$\theta_1 = \frac{z + R}{1 + C_2 \cdot p \cdot (z + R)} \cdot \Phi_1$
Group 4	Approximated step response	$T_1 = \frac{2q\sqrt{t}}{b\sqrt{\pi}}$	$T_1 = \frac{2q\sqrt{t}}{b\sqrt{\pi}} + R \cdot q$	$T_1 = R \cdot q \left( 1 - e^{-\frac{t}{R^2 C_2^2}} \right)$ (With assumption: $b \rightarrow \infty$ )

Where  $z = \frac{1}{b\sqrt{p}}$ ,  $b$  is the thermal effusivity of concrete;  $q$  is the heat flux;  $R$  is the thermal resistance of insulation;  $C_2$  is the heat capacity of plaster; **subscript:**  $P$  stands for plaster layer;  $I$  stands for insulation layer;

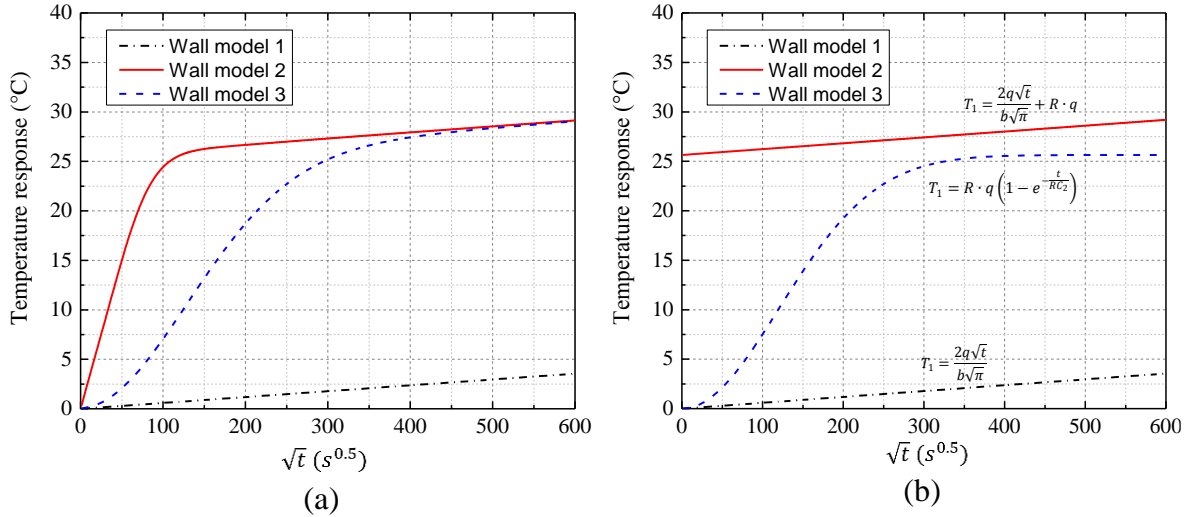


Fig. 4-27 Estimation of front face step response for three wall models at semi-infinite condition (a) exact quadrupoles model (b) approximated quadrupoles model

In order to physically analyze the step response curves in Fig. 4-27 (a), approximated solutions are proposed. The exact quadrupole equations of group 1 in Table 4-6 can be approximated by assuming that the insulating layer is totally thermally resistive and the plaster layer is totally capacitive. Approximated expressions of each wall model are shown in group 2. Through the inverse Laplace of equations in group 3, expressions of the front step responses of each wall model can be simplified, as shown in equations of group 4. Fig. 4-27(b) shows the approximated curves of three wall models.

As shown in Fig. 4-27(a), the slopes (temperature increase rate) of the three wall models are obviously different at the beginning of the simulation. For the wall model 1, the slope of this curve is low and always remains the same value of  $\frac{2q}{b\sqrt{\pi}}$ , which is determined by the effusivity of concrete. For wall model 2, this curve increases sharply at beginning in a short time then the increase slows and reaches a stable value quickly. Comparing with the approximated quadrupoles model in Fig. 4-27(b), this stable slope value is the same value with wall model 1 of  $\frac{2q}{b\sqrt{\pi}}$ , and the intercept of this stable period curve is  $R \cdot q$ . This intercept characterizes the thermal resistance of the insulating layer. For wall model 3, the curve performs at a middle behavior between model 1 and model 2, and turns into the stable slope period in a relative long characterization time. According to the approximated expression in Fig. 4-27(b), this transition characterization time is determined by heat capacity of plaster and thermal resistance of insulating layer ( $R \cdot C_2$ ).

In summary, the analysis of temperature response at a semi-infinite condition makes it possible to identify the component of first layer: light insulating, insulating and slightly capacitive, or

contrarily highly effusive. The thermal resistance of insulation layer and thermal effusivity of concrete can be roughly estimated by the intercepts and slope trends of temperature curves.

The previous physical analysis allows us to choose out the highly sensitive parameters of this system in an iterative estimation method with the exact model. For the semi-infinite condition, only the effusivity of concrete and thermal resistance of insulation are sensitive. The analyses are promising because the two parameters are the main characteristics that we aims to obtain in the thermal diagnosis of walls.

This result can also be obtained through a local sensitivity analysis method. Different sensitivity analysis techniques have been studied [108], including local and global methods. Global methods vary all the parameters and can obtain information for a subset of input variables in a wider domain. The local method is simple and easy to use. It involves taking the partial derivative of the output with respect to an input factor to obtain a qualitative information of the importance of each factor. A model with  $k$  independent inputs  $X_i$  ( $i=1, \dots, k$ ) is considered.  $Y$  is the output value. For a given value of  $X$ , the local sensitivity of the  $i$ th input factor is calculated as Equ. 4-43. The sensitivity of front face temperature to the thermal parameters is calculated by Equ. 4-45.

$$S_i(t) = X_i \frac{\partial Y_k(t)}{\partial X_i} \quad 4-43$$

The approximated expression is the followings.

$$S_i(t) = X_i \frac{\Delta Y_k(t)}{\Delta X_i} \quad 4-44$$

$$S_i(t) = X_i \frac{[Y(X_1, X_2, \dots, X_{i+\Delta i}, \dots, X_k) - Y(X_1, X_2, \dots, X_i, \dots, X_k)]}{\Delta X_i} \quad 4-45$$

Fig. 4-28 shows the sensitivity of front face temperature to thermal parameters based on the case of wall model 3. These sensitivity results have a good agreement with the results obtained previously through the physical analysis method. For the semi-infinite condition, the thermal resistance of insulation is the most sensitive parameter. The temperature is lightly sensitive to the effusivity, which will make it difficult to be estimated. The sensitivity curve of insulation effusivity presents a high value at beginning but only keeps for a very short time, which is also difficult to make the estimation.

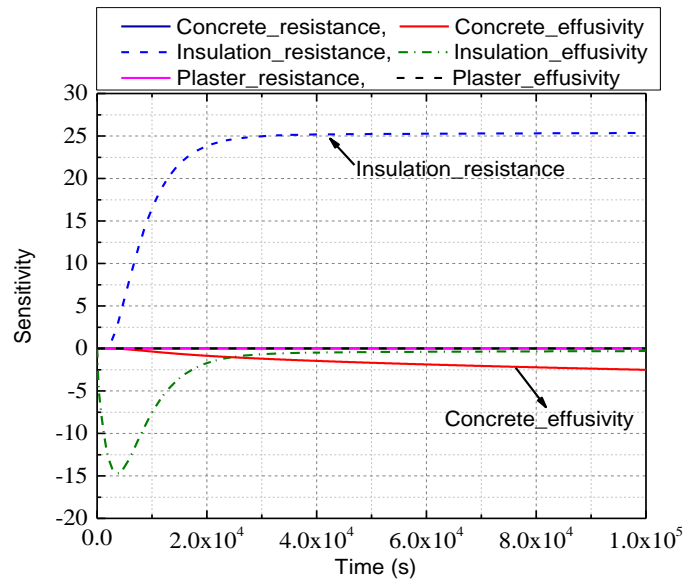


Fig. 4-28 Sensitivity of front face temperature to thermal parameters

According to the sensitivity analysis, the thermal probe method can not characterize all the wall parameters simultaneously. Only some of the parameters are sensitive to estimate. Other parameters, such as thicknesses, can not be estimated.

#### 4.4.2 Experimental results of step response

The nearly constant heat flux data were chosen to be analyzed for two experiment cases.

##### 4.4.2.1 In laboratory case

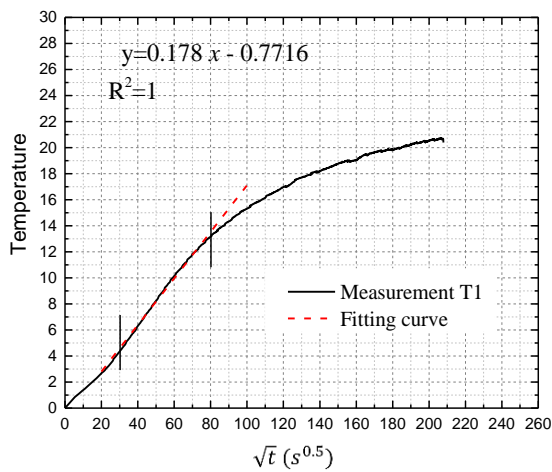
For the tests in laboratory case, as described in section 2.4, the objective wall has four layers with the concrete block layer located near the front face, which is corresponding to the wall model 3 in Fig. 4-26. According to the analysis in Fig. 4-27 (a), under a semi-infinite condition, the front face step response is a linear curve determined by the effusivity of concrete block and heat flux. The effusivity of concrete block is estimated with the measured temperature. Three tests in Appendix F will be analyzed, as shown in Fig. 4-29 and Table 4-7.

For Test 1, the measured relative temperature is shown in Fig. 4-29(a). There are three stages for this temperature curve. In a very short time ( $\sqrt{t} < 30$ ), the curve is linear and determined by the effusivity of mortar layer. When  $30 < \sqrt{t} < 80$ , it is another linear curve and characterized by the effusivity of concrete block. After  $\sqrt{t} > 80$ , the concrete layer is penetrated totally. There are only a few data for the mortar layer, so that we focused on the estimation of concrete layer hereby. Therefore, the linear stage ( $30 < \sqrt{t} < 80$ ) is used to estimate the effusivity of concrete block. The average heat flux of this stage is  $180.39 \pm 4.15$

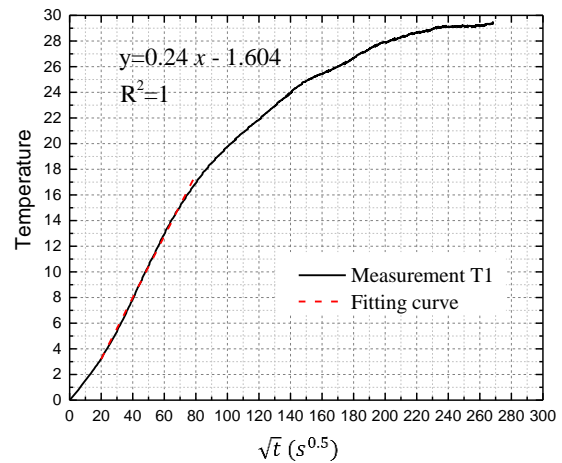
#### 4.4 Step response curve method

$W/m^2$ . The red curve in Fig. 4-29(a) is the linear fitting results. With previously analysis, it is known that  $\frac{2q}{b\sqrt{\pi}} = 0.178$ ,  $b=1145.96\pm 26.36$ , which is 27.31% relative error with the reference value.

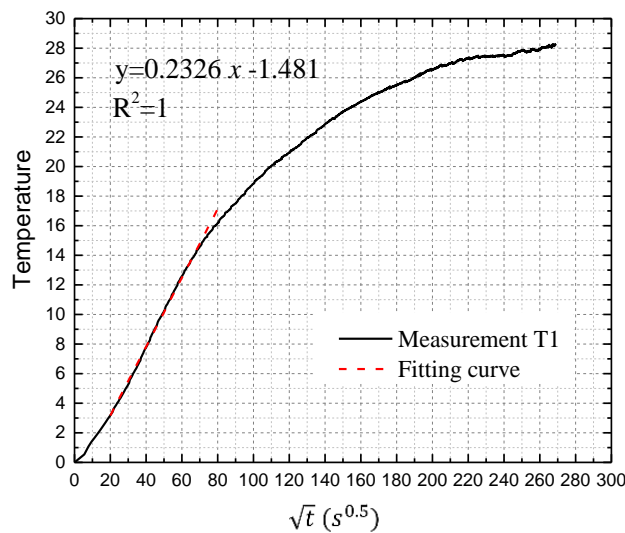
The same way, the results for Test 2 and Test 3 are obtained. In Table 4-7, the effusivity values of concrete block are much higher than the reference values, the relative error ( $e_r$ ) is more than 40%. However, comparing these results with the optimal values obtained by inverse method (subsection 4.5.2), the relative error is within 26%.



(a) Test 1



(b) Test 2



(c) Test 3

Fig. 4-29 Measured front face temperature and its linear fitting in the laboratory case

#### 4.4 Step response curve method

Table 4-7 Concrete block effusivity results through analyzing temperature response method

Test	$q$ (W/m <sup>2</sup> )	Slope $(\frac{2q}{b\sqrt{\pi}})$	R <sup>2</sup>	$J \cdot K^{-1}m^{-2}s^{-0.5}$	$e_r$ with reference value (896)	$e_r$ with optimal value in subsection 4.5.2 (1014)
Test 1 (Appendix F(a))	180.39	0.1779	1	1146±26	28%	13%
Test 2 (Appendix F (c))	267.24	0.2400	1	1258±20	40%	24%
Test 3 (Appendix F (e))	262.85	0.2326	1	1277±20	43%	26%

#### 4.4.2.2 In situ case

As described in section 2.4, the tests were carried out on a building wall on site. The wall has four layers: plaster, insulation, concrete block and mortar, corresponding to wall model 3 in Fig. 4-26. The insulation layer is placed near indoor surface of wall. The results of three tests will be analyzed in this section.

For Test 1 with a step heating signal (Appendix G(d)), the average heat flux of front face is 6.14 W/m<sup>2</sup>. A semi-infinite boundary condition is assumed in the 8 hours. According to the sensitivity analysis in Fig. 4-28(a), only the resistance of insulation can be estimated in this test. Fig. 4-30 (a) shows the relative temperature of front face and its linear fitting result. The temperature increases sharply at beginning and then becomes linear, corresponding to curve of model 3 in Fig. 4-27(a). According to the model analysis in subsection 3.2, the value of  $q \cdot R$  is 12.65. The uncertainty of heat flux is 0.56 W/m<sup>2</sup>. The thermal resistance of insulation is 2.06±0.19 m<sup>2</sup>·K·W<sup>-1</sup>, -41% relative error with the reference value ( $R_{refe}=2.9$  m<sup>2</sup>·K/W).

Similarly, thermal resistance results for Test 2 (Appendix G(e)) and Test 3 (Appendix G (f)) are calculated, as shown in Fig. 4-30 (b) and (c). Table 4-8 lists the results for the three tests. The three values estimated by this method are smaller than the reference value but closed to themselves. These thermal resistance values were obtained without information of wall structure and thicknesses.



#### 4.4 Step response curve method

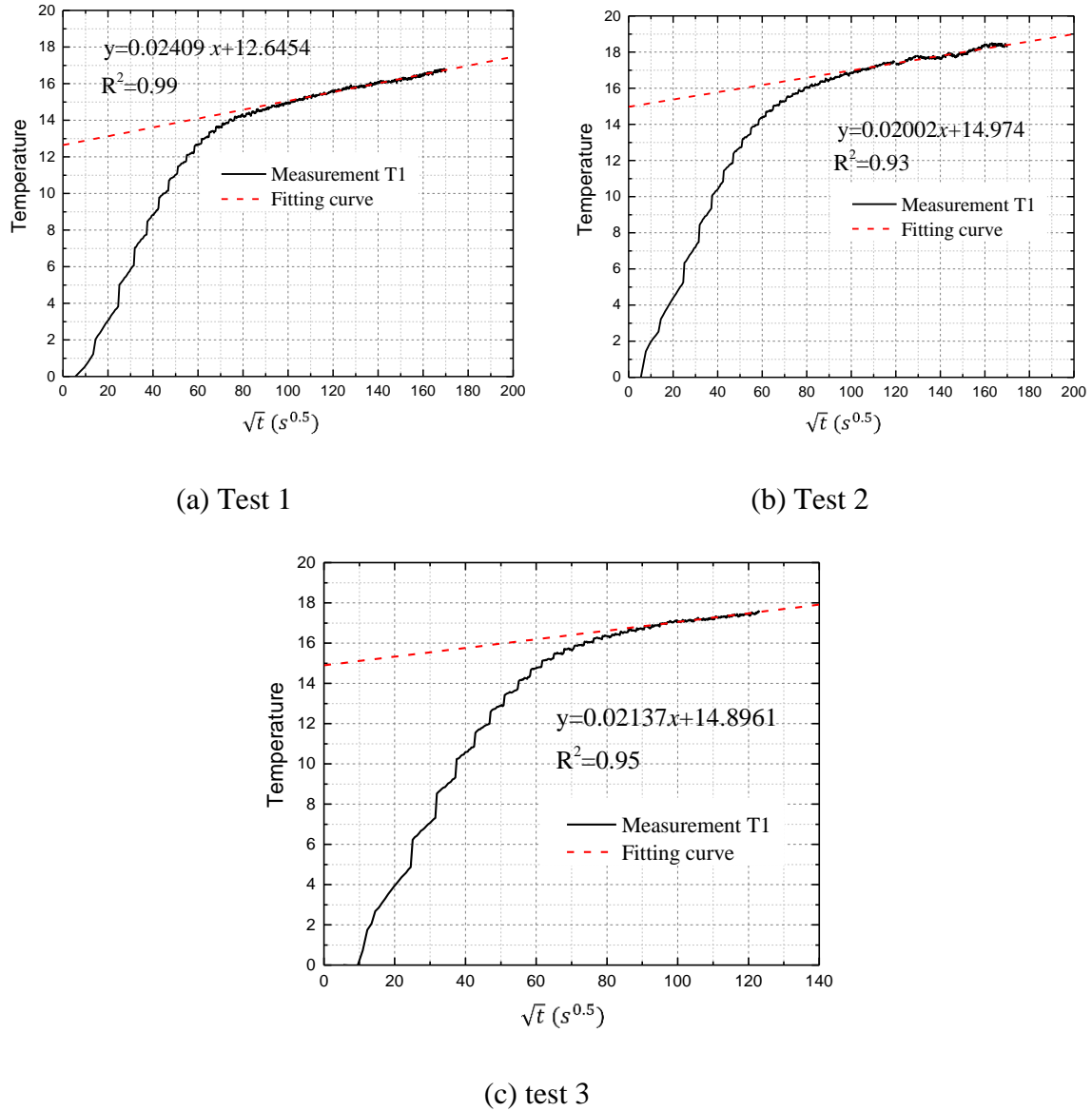


Fig. 4-30 Measured front face temperature and its linear fitting (Test 1)

Table 4-8 Thermal resistance results through analyzing temperature response method

Test	$q$ (W/m <sup>2</sup> )	Fitting curve	$R^2$	$R$ (m <sup>2</sup> ·K/W)	Relative error with reference values
Test 1 Appendix G (d)	6.14	$y=0.02409x+12.6454$	0.99	$2.06\pm 0.19$	-41%
Test 2 Appendix G (e)	9.65	$y=0.02002x+14.974$	0.93	$1.55\pm 0.09$	-87%
Test 3 Appendix G (f)	7.35	$y=0.02137x+14.8961$	0.95	$2.02\pm 0.15$	-44%

## 4.5 Inverse method to estimate thermal parameters

Inverse method is an approach to estimate the thermal parameters by minimizing the predicted results by model with the measured values through numerical iterations. This method is suitable for the cases knowing the wall structure and thickness of each layer, such as for the new building accreditation.

### 4.5.1 Inverse method basics

To study a physical system by the inverse method [49], the following steps shall be considered:

- (1) Direct modeling: parameterize the system with a minimal set of model parameters, whose values completely characterize the system. Then choose a physical law (heat transfer equations or models), allowing us, with the given values of the model parameters, to make predictions on the measurement results of some observable parameters.
- (2) Sensitivity analysis: compute the sensitivity of the predicted results to each model parameter, and chose out the sensitive ones to estimate.
- (3) Design an experiment in order to obtain the accurate output of the model with fixed model parameters.
- (4) Inverse algorithm: use the actual measurement results of the observable parameters to infer the actual values of the sensitive parameters by minimizing the differences between the measurement results and predicted results.

The direct modeling of wall is based on the thermal quadrupoles model introduced previously in subsection 4.1. According to Equ. 4-20, this modeling involves the surface heat flux and temperature of both front face and rear face of wall, the parameters of properties for each layer of wall (thermal conductivity, heat capacity and thickness) and the convection coefficient of the rear face. The surface heat flux  $q$ , the convection coefficient and the parameters of wall properties are the given parameters. With the given parameters, the surface temperatures are predicted.

In order to estimate property parameters of the 4 layer-wall (heat capacity and conductivity of each layer), the sensitivities for the 8 parameters should be analyze in the direct modeling. In this work, the local sensitivity analysis method is applied, as described in subsection 4.4.1.

After the sensitivity analysis of the 8 parameters, the sensitive ones are chosen and grouped as an array  $U$ ,  $U=(\lambda,\rho c\dots)$ . The flow chart of parameters estimation is shown in Fig. 4-31. Firstly, the heat flux measured by shiny and black heat flux sensors are used to calculate the wall heat flux ( $q_1$  and  $q_2$ ) through the heat flux balance equations (subsection 3.2). Then, the wall heat flux and an initial parameters array  $U_0$  are input to the quadrupoles modeling to predict the

temperatures. The unknown parameters array  $U$  can be obtained by minimizing the difference between this predicted temperature and the measured temperature. The minimizing issue is solved by the Levenberg-Marquardt algorithm [109], [110]. This algorithm is done by the `Lsqnonlin` function in Matlab, as described in Appendix J. In our work,  $T_1$  and  $T_2$  were respectively used as the output parameters of model to estimate the parameters of thermal properties.

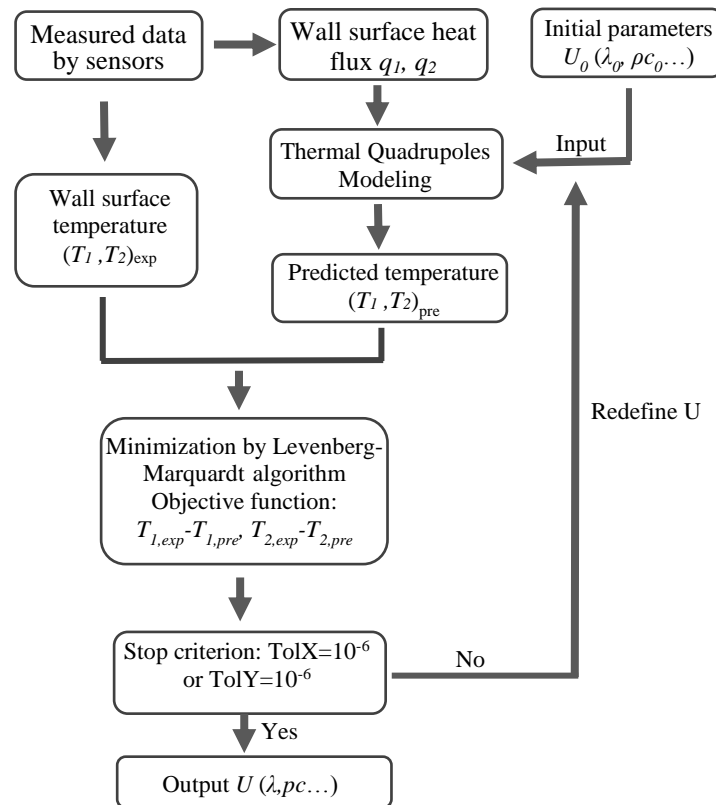


Fig. 4-31 Inverse method flow chart

### 4.5.2 Optimal results

As described before, two walls were tested. Though the two walls are four layers, the mortar layer and plaster layer can be ignored because they are too thin to make significant influence on the wall thermal performance. Normally, insulation layer and concrete layer are the two important layers in the wall. In the lab-case, the concrete block layer is placed near the front face of wall (near the heat source), while, in the in situ-case, the insulation layer is near the front face. These layer orders are two typical structures of walls. This section will show the optimization results of the two walls.

#### 4.5.2.1 Optimization results in the laboratory-case

As an example, the data processing of one test is described in detail hereby. In this test, the wall is heated by a periodic square wave heating signal of period 24 hours.

Firstly, the sensitivity is calculated. Fig. 4-32 shows the sensitivity of front face temperature ( $T_1$ ) to the 8 parameters and Fig. 4-33 shows the sensitivity of the rear face temperature ( $T_2$ ).

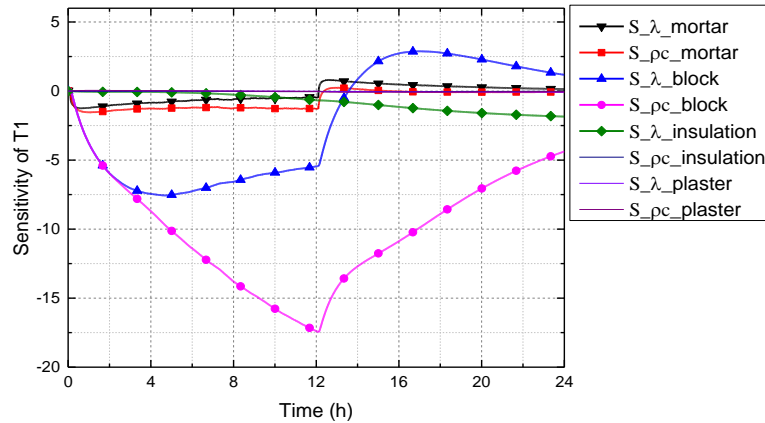


Fig. 4-32 The sensitivity of front face temperature ( $T_1$ ) to the 8 thermal parameters

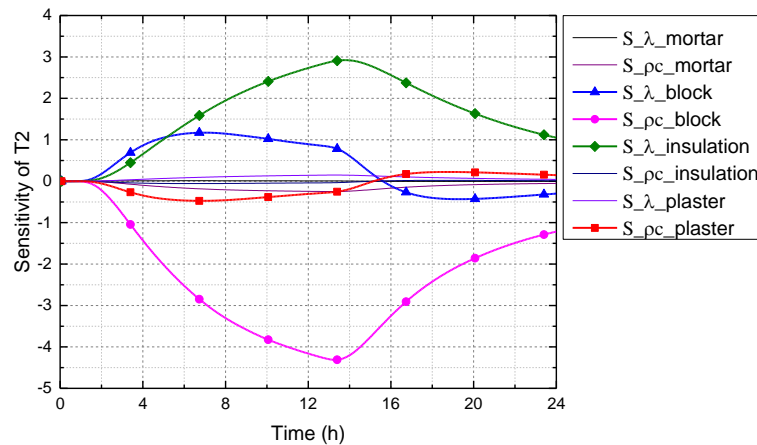


Fig. 4-33 The sensitivity of rear face temperature ( $T_2$ ) to the 8 thermal parameters

In Fig. 4-32,  $T_1$  is obviously sensitive to the heat capacity and conductivity of concrete block, the heat capacity and conductivity of mortar is lightly sensitive. The insulation layer begins to be sensitive since 12 hours. Considering the sensitivity values and the characterization time, the input unknown array  $U$  is set as  $(\lambda_{block} \rho C_{block})$ . The characterization time ranges from 2 to 8 hours. The correlation between the two parameters was studied (Fig. 4-34). The correlation

coefficient of the two parameters is -0.2678, therefore, it is possible to estimate the two parameters simultaneously.

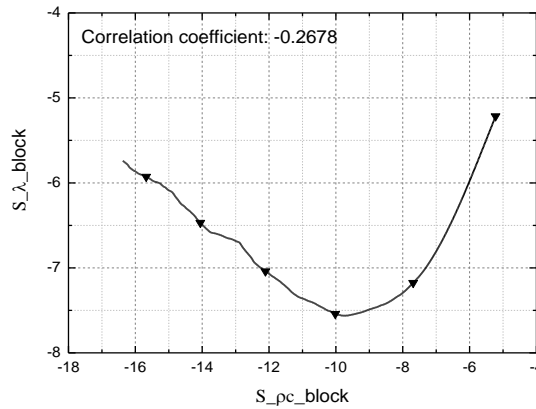


Fig. 4-34 Correlation study of sensitivities between  $\lambda_{block}$  and  $\rho C_{block}$

In Fig. 4-33, 4 parameters effect obviously on the rear face temperature:  $\lambda_{block}$ ,  $\rho C_{block}$ ,  $\lambda_{insulation}$  and  $\rho C_{plaster}$ . As the block layer can be estimated by  $T_1$ ,  $\lambda_{block}$  and  $\rho C_{block}$  are considered as known parameters hereby. Meanwhile, the plaster layer is unimportant to influence the performance of building walls, allowing us to ignore to estimate the  $\rho C_{plaster}$ . Finally, the unknown parameters array is chosen as  $U=(\lambda_{insulation})$  when using  $T_2$  to make estimation. The characterization time ranges from 2 to 10 hours.

Then, the data was processed by the function 'lsqnonline' in Matlab (details in Appendix J).

For example, estimation with  $T_1$ , the input initial U values:  $U_0=[1 \ 1]$

The Output solution:  $U=[0.9909 \ 0.9903]$

Table 4-9 shows the information of each iteration. The residual and norm of step decrease with the increase of iteration number. 43 times for the function evaluations.

With the output solution  $U$ ,  $T_1$  is re-predicted. Fig. 4-35 (a) shows the comparison for the re-predicted temperature ( $T_{pre-opti}$ ), the measured temperature ( $T_{exp}$ ) and the predicted temperature with the reference parameter values ( $T_{pre-refe}$ ). It is obvious that the optimal solution can match the measurement much better than the given reference values.

## 4.5 Inverse method to estimate thermal parameters

Table 4-9 Iteration information

Iteration	Func-count	Residual	First-Order optimality	Norm of step
0	3	179.927	1.73e+03	
1	6	3.84136	146	0.0933068
2	9	2.70241	5.31	0.0203248
3	12	2.70189	1.45	0.00380754
4	24	2.70187	0.566	4.50132e-05
5	27	2.70183	1.31	7.24776e-05
6	30	2.7018	1.12	0.000162103
7	33	2.70106	0.707	0.00195376
8	37	2.7008	0.227	0.00392419
9	40	2.70076	0.0131	0.00037743
10	43	2.70073	0.496	0.000228024

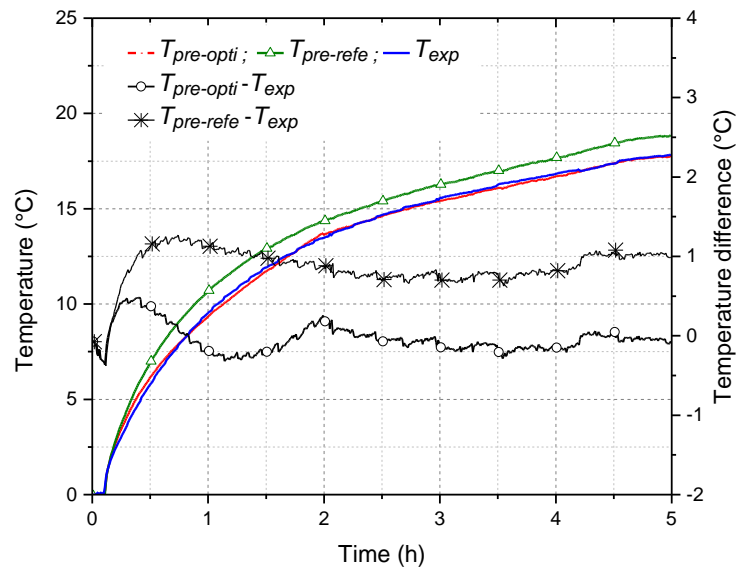


Fig. 4-35 The predicted temperature versus measured temperature

In order to analyze the optimal results clearly, the average residual ( $r$ ) and the relative error ( $e_r$ ) are considered. The average residual ( $r$ ) expresses the temperature difference between the estimated temperature ( $T_{cal}$ ) and the measured temperature ( $T_{exp}$ ). The relative error ( $e_r$ ) shows the relative difference of the optimal value of one parameter ( $P_{opti}$ ) with the given reference value ( $P_{refe}$ ).

$$r = \frac{\sum_{i=1}^n |T_{exp}(i) - T_{cal}(i)|}{n} \quad (n \text{ is the number of data}) \quad 4-46$$

$$e_r = \frac{P_{refe} - P_{opti}}{P_{opti}} \quad (P \text{ is a certain parameter}) \quad 4-47$$

### The influence of initial values $U_0$

The influence of initial values of  $U$  is analyzed. 7 groups of initial values ( $U_0$ ) were considered to estimate ( $\lambda_{block} \rho C_{block}$ ) in the same characterization time (1-5 hours). Table 4-10 shows the output solutions of the 7 estimations.

Table 4-10 Output solutions with different initial values

	$U_0$	Solution $U$	residual	Number of iteration	Profile time (s)
Estimation 1	(0.87 0.9)	(0.9009 0.9903)	0.0709	4	348
Estimation 2	(1 1)	(0.9017 0.9895)	0.0710	10	664
Estimation 3	(0 0)	(0.8996 0.9916)	0.0709	10	649
Estimation 4	(0.435 0.45)	(0.9016 0.9896)	0.0710	7	483
Estimation 5	(1.305 1.35)	(0.9010 0.9902)	0.0710	8	549
Estimation 6	(1.74 1.8)	(0.9016 0.9896)	0.0710	10	676
Estimation 7	(10 10)	(0.9004 0.9907)	0.0709	21	1321

In Table 4-10, Estimation 1 uses the reference values of parameters as the initial values. Estimation 2 uses the values at the same magnitude with the reference values and the output solution is very close to the results of Estimation 1. Estimation 3 to 6 respectively use the 0%, 50%, 150% and 200% of the reference values as the input values. The influence on the output solutions is insignificant. For Estimation 7, the initial values are even not at the same magnitude with the reference values and far away with the reference values, the output solution has not been influenced except a longer profile time is needed.

The input initial values hardly have influence on the output solution. However, to reduce the running time, the initial values should be reasonable, the closer to the real values, the better. The initial values at the same magnitude with the real values, or in  $\pm 100\%$  of real values, are suggested. These values can be forecasted from the reference of materials properties.

**The influence of characterization time**

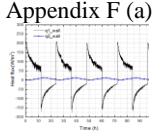
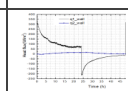
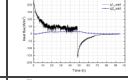
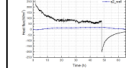
The chosen of the characterization time should also be considered. Based on the sensitivity analysis (Fig. 4-32), the sensitivities increases form 0 to 12 hours, but an obvious sensitivity begins at 2 hours. This is the prerequisite range to choose the characterization time. 4 ranges of characterization time were chosen to estimate  $U$  ( $\lambda_{block} \rho C_{block}$ ) with the same initial value  $U_0$ . Table 4-11 shows the output solutions of the 4 estimations. For the 4 characterization time: 2-5, 2-6, 2-7, 2-8 hours, the output solutions are similar and have no significant change. The slight change of characterization time has little influence on the output solution.

Table 4-11 Output solutions in different characterization time

	time (h)	Number of data	Solution $U$	residual	Number of iteration	Profile time (s)
Estimation 1	2-5	360	(0.9009 0.9903)	0.0709	4	348
Estimation 2	2-6	480	(0.8957 0.9952)	0.0659	4	463
Estimation 3	2-7	600	(0.9058 0.9853)	0.0606	3	595
Estimation 4	2-8	720	(0.8836 1.0058)	0.0714	5	969

Data of the other tests is processed in the same way, and the results of optimal values are shown in Table 4-12 and Table 4-13.

Table 4-12 Optimal values with front face temperature

		$\lambda_{block}$ (W/(mK))	$e_r$	$\rho C_{block}$ ( $10^6$ J/m <sup>3</sup> K)	$e_r$	$r$ (with reference)	$r$ (with optimum)
Reference value		<b>0.87</b>		<b>0.9</b>			
Test 1 (4 periods) Appendix F (a) 	Period 1	<b>0.9009</b>	3.55%	<b>0.9903</b>	10.03%	0.9070	0.0709
	Period 2	<b>1.1320</b>	30.11%	<b>0.9074</b>	0.82%	1.6817	0.0567
	Period 3	<b>1.0385</b>	19.37%	<b>0.9501</b>	5.57%	1.4180	0.0386
	Period 4	<b>1.0482</b>	16.47%	<b>0.9312</b>	3.47%	1.3730	0.0595
Test 2 Appendix F (c)		<b>0.9199</b>	5.74%	<b>1.0712</b>	19.02%	1.6257	0.0296
Test 3 Appendix F (d)		<b>0.9406</b>	8.11%	<b>1.2610</b>	40.11%	0.9650	0.0378
Test 4 Appendix F (e)		<b>1.0691</b>	22.89%	<b>1.0342</b>	14.91%	2.2020	0.0394
Average results		1.01±0.08 (8%)	15.18%	1.02±0.11 (11%)	13.42%		

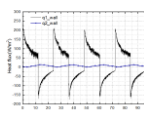
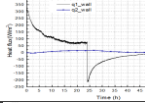
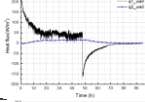
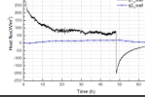


#### 4.5 Inverse method to estimate thermal parameters

According to the results of 7 groups in Table 4-12, the average value of  $\lambda_{block}$  is  $1.01\pm 0.08$ , value of  $\rho c_{block}$  is  $1.02\pm 0.11$ . The two results are stable with the RSD (relative standard deviation) of 8% and 10.94%. Comparing with the reference values, the optimal values is a little higher than the reference values, the relative errors ( $e_r$ ) of  $\lambda_{block}$  is 15.18%, relative errors ( $e_r$ ) of  $\rho c_{block}$  is 13.42%. This difference may be caused by the water infiltration and aging of walls. The reference values are strongly uncertain because of some reasons: such as manufacture, construction. These relative errors are acceptable. Even for some standard methods, for example, ISO9869, the errors ranges from 14%-28% [22]. According to the residual ( $r$ ) values, the residual that calculated with the optimal values of parameter is much lower than that calculated with the reference values. The difference between the measured temperature and predicted temperature has been minimized.

Table 4-13 shows the optimal results of  $\lambda_{insulation}$  basing on the minimization of rear face temperature. Optimal values of ( $\lambda_{block} \rho c_{block}$ ) obtained previously were used in this estimation. The optimal results range from 0.0311 to 0.0405. The average result is  $0.0355\pm 0.00293$ . It is 8.57% lower than the reference value, indicating a higher thermal resistance is obtained. This phenomenon is possible caused by the connection resistance of each layer, the aging of wall, or the uncertainty of reference value.

Table 4-13 Optimal values with rear face temperature

		$\lambda_{insulation}$ (W/(mK))	$e_r$	$r$ (with reference)	$r$ (with optimum)
Reference value		<b>0.038</b>			
Test 1 (4 periods) Appendix F (a) 	Period 1	<b>0.0344</b>	-9.47%	0.6811	0.0540
	Period 2	<b>0.0373</b>	-1.84%	0.4800	0.0443
	Period 3	<b>0.0338</b>	-11.05%	0.9321	0.0215
	Period 4	<b>0.0311</b>	-18.16%	1.4129	0.0352
Test 2 Appendix F (c)		<b>0.0405</b>	6.58%	0.6502	0.0477
Test 3 Appendix F (d)		<b>0.0335</b>	-11.84%	0.8857	0.0264
Test 4 Appendix F (e)		<b>0.0376</b>	-1.05%	0.6492	0.0572
Average results		$0.0355\pm$ $0.00293$ (8.26%)	-8.57%		

To summary, in the lab-case, three parameters ( $\lambda_{block}$   $\rho C_{block}$   $\lambda_{insulation}$ ) were estimated. These parameters are significant roles in determining the thermal performances of walls. The average optimal results are acceptable. The instability of the results can be avoided by repeating the test to choose the reliable results and obtain the average value of each parameter. It is also found that a continue step heating signal of 10 hours is advised in the inverse method.

**4.5.2.2 Optimization results in the in situ-case**

The objective wall in the in situ-case is also four layers. When the test is carried out in situ, it is difficult to use the rear face temperature to estimate the parameters. The rear face temperature has been affected by many factors, such as convection and radiations, so it is difficult to use the rear face temperature to estimate the thermal parameters. Only the front face temperature were analyzed in the in situ case.

The sensitivity of front face temperature is shown in Fig. 4-36.

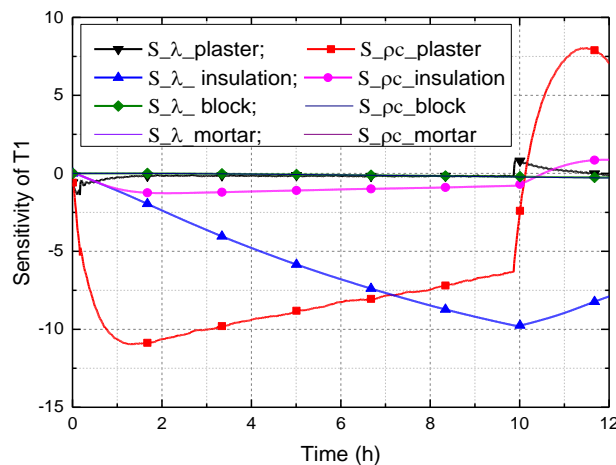


Fig. 4-36 Sensitivity of front face temperature ( $T_1$ ) for the 8 thermal parameters

In Fig. 4-36,  $T_1$  is sensitive to three parameters:  $U$  ( $\rho C_{plaster}$   $\lambda_{insulation}$   $\rho C_{insulation}$ ). The correlation of the three parameters are nonlinear, it is possible to estimate these parameters simultaneously. Table 4-14 shows the optimal results of  $U$  by minimization of  $T_1$ .

In Table 4-14, Test 1 and test 2 are with the suggested step heating signal, the optimal values of  $\rho C_{plaster}$  and  $\lambda_{insulation}$  are reasonable in the acceptable relative error. While, the error of  $\rho C_{insulation}$  in test 1 reaches to 36.9%. It is because the sensitivity of  $\rho C_{insulation}$  is much lower than that of  $\rho C_{plaster}$  and  $\lambda_{insulation}$ , a large uncertainty is possible.  $\rho C_{insulation}$  is not a critical parameter of wall.

For the other four tests with the random signal and short periodic signals (test 3-6), the output solutions of  $U$  are unreasonable and unstable, errors even reach to 129%. One of the reasons is

#### 4.5 Inverse method to estimate thermal parameters

that for the periodic or random signals, the sudden stop or launch of heating signal can cause the unstable and inaccuracy of heat flux, this incorrect heat flux will influence on the inverse calculation. The other reason is that the heat flux in the cooling period is low, the sensitivity of the parameters decreases and becomes weak, it is difficult to make the optimization in the cooling period. So a continue step heating signal is suggested to apply the inverse method.

Table 4-14 Optimal results with the front face temperature in the in situ-case

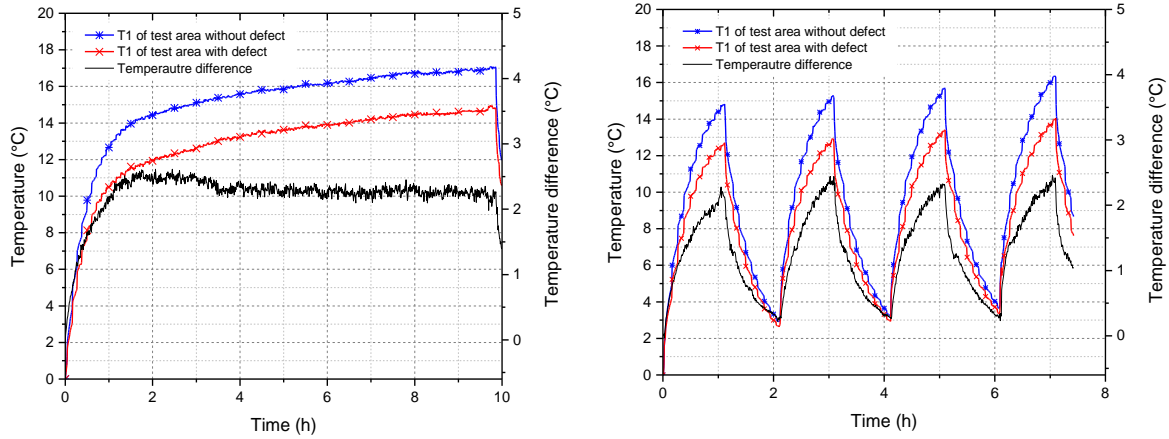
Test	Heating signal	$\rho C_{plaster}$ $10^6$ J/m <sup>3</sup> K)	( $e_r$ )	$\lambda_{insulation}$ (W/(mK))	( $e_r$ )	$\rho C_{insulation}$ ( $10^4$ J/m <sup>3</sup> K)	( $e_r$ )	$r$ (with optimal values)
	Reference value	<b>0.9</b>		<b>0.034</b>		3		
Test 1 Appendix G(d)	Continue step	<b>0.9319</b>	3.54%	<b>0.0291</b>	- 14.41%	1.8931	- 36.90%	0.0891
Test 2 Appendix G (e)	Continue step	<b>0.9549</b>	6.10%	<b>0.0391</b>	15%	2.4903	- 16.99%	0.0735
Test 3 Appendix G (f)	Random signal	1.0847	20.52%	0.0733	115.59 %	2.0518	- 31.61%	0.1700
Test 4 Appendix G(b)	P6h	1.0209	13.43%	0.0170	-50%	4.2601	42.00%	0.3842
Test 5 Appendix G (c)	P2h	1.0577	17.52%	0.0496	45.88%	6.8649	128.83 %	0.2192
Test 6 Appendix G (a)	P1h	1.0352	15.02%	0.0006	- 98.24%	3.0050	0.17%	0.3951

Fig. 4-37 shows the comparison of front temperatures ( $T_1$ ) in the test areas without defect and with defect. It is obviously found that the  $T_1$  of defect-area is about 2 °C lower than  $T_1$  of without defect-area, it indicates that the thermal resistance in the defect-area is lower than that in the without defect-area. This defect weakens the thermal resistance of insulation layer (CALIBEL APV+plaster).

According to our knowledge of this building and the pre-detect with IR camera (see in Fig. 2-24), this defect is caused by the wires channel embedded in the insulation board. The thickness of insulation layer is reduced in the defect-area. This thickness ( $e_{insulation}$ ) is estimated with knowing the thermal properties obtained from without defect-area.

Table 4-15 shows the optimal thickness values. The thickness of insulation without defect is 0.1 m, while, it reduces to less than 0.03 m with the defect.

This is a rough estimation for the defect, it is based on a 1D heat transfer regime and neglects the thermal resistance of the wires. The accuracy of the defect estimation will be improved in the future work.



(a) A continue step heating

(b) A periodic heating signal

Fig. 4-37 T<sub>1</sub> of test area without defect VS T<sub>1</sub> of test area with defect

Table 4-15 Optimal thickness of insulation in defect-area

Test	$L$ (m)
Continue step 1	0.0215
Continue step 2	0.0282

#### 4.5.2.3 Conclusion of inverse method

Two cases were analyzed in this work, one case is the concrete block side is near the heating source (the lab-case), the other case is the insulation layer is near the heating source (in situ-case). The two cases are the most common diagnosis situations. The characterization time is less than 10 hours. Generally, a continue step heating signal is suggested.

When the heating source is on the concrete block side, the heat capacity and conductivity of concrete block layer can be estimated by minimizing the measured and predicted front face temperature in a short characterization time (5 hours). The estimation of insulation layer needs a longer time (10 hours, even 20 hours), or it can be estimated based on the rear face temperature at an adiabatic boundary condition.

When the heating source is on the insulation side, the insulation layer can be estimated with the front face temperature, while, it is very difficult to estimate the concrete block layer in 10 hours.

For the critical and sensitive parameters ( $\rho_{Cplaster}$   $\lambda_{block}$   $\rho_{Cblock}$   $\lambda_{insulation}$ ), the relative error is less than 22%, several trials should be carried out to improve the repeatability and reliability of results and avoid the unreasonable data.

It is concluded that for any diagnosis situation, the properties of the critical layer near the front face can be estimated by the front face temperature. As we know that, generally, there are two critical layers in the wall, concrete layer and insulation layer. Therefore, it is possible to obtain the properties of the two layer by implementing test on the two faces of the wall. Each test needs about 10 hours.

Several steps are proposed to characterize thermal properties through this inverse method:

Step 1: Implement an experiment on the objective wall: heat one surface of the wall with a step heating signal for about 10 hours, measure the wall surface temperature, measure the heat flux at the same surface of wall with two heat flux sensors. The emissivity and absorption of the two heat flux sensors are different.

Step 2: Calculate the wall heat flux through the heat flux balance equations. Generally, the heat flux measured by sensors is not the wall heat flux because the absorption and emissivity of sensors and wall are different.

Step 3: Build the direct modeling of wall based on the thermal quadrupoles solutions and analyze the boundary conditions. This direct modeling involves the wall heat flux, wall front face temperature and wall thermal properties.

Step 4: Analyze the sensitivities to all the thermal parameters of wall and choose out the sensitive ones to form the unknown parameters array  $U$ . Choose a suitable characterization time.

Step 5: Obtain the optimal  $U$  value by minimizing the predicted values of model and measurement values through this inverse approach.

Step 6: To ensure the accuracy of results, work of step 1-5 can be repeated optionally to get an average value of  $U$ . Normally, the properties of the layers near the front face can be obtained. The properties of the layers near the rear face is less sensitive.

Step 7: If it is possible, implement the same test (step 1-6) on the other face of this wall to obtain the properties of layers near the rear face of wall.

### 4.6 Comparisons of the three methods

In conclusion, this chapter firstly introduced the basics of thermal quadrupoles solution. A heat transfer modeling of multilayer walls that adapts to in situ conditions were built. Based on this model, three estimation methods have been analyzed to estimate thermal parameters of walls: pulse response curve method, step response curve method and inverse method.

The pulse response can be calculated by a deconvolution approach with only the inconstant wall heat flux and surface temperature. The wall structure is not an essential information. This pulse response curve is directly characterized by the thermal effusivity and heat capacity. The pulse response curve has obvious data noise. The effective characterization time is between 1000 s to 24 hours. Actually, the pulse response curve method is more adapted for laboratory cases, for which the measurement noise can be reduced and a shorter time is needed.

There are fewer data noises for the step response curve, even in a long time. The thermal resistance of insulation layer and effusivity of concrete layer can be roughly estimated. This step response curve method is more useful for the diagnosis of wall in situ. In order to reduce the characteristic time, a semi-infinite assumption of concrete layer was proposed. With this semi-infinite assumption, we do not have to wait the response of the rear face of wall. However, the wall heat flux should be close to a constant value during the measurements to form a step signal.

The inverse method is a classic method that needs the wall structure and thickness of each layer. The sensitivities of all the thermal parameters should be analyzed before the optimization and only the sensitive ones can be estimated. The numerical heat transfer modeling of wall should be precisely built and adapted to the in situ conditions, such as the boundary condition.



# Chapter 5

## Terahertz Radiation Diagnostic Method

---

---

This chapter will propose a new NDE diagnostic method using terahertz (THz) radiation to penetrate building materials and characterize the absorption coefficient of each material. This THz radiation method will be proposed to combine with the step response method described in section 4.3 to provide complementary information.

### 5.1 Introduction

On one hand, more and more studies have been done over the past decades on the technologies exploiting THz radiation. Indeed, this frequency band has some remarkable properties and has been widely used in fields such as safety inspection, NDE, atmospheric physics, biology, military applications, ecology and medicine [111], [112]. In this research, THz radiation is used for characterizing the radiative absorption of non-metallic materials with low water content.



Absorption properties will be studied for a wide range of standard building materials. The main disadvantage is that this method is sensitive to the presence of dense materials, while it is less sensitive to the insulating materials. Therefore, it is difficult to distinguish the insulating materials in the wall, and it is also impossible to identify the position of each constituent of walls and the layer order because a complete tomography is difficult to carry out in situ in the case of multilayers.

On the other hand, as described in Chapter 4, the thermal probe method is sensitive to the presence of insulating materials, which make it possible to distinguish the order of layers in some cases and estimate the thermal resistance of insulation layers. However, it is difficult to estimate all the wall parameters simultaneously, such as thickness.

This chapter will show the preliminary experimental results of characterizing building materials by THz radiation, then the combination of the THz radiation method and thermal probe method will be discussed in order to propose a fast, NDE method for the thermal diagnosis of thick walls. A review of THz method has been described in section 1.2.4. The CW (Continuous-wave) THz method presented in this paper only yields intensity data and does not provide any depth (frequency-domain or time-domain information about the subject) when a fixed-frequency source and a single detector are used.

The absorbance of a material is determined by the emitted intensity of signal source and captured intensity by receptor based on the Beer-Lambert law (Equ. 5-1):

$$A = -\log_{10}\left(\frac{I_t}{I_0}\right) = \kappa L \tag{5-1}$$

Where  $A$  is the absorbance of material,  $I_0$  is the intensity of input signal (V),  $I_t$  is the intensity of output signal (V),  $\kappa$  is the absorption coefficient,  $L$  is the thickness of sample (m).

For multilayer samples (Fig. 5-1), the overall absorbance is the sum of absorbance for each layer (Equ. 5-2). The layers are assumed in perfect contact. According to Equ. 5-2, the layer order makes no influence on the overall absorbance.

$$A = -\log_{10}\left(\frac{I_t}{I_0}\right) = A_1 + A_2 + \dots + A_n = \kappa_1 L_1 + \kappa_2 L_2 + \dots + \kappa_n L_n \tag{5-2}$$

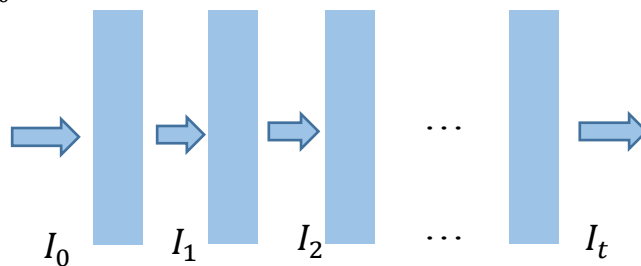


Fig. 5-1 Beer-Lambert law for multilayer materials

## 5.2 Experimental setup

CW-THz method system [71] is used in our measurement. As shown in Fig. 5-2, this system comprises a computer (to control the test conditions and record data), a THz source (producing a signal of 0.11 THz with power of 200 mW), a support (a frame for maintaining the materials), a controller (electronic control board and data acquisition) and a power supplier.

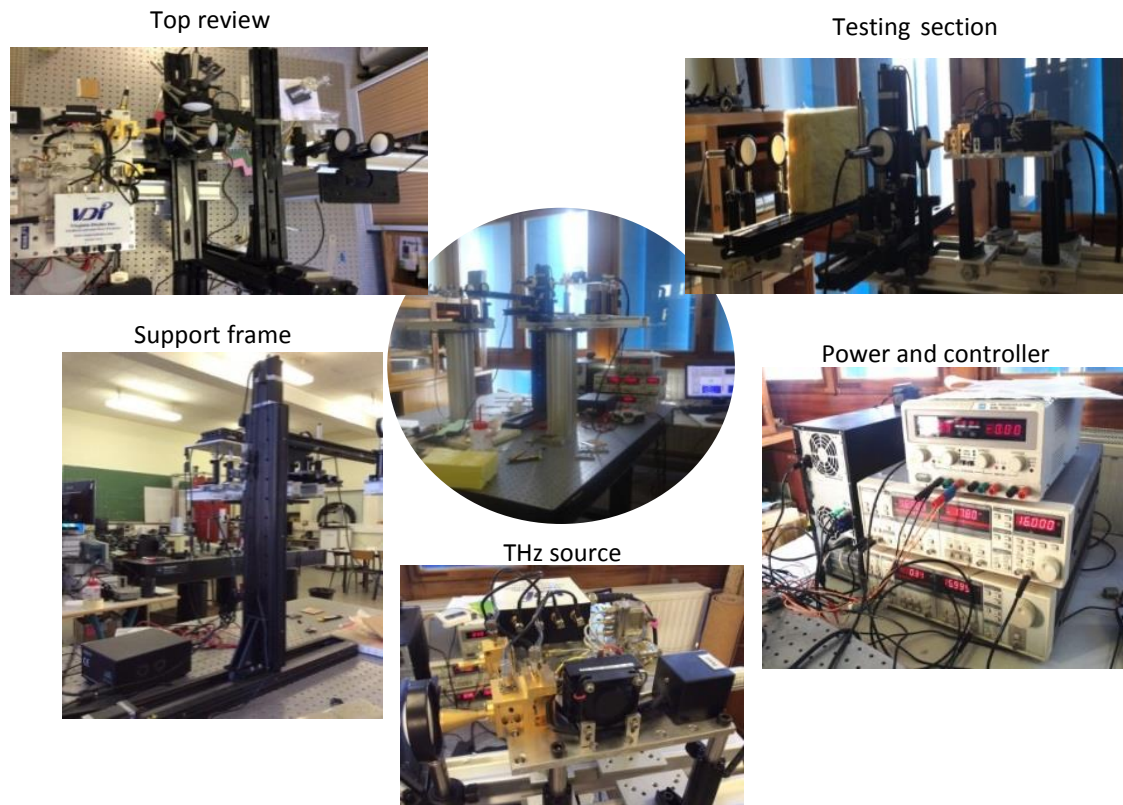


Fig. 5-2 The CW THz method system

The test section (see Fig. 5-3) includes a receptor sensor, lenses, a rotary shutter, a signal source and the sample. All these devices are aligned. The signal is modulated by a shutter which rotates at a frequency of 16 Hz. The angular resolution is limited by diffraction: the minimum resolution depends on the magnitude of wavelength.

A sample is fixed on the frame. The signal emitted by the THz source is focused on one point of the sample after passing through two Teflon lenses which are transparent for THz waves. Then this signal penetrates through the sample and is received by the receptor sensor. So that one point on the sample is tested. After, the frame moves one pixel (1 mm) away and the incident signal will focus on a new point of the sample to test. Therefore, a step-moving system has been built to test an area of 30×30 or 50×50 pixels. The absorption coefficient of each pixel is obtained by Equ. 5-1. 6 repetitive tests were carried out for the same area in order to ensure

## 5.2 Experimental setup

the reproducibility and reliability of the measurement. 15 samples of standard building materials (Fig. 5-4) have been tested, including dense materials and insulation materials.

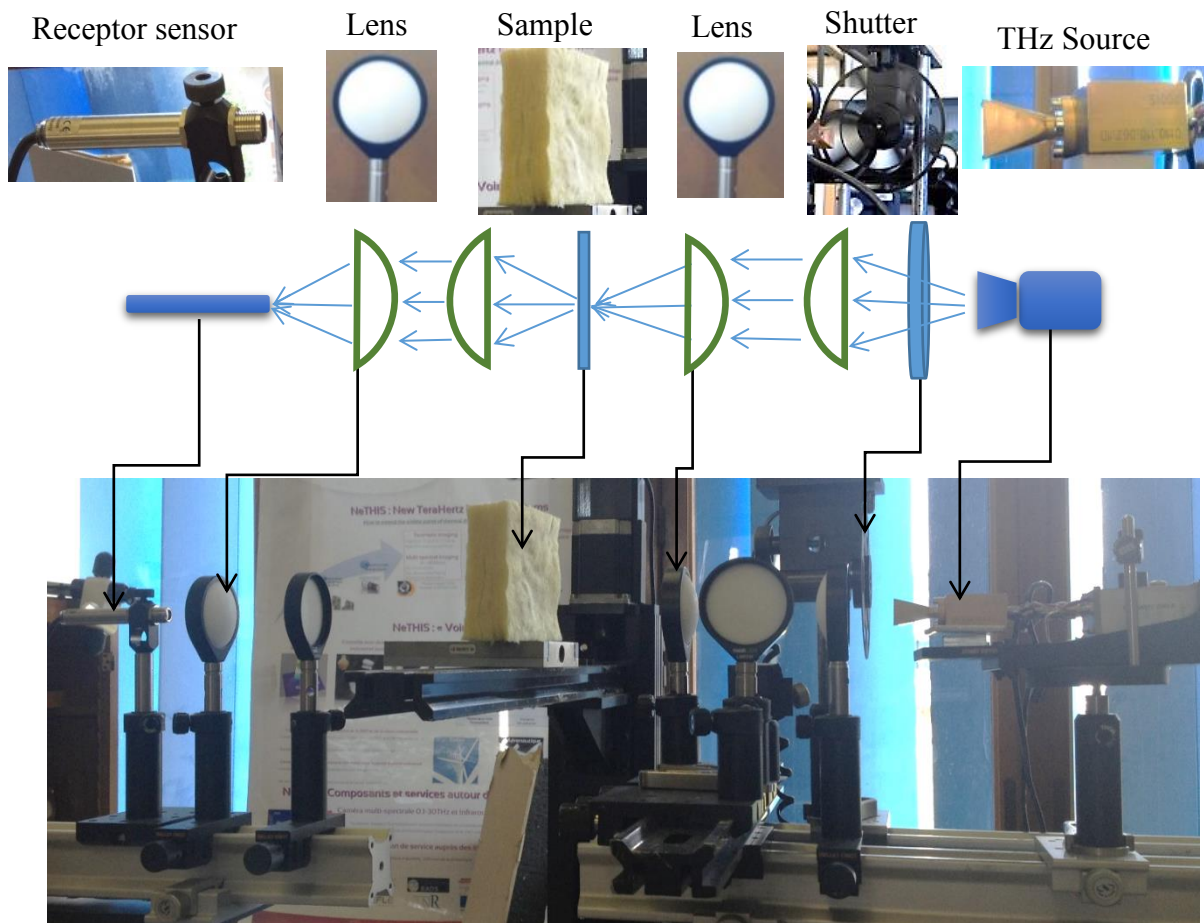
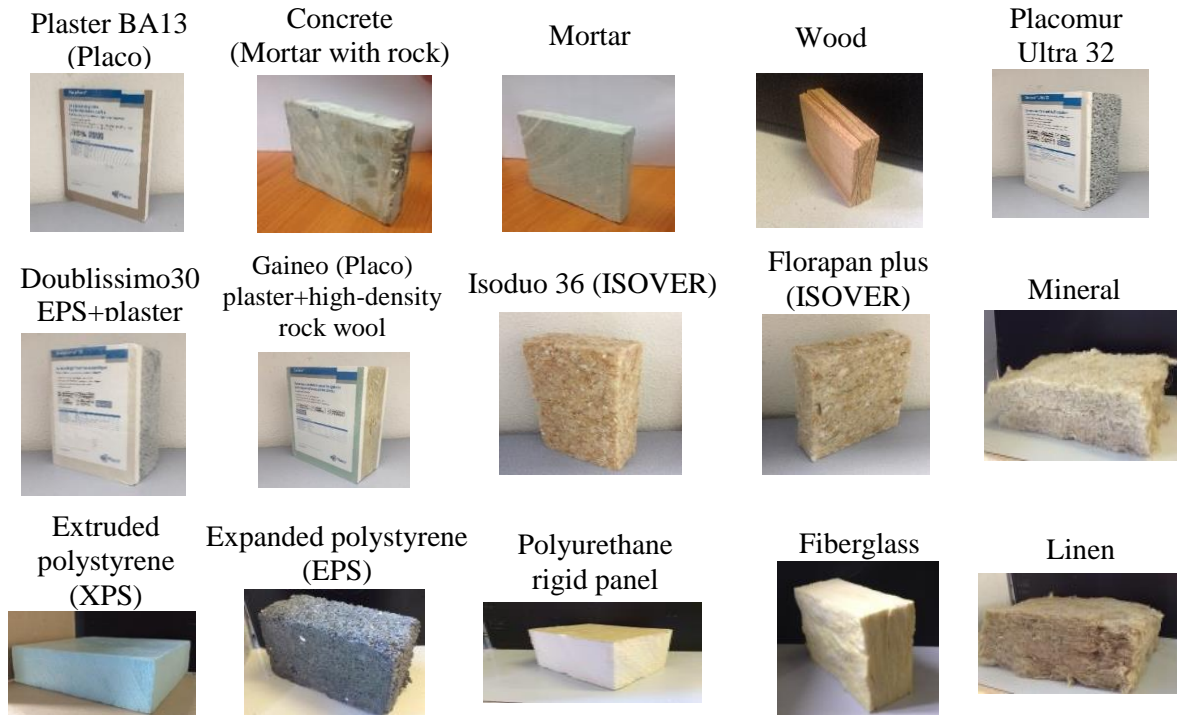


Fig. 5-3: Experimental setup

## 5.2 Experimental setup



**Remarks:** *Isoduo 36 is the combination of wood fiber and glass wool; Florapan plus is an insulating material made of hemp fibers, cotton and fusible polyester fibers (15%) for bonding. Placo and ISOVER are the names of manufacture.*

Fig. 5-4: Building materials tested by THz wave

In order to analyze the effect of water presence on concrete, wood and mortar, these samples were dried in an oven at 105 °C for 3 days and then sealed in vacuum box. The dried sample will be tested after cooling down (about 20 °C). For example, Fig. 5-5 is the dried concrete inside the vacuum box.

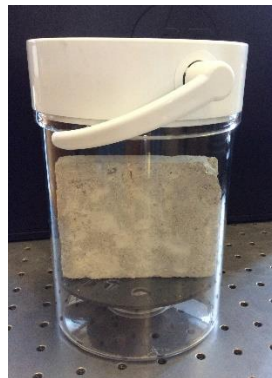


Fig. 5-5: Dried concrete in vacuum box.

## 5.3 Results and analysis

As far as we know, there is very few reference database on the optical properties of materials subjected to THz radiation. We have carried out these measurements in our laboratory to characterize the absorption coefficients of standard building materials.

Firstly, three examples of absorption coefficient map were chosen to analyze: extruded polystyrene (XPS), concrete and fiberglass. As shown in Fig. 5-6,  $x$  axis and  $y$  axis are the horizontal and vertical pixel numbers of the test area. The colour rendering is the field of absorption coefficient. The concrete has the largest absorption coefficients. Values for XPS and fiberglass are similar. XPS is relative homogeneous except the edge effect, while the concrete and fiberglass are not uniform. These non-uniformities are probably caused by uneven thickness, water content and the inhomogeneity of the material itself. These figures indicate that the THz imaging can show some defects inside the materials. The THz imaging can be effectively applied to the qualitative diagnosis of building materials. In this work, we have avoided the inhomogeneous samples to obtain a precise absorption coefficient.

Then, the absorptive properties results of all the 15 materials are given in Table 5-1.  $L$  is the thickness of sample. Thermal conductivities ( $\lambda$ ) are obtained from the manufacturer or reference [113], [114]. The absorption coefficient ( $\kappa$ ) is taken as the average value of all the pixels,  $\delta$  is the standard deviation when calculating this average value.

As shown in Table 5-1, all the tested materials are permeable to THz, even for materials with high density. The lower the absorption coefficient is, the more the materials are transparent to THz. THz radiation is less sensitive to the insulating materials. Some materials, for example, fiberglass and linen, have similar absorption coefficient. Thus, a measured value close to this absorption coefficient does not allow to distinguish fiberglass and linen. Conversely, other materials are readily distinguishable. For example, concrete has a very different characteristic from insulating materials. Since the measured coefficient of dry concrete is 38.19, the maximum thickness that is transparent to THz wave (if 1% intensity is transmitted) is about  $2 \times (1/38.19) = 5.2$  cm at 0.11 THz. However, the absorption coefficient also depends of source frequency, so applying higher power multi-spectral signal, with another range of wavelengths, can allow denser materials with a larger thickness to be transparent. Therefore, THz waves can potentially globally identify the nature of less transparent layers in a building wall.

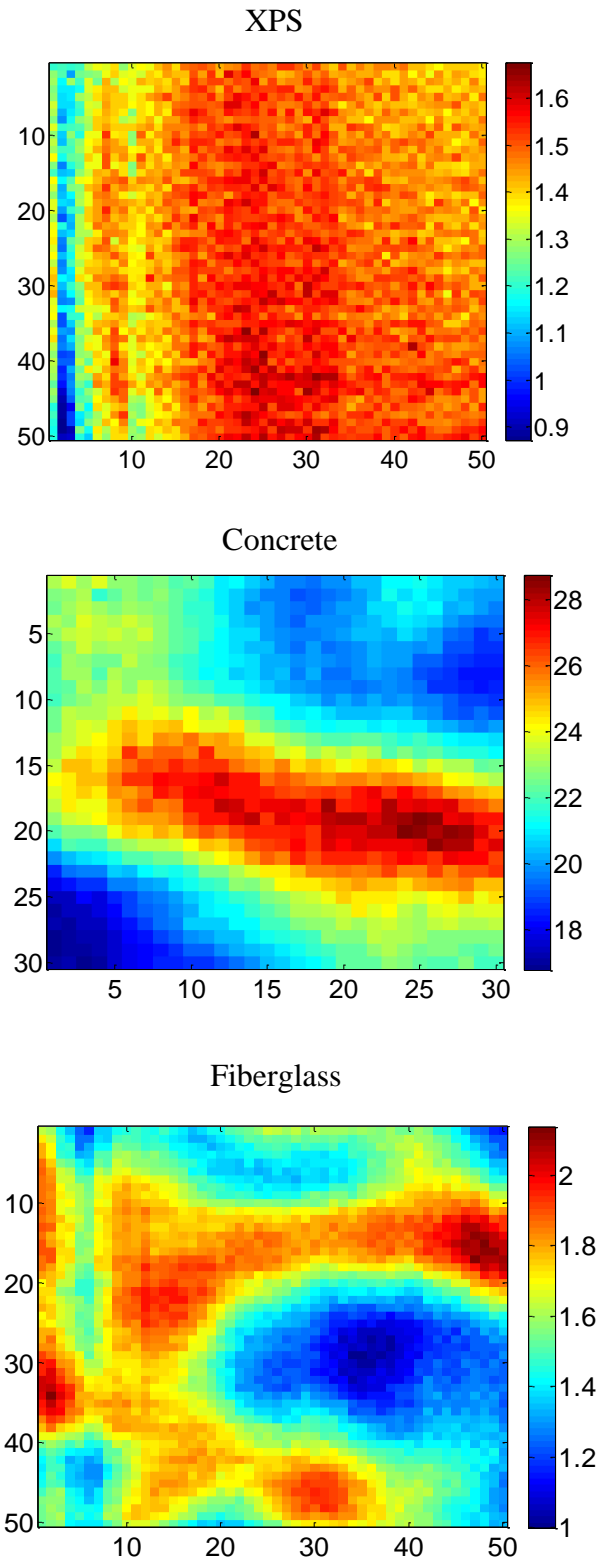


Fig. 5-6: Absorption coefficient results for XPS, plaster and fiberglass

### 5.3 Results and analysis

Table 5-1 Absorption coefficient results for 15 building materials

	$L(\text{cm})$	$\lambda$ ( $\text{W}\cdot\text{m}^{-1}\cdot\text{K}^{-1}$ )	$\kappa\pm\sigma$ ( $\text{m}^{-1}$ )
Plaster (BA13)	1.25	0.313	25.54±2.00
Concrete	1.83	1.4-2.9	96.14±13.87
Concrete (after drying)	1.83	1.4	38.19±5.74
Mortar	1.46	1.2-2.1	119.71±7.09
Mortar (after drying)	1.46	1.2	49.70±3.19
Wood	0.96	0.14-0.16	67.36±13.64
Wood (after drying)	0.96	0.14	48.22±6.76
Placomur Ultra 32	9.0 (1+8)	0.034	2.91±0.27
Doublissimo30	8.25(1.25+7)	0.030	4.13±0.37
Gaineo	7.0(1+5+1)	0.047	13.77±1.55
Isoduo 36	4.15	0.036	4.17±0.72
Florapan plus	4.03	0.041	3.72±0.40
Mineral wool	7.2	0.035-0.040	3.55±0.33
XPS	5.9	0.029	1.28±0.11
EPS	10	0.036	0.29±0.03
Polyurethane rigid panel	8.2	0.020-0.029	0.46±0.07
Fibergalss	10	0.050	1.74±0.19
Linen	7.2	0.036-0.042	1.83±0.47

Plasters with different thicknesses were characterized (Table 5-2). The absorption coefficients obtained were nearly constant within the uncertainty range when the thickness varies, which is in accordance with the Beer-Lambert law. Fig. 5-7 shows the linear fit of absorbance and thickness of samples, where the slope is the absorbance coefficient.

Table 5-2 Results of Plaster at different thickness

	$L(\text{cm})$	$A$	$\kappa (\text{m}^{-1})$
<i>Plaster (BA13)</i>	1.25	0.319±0.025	25.54±2.00
	2.50	0.720±0.097	28.79±3.89
	3.75	1.042±0.119	27.79±3.17
	5.00	1.29±0.107	25.75±2.13
	6.25	1.760±0.249	28.16±3.98

### 5.3 Results and analysis

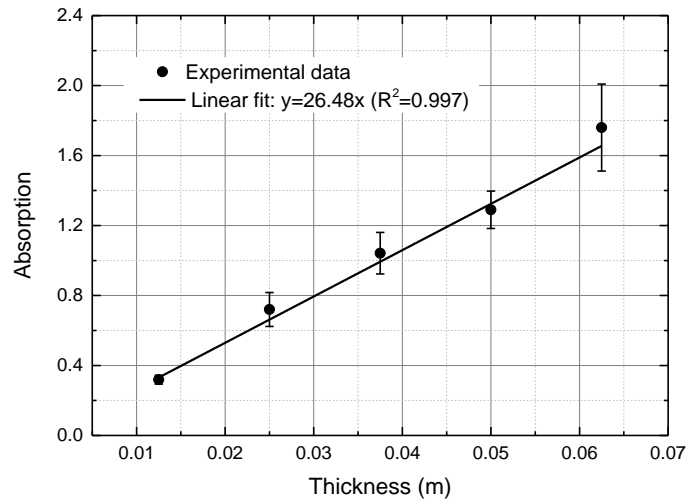


Fig. 5-7: Absorbance of plaster at different thickness

Multilayer samples were also tested and the results are shown in Table 5-3. The samples in each group use the same materials but in different layer orders. For example, in Group 1, the absorption coefficients for the two samples (IP and PI) are closed. The values in other groups present the similar phenomenon. The absorption coefficient does not depend on the structure of the samples (order of layers). The THz method is difficult to distinguish the structure and the position of the constituents in the case of a multilayer wall. Due to this drawback, the classical thermal probe method is analyzed in the next section in order to provide complementary information.

Table 5-3 Absorption coefficient for multilayer samples

	<i>Structure/thickness</i>	<i>L(cm)</i>	<i>A</i>	$\kappa (m^{-1})$
BA13 + Fiberglass	IP/5.3cm+2.5cm	7.8	0.675±0.078	8.65±1.00
	PI/2.5cm+5.3cm	7.8	0.656±0.070	8.41±0.89
	IP/5.3cm+1.25cm	6.55	0.376±0.030	5.74±0.46
	PI/1.25cm+5.3cm	6.55	0.300±0.035	4.57±0.53
	IP/4cm+2.5cm	6.5	0.722±0.025	11.10±0.38
	IPIP/2+1.25+2+1.25cm	6.5	0.957±0.123	14.73±1.90
Polystyrene + plaster	IP/10cm+1cm	11	0.259±0.014	2.35±0.13
	PI/1cm+10cm	11	0.329±0.033	2.99±0.30
Mineral wool +plaster	IP/3.6cm+2.5cm	6.1	0.642±0.031	10.52±0.50
	PI/2.5cm+3.6cm	6.1	0.738±0.018	12.10±0.29

(Where *I* is insulating materials, *P* is plaster; *IP* means the first layer is the insulating material; *PI* means the first layer is plaster. *IPIP* means the layers are separated equally)



## 5.4 Discussion of combination

Basing on the analysis of THz method and thermal probe method, we know that THz method is able to characterize dense layers of building walls, such as the concrete. While the thermal probe method can diagnose lightly insulating layer when this layer is near the front face. The combination of the two methods can provide a new efficient approach for thermal diagnosis of building walls.

For a multilayer concrete-supporting wall with unknown structure, firstly we can implement experiments of thermal probe method on this wall. This experiment needs to heat one surface of this wall and measure the temperature of the same surface (front face) to plot the temperature response curve. With the temperature response curve, the layer near front face can be analyzed if it is a concrete layer (highly effusive), a light insulating layer (resistance-dominated) or an insulating and slightly capacitive layer.

For example, in one case (case 1), if the measured temperature response curve is linear and the slope is relative low, performing similarly as curve of model 1 in Fig.4-19 (a) and Fig.4-20 (a), with a great possibility, the first layer is concrete (dense materials with highly effusivity). Else case (case 2), if the front temperature increases sharply at the beginning in a short time but becomes slowly and reaches to a stable slope period quickly, mostly the first layer of wall is light insulation. Thermal resistance of this layer can be estimated by the intercept of temperature curve in the stable slope period. Another case (case 3), if the temperature response performs at a middle level between case 1 and case 2, it means the layers that near the front face is both insulating and slightly capacitive. The transition time that curve turns into the stable slope period is characterized by  $R \cdot C$  (thermal resistance and heat capacity). According to this analysis, the layers near the front face of wall can be roughly predicted.

Similarly, temperature response curve of the opposite surface of wall can be obtained and analyzed in the same way. Since the thermal probe method is applied to each side of the wall, the wall structure can be more efficiently predicted, and the insulating layer can be identified and its thermal properties (thermal resistance and heat capacity) can be characterized.

After the preliminary analysis of wall structure, the overall absorption coefficient of THz radiation will be tested. The overall absorption coefficient is correlated with the materials of each layer and their thicknesses (Equ. 5-2), and is especially sensitive for dense materials (semi-transparent materials), so that we can improve the identification of material and thicknesses based on the preliminary analysis of wall structure and absorption coefficient database.

The preliminary results of this study are encouraging because the building materials we measured are sufficiently transparent to THz radiation (even for concrete and plaster). The THz imaging can be effectively applied to the qualitative diagnosis on building materials. The absorption coefficients of 15 materials were characterized. The same material with different thicknesses and multilayer samples with different layer order were measured as well. The THz method can potentially characterize the dense layers in a wall, however, it is less sensitive to the light insulating materials and it is not able to distinguish the structure and the position of the constituents in the multilayer cases.

Combining with the analysis of three typical multilayer wall models in section 4.3, the thermal probe method, which carried out in a reasonable time, can provide additional information on the position of each constituent of walls and their layer order by analyzing the temperature response curves when the wall is heated. The thermal resistance and heat capacity of light materials can be roughly estimated by the intercepts and slope trends of temperature response curves, which is an efficiently complement to the THz radiation method.

Therefore, both the dense materials and light insulating materials can be characterized by using these two methods together. The combined use of both methods is significant for the thermal diagnostic of thick walls. In the future, other terahertz sources of higher power will be applied in the experiments for characterizing these materials to improve the sensitivity of this method. More experiments of thermal probe method should be carried out. The combination of these two methods will be deeply analyzed and validated.



# Chapter 6

## Conclusion and perspectives

---

---

This work has focused on the thermal quantitative diagnosis methodologies of building walls. On one hand, experiments were carried out to investigate the utilization of sensors and instruments to provide some guidelines for the future measurement. On the other hand, the estimation approaches have been studied to estimate the thermal parameters using the wall surface heat flux and temperatures.

Firstly, a review of thermal diagnostic methods is made. Most of the standards and well developed methods are based on the steady-state heat transfer, for example, ISO 9869:2014 and ASTM C236. However, these methods need a very long characteristic time and the experimental conditions required are difficult to achieve in situ. More researches are needed for the transient techniques focusing on multi-layers heat transfer modeling. The application of infrared thermography (IRT) technique on the evaluation of wall is also a necessary trend because of its real time remote sensing globally. Other electromagnetic waves, such as THz radiation, can be applied to the NDE of wall to provide supplementary information. A new developing method should be precise, fast, non-contacted, less-cost, and fewer instruments which could be widely used.

Secondly, with the experiments carried out on two walls: one was tested in the laboratory by placing the heating source on the concrete layer side, the other was implemented in situ whose

insulation layer side was near the heating source. The emissivities of the wall and sensors were measured by the IR camera based on the standard ISO 18434. This measurement has been improved through an equation deduction. This emissivity calculation should use the data in the cooling period in order to avoid the influence of other radiance. The measurement is more accuracy and stable for high emissivity object, it is a good method to measure the emissivity of building materials (emissivity generally between 0.85-0.95). For the low emissivity objects, the reflected apparent temperature effect a lot during the measurement. The emissivity values are available only when there is a high temperature difference between the target surface and the ambient.

The heat flux that measured by heat flux sensors is not the value of wall heat flux because the emissivity and absorptivity of sensors are different with that of wall. Therefore, the wall heat flux was calculated indirectly according to the heat flux balance equation by using two heat flux sensors: one with shiny surface (shiny heat flux sensor) and the other painted black (black heat flux sensor). For each target surface, the total heat flux is the sum of total radiation and convection between the target and air. This total radiation involves the heat flux of ambient radiation, emittance radiation and reflective radiation by the target surface. Through this approach, the convection, radiation and total heat flux of wall and each sensor were split. The accuracy of wall heat flux has been improved by considering the ambient radiation, convection with air and emittance by itself, which has improved the thermal parameters consequently.

The innovative application of Peltier module as a heat flux sensor has been studied. According to the Seebeck effect, the presence of heating or cooling at an electric junction of two different conductors can be converted into an electrical signal, which will be detected as an output voltage. This theory is similar to the traditional heat flux sensor (Fluxmeter of Captec). All the sensors have been calibrated in laboratory. Peltier sensor is economical, more sensitive because of its high sensibility but the response time is longer. When measuring the heat flux with Peltier sensors, the convection coefficient of Peltier sensors is not the same with the wall due to the thickness of this sensor, which enhances the convection coefficient. The convection coefficient of wall should be obtained by other approaches, such as numerical model prediction.

The IR camera can also be used to measure the wall surface temperature and present a global scene of the test area. When using IR camera in generally way, the temperature measured by IR camera is not always the same with the temperature measured by thermocouples, especially for high temperatures in the heating period. This is because the reflected temperature is set as a constant value. While, during the heating period, the reflected temperature increases obviously. This work used an improved calculation approach to solve this problem. This reflected temperature was measured by a crumpled aluminum. The wall surface temperature was re-calculated by correcting the reflected temperature. The wall surface temperature that

calculated by this new approach has a good agreement with the temperature from thermocouples.

This work has analyzed the methods of thermography processing. In order to analyze the characteristic properties by observing numerous IR images directly, the SVD algorithm is applied to reduce the matrix  $M$  to a compact statistical expression in order to describe the spatial variations and temporal variations. This method is based on the principal component thermography (PCT) technology. The thermographic 3D matrix can be rearranged as a 2D matrix with time along the columns and space. After applying the SVD to the 2D matrix, the resulting  $U$  matrix, which provides the spatial information, can be rearranged as a 3D sequence. The first mode ( $U_1$  and  $w_1 \times V_1^t$ ) represents the global dynamic behavior of the data set: the special variation described by  $U_1$  and the temporal variation described by  $w_1 \times V_1^t$ . This temporal variation is corresponding to the temperature response. For the second and third mode,  $w_2 \times V_2^t$  and  $w_3 \times V_3^t$  are much lower than  $w_1 \times V_1^t$ , which means the second and third mode are the corrections of the global behavior. Generally, this processing approach is efficient to the qualitative diagnosis on a complex surface to highlight the obvious abnormal behavior.

Thirdly, with the wall heat flux and surface temperature, three estimation approaches are proposed to characterize the thermal parameters of wall: pulse response curve method, step response curve method and inverse method. All these methods are based on a thermal quadrupoles solution. Two multilayer walls formed by mortar, concrete block, insulation material and plaster board were tested. This structure of the two walls has been widely used in the concrete-supporting walls with insulation materials inside. The concrete block and insulation materials are the effective layers in the wall, while the mortar and plaster board are the layers to provide protection, which have lightly influence on the thermal performance of the wall. Results of two cases were analyzed: the heating source on the concrete layer side or on the insulation layer side.

For inverse method, the numerical modeling for multi-layer wall was built with the known information of the wall structures and thicknesses. The input parameters of optimization system are: heat flux, front face or rear face temperature and thickness. The thermal conductivity and heat capacity of concrete layer are sensitive and can be estimated when the heating source is on the concrete layer, the thermal conductivity of insulation can be obtained when the insulation layer was near the heating source.

When the wall structure is unknown, the step response curve method was suggested. Semi-infinite boundary condition at the rear face is assumed in this method. The heat flux should be close to a constant value. This method can only roughly estimate some highly sensitive parameters. For semi-infinite condition, the thermal resistance of insulation layer is estimated when the insulation layer is near the heating source, the thermal effusivity of concrete is

obtained when the concrete layer is near the heating source. This method can also identify the layer orders by comparing the tests at both faces of wall (identify which face is concrete or insulation).

If the heat flux is not constant and the wall structure is unknown, the pulse response curve method was proposed. With the wall heat flux and surface temperature, the pulse response curve can be obtained through a deconvolution calculation. This pulse response curve is directly characterized by the thermal parameters. Plotting in the logarithmic axis amplifies the characterization and make it easy to analyze the thermal parameters. The pulse responses of simulation and experiments were compared. The experimental pulse response results are encouraging and the analysis is preliminary. When the heating source is on the concrete layer, at a semi-infinite condition, the pulse response is a linear curve characterized by the thermal effusivity of concrete. So this thermal effusivity were estimated by the linear fitting of the experimental data. The estimation results for the laboratory case is promising. A global thermal effusivity was obtained with a high accuracy. In the future, more analyses are needed on this pulse response curve to obtain other thermal properties quantitatively. More experiments should be carried out on the building walls in situ to repeat the application of the sensors and validate the three estimation methods.

Finally, a new NDE diagnostic method using THz radiation was proposed. 15 building materials were tested. The materials tested were sufficiently transparent to THz radiation (concrete and plaster). The THz images can be also effectively applied to the qualitative diagnosis on building materials. The THz method can potentially identify the dense layer and thickness of this layer in a wall, however, it is less sensitive to the light insulating materials and it is not able to distinguish the structure and the position of the constituents in the multilayer cases. The THz method can be combined with the previously three methods to provide additional information for the wall diagnosis. In the future, other terahertz sources of higher power should be applied in the experiments to improve the sensitivity of this method. The combination with the thermal methods will be deeply analyzed and validated.

Additional works need to be done in the future in order to form an accurate, fast, convenient and widely used diagnostic method for building envelopes. We will continue study the pulse and step response methods. IR camera should be further studied and extended applied to achieve a goal of non-contact diagnosis. The thermal image will be processed in 3D to detect the structures and defects such as thermal bridge. Passive measurements (without artificial heating source) should be carried out and analyzed by these methods proposed in this research. Multi-spectral THz sources should be applied. Other tomography technologies should also be considered and explored for the thick walls.

# Bibliography

---

---

- [1] “Word Energy Perspectives-Energy efficiency 2016, WORLD ENERGY COUNCIL.” .
- [2] L. Pérez-Lombard, J. Ortiz, and C. Pout, “A review on buildings energy consumption information,” *Energy Build.*, vol. 40, no. 3, pp. 394–398, Jan. 2008.
- [3] “Technology roadmap-energy efficient building envelops.” International Energy Agency, 2013.
- [4] “U.S. Energy Information Administration, International Energy Outlook 2013, [www.eia.gov/ieo/](http://www.eia.gov/ieo/).” Jul-2013.
- [5] Eurostat, “Energy, transport and environment indicators (2011). Available at: <http://ec.europa.eu/eurostat/documents/3930297/5966062/KS-DK-11-001-EN.PDF/a1caaacc-1f22-42fc-8bab-93d0f808ea75?version=1.0> (Accessed 17 November 2016).” .
- [6] International Energy Agency, “Transition to Sustainable Buildings – Strategies and Opportunities to 2050 – Executive Summary (2013). Available at: <http://www.iea.org/Textbase/npsum/building2013SUM.pdf> (Accessed 17 November 2016).”
- [7] “2011 Building energy data book, United States Department of Energy.” .
- [8] B. Yesilata and P. Turgut, “A simple dynamic measurement technique for comparing thermal insulation performances of anisotropic building materials,” *Energy Build.*, vol. 39, no. 9, pp. 1027–1034, Sep. 2007.
- [9] “ISO 8302:1991, Thermal insulation — Determination of steady-state thermal resistance and related properties — Guarded hot plate apparatus.” .
- [10] “ASTM C518 – Standard Test Method for Steady-State Thermal Transmission Properties by Means of the Heat Flow Meter Apparatus.” .
- [11] “ISO 8301:1991, Thermal insulation — Determination of steady-state thermal resistance and related properties — Heat flow meter apparatus.” .
- [12] “ISO 8990:1994 Preview Thermal insulation -- Determination of steady-state thermal transmission properties -- Calibrated and guarded hot box.” .
- [13] F. Asdrubali and G. Baldinelli, “Thermal transmittance measurements with the hot box method: Calibration, experimental procedures, and uncertainty analyses of three different approaches,” *Energy Build.*, vol. 43, no. 7, pp. 1618–1626, Jul. 2011.
- [14] “L. Kubicar, C. Bohac .review of several dynamic method of measuring thermal physical parameters.135-149. Thermal Conductivity 24/Thermal Expansion 12.”
- [15] V. Bohác and others, “A step-wise method for measuring thermophysical parameters of materials,” *Meas. Sci. Technol.*, vol. 11, no. 3, p. 252, 2000.



- 
- [16] M. J. Assael, M. Dix, K. Gialou, L. Vozar, and W. A. Wakeham, "Application of the transient hot-wire technique to the measurement of the thermal conductivity of solids," *Int. J. Thermophys.*, vol. 23, no. 3, pp. 615–633, 2002.
- [17] S. E. Gustafsson, M. A. Chohan, K. Ahmed, and A. Maqsood, "Thermal properties of thin insulating layers using pulse transient hot strip measurements," *J. Appl. Phys.*, vol. 55, no. 9, p. 3348, 1984.
- [18] W. J. Parker, R. J. Jenkins, C. P. Butler, and G. L. Abbott, "Flash Method of Determining Thermal Diffusivity, Heat Capacity, and Thermal Conductivity," *J. Appl. Phys.*, vol. 32, no. 9, p. 1679, 1961.
- [19] G. Wei, X. Zhang, F. Yu, and K. Chen, "Thermal Diffusivity Measurements on Insulation Materials with the Laser Flash Method," *Int. J. Thermophys.*, vol. 27, no. 1, pp. 235–243, Jan. 2006.
- [20] J. Xue and R. Taylor, "An evaluation of specific heat measurement methods using the laser flash technique," *Int. J. Thermophys.*, vol. 14, no. 2, pp. 313–320, 1993.
- [21] A. Ahmad, M. Maslehuddin, and L. M. Al-Hadhrami, "In situ measurement of thermal transmittance and thermal resistance of hollow reinforced precast concrete walls," *Energy Build.*, vol. 84, pp. 132–141, Dec. 2014.
- [22] "ISO 9869-1:2014:Thermal insulation-Building elements- in-situ measurement of thermal resistance and thermal transmittance-art 1: Heat flow meter method." .
- [23] American Society for Testing and Materials, "ASTM C236-89: Standard test method for steady-state thermal performance of building assemblies by means of a guarded hot box," *West Conshohocken*, vol. 04.06, PA 2001.
- [24] B. Abad, D.-A. Borca-Tasciuc, and M. S. Martin-Gonzalez, "Non-contact methods for thermal properties measurement," *Renew. Sustain. Energy Rev.*, vol. 76, pp. 1348–1370, Sep. 2017.
- [25] I. Naveros, M.J. Jimenez, and M.R. Heras, "Analysis of capabilities and limitations of the regression method based in averages, applied to the estimation of the U value of building component tested in Mediterranean weather," *Energy Build.*, vol. 55, pp. 854–872, 2012.
- [26] V. Richalet, F.P. Neirac, F. Tellez, and J. Marco, "house energy labelling procedure: methodology and present results," *Energy Build.*, vol. 33, pp. 229–233, 2001.
- [27] J.J. Bloem and S. Martin, "A pseudo dynamic analysis tool for thermal certification of dwellings," *Energy Build.*, vol. 33, pp. 207–212, 2001.
- [28] C. Peng and Z. Wu, "In situ measuring and evaluating the thermal resistance of building construction," *Energy Build.*, vol. 40, no. 11, pp. 2076–2082, Jan. 2008.
- [29] G. Desogus, S. Mura, and R. Ricciu, "Comparing different approaches to in situ measurement of building components thermal resistance," *Energy Build.*, vol. 43, no. 10, pp. 2613–2620, Oct. 2011.
- [30] L. F. Cabeza, A. Castell, M. Medrano, I. Martorell, G. Pérez, and I. Fernández, "Experimental study on the performance of insulation materials in Mediterranean construction," *Energy Build.*, vol. 42, no. 5, pp. 630–636, May 2010.

- 
- [31] G. Ficco, F. Iannetta, E. Ianniello, F. R. d'Ambrosio Alfano, and M. Dell'Isola, "U-value in situ measurement for energy diagnosis of existing buildings," *Energy Build.*, vol. 104, pp. 108–121, Oct. 2015.
- [32] T. Nussbaumer, K. G. Wakili, and C. Tanner, "Experimental and numerical investigation of the thermal performance of a protected vacuum-insulation system applied to a concrete wall," *Appl. Energy*, vol. 83, no. 8, pp. 841–855, Aug. 2006.
- [33] P. R. Achenbach, "Design of a calibrated hot-box for measuring the heat, air, and moisture transfer of composite building walls," *Therm. Perform. Exter. Envel. Build. Proc.-1*, pp. 308–324, 1981.
- [34] R.R. Zarr, D.M. Burch, T.K. Faison, C.E. Arnold, "Thermal resistance measurements of well-insulated and superinsulated residential walls using a calibrated hot box," *ASHRAE Trans.*, vol. 96, pp. 604–619, 1986.
- [35] "ASTM C1363-11:Standard Test Method for Thermal Performance of Building Materials and Envelope Assemblies by Means of a Hot Box Apparatus."
- [36] C. Maierhofer, A. Brink, M. Röllig, and H. Wiggenger, "Quantitative impulse-thermography as non-destructive testing method in civil engineering – Experimental results and numerical simulations," *Constr. Build. Mater.*, vol. 19, no. 10, pp. 731–737, Dec. 2005.
- [37] K. Chaffar, A. Chauchois, D. Defer, and L. Zalewski, "Thermal characterization of homogeneous walls using inverse method," *Energy Build.*, vol. 78, pp. 248–255, Aug. 2014.
- [38] J. Berger, H. R. B. Orlande, N. Mendes, and S. Guernouti, "Bayesian inference for estimating thermal properties of a historic building wall," *Build. Environ.*, vol. 106, pp. 327–339, Sep. 2016.
- [39] M. Hafid and M. Lacroix, "Inverse heat transfer prediction of the state of the brick wall of a melting furnace," *Appl. Therm. Eng.*, vol. 110, pp. 265–274, Jan. 2017.
- [40] S. Van Dessel and B. Foubert, "Active thermal insulators: Finite elements modeling and parametric study of thermoelectric modules integrated into a double pane glazing system," *Energy Build.*, vol. 42, no. 7, pp. 1156–1164, Jul. 2010.
- [41] J. Peng, L. Lu, H. Yang, and J. Han, "Investigation on the annual thermal performance of a photovoltaic wall mounted on a multi-layer façade," *Appl. Energy*, vol. 112, pp. 646–656, Dec. 2013.
- [42] Denis Maillet, Stephane Andre, Jean-Christophe Batsale, Alain Degiovanni, and Christian Moyne, *Thermal Quadrupoles: Solving the Heat Equation through Integral Transforms*. John Wiley & Sons Ltd, 2000.
- [43] Tingting Vogt-WU, "Formalisme des impedances thermiques généralisées. Application à la caractérisation thermique de parois de batiments," Thèse de Doctorat, Béthune, 2011.
- [44] V. Feuillet, L. Ibos, M. Fois, J. Dumoulin, and Y. Candau, "Defect detection and characterization in composite materials using square pulse thermography coupled with singular value decomposition analysis and thermal quadrupole modeling," *NDT E Int.*, vol. 51, pp. 58–67, Oct. 2012.

- [45] B. Remy and A. Degiovanni, "Parameters estimation and measurement of thermophysical properties of liquids," *Int. J. Heat Mass Transf.*, vol. 48, no. 19–20, pp. 4103–4120, Sep. 2005.
- [46] L. Cattani, D. Maillet, F. Bozzoli, and S. Rainieri, "Estimation of the local convective heat transfer coefficient in pipe flow using a 2D thermal Quadrupole model and Truncated Singular Value Decomposition," *Int. J. Heat Mass Transf.*, vol. 91, pp. 1034–1045, Dec. 2015.
- [47] N. Laaroussi, G. Lauriat, M. Garoum, A. Cherki, and Y. Jannot, "Measurement of thermal properties of brick materials based on clay mixtures," *Constr. Build. Mater.*, vol. 70, pp. 351–361, Nov. 2014.
- [48] D. Defer, J. Shen, S. Lassue, and B. Duthoit, "Non-destructive testing of a building wall by studying natural thermal signals," *Energy Build.*, vol. 34, no. 1, pp. 63–69, 2002.
- [49] Albert TARANTOLA, *Inverse Problem Theory-and Method for model parameters estimation*. 2005.
- [50] M. Necati Ozisik and Helcio R. B. Orlande, *Inverse heat transfer-Fundamentals and applications*. Taylor&Francis, 2000.
- [51] R. Kramer, J. van Schijndel, and H. Schellen, "Inverse modeling of simplified hygrothermal building models to predict and characterize indoor climates," *Build. Environ.*, vol. 68, pp. 87–99, Oct. 2013.
- [52] Y. Wang, J. Kuckelkorn, F.-Y. Zhao, H. Spliethoff, and W. Lang, "A state of art of review on interactions between energy performance and indoor environment quality in Passive House buildings," *Renew. Sustain. Energy Rev.*, vol. 72, pp. 1303–1319, May 2017.
- [53] Y. Luo, L. Zhang, Z. Liu, Y. Wang, F. Meng, and J. Wu, "Thermal performance evaluation of an active building integrated photovoltaic thermoelectric wall system," *Appl. Energy*, vol. 177, pp. 25–39, Sep. 2016.
- [54] Y. Zhang, Z. O'Neill, B. Dong, and G. Augenbroe, "Comparisons of inverse modeling approaches for predicting building energy performance," *Build. Environ.*, vol. 86, pp. 177–190, Apr. 2015.
- [55] S. Grieu, O. Faugeroux, A. Traoré, B. Claudet, and J.-L. Bodnar, "Artificial intelligence tools and inverse methods for estimating the thermal diffusivity of building materials," *Energy Build.*, vol. 43, no. 2–3, pp. 543–554, Feb. 2011.
- [56] R. P. Niu, G. R. Liu, and M. Li, "Inverse analysis of heat transfer across a multilayer composite wall with Cauchy boundary conditions," *Int. J. Heat Mass Transf.*, vol. 79, pp. 727–735, Dec. 2014.
- [57] A. Moftakhari, F. Torabi, and C. Aghanajafi, "A novel energy simulation approach for thermal design of buildings equipped with radiative panels using inverse methodology," *Energy Build.*, vol. 113, pp. 169–181, Feb. 2016.
- [58] R. Derbal, D. Defer, A. Chauchois, and E. Antczak, "A simple method for building materials thermophysical properties estimation," *Constr. Build. Mater.*, vol. 63, pp. 197–205, Jul. 2014.

- [59] A. J. Robinson *et al.*, “A new transient method for determining thermal properties of wall sections,” *Energy Build.*, vol. 142, pp. 139–146, May 2017.
- [60] A. Rasooli, L. Itard, and C. I. Ferreira, “A response factor-based method for the rapid in-situ determination of wall’s thermal resistance in existing buildings,” *Energy Build.*, vol. 119, pp. 51–61, May 2016.
- [61] C. A. Balaras and A. A. Argiriou, “Infrared thermography for building diagnostics,” *Energy Build.*, vol. 34, no. 2, pp. 171–183, 2002.
- [62] A. Taileb and H. Dekkiche, “Infrared Imaging as a Means of Analyzing and Improving Energy Efficiency of Building Envelopes: The case of a LEED Gold Building,” *Procedia Eng.*, vol. 118, pp. 639–646, 2015.
- [63] F. Bisegna, D. Ambrosini, D. Paoletti, S. Sfarra, and F. Gugliermetti, “A qualitative method for combining thermal imprints to emerging weak points of ancient wall structures by passive infrared thermography – A case study,” *J. Cult. Herit.*, vol. 15, no. 2, pp. 199–202, Mar. 2014.
- [64] R. Plesu, G. Teodoriu, and G. Taranu, “Infrared thermography applications for building investigation,” *Bul. Institutului Politeh. Din Lasi Sect. Constr. Arhit.*, vol. 58, no. 1, p. 157, 2012.
- [65] Xavier Maldague, “Trends in Optical Nondestructive Testing (invited chapter),” *Pramod Rastogi Ed*, pp. 591–609, 2000.
- [66] Xavier Maldague, “Nondestructive evaluation of materials by infrared thermography.” John Wiley & SonsPub, 2001.
- [67] Xavier Maldague, “Infrared Methodology and Technology.” 1994.
- [68] A. Kylili, P. A. Fokaidis, P. Christou, and S. A. Kalogirou, “Infrared thermography (IRT) applications for building diagnostics: A review,” *Appl. Energy*, vol. 134, pp. 531–549, Dec. 2014.
- [69] N.P. Avdelidis, T-H. Gan, and C. Ibarra-Castanedo, “Infrared thermography as a non-destructive tool for materials characterisation and assessment,” presented at the Thermal Infrared Applications XXXIII, Orlando, Florida, USA, 2011, pp. 26–28.
- [70] R. Albatici and A. M. Tonelli, “Infrared thermovision technique for the assessment of thermal transmittance value of opaque building elements on site,” *Energy Build.*, vol. 42, no. 11, pp. 2177–2183, Nov. 2010.
- [71] N. Karpowicz, H. Zhong, J. Xu, K.-I. Lin, J.-S. Hwang, and X.-C. Zhang, “Comparison between pulsed terahertz time-domain imaging and continuous wave terahertz imaging,” *Semicond. Sci. Technol.*, vol. 20, no. 7, pp. S293–S299, Jul. 2005.
- [72] M. L. Youcef, V. Feuillet, L. Ibos, Y. Candau, P. Balcon, and A. Filloux, “In situ quantitative diagnosis of insulated building walls using passive infrared thermography,” in *Proceedings of the 11th international conference on quantitative infrared thermography. Naples Italy*, 2012.
- [73] J.-P. Monchau, L. Ibos, and V. Feuillet, “Diagnosis of insulated building walls using passive infrared thermography and numerical simulations,” in *EWSHM-7th European Workshop on Structural Health Monitoring*, 2014.

- [74] B. Więcek and M. Poksińska, "Passive and active thermography application for architectural monuments," in *8th Conference on Quantitative Infrared Thermography–QIRT*, 2006.
- [75] P.D. Pastuszak and A. Muc, "Methods of infrared non-destructive techniques: review and experimental studies," *Key Eng. Mater.*, vol. 542, pp. 131–141, 2013.
- [76] Michael Shur, "Terahertz technology: devices and applications," *Proc. ESSCIRC*, pp. 13–21, 2005.
- [77] K. Tribikram, "Chapter 15," in *Ultrasonic and Electromagnetic NDE for Structure and Material Characterization: Engineering and Biomedical Applications*, Presses CRC, 2012.
- [78] E. K. Rahani, T. Kundu, Z. Wu, and H. Xin, "Heat Induced Damage Detection by Terahertz (THz) Radiation," *J. Infrared Millim. Terahertz Waves*, vol. 32, no. 6, pp. 848–856, Jun. 2011.
- [79] E. K. Rahani, T. Kundu, Z. Wu, and H. Xin, "Mechanical Damage Detection in Polymer Tiles by THz Radiation," *IEEE Sens. J.*, vol. 11, no. 8, pp. 1720–1725, Aug. 2011.
- [80] C. D. Stoik, M. J. Bohn, and J. L. Blackshire, "Nondestructive evaluation of aircraft composites using transmissive terahertz time domain spectroscopy," *Opt. Express*, vol. 16, no. 21, pp. 17039–17051, 2008.
- [81] M. Naftaly and R. E. Miles, "Terahertz Time-Domain Spectroscopy for Material Characterization," *Proc. IEEE*, vol. 95, no. 8, pp. 1658–1665, Aug. 2007.
- [82] A. Abina, U. Puc, A. Jeglič, and A. Zidanšek, "Structural analysis of insulating polymer foams with terahertz spectroscopy and imaging," *Polym. Test.*, vol. 32, no. 4, pp. 739–747, Jun. 2013.
- [83] A. Abina, U. Puc, A. Jeglič, and A. Zidanšek, "Structural characterization of thermal building insulation materials using terahertz spectroscopy and terahertz pulsed imaging," *NDT E Int.*, vol. 77, pp. 11–18, Jan. 2016.
- [84] R. Piesiewicz, C. Jansen, S. Wietzke, D. Mittleman, M. Koch, and T. Kürner, "Properties of Building and Plastic Materials in the THz Range," *Int. J. Infrared Millim. Waves*, vol. 28, no. 5, pp. 363–371, Apr. 2007.
- [85] A. Costanzo, M. Minasi, G. Casula, M. Musacchio, and M. Buongiorno, "Combined Use of Terrestrial Laser Scanning and IR Thermography Applied to a Historical Building," *Sensors*, vol. 15, no. 1, pp. 194–213, Dec. 2014.
- [86] Y. Oyama, L. Zhen, T. Tanabe, and M. Kagaya, "Sub-terahertz imaging of defects in building blocks," *NDT E Int.*, vol. 42, no. 1, pp. 28–33, Jan. 2009.
- [87] Byrnes, James, *Unexploded Ordnance Detection and Mitigation*. Springer, 2009.
- [88] FLIR, "The ultimated infrared handbook for R&D professionals: [http://www.flirmedia.com/MMC/THG/Brochures/T559243/T559243\\_EN.pdf](http://www.flirmedia.com/MMC/THG/Brochures/T559243/T559243_EN.pdf)."
- [89] Richard M. Park, "Thermocouple Fundamentals: <http://www.advindsys.com/ApNotes/tcfundamentals.pdf>."

- [90] “CAPTEC SCIENTIFIC CATALOGUE: [http://www.techno-office.com /file/captec-scientific-catalog.pdf](http://www.techno-office.com/file/captec-scientific-catalog.pdf).” .
- [91] “Thermoelectric cooling: [https://en.wikipedia.org/wiki/Thermoelectric\\_cooling](https://en.wikipedia.org/wiki/Thermoelectric_cooling).” .
- [92] “RÈGLES Th-U FASCICULE 2 : MATÉRIAUX :<http://www.panseo.fr/wp-content/uploads/2011/05/Table-RT2005-Conductivit%C3%A9-thermique-des-mat%C3%A9riaux.pdf>.” .
- [93] “HEAT CAPACITY (HC) VALUES FOR CONCRETE MASONRY WALLS: <http://www.ncma-br.org/pdfs/5/TEK%2006-16A.pdf>.” .
- [94] “HEAT, AIR, AND MOISTURE CONTROL IN BUILDING ASSEMBLIES— MATERIAL PROPERTIES: <http://edge.rit.edu/content/C09008/public/2009%20ASHRAE%20Handbook>.” .
- [95] “Tungsten-halogen lamp information at Karl Zeiss Online Campus site (accessed Nov. 2 2010).”
- [96] Neumann G.M., “Betriebgesteue der Halogenglühlampe Lichttechnik,” vol. 21(6), p. 63A–65A.
- [97] M. Necati Ozisik, *Heat transfer: A basic approach* . .
- [98] R. Usamentiaga, P. Venegas, J. Guerediaga, L. Vega, J. Molleda, and F. Bulnes, “Infrared Thermography for Temperature Measurement and Non-Destructive Testing,” *Sensors*, vol. 14, no. 7, pp. 12305–12348, Jul. 2014.
- [99] Yunus A. Cengel, *Heat and mass transfer* . .
- [100] Churchill, S.W. and H. H. Chu, “correlating equations for laminar and turbulent free convection from a vertical plate,” *Int J Heat Mass Transf.*, vol. 18:1323, 1975.
- [101] Per Christian Hansen, “The truncated SVD as a method for regularization,” *BIT*, vol. 27, pp. 534–553, 1987.
- [102] P. C. Hansen, “Analysis of discrete ill-posed problems by means of the  $L$ -curve,” *SIAM Rev. I*, vol. 34(4), pp. 561–580, 1992.
- [103] N. Rajic, “Principal component thermography for flaw contrast enhancement and flaw depth characterisation in composite structures,” *Compos. Struct.*, vol. 58, no. 4, pp. 521–528, 2002.
- [104] S. Marinetti *et al.*, “Statistical analysis of IR thermographic sequences by PCA,” *Infrared Phys. Technol.*, vol. 46, no. 1–2, pp. 85–91, Dec. 2004.
- [105] Ibarra Castanedo, González, D, Galmiche, F., Maldague, X. P., and Bendada, A., “Discrete signal transforms as a tool for processing and analyzing pulsed thermographic data,” *Proc. SPIE*, vol. 6205, 2006.
- [106] David C. Lay, Steven R. Lay, and Judi J. McDonald, *Linear algebra and its applications* . .
- [107] V. A. Morozov, *Methods for Solving Incorrectly Posed Problems*. 1984.
- [108] D. Garcia Sanchez, B. Lacarrière, M. Musy, and B. Bourges, “Application of sensitivity analysis in building energy simulations: Combining first- and second-order elementary effects methods,” *Energy Build.*, vol. 68, pp. 741–750, Jan. 2014.

- [109] D. Marquardt, “An algorithm for least-squares estimation of nonlinear parameters,” *SIAM J Appl Math*, vol. 11, p. . 431–441, 1963.
- [110] K. Levenberg, “A method for the solution of certain problems in least squares,” *Quart Appl Math*, vol. 2, pp. 164–168, 1944.
- [111] P. U. Jepsen, D. G. Cooke, and M. Koch, “Terahertz spectroscopy and imaging - Modern techniques and applications,” *Laser Photonics Rev.*, vol. 5, no. 1, pp. 124–166, Jan. 2011.
- [112] D. Dufour *et al.*, “Review of terahertz technology development at INO,” *J. Infrared Millim. Terahertz Waves*, vol. 36, no. 10, pp. 922–946, Oct. 2015.
- [113] *ASHRAE Handbook—Fundamentals: Chapter 26-HEAT, AIR, AND MOISTURE CONTROL IN BUILDING ASSEMBLIES—MATERIAL PROPERTIES*. 2013.
- [114] W. Zhang, H. Min, X. Gu, Y. Xi, and Y. Xing, “Mesoscale model for thermal conductivity of concrete,” *Constr. Build. Mater.*, vol. 98, pp. 8–16, Nov. 2015.
- [115] “<http://www.iesve.com/downloads/help/ve2012/Thermal/ApacheTables.pdf>.” Intergrated Enviromental Solutions limited.
- [116] “<http://www.bd.gov.hk/english/documents/code/OTTV-02.pdf>” .
- [117] “<http://www.redrok.com/concept.htm#emissivity>.” .
- [118] M. Ozel, “Thermal performance and optimum insulation thickness of building walls with different structure materials,” *Appl. Therm. Eng.*, vol. 31, no. 17–18, pp. 3854–3863, Dec. 2011.
- [119] ö. Kaşka and R. Yumrutaş, “Comparison of experimental and theoretical results for the transient heat flow through multilayer walls and flat roofs,” *Energy*, vol. 33, no. 12, pp. 1816–1823, Dec. 2008.

# Appendix

## Appendix A: Infrared camera, FLIR A325

### FLIR A325 (60 Hz)

P/N: 48001-0101



Imaging and optical data	
Field of view (FOV) / Minimum focus distance	25° × 18.8° / 0.4 m (1.31 ft)
Focal length	18 mm (0.7 in.)
Spatial resolution (IFOV)	1.36 mrad
Lens identification	Automatic
F-number	1.3
Thermal sensitivity/NETD	< 0.05°C @ +30°C (+86°F) / 50 mK
Image frequency	60 Hz
Focus	Automatic or manual (built in motor)
Detector data	
Focal Plane Array (FPA) / Spectral range	Uncooled microbolometer / 7.5–13 µm
IR resolution	320 × 240 pixels
Detector pitch	25 µm
Detector time constant	Typical 12 ms
Measurement	
Object temperature range	-20 to +120°C (-4 to +248°F) 0 to +350°C (+32 to +662°F)
Accuracy	±2°C (±3.6°F) or ±2% of reading
Measurement analysis	
Atmospheric transmission correction	Automatic, based on inputs for distance, atmospheric temperature and relative humidity
Optics transmission correction	Automatic, based on signals from internal sensors
Emissivity correction	Variable from 0.01 to 1.0
Reflected apparent temperature correction	Automatic, based on input of reflected temperature
External optics/windows correction	Automatic, based on input of optics/window transmission and temperature
Measurement corrections	Global object parameters
Ethernet	
Ethernet	Control and image
Ethernet type	Gigabit Ethernet
Ethernet standard	IEEE 802.3
Ethernet connector type	RJ-45
Ethernet communication	TCP/IP socket-based FLIR proprietary and GeniCam protocol
Ethernet image streaming	16-bit 320 × 240 pixels - Signal linear - Temperature linear - Radiometric GigE Vision and GeniCam compatible
Ethernet protocols	TCP, UDP, SNMP, RTSP, RTP, HTTP, ICMP, IGMP, FTP, SMTP, SMB (CIFS), DHCP, MDNS (Bonjour), uPnP
Digital input/output	
Digital input purpose	Image tag (start, stop, general), Image flow ctrl. (Stream on/off), Input ext. device (programmatically read)

Digital input	2 opto-isolated, 10–30 VDC
Digital output purpose	Output to ext. device (programmatically set)
Digital output	2 opto-isolated, 10–30 VDC, max 100 mA
Digital I/O isolation voltage	500 VRMS
Digital I/O supply voltage	12/24 VDC, max 200 mA
Digital I/O connector type	6-pole jackable screw terminal
Power system	
External power operation	12/24 VDC, 24 W absolute max
External power connector type	2-pole jackable screw terminal
Voltage	Allowed range 10–30 VDC
Environmental data	
Operating temperature range	-15°C to +50°C (+5°F to +122°F)
Storage temperature range	-40°C to +70°C (-40°F to +158°F)
Humidity (operating and storage)	IEC 60068-2-30/24 h 95% relative humidity +25°C to +40°C (+77°F to +104°F)
EMC	
	<ul style="list-style-type: none"> <li>EN 61000-6-2:2001 (Immunity)</li> <li>EN 61000-6-3:2001 (Emission)</li> <li>FCC 47 CFR Part 15 Class B (Emission)</li> </ul>
Encapsulation	IP 40 (IEC 60529)
Bump	25 g (IEC 60068-2-29)
Vibration	2 g (IEC 60068-2-6)
Physical data	
Weight	0.7 kg (1.54 lb.)
Camera size (L × W × H)	170 × 70 × 70 mm (6.7 × 2.8 × 2.8 in.)
Tripod mounting	UNC 1/4"-20 (on three sides)
Base mounting	2 × M4 thread mounting holes (on three sides)
Housing material	Aluminium
Scope of delivery	
	<ul style="list-style-type: none"> <li>Hard transport case or cardboard box</li> <li>Infrared camera with lens</li> <li>Application CD-ROM</li> <li>Calibration certificate</li> <li>Ethernet™ cable</li> <li>Mains cable</li> <li>Power cable, pig-tailed</li> <li>Power supply</li> <li>Printed Getting Started Guide</li> <li>Printed Important Information Guide</li> <li>User documentation CD-ROM</li> <li>Utility CD-ROM</li> <li>Warranty extension card or Registration card</li> </ul>

© 2010, FLIR Systems, Inc. All rights reserved worldwide. Ref: 48001-0101, ver. 1.05. Generated Thursday, 4 November 2010, (12:30AM). Specifications subject to change without further notice. Camera models and accessories subject to regional market considerations. License procedures may apply. Information and equipment described herein may require US Government authorization for export purposes. D version contrary to US law is prohibited.

Page 1 (of 1)



01E\_0101\_0101



## Appendix B: Thermocouples fundamentals

In 1821, Thomas Seebeck discovered if metals of two different materials were joined at both ends and one end was at a different temperature than the other, a current was created. This phenomenon is known as the Seebeck effect and is the basis for all thermocouples.

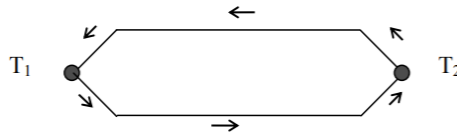


FIGURE 1

A thermocouple is a type of temperature sensor, which is made by joining two dissimilar metals at one end. The joined end is referred to as the HOT JUNCTION. The other end of these dissimilar metals is referred to as the COLD END or COLD JUNCTION. The cold junction is actually formed at the last point of thermocouple material.

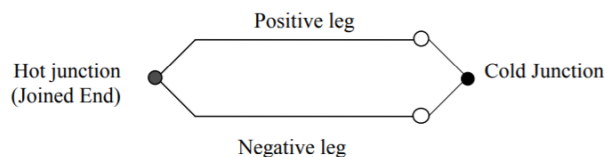


FIGURE 2

Certain combinations of metals must be used to make up the thermocouple pairs. If there is a difference in temperature between the hot junction and cold junction, a small voltage is created. This voltage is referred to as an EMF (electro-motive force) and can be measured and in turn used to indicate temperature.

The voltage created by a thermocouple is extremely small and is measured in terms of millivolts (one millivolt is equal to one thousandth of a volt). In fact, the human body creates a larger millivolt signal than a thermocouple. To establish a means to measure temperature with thermocouples, a standard scale of millivolt outputs was established. This scale was established using 32 deg. F ( $0^{\circ}\text{C}$ ) as the standard cold junction temperature (32 deg. F ( $0^{\circ}\text{C}$ ) = 0 millivolts output).

### COLD JUNCTION COMPENSATION

As we mentioned earlier, the last point of thermocouple material is known as the cold junction. The amount of output the t/c produces is determined by the difference between the hot junction and the cold junction temperatures. The cold junction temperature must be known to accurately determine the temperature.

Let's look at the following examples.

- If we had a thermocouple in a heat treat furnace and wanted to know what temperature it was in that furnace, we could attach a voltmeter to the cold junction and measure the voltage.
- Let's say that the furnace is operating at 1000 deg. F. and it is 100 deg. F at the cool end of the T/C. Since we said that a T/C measures the difference between the hot and cold junctions, our formula would be:

$$1000 \text{ (hot junction)} - 100 \text{ (cold junction)} = 900 \text{ deg. F.}$$

- There seems to be a problem since we said that the furnace was at 1000 deg. F. This brings us to COLD JUNCTION COMPENSATION.

COLD JUNCTION COMPENSATION is usually done automatically by the measuring instrument. The instrument measures the temperature at the cold junction and adds it back to the equation.

$$1000 \text{ (hot junction)} - 100 \text{ (cold junction)} = 900 \text{ deg. F} + 100 \text{ deg. F} \\ \text{(cold junction temp)} = 1000 \text{ deg F}$$

This way the instrument indicates the actual temperature of the hot junction.

This COLD JUNCTION compensator is usually located at the terminals on the back of the indicating instrument and you must maintain T/C material all the way to this point.

For a thermocouple to function properly, there must be no other metals used between the hot junction and the cold junction. If wire is needed to connect the T/C to the indicating instrument, the lead wire must be made of the same material as the T/C. It is acceptable to use terminal blocks and lugs made of plain copper in a thermocouple circuit as long as the positive and negative terminals are at the same temperature. (Example: terminal blocks in heads or spade lugs on wire).

If you were to use plain copper wire instead of T/C extension wire to run to the instrument, your cold junction would be formed at the junction between the copper and the T/C wire. This junction would most likely not be at the same temperature as the back of the instrument where the compensator is located. This would then create an error in the indicated temperature.

If a customer were to use the wrong T/C extension wire, the same problem could appear. This is why we must use the correct T/C extension wire on our assemblies.

It is also acceptable to have a third metal in the hot junction as long as that metal is at the same temperature as the thermocouple material.

### THERMOCOUPLE TYPES

Base metal thermocouples are known as Types E, J, K, T and N and comprise the most commonly used category of Thermocouple. The conductor materials in base metal thermocouples are made of common and inexpensive metals such as Nickel, Copper and Iron.

Type T: The Type T thermocouple has a Copper positive leg and a Constantan negative leg. Type T thermocouples can be used in oxidizing, reducing or inert atmospheres, except the copper leg restricts their use in air or oxidizing environments to 700°F or below. The temperature range for Type T is -330 to 700°F and its wire colour code is blue and red.

## Appendix C: Calibration results of thermocouples

Figure is the calibrated results of 15 thermocouples in Nantes. The calculation method is in the same way with the ones for 17 thermocouples in IUT.

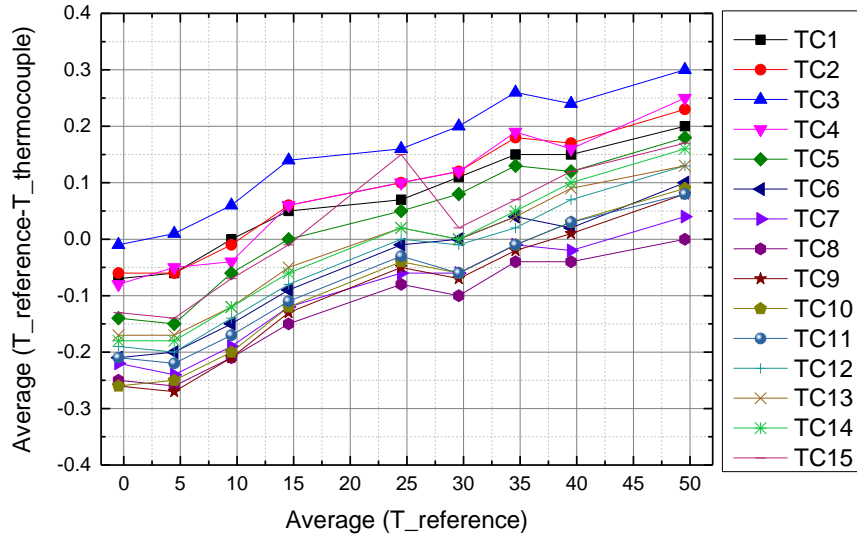


FIGURE 3 Calibrated results of 15 thermocouples in Nantes

Table 1 Calibrated results of 15 thermocouples in Nantes

Thermocouples	$m$	$n$	$R'$	Uncertainty $\Delta T$
TC1	0.0048	-0.036	0.984	0.046
TC2	0.0054	-0.030	0.983	0.047
TC3	0.0055	0.039	0.977	0.043
TC4	0.0057	-0.037	0.979	0.041
TC5	0.0059	-0.095	0.976	0.042
TC6	0.0056	-0.164	0.979	0.043
TC7	0.0048	-0.188	0.974	0.043
TC8	0.0046	-0.208	0.972	0.044
TC9	0.0061	-0.219	0.981	0.045
TC10	0.0062	-0.211	0.985	0.045
TC11	0.0052	-0.175	0.981	0.045
TC12	0.0057	-0.154	0.986	0.045
TC13	0.0053	-0.126	0.981	0.044
TC14	0.0061	-0.140	0.987	0.044
TC15	0.0054	-0.085	0.906	0.044

## Appendix D: Calibration of halogen lamps

The calibration test was implemented in the enclosed climatic chamber without any other radiation (sunlight or lamplight) to reduce the ambient influence.

The intensity sensor, Silicon Pyranometer (SP Lite2) in FIGURE 1, is used. The sensitivity of SP Lite2 is  $67 \text{ uV/Wm}^{-2}$ , the spectral range is from 400-1100 nm and the directional error is less than  $10 \text{ W/m}^2$ . In the calibration test, the SP Lite2 was fixed on the wall surface to measure the heat flux density that the lamps effect on the wall.



FIGURE 4 Silicon Pvrnometer for lambs calibration

Six positions on the wall are selected to calibrate (see positions in FIGURE 2): positions 1-4 are 10 cm away to the wall edges. Position 5 is nearly the largest intensity when irradiated by six lamps, which is about 10 cm upper than position 6. Position 6 is the center of wall, where heat flux sensors and thermocouples are installed.

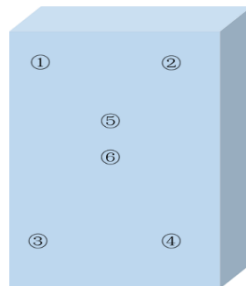
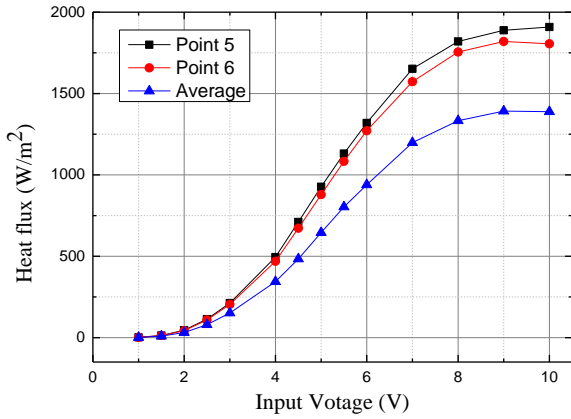


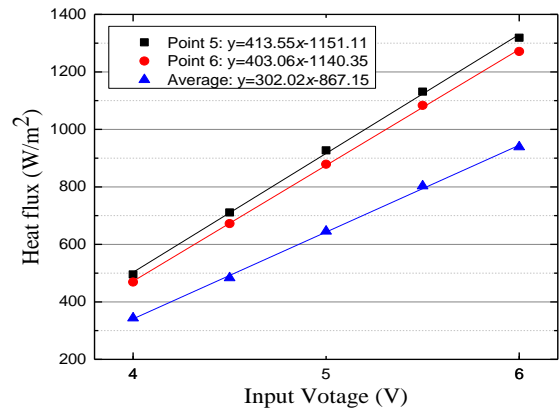
FIGURE 5 6 positions for calibration of lamps

The irradiation intensity of each position is measured by SP Lite2 when the input voltage of lamps varies from 1 V to 10V. FIGURE 6(a) shows the measured heat flux varies with the input voltage when 6 lamps were launched. Obviously, there is a linear relationship between 4V to 6V of input voltage. FIGURE 6(b) shows the fitting curves. With this fitting curves, the irradiation heat flux on the wall is regulated by setting the input voltage when carrying out the thermal properties diagnostic test.

FIGURE 7 and FIGURE 8 show the calibration results of 4 lamps launched and 2 lamps launched respectively.

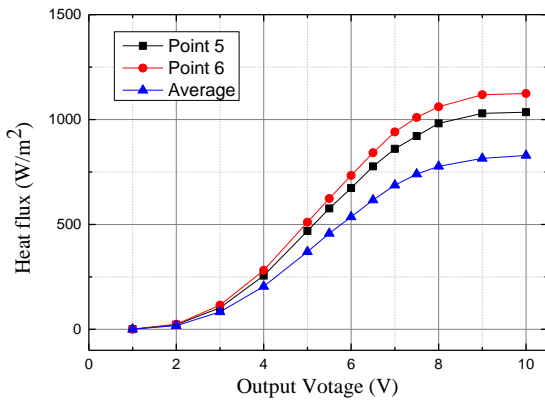


(a)

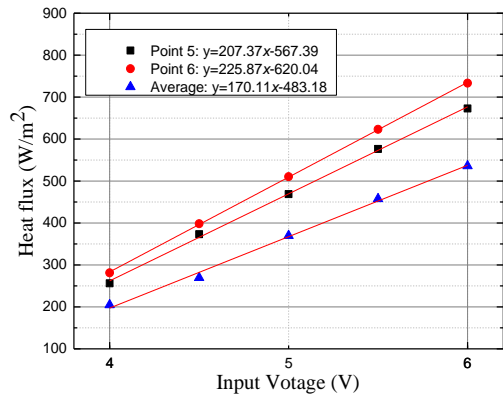


(b)

FIGURE 6 Calibration results: (a) calibration curves of 6 lamps launched. (b) fitting curves between 4V to 6V of input voltage

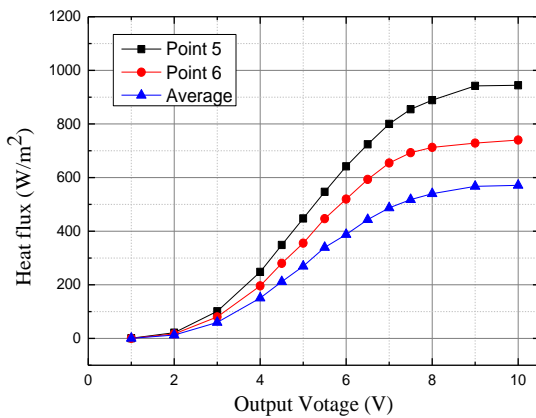


(a)

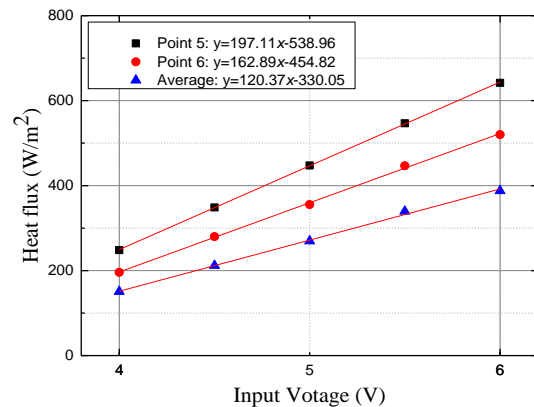


(b)

FIGURE 7 (a): calibration results of 4 lamps launched; (b): fitting function between 4V to 6V of input voltage



(a)



(b)

FIGURE 8 (a): calibration results of 2 lamps launched; (b): fitting function between 4V to 6V of input voltage

## **Appendix E: ISO 18434-1:2008(E)**

### **(a) Standards of emissivity measurement**

#### ***Method 1: contact method***

The procedure for determining the emissivity,  $\epsilon$ , using the contact method shall be as follows.

- a) Place the IRT camera at the desired location and distance from the target to be measured.
- b) Measure and compensate for the target's reflected apparent temperature.
- c) Aim and focus the IRT camera on the target and, if possible, freeze the image.
- d) Use an appropriate camera measurement function (such as spot temperature, cross hairs or isotherms) to define a measurement point or area in the centre of the camera's image.
- e) Use a contact or mirrored thermometer to measure the temperature of the point or area just defined by the camera's measurement function. Note this temperature.
- f) Without moving the camera, adjust the emissivity control until the indicated temperature is the same as the contact temperature just taken. The indicated emissivity value is the emissivity of this temperature target measured with this waveband camera.
- g) For greater accuracy, repeat procedures b) to f) a minimum of three times and average the emissivity values.
- h) Compensate for emissivity by entering the averaged emissivity value in the IRT camera under the emissivity input (commonly referred to as “ $\epsilon$ ”, “emissivity”).

#### ***Method 2: Reference emissivity material method***

The reference emissivity material method is as follows.

- a) Place the IRT camera at the desired location and distance from the target to be measured. Aim and focus the IRT camera on the target.
- b) Measure and compensate for the target's reflected apparent temperature.
- c) Apply the surface-modifying material on or immediately adjacent to the target you are measuring. Make sure the surface modifying material is dry and/or in good contact with the target.
- d) Enter the known emissivity of the surface-modifying material in the emissivity input.

e) Aim and focus the IRT camera on the surface-modifying material, allow enough time for the temperatures to stabilize, freeze the image, and measure and note the indicated temperature.

f) Aim and focus the IRT camera on the target immediately adjacent to the surface-modifying material, or remove the surface-modifying material and aim and focus the camera on the previously modified surface.

Be sure to allow enough time for the temperature to stabilize, freeze the image, and measure and note the indicated temperature.

g) Using the frozen image, adjust the emissivity control until the indicated temperature is the same as the just taken, non-contact temperature of the surface-modifying material. The indicated emissivity value is the emissivity of this temperature target measured with this waveband camera.

h) For greater accuracy, repeat procedures b) to g) a minimum of three times and average the emissivity values.

i) Compensate for emissivity by entering the averaged emissivity value in the IRT camera under the emissivity input (commonly referred to as “ $\epsilon$ ”, “emissivity”)

### **(b) Standards measurement of reflected apparent temperature**

#### ***The reflector method***

The procedure for determining the reflected apparent temperature,  $T_{refl}$ , using the reflector method shall be as follows.

a) Set the IRT camera's emissivity control to 1,00m and distance to 0.

b) Place the IRT camera at the desired location and distance from the target to be measured. Aim and focus the IRT camera on the target.

c) Place the reflector in the field-of-view of the IRT camera. The reflector shall be placed in front of, and in the same plane as, the target surface (see Figure A.1). Maintain a safe working distance from any energised or potentially dangerous targets.

d) Without moving the camera, measure the apparent surface temperature of the reflector with the camera. Note this temperature, which is the reflected apparent temperature,  $T_{refl}$ , of the target.

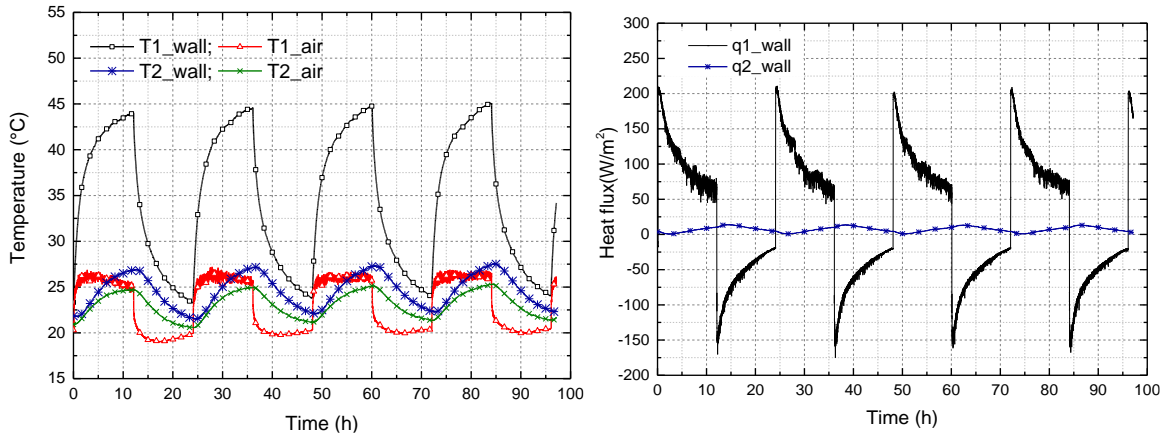
e) For greater accuracy, repeat procedures b) to d) a minimum of three times and average the temperatures.



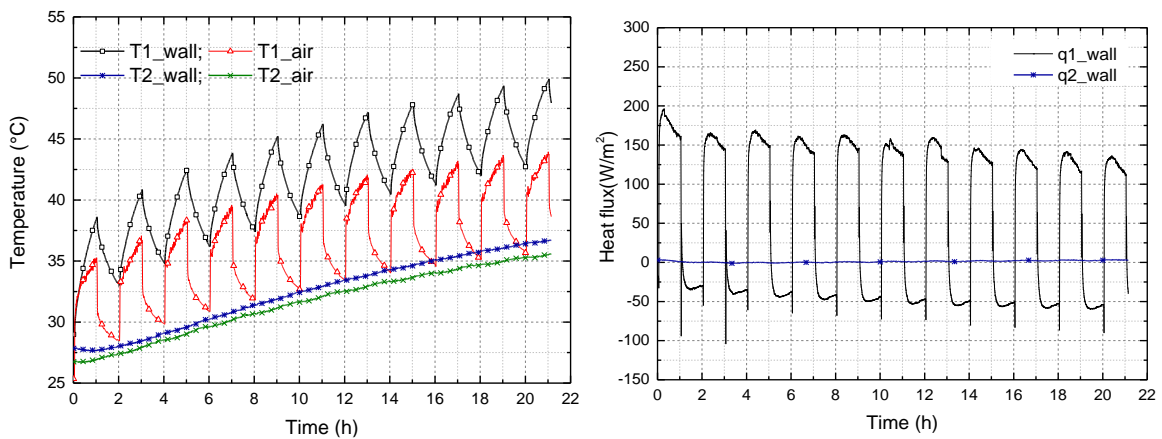
f) Compensate for the reflected apparent temperature by entering the averaged reflected apparent temperature in the IRT camera under the Trefl input (sometimes referred to as “TAM”, “amb. temp.”, “reflected apparent temperature” or “background temperature”).

## Appendix F: Temperature and heat flux results of the laboratory-case ( $T_1$ $T_2$ $q_1$ $q_2$ )

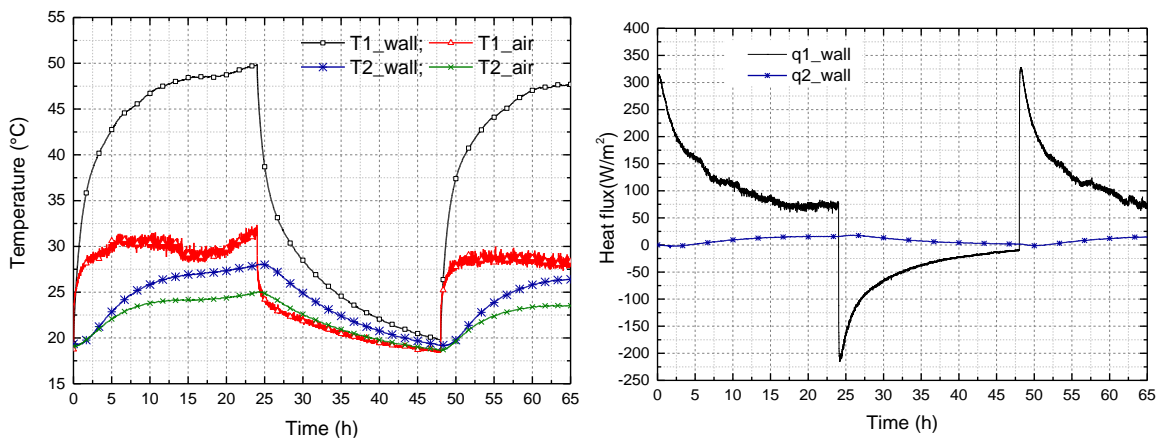
(a) Period of 24h



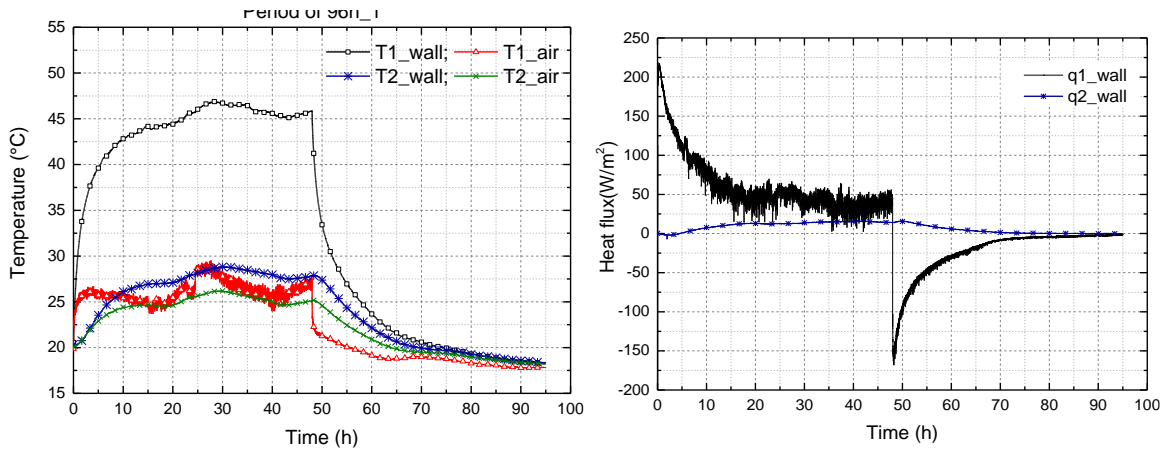
(b) Period of 2h



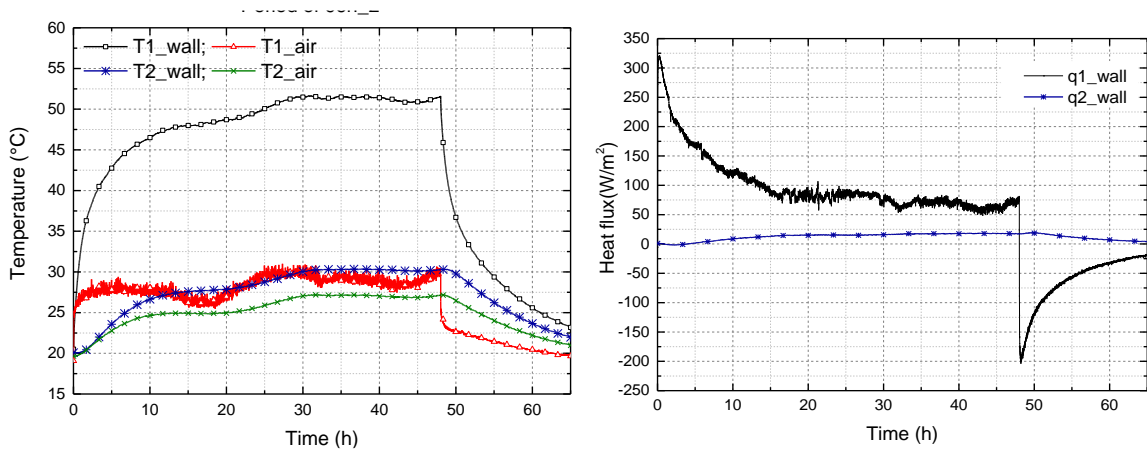
(c) Period of 48h



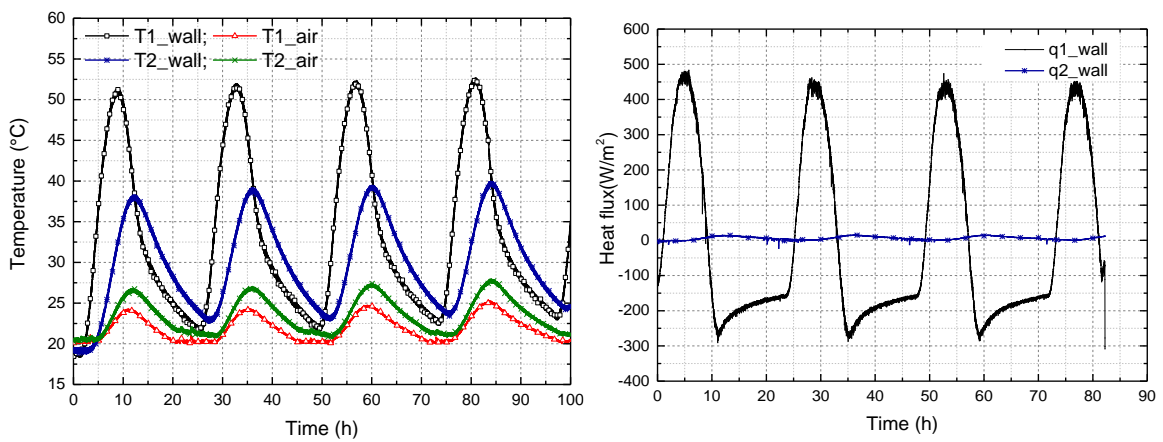
(d) Period of 96h



(e) a step signal

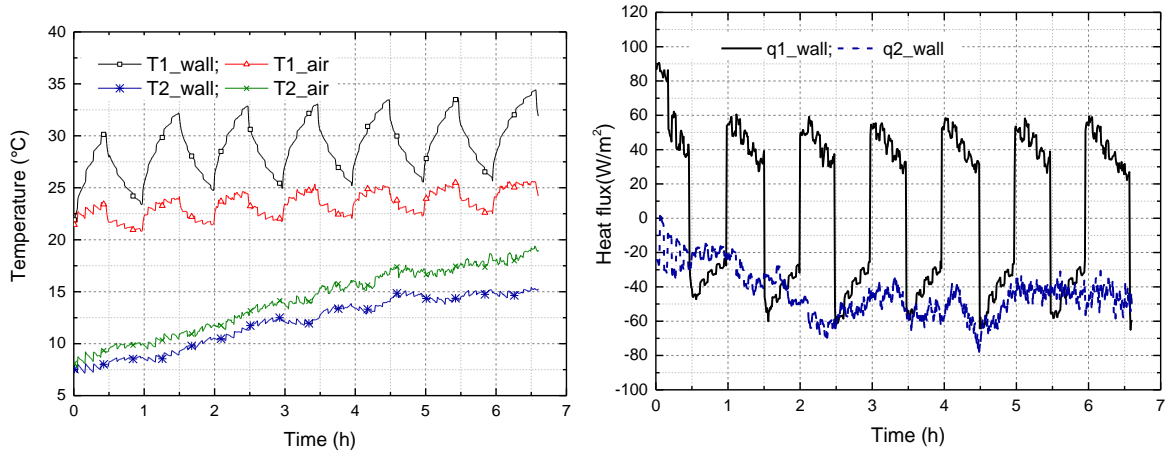


(f) Half sine wave with period of 24h

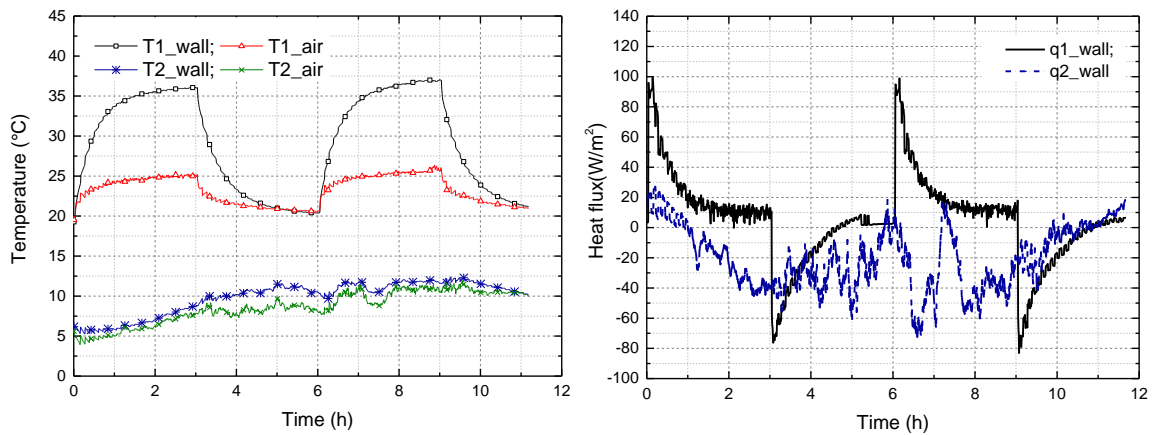


## Appendix G: Temperature and heat flux results of in situ-case ( $T_1$ $T_2$ $q_1$ $q_2$ )

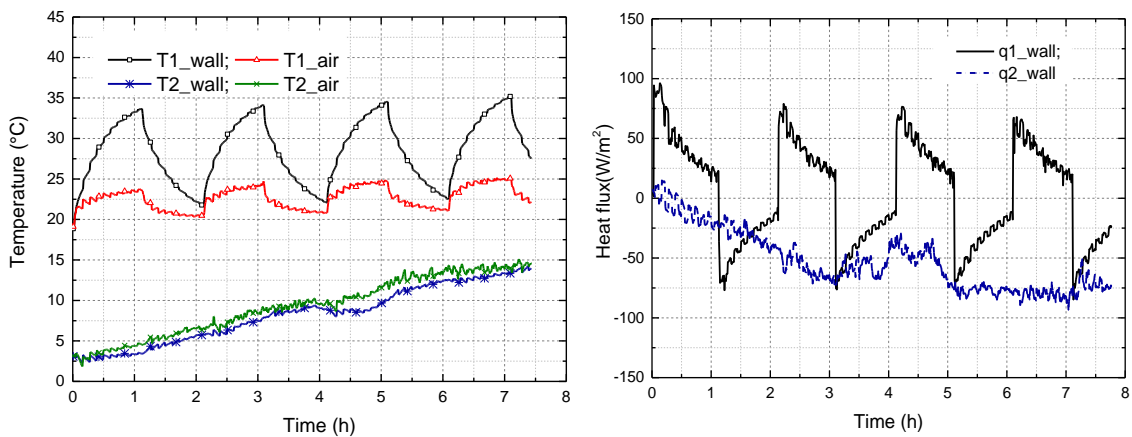
(a) Period of 1h



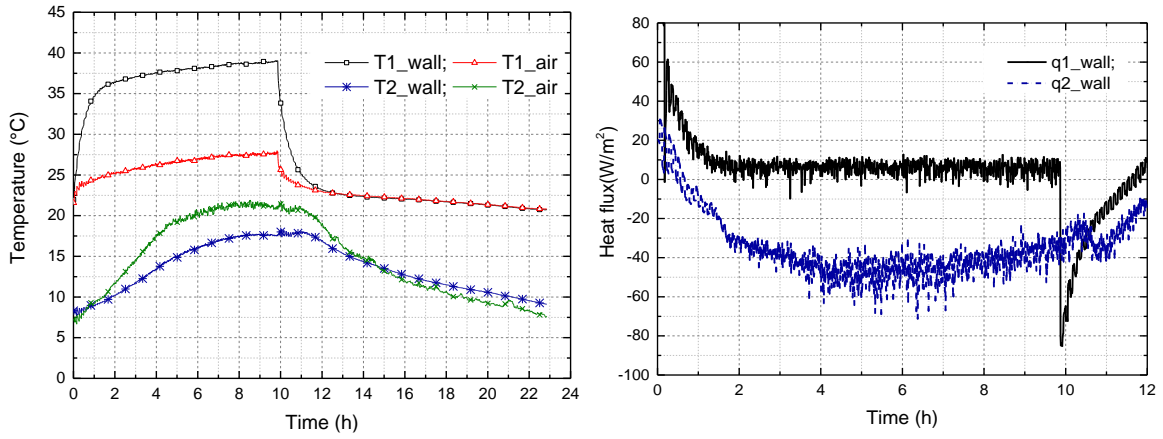
(b) Period of 6h



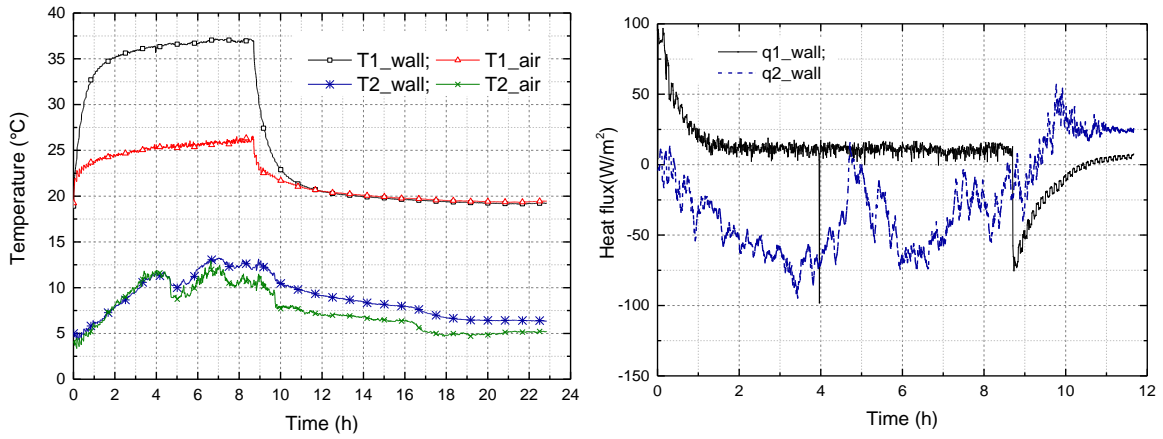
(c) Period of 2h



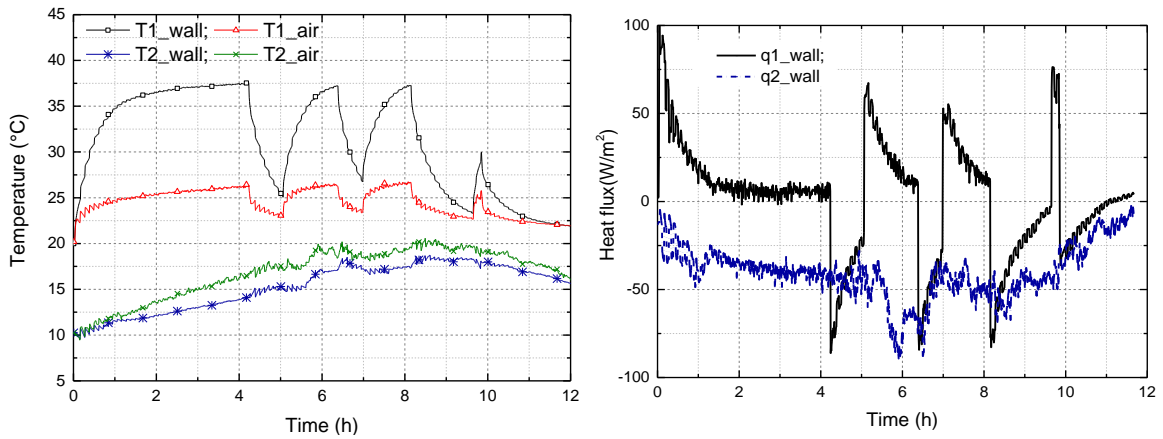
(d) A step signal



(e) A step signal



(f) A random signal



## Appendix H: Absorbance and emissivity values of references

absorbance	absorbance	emissivity	reference
Concrete	0.65		[8],[9][97]
Concrete	0.6	0.88	[117] [99]
wall	0.8		[118], [119]
Mortar	0.8	0.93	[115]
Aluminum Polished	0.2	0.04	[115]
Aluminum	0.09	0.03	[99]
Aluminum Foil	0.15	0.04	[97]
Aluminum Foil	0.15	0.05	[117] [99]
Aluminum Polished	0.1	0.038-0.6	[97]
Copper	(tarnished) 0.65	Polished 0.02 oxidised 0.6	[115]
Copper	0.40 - 0.65	0.2-0.3	[117]
Polished copper	0.18	0.03	[99]
Polished copper	0.18	0.05	[97]
Black paint	0.97	0.97	[99]

## Appendix I: Usual Laplace transform

f(t)	F(p)
Constant a	$a/p$
$t^n; n = 1, 2, 3 \dots$	$\frac{n!}{p^{n+1}}$
$\sqrt{t}$	$\frac{\sqrt{\pi}}{2p^{1.5}}$
$1/\sqrt{\pi t}$	$1/\sqrt{p}$
$\frac{2}{\sqrt{\pi}}\sqrt{t}$	$\frac{1}{p\sqrt{p}}$
$1 - e^{-at}$	$\frac{a}{p(p+a)}$
$\exp(at)$	$\frac{1}{(p-a)}$
$\operatorname{erf}(\sqrt{t})$	$\frac{1}{p\sqrt{p+1}}$
$\frac{1}{\sqrt{\pi t}}\exp(-\frac{x^2}{4t})$	$\exp(-x\sqrt{p})/\sqrt{p}; x \geq 0$
$\cos(at)$	$\frac{p}{(p^2 + a^2)}$
$\sin(at)$	$\frac{a}{(p^2 + a^2)}$
$\cos h(at)$	$\frac{p}{(p^2 - a^2)}$
$\sin h(at)$	$\frac{a}{(p^2 - a^2)}$

## Appendix J: Matlab algorithm

The `Lsqnonlin` function in Matlab is used for the optimization of experimental data and model estimated data in order to obtain the unknown parameters. Levenberg-marquardt algorithm is called for this computation.

The function  $(T_{exp} - T_{cal})$  is minimized.

The code of function call is:

```
[U, resnorm, residual, exitflag, output]=lsqnonlin('myfun',U_0, [], [], options)
```

Where `U` is the output solution, which returned as a real vector or real array. Typically, `U` is a local solution to the problem when `exitflag` positive.

'`myfun`' is the function of difference between experimental data and model estimated data

'`U_0`' is the initial input array of `U`.

'`resnorm`' is the squared norm of the residual

'`residual`' is the value of objective function at solution

'`exitflag`' is reason the solver stopped

'`output`' is information about the optimization process, including:

Output information of Matlab

<code>firstorderopt</code>	Measure of first-order optimality
<code>iterations</code>	Number of iterations taken
<code>funcCount</code>	The number of function evaluations
<code>cgiterations</code>	Total number of PCG iterations (trust-region-reflective algorithm only)
<code>stepsize</code>	Final displacement in <code>x</code>
<code>algorithm</code>	Optimization algorithm used
<code>message</code>	Exit message



